

Bayesian Hierarchical Modelling of Young Stellar Clusters

DISSERTATION

**Submitted in Partial Fulfillment of
the Requirements for
the Degree of**

DOCTOR OF PHILOSOPHY (Astrophysics)

at the

**University of Grenoble Alpes
National University of Distance Education**

by

Javier Olivares Romero

July 2017

Abstract

The origin and evolution of stellar populations is one of the greatest challenges in modern astrophysics. It is known that the majority of the stars has its origin in stellar clusters (Carpenter 2000; Porras et al. 2003; Lada & Lada 2003). However, only less than one tenth of these clusters remains bounded after the first few hundred million years (Lada & Lada 2003). Ergo, the understanding of the origin and evolution of stars demands meticulous analyses of stellar clusters in these crucial ages.

The project Dynamical Analysis of Nearby Clusters (DANCe)¹, from which the present work is part of, provides the scientific framework for the analysis of Nearby Young Clusters (NYC) in the solar neighbourhood (≤ 500 pc). The DANCe carefully designed observations of the well known Pleiades cluster provide the perfect case study for the development and testing of statistical tools aiming at the analysis of the early phases of cluster evolution.

The statistical tool developed here is a probabilistic intelligent system that performs Bayesian inference for the parameters governing the Probability Density Function of the Cluster Population (PDFCP). It has been benchmarked with the Pleiades photometric and astrometric data of the DANCe survey. As any Bayesian framework, it requires the setting up of prior probabilities of its parameters. To avoid most of the subjectivity of these priors, the intelligent system establish them using the Bayesian Hierarchical Model (BHM) approach. In it, the parameters of prior distributions, which are also inferred from the data, are drawn from other distributions in a hierarchical way.

In this BHM intelligent system, the true values of the PDFCPs are specified by stochastic and deterministic relations representing the state of knowledge of the NYC. To perform the parametric inference, the likelihood of the data, given these true values, accounts for the properties of the data set, especially its heteroscedasticity and missing value objects. By accounting for these properties, the intelligent system: i) Increases the size of the data set, with respect to previous studies working exclusively on fully observed objects, and ii) Reduces the biases associated to fully observed data sets, and restrictions to low-uncertainty objects (σ -clipping procedures).

The BHM returns the posterior Probability Density Functions (PDFs) of the parameters in the PDFCPs, particularly of the spatial, proper motions and luminosity distributions. In the BHM each object in the data set contributes to the PDFs of the parameters proportionally to its likelihood. Thus, the PDFCPs are free of biases resulting from typical high membership probability selections (sampling bias).

As a by-product, the BHM also gives the PDFs of the cluster membership probability for each object in the data set. These PDFs together with an optimal probability classification threshold, which is obtained from synthetic data sets, allow the classification of objects into cluster and field populations. This by-product classifier shows excellent results when

¹<http://project-dance.com>

applied on synthetic data sets (with an area under the Receiver Operating Characteristic (ROC) curve of 0.99). From the analysis of synthetic data sets, the expected value of the contamination rate for the PDFCPs is $5.8 \pm 0.2\%$.

The following are the most important astrophysical results of the BHM applied to the Pleiades cluster. First, used as a classifier, it finds ~ 200 new candidate members, representing 10% new discoveries. Nevertheless, it shows outstanding agreement (99.6% of the 10^5 objects in the data set) with previous results from the literature. Second, the derived Present-Day System Mass Distribution (PDSMD) is in general agreement with the previous results of [Bouy et al. \(2015\)](#).

Thus, by better modelling the data set and eliminating unnecessary restrictions to it, the new intelligent system, developed and tested in the present work, represents the state of the art for the statistical analysis of NYC populations.

French abstract

Il semble maintenant établi que la majorité des étoiles se forment dans des amas (Carpenter 2000; Porras et al. 2003; Lada & Lada 2003). Comprendre l'origine et l'évolution des populations stellaires est donc l'un des plus grands défis de l'astrophysique moderne. Malheureusement, moins d'un dixième de ces amas restent gravitationnellement liés au delà de quelques centaines de millions d'années (Lada & Lada 2003). L'étude des amas stellaires doit donc se faire avant leur dissolution dans la galaxie.

Le projet Dynamical Analysis of Nearby Clusters (DANCe)², dont le travail fait partie, fournit le cadre scientifique pour l'analyse des amas proches et jeunes (NYC) dans le voisinage solaire. Les observations de l'amas ouvert des Pléiades par le projet DANCe offrent une opportunité parfaite pour le développement d'outils statistiques visant à analyser les premières phases de l'évolution des amas.

L'outil statistique développé ici est un système intelligent probabiliste qui effectue une inférence bayésienne des paramètres régissant les fonctions de densité de probabilité de la population de l'amas (PDFCP). Il a été testé avec les données photométriques et astrométriques des Pléiades du relevé DANCe. Pour éviter le plus possible la subjectivité de ces choix des priors du parameters, le système intelligent les établit en utilisant l'approche hiérarchique bayésienne (BHM). Dans ce cas, les paramètres de ces distributions, qui sont également déduits des données, proviennent d'autres distributions de manière hiérarchique.

Dans ce système intelligent BHM, les vraies valeurs du PDFCPs sont spécifiées par des relations stochastiques et déterministes représentatives de notre connaissance des paramètres physiques de l'amas. Pour effectuer l'inférence paramétrique, la vraisemblance (compte tenu de ces valeurs réelles), tient en compte des propriétés de l'ensemble de données, en particulier son hétérosécédasticité et des objects avec des valeurs manquantes.

Le BHM obtient les PDF postérieures des paramètres dans les PDFCPs, en particulier celles des distributions spatiales, de mouvements propres et de luminosité, qui sont les objectifs scientifiques finaux du projet DANCe. Dans le BHM, chaque étoile du catalogue contribue aux PDF des paramètres de l'amas proportionnellement à sa probabilité d'appartenance. Ainsi, les PDFCPs sont exempts de biais d'échantillonnage résultant de sélections tronquées au-dessus d'un seuil de probabilité défini plus ou moins arbitrairement.

Comme produit additionnel, le BHM fournit également les PDF de la probabilité d'appartenance à l'amas pour chaque étoile du catalogue d'entrée, qui permettent d'identifier les membres probables de l'amas, et les contaminants probables du champ. La méthode a été testée avec succès sur des ensembles de données synthétiques (avec une aire sous la courbe ROC de 0,99), ce qui a permis d'estimer un taux de contamination pour les PDFCPs de seulement 5,8 %.

Ces nouvelles méthodes permettent d'obtenir et/ou de confirmer des résultats impor-

²<http://project-dance.com>

tants sur les propriétés astrophysiques de l'amas des Pléiades. Tout d'abord, le BHM a découvert 200 nouveaux candidats membres, qui représentent 10% de la population totale de l'amas. Les résultats sont en excellent accord (99,6% des 100 000 objets dans l'ensemble de données) avec les résultats précédents trouvés dans la littérature, ce qui fournit une validation externe importante de la méthode. Enfin, la distribution de masse des systèmes actuelle (PDSMD) est en général en bon accord avec les résultats précédents de [Bouy et al. \(2015\)](#), mais présente l'avantage inestimable d'avoir des incertitudes beaucoup plus robustes que celles des méthodes précédentes.

Ainsi, en améliorant la modélisation de l'ensemble de données et en éliminant les restrictions inutiles ou les hypothèses simplificatrices, le nouveau système intelligent, développé et testé dans le présent travail, représente l'état de l'art pour l'analyse statistique des populations de NYC.

Contents

Abstract	ii
French abstract	iv
1 Introduction	1
1.1 The initial mass function of stellar clusters	2
1.2 Numerical simulations of the early stages of star formation	7
1.3 The DANCe project	8
1.4 Methodologies for the classification of cluster members	11
1.5 A new intelligent system: the Bayesian Hierarchical Model	17
2 The Pleiades as a benchmark	20
2.1 Generalities	20
2.2 The distance to the Pleiades	20
2.3 Projected spatial distribution	23
2.4 Velocity Distribution	25
2.5 Luminosity Distribution	29
2.6 Mass Distribution	33
2.7 The Pleiades DANCe DR2	38
2.8 The Restricted DANCe Data Release 2 (RDDR2)	52
2.9 The Tycho+DANCe candidate members	54
3 Bayesian formalism	59
3.1 Introduction to probability theory.	59
3.2 Bayesian Hierarchical Models	69
3.3 The BHM for the Pleiades DANCe data set	71
3.4 Priors	103
3.5 Sampling the posterior distribution	113
3.6 Codes	122
3.7 The methodology for the analysis of the PSD	128
4 Results	137
4.1 Performance of the classifier	137
4.2 Comparison with the literature	146

4.3	The statistical distributions of the Pleiades.	158
4.4	Projected spatial distribution	162
4.5	Proper motions distribution	170
4.6	Luminosity distribution	176
4.7	Mass distribution	179
4.8	The mass distribution on time	186
4.9	Updating priors and assumptions	191
5	Conclusions and future work	194
5.1	Current issues and future improvements	196
A	Posterior distributions of the PSD	199
A.1	Models with radial symmetry	200
A.2	Models with biaxial symmetry	200
A.3	Models with luminosity segregation	212
Bibliography		212
Acronyms		232

Chapter 1

Introduction

The majority of the stars are born together. Carpenter (2000) reports that 50 – 70% of very young, ≤ 10 millions of years (Myr), and 25 – 70% of the young, ≤ 100 Myr, stellar populations are formed in groups. Porras et al. (2003) and Lada & Lada (2003) find that among 80% to 90% of the stars are formed in groups with more than 100 members, which are called star clusters. Furthermore, as indicated by the former authors, these populous clusters represent 22% of the regions where stars form. The remaining of the star forming regions are small associations, with 5 to 30 members, where only up to 10% of the stars are formed. However, only less than 7% of these populous clusters survives as gravitationally bounded clusters when reaching an age of a few hundred Myr (Lada & Lada 2003). The remaining 93% of the star forming regions will become unbound and their stars will freely populate the galaxy. Thus, to understand the general rules that govern how the majority of stars forms, as well as the properties of the stars that populate our galaxy, it is crucial to fully decode the formation and early evolution of stellar clusters.

Astrophysicists, like archeologists and palaeontologists, can not willingly reproduce the vast majority of their studied phenomena. Although some experiments can be performed in specific situations (e.g. the chemical and physical properties of dust and gas), astrophysics remains an observational science. For this reason, to test the validity of their hypotheses, astrophysicists rely on statistical studies carried out over carefully designed observations. In particular, the understanding of the star formation process requires carefully designed observations of stellar clusters whose ages cover the early stages of their evolution.

The objective of this work is the construction, test and validation of a statistical tool, an intelligent system specifically, that given the carefully designed data of a stellar cluster, recovers the statistical distributions of its populations. In particular, it should deliver the cluster luminosity distribution, which can be transformed into the mass distribution given an evolutionary model and the cluster age. The mass distribution is a fundamental product of the star formation process. It contains the fingerprints of the early phases of star formation and subsequent cluster evolution.

An homogeneous and precise mass distribution inventory for clusters of diverse ages

and forming environments will allow the astrophysical community to test the current theories of the star formation process. In particular, it will allow to solve the questions about universality of the Initial Mass Function (IMF) (see next Section) and the role played by the physical properties of the cluster environment.

The remaining of this Chapter is structured as follows. In Section 1.1, I describe the importance of the initial mass distribution and some of its current models. In Section 1.2, I report the current status of numerical simulations of cluster formation and its impact on the understanding of the star formation process. In Section 1.3, I describe the project DANCe, its objectives and its carefully designed observations of stellar clusters. This work is part of that project and makes use of its observations. In Section 1.4, I comment on the past and current methodologies to select members of clusters and associations. Finally in Section 1.5, I briefly describe the methodology adopted for this new statistical tool, and its advantages over the previous works.

1.1 The initial mass function of stellar clusters

In his seminal work ([Salpeter 1955](#)), Edwin Salpeter defined the *original mass function*, $\xi(M)$, as

$$dN = \xi(M)d(\log_{10} M)\frac{dt}{T_0},$$

where dN is the number of stars in the mass range dM created in the time interval dt per cubic parsec, and T_0 is the age of the galaxy. Following [Chabrier \(2003a\)](#), the Mass Function (MF) at the observed time t , is

$$\xi(\log_{10} M) = \frac{dN}{d(\log_{10} M)},$$

where N is the stellar number density, and M the mass. The IMF is defined as the MF at the time of stellar formation $t = t_0$. The logarithmic transformation of the mass,

$$\xi(M) = \frac{1}{M \ln 10} \xi(\log_{10} M),$$

is convenient due to the large range of masses covered by the star formation process.

Notice that neither the IMF nor the MF are probability PDFs of the mass (see Section 3.1 for the definition of a PDF). Nevertheless, they can be transformed into PDFs by a normalisation constant, which can be computed by integrating them as functions of the mass over the mass domain. In this work, I will use the Mass Distribution (MD) in the logarithmic scale, denoted by $\xi_L(\log_{10} M)$, as a proxy for the MF. Thus,

$$\xi_L(\log_{10} M) \propto \xi(\log_{10} M).$$

The measuring and understanding of the IMF is a central topic in the study of star formation. It is also essential in other areas of astrophysics, from planetary formation, where it appears that the mass of the host star plays an important role in the formation of the planetary system (see for example [Mulders et al. 2015](#)), to galactic evolution ([Kennicutt 1998](#)) and cosmology (see for example [Narayanan & Davé 2012](#)).

The theories that predict the origin of the IMF can be categorised into deterministic and stochastic ([Offner et al. 2014](#)). The former postulate that stellar masses are deterministically inherited from the initial core masses via accretion from the gas reservoir of the parent molecular cloud. Thus, the IMF can be directly mapped from the distribution of initial core masses, and the understanding of the former reduces to that of the latter. On the other hand, stochastic models postulate that the stellar masses are independent of the initial core masses. Among these models, there are those proposing that stellar masses are determined by dynamical interactions and competitive accretion. For more details see [Offner et al. \(2014\)](#) and references therein.

The observational studies of the IMF are conditioned on the ages of the stellar populations under analysis (their MF at their corresponding ages), and rely deeply on the assumed processes that link the observed present-day MF to the IMF. While the resulting models for the IMF are analytical functions of the mass, the observed MF are commonly expressed with points, histograms or Kernel Density Estimators (KDEs)¹.

The most common forms to describe the IMF are the power-law functions of Salpeter ([Salpeter 1955](#)), Miller and Scalo ([Miller & Scalo 1979](#)), and Kroupa ([Kroupa 2001, 2002; Kroupa et al. 2013; Thies & Kroupa 2007, 2008](#)), and the log-normal functions of Chabrier ([Chabrier 2003b,a, 2005](#)). Other functional forms include the truncated exponential ([de Marchi & Paresce 2001](#)), the Pareto-Levy family distribution ([Cartwright & Whitworth 2012](#)), and a log-normal with power-laws at high and low mass ranges ([Maschberger 2013](#)). For the sake of simplicity, I will only explain the classical ones of Salpeter, Chabrier, and Kroupa.

[Salpeter \(1955\)](#) derived his famous IMF using a luminosity function resulting from the compilation of the works of [Luyten \(1939, 1941\)](#) and [van Rhijn \(1925, 1936\)](#). Then, he transformed it into a MF using a mass-luminosity relation that he obtained after adopting a series of masses and luminosities from the literature. His MF has the form

$$\xi(M) = 0.03 \left(\frac{M}{M_{\odot}} \right)^{-1.35},$$

with M in the range $0.3 M_{\odot}$ to $17 M_{\odot}$. Its units are $M_{\odot}^{-1} \cdot pc^{-3}$.

[Chabrier \(2003b,a\)](#) derived his Present-Day Mass Function (PDMF) from the nearby luminosity functions of both the V band ([Dahn et al. 1986](#)) and the K band ([Henry & McCarthy 1990](#)) for the solar neighbourhood (≤ 5 pc). He used the [Delfosse et al. \(2000\)](#)

¹KDEs are non-parametric ways to estimate a probability density function by means of an independently and identically distributed sample drawn from it.

and Baraffe et al. (1998) mass-magnitude relations in V and K bands, respectively, to transform the luminosity functions into masses. Then, he fitted a log-normal form to the single objects with masses below $1 M_{\odot}$. The PDMF he found, in units of $(\log M_{\odot})^{-1} \cdot pc^{-3}$, is

$$\xi(\log m)_{m \leq 1M_{\odot}} = 0.158_{-0.046}^{+0.051} \times \exp \left\{ -\frac{(\log m - \log 0.079_{-0.016}^{+0.021})^2}{2 \times (0.69_{-0.01}^{+0.05})^2} \right\}.$$

As shown by Scalo (1986), $1 M_{\odot}$ is the limit at which the PDMF starts to differ from the IMF. Therefore, Chabrier (2003a) uses his PDMF as the IMF below the $1 M_{\odot}$ limit. Above it, he adopts the Salpeter IMF,

$$\xi(\log m)_{m > 1M_{\odot}} = 4.43 \times 10^{-2} \cdot m^{-1.3 \pm 0.3}.$$

As shown by Kroupa et al. (1991), the discrepancies between the luminosity functions derived from photographic samples and from trigonometric parallaxes of nearby stars can be accounted with unresolved binaries. For this reason, Chabrier (2003b) derived the Present-Day System Mass Function (PDSMF) for unresolved systems. It takes into account each object as a possible unresolved binary or system. This PDSMF has the form,

$$\xi(\log m)_{m \leq 1M_{\odot}} = 0.086 \times \exp \left\{ -\frac{(\log m - \log 0.22)^2}{2 \times (0.57)^2} \right\},$$

with the same normalisation and coefficients of the IMF above $1 M_{\odot}$.

Later, Chabrier (2005) included in his analysis the revision that Reid et al. (2002) made to the sample of (Dahn et al. 1986), and the extended sample of 8 pc from Reid et al. (2004). His new PDMF is

$$\begin{aligned} \xi(\log m)_{m \leq 1M_{\odot}} &= 0.093 \times \exp \left\{ -\frac{(\log m - \log 0.2)^2}{2 \times (0.55)^2} \right\}, \\ \xi(\log m)_{m > 1M_{\odot}} &= 0.041 \times m^{-1.3 \pm 0.3}. \end{aligned}$$

And his new PDSMF is

$$\begin{aligned} \xi(\log m)_{m \leq 1M_{\odot}} &= 0.076 \times \exp \left\{ -\frac{(\log m - \log 0.25)^2}{2 \times (0.55)^2} \right\}, \\ \xi(\log m)_{m > 1M_{\odot}} &= 0.041 \times m^{-1.3 \pm 0.3}. \end{aligned} \tag{1.1}$$

The canonical IMF of Kroupa (Kroupa et al. 2013) is a three-segment power-law, with two segments describing the IMF of the stars, while the third does it for Brown Dwarfs

(BD)². It has the following analytical representation

$$\xi_{BD}(m) = \frac{k}{3} \cdot \left(\frac{m}{0.07} \right)^{-0.3 \pm 0.4}, \quad 0.01M_\odot < m \leq 0.15M_\odot, \quad (1.2)$$

$$\begin{aligned} \xi(m) &= k \cdot \left(\frac{m}{0.07} \right)^{-1.3 \pm 0.3}, & 0.07M_\odot < m \leq 0.5M_\odot, \\ \xi(m) &= k \cdot \left(\frac{0.5}{0.07} \right)^{-1.3 \pm 0.3} \cdot \left(\frac{m}{0.5} \right)^{-2.3 \pm 0.36}, & 0.5M_\odot < m \leq 150M_\odot, \end{aligned} \quad (1.3)$$

where k is a constant.

[Thies & Kroupa \(2007\)](#) explored the parametric space of the IMF for the BD population. They performed a χ^2 fit of the maximum BD mass ($m_{max,BD}$), the slope of the BD IMF (α_{BD} in Eq. 1.2), and the population ratio (\mathcal{R}_{pop}), which is the ratio of individual BD to individual stars. They performed this fit on literature data from the Trapezium, Taurus, IC 348 and the Pleiades nearby clusters. Figure 1.1, which reproduces their Figure 7, shows their results in these four clusters. In their work, the stellar IMF is the canonical one (Eq. 1.3). In the case of the Pleiades and IC 348, the slope of the BD IMF remained the canonical value $\alpha_{BD} = 0.3$ due to the sparse data, and the Pleiades incomplete data particularly. The resulting system IMF is also shown as the solid curve. It results from the addition of the two IMFs (BD and stars) but without an overlap or discontinuity between them (see [Thies & Kroupa 2007](#), for details).

As shown in this Section, the IMF has been the subject of several studies which have transformed our knowledge about it. This knowledge evolved from the simple and efficient model of [Salpeter \(1955\)](#) in the high mass range, to the more complicated and still controversial models of [Thies & Kroupa \(2007\)](#); [Kroupa et al. \(2013\)](#) for the BD and low-mass stars. In the literature, the IMF of Chabrier ([Chabrier 2003b,a, 2005](#)) is often the preferred one. Although these models currently explain many of the observed phenomena, our knowledge of the physical processes that lead to the observed IMF is still incomplete. In an attempt to address the latter, the numerical simulations of the star formation process have done great progress. The next section is a tiny review of what these simulations have achieved in the past years.

²Brown-dwarfs are substellar objects with masses in the range from 10 to 80 Jupiter masses ($0.01M_\odot$ to $0.075 M_\odot$). Because there is no fusion of hydrogen in their cores, these objects are not classified as stars.

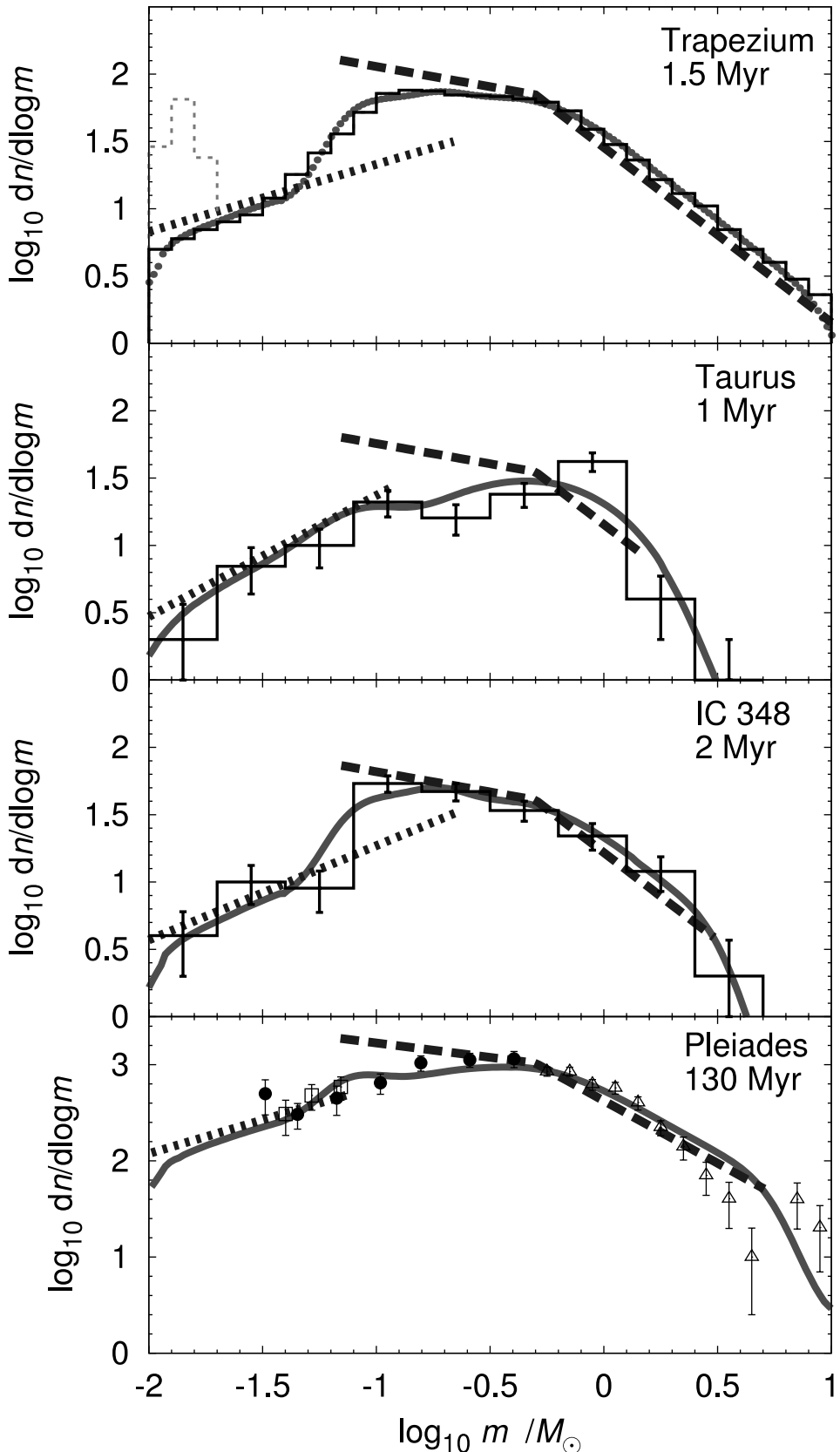


Figure 1.1: Observed mass distribution (histograms and dots) of the Trapezium, Taurus, IC348 and the Pleiades nearby clusters (from top to bottom). Also shown are the canonical stellar (long dashed line), fitted BD (dotted), and system (solid curve) IMFs of Thies & Kroupa (2007) . Reproduced from Figure 7 of Thies & Kroupa (2007), *A Discontinuity in the Low-Mass Initial Mass Function*, ApJ, Vol. 671

1.2 Numerical simulations of the early stages of star formation

In the first decade of this century, numerical simulations of star forming regions have proven to be of paramount importance in decoding the very early stages of the star formation process (e.g [Bate et al. 2003](#); [Jappsen et al. 2005](#); [Bate 2009a,c,b](#)). For example, [Bate et al. \(2003\)](#) using smooth particle hydrodynamics were able to simulate the collapse and fragmentation of a large-scale ($50 M_{\odot}$ within 0.375 pc radius) turbulent molecular cloud to form a stellar cluster. During the very first 0.1 Myr, which was the time covered by their simulation, they were able to simultaneously form discs and binary stars. The cloud formed roughly equal numbers of stars and BD (23 and 27, respectively) resulting in a mass distribution with a flat slope in the range $0.01 - 0.5 M_{\odot}$ (see Fig. 1.2). [Offner et al. \(2014\)](#) provides a review of the stellar initial mass distribution, and of the physical effects included in numerical simulations (radiative feedback, competitive accretion, dynamical interactions, magnetic fields) particularly.

In recent years, the works of [Kuznetsova et al. \(2015\)](#) and [Ballesteros-Paredes et al. \(2015\)](#), using the cold collapse paradigm (neglecting magnetic fields, radiative transfer and feedback), were able to probe that the main source driving the star formation process is gravity. Their simulations were typically run until 0.85 Myr in a box of 3 pc of side, and with masses in the few thousands of M_{\odot} . The mass distribution obtained by [Kuznetsova et al. \(2015\)](#) reproduces reasonably well the current models of the initial mass distribution. In particular, the IMF of [Chabrier \(2005\)](#) down to $0.1 M_{\odot}$ (see Fig. 1.3). However, they produce too few low-mass stars and brown dwarfs.

Numerical simulations are of great use in the understanding of the star formation process, in the very early phases (≤ 1 Myr) of its evolution particularly. Despite the fact that many of these simulations are in agreement with the observed mass distributions, currently they i) do not incorporate all astrophysical effects, ii) resolve close binaries and multiple systems, and iii) produce enough stellar objects to improve the statistics ([Offner et al. 2014](#)). Furthermore, these simulations require input from the observations (e.g. density, turbulence and magnetic fields in the molecular cloud). More importantly, they require feedback from the observations in order to fine tune the parameters of the physical processes. Real and simulated data must be compared in order to improve the latter. Thus, to constrain the current theories of the star formation process, precise and detailed studies of the early phases of cluster formations are still required. This is the objective of the DANCe project, from which the present work is part of.

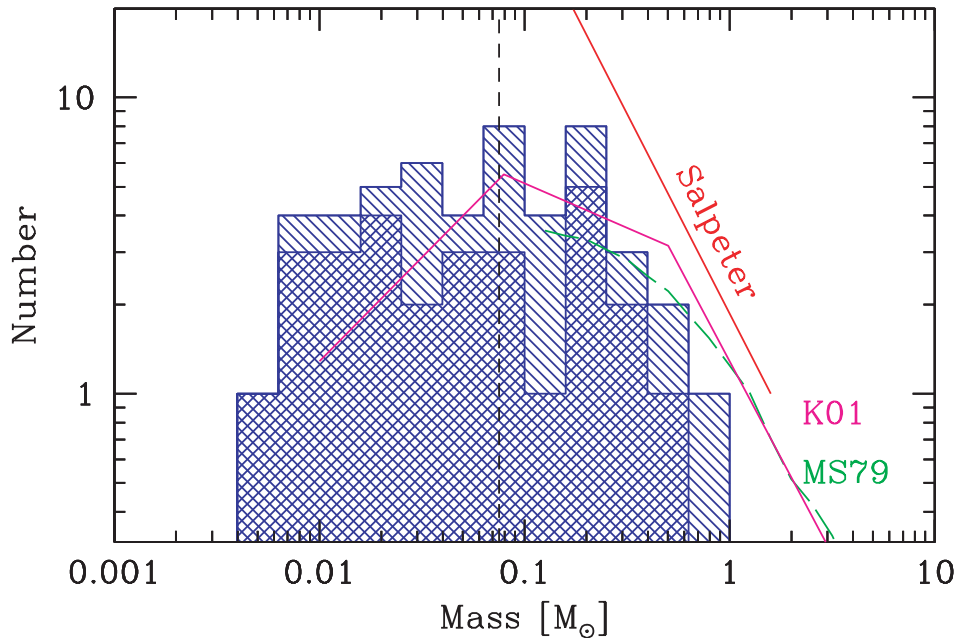


Figure 1.2: Mass distribution resulting from the numerical simulation of Bate et al. (2003). The lines show the mass distributions of Salpeter (1955), Miller & Scalo (1979) and Kroupa (2001). Reproduced from Figure 10 of Bate et al. (2003), *The formation of a star cluster: predicting the properties of stars and brown dwarfs*, MNRAS, Vol. 339

1.3 The DANCe project

The DANCe³ project is an international and multidisciplinary collaboration of researchers whose main objective is *unravelling the origin of the mass function* of stellar NYCs. This objective demands a thorough compilation of resolved star forming populations over the entire mass spectrum and in diverse star forming environments. It requires complete catalogues of the star cluster members, and only those members. Disentangling star cluster members from the field population is a titanic task that the astrophysical community is on the verge of completing thanks to the future *Gaia* (Gaia Collaboration et al. 2016a) data. However, even with Gaia, the development and success of star formation theories will be pending a comprehensive identification of the sub-stellar populations and the internal dynamics of embedded cluster cores. *Gaia* will leave aside the most massive BD and planets, reaching only down to $0.03 M_{\odot}$ on the best cases (Sarro et al. 2013). Furthermore, *Gaia* reaches the 20 mag limit in the *G* band (350 nm to 1000 nm Jordi et al. 2010) what makes it almost blind to the dust and gas in which the majority of the star forming regions are still embedded.

The DANCe photometric and astrometric measurements will complement *Gaia*'s exquisite astrometric precision in a selected list of star forming regions, which is shown in Table 1.1. In addition, its secondary targets are also listed in Table 1.2. A pilot study of

³<http://project-dance.com>



Figure 1.3: Mass distribution resulting from the numerical simulation of [Kuznetsova et al. \(2015\)](#). The High (solid line) and Low (dashed line) resolution simulations reach $0.05 M_\odot$ (solid vertical line) and $0.15 M_\odot$ (dashed vertical line), respectively. Also shown the normalised IMF of [Chabrier \(2005\)](#) (red dashed line). Reproduced from Figure 11 of [Kuznetsova et al. \(2015\)](#), *Signatures of Star Cluster Formation by Cold Collapse*, ApJ, Vol. 815

the DANCe data properties has already been conducted on the Pleiades cluster. For more details on it I refer the reader to Section 2.7 and to [Bouy et al. \(2013\)](#).

The unravelling of the mass function requires in addition to accurate, precise, and complete data sets of NYCs, a statistical methodology able to deal not just with the properties of the data sets and the particularities of each NYCs, but with the capacity to disentangle the few hundreds cluster members from within the millions of sources of the field population. Working with individual stars one by one is no longer possible. Under the current paradigm of artificial intelligence, the intelligent systems offer a viable solution to the classical needle in a haystack problem. The DANCe project has already successfully tested its first intelligent classifier. Its methodology and astrophysical results on the Pleiades clusters are detailed in the works of [Sarro et al. \(2014\)](#) and [Bouy et al. \(2015\)](#), respectively.

With both the precise and accurate data and methodology, the DANCe project will be able to not just complement *Gaia* in the low-mass regime, but also deliver a complete inventory of the early phases of cluster formation in different environments. It will unravel the roles of the environment and initial condition in the final mass distribution, which is the ultimate goal of the DANCe project.

The present work is the second generation of the DANCe Intelligent Systems (ISs).

Table 1.1: Main targets

Name	R.A. (J2000)	Dec (J2000)	Distance (pc)	Age (Myr)	$\mu_\alpha \cos(\delta)$ (mas/yr)	μ_δ (mas/yr)
Pleiades	56.750	+24.117	120	120	19	-44
IC2391	130.133	-53.033	175	50	-25	23
IC2602	160.742	-64.400	160	50	-22	10
γ^2 Vel	122.383	-47.336	350	5~10	-6	10
NGC 2547	122.6071	-49.1675	450	20~35	-6	10
IC 348	56.142	+32.163	~300	2	7	-9
NGC 1333	52.258	+31.348	~300	1	?	?
CrA	285.462	-36.982	130	1	?	?
η -Cha	130.525	-79.027	97	5~9	-30	28
ϵ -Cha	179.90657	-78.22184	111	5~9	-38	-1
Upper Scorpius	243.0	-23.4	120	5~10	-9	-25
Lupus I	235.7587	-34.1517	140	1~3	~-15	~-25
Lupus II	239.283	-37.785	140	1~3	~-15	~-25
Lupus III	242.40	-39.05	140	1~3	~-15	~-25
Serpens	277.487	+01.240	~400	1~3	?	?
Ophiuchus	247.025	-24.542	125	1~3	-6	-25
Taurus	70.25	+25.87	140	1~3	8	-21
Blanco 1	1.029	-29.833	250	~100	21	3
Orion	83.8221	-05.3911	450	1~3	1.7	-0.3
NGC2451A	116.35	-37.97	197	50~80	-22	14
NGC2451B	116.35	-37.97	360	50~80	-10	14
CygOB2	308.30	+41.32	1450	1~7	-1.6	-4.7
IC4665	266.575	+05.717	350	~35	-0.5	-7
Collinder 359	270.275	+02.900	450	~100	-0.4	-8.
λ -Ori	83.775	+09.933	450	3~5	0.8	-3.
σ -Ori	84.675	-02.600	450	3~5	1.7	0.5
Cha I	166.700	-77.300	160~180	1~3	-21	1
Cha II	193.4	-77.2	160~180	1~3	-24	-8
Cha III	189.4142	-80.2533	160~180	1~3	?	?
NGC2516	119.51667	-60.75333	410	135	-4	11

Table 1.2: Secondary targets

Name	R.A. (J2000)	Dec (J2000)	Distance (pc)	Age (Myr)	$\mu_\alpha \cos(\delta)$ (mas/yr)	μ_δ (mas/yr)
NGC 752	29.421	+37.785	460	1000	8	-12
NGC 6774	289.175	-16.283	~300	3000	-1	-29
α -Per	51.079	+49.862	171~200	50~70	22	-25
Praesepe	130.100	+19.667	600~700	1~3	?	?
NGC 2264	100.242	+09.895	920	3~5	-0.6	4.
M35	92.225	+24.333	850	~130	2.7	-3.5
M67	132.825	+11.800	860	3200~5000	-6.5	-4.5
NGC 6791	290.221	+37.772	4100	~4300	4.0	0.6
Coma Berenices	185.6262	+25.8450	96	~400	-12.4	-9.4
M39	322.950	+48.433	325	250	-8	-20
Trumpler 10	131.975	-42.450	425	180	-12	7
Collinder 285	220.22	+69.57	25	200	?	?
M41	101.504	-20.757	240	700	?	?
Stock2	33.679	+59.485	300	100	15	15
μ -Oph group	264.46129	-08.1188	120	-12	-21	
Upgren 1	188.75417	36.36667	110	?	-98	-49

This new IS minimises the biases of the previous one and those present in most of the current classifiers in the literature. It steps ahead of the classification paradigm, the current one in the literature, and focuses on a new one: *learning the kinematic and photometric distributions of the cluster populations*, both single and binary stars. The classification task is now a by-product of this new IS. In the following section, I describe the properties of the previous DANCe IS classifier (the one from Sarro et al. 2014), together with the current ones from the literature.

1.4 Methodologies for the classification of cluster members

As mentioned above, the vast majority of the past and current methodologies for the analysis of stellar clusters work under the classification paradigm. Given the objects observables and the current knowledge of the cluster, they assign cluster membership probabilities. These are then used to classify the objects into the field or cluster populations. The classification depends on a probability threshold, which beside imposing a trade-off between completeness and contamination in the resulting sample, is not always established in an objective way.

In his pioneer work, which was also conducted in the Pleiades cluster, Trumpler (1921) selected candidate members using three criteria:

1. projected distance to the cluster centre,

2. similarity of the proper motions to those of the cluster, and
3. the degree of accordance with the relation between colour and brightness of the cluster.

During almost one century since the publication of Trumpler's work, his three criteria remain valid and are still widely used.

[Vasilevskis et al. \(1958\)](#) and [Sanders \(1971\)](#) put a solid probabilistic background to Trumpler's second criterium. [Vasilevskis et al. \(1958\)](#) expressed (in their Eq. 4) the probability of an object to belong to the cluster as

$$p_c = \frac{N_c \cdot \Phi_c(\lambda, \beta)}{N_c \cdot \Phi_c(\lambda, \beta) + N_f \cdot \Phi_f(\lambda, \beta)},$$

with N_c and N_f the number of cluster and field stars, respectively. Φ_c and Φ_f represent the bivariate normal distributions of cluster and field, respectively, and λ, β are the proper motions in galactic coordinates. The selection of galactic coordinates and the symmetry of the proper motion uncertainties allowed them to assume that the cluster bivariate normal distribution, Φ_c , had circular symmetry (i.e. a diagonal covariance matrix). They fitted the means of these bivariate normal distribution by eye using histograms for each coordinate. [Sanders \(1971\)](#) used the same procedure of [Vasilevskis et al. \(1958\)](#), but fitted the parameters using the maximum-likelihood principle. This methodology remained almost intact during the following decades.

Later, [de Graeve \(1979\)](#) included the spatial information (Trumpler's first criterium) into the membership probability determination. Although his work is not available on-line, his formulation is given in the work of [Kozhurina-Platais et al. \(1995\)](#). In the latter, the cluster membership probability of an object, given its positions and proper motions, is

$$P_{\mu, \alpha, \delta} = \frac{N_c \cdot S_c(\alpha, \delta) \cdot \Phi_c(\mu_\alpha, \mu_\delta)}{N_c \cdot S_c(\alpha, \delta) \cdot \Phi_c(\mu_\alpha, \mu_\delta) + N_f \cdot S_f(\alpha, \delta) \cdot \Phi_f(\mu_\alpha, \mu_\delta)},$$

with α and δ the stellar positions in equatorial coordinates, and S_c and S_f the cluster and field spatial (positional) distributions. [Kozhurina-Platais et al. \(1995\)](#) assumed exponentially decaying and uniform distributions for the cluster and field spatial distributions, respectively. To model the proper motion distributions they also used bivariate normal distributions.

In the first decade of this century, authors started to incorporate Trumpler's third criterium in the selection of members. For example [Moraux et al. \(2003\)](#); [Deacon & Hambly \(2004\)](#); [Balaguer-Núñez et al. \(2007\)](#); [Lodieu et al. \(2012\)](#) used hard cuts in the colour, or in the Colour Magnitude Diagrams (CMDs) to discriminate candidates. [Moraux et al. \(2003\)](#) used conservative cuts based on the theoretical isochrone models of [Baraffe et al. \(1998\)](#), while [Deacon & Hambly \(2004\)](#); [Balaguer-Núñez et al. \(2007\)](#); [Lodieu et al. \(2012\)](#) used arbitrary cuts in the CMDs diagrams. However, despite the conservative

or objective these cuts may be, as pointed out by Sarro et al. (2014) they have at least two drawbacks. They render membership probabilities i) which are inconsistent across magnitude bins, and ii) only for those sources with measurements in the CMDs used for selection.

The previous works incorporated most of the observables (positions, proper motions and photometry) available for the vast majority of the stars. Other useful observables for the discrimination of cluster members are the parallax, the radial velocities and other indicators of youth (e.g. lithium abundance, photospheric activity, rotation, see for example Barrado et al. 2016). Although these observables can be of great use, they are only available for limited samples of objects. Furthermore, they tend to be biased towards the brighter objects. For these reasons, the members selection has been done using the astrometric and photometric observables: positions, proper motions and photometric bands.

In recent years, the astrophysical community started to develop automated methodologies for the cluster members selection. This development has been motivated by two main reasons. First, computing power has become widely available thus allowing the implementation of more complicated and computing demanding techniques. Second, the arrival of automated surveys providing incredible amounts of data for millions of objects have rendered obsolete the previous object-by-object oriented techniques. In the following, I will review the methodologies of Malo et al. (2013); Gagné et al. (2014); Riedel et al. (2017) for stellar associations, and the ones of Krone-Martins & Moitinho (2014); Sarro et al. (2014); Sampedro & Alfaro (2016) for star clusters. Although this work focuses only on the analysis of star clusters, the methodologies applied to associations are related and some times also applied to them. Thus, I review them as well.

Malo et al. (2013) develop a code for the Bayesian Analysis of Nearby AssociatioNs (BANYAN). It establishes membership probabilities for seven nearby young moving groups (β Pictoris, Tucana-Horologium, AB Doradus, Columba, Carina, TW Hydræ, and Argus) using a naive (no correlations included) Bayesian classifier. Their classification uses kinematic and photometric models of the seven nearby young moving groups (NYMGs) and the field. These models are constructed with the previously known *bona fide* members and field objects. The photometric model in the low-mass range is extended beyond the known members using evolutionary models. One of the great advantages of this work is its ability to simultaneously obtain membership probabilities for the seven nearby young moving groups. It works on a six dimension observable space: I_c and J bands, proper motions and stellar positions. The recovery (true positive) and false alarm (false positive) rates of this classifier are 90% and 10%, respectively; the latter varying according to the moving group.

Gagné et al. (2014) improve Malo et al. (2013) methodology by developing BANYAN-II. It is tuned to identify low-mass stars and brown dwarfs by the use of redder photometric colours from *2MASS* and *WISE*. The spatial and kinematic distributions are modelled

1.4. METHODOLOGIES FOR THE CLASSIFICATION OF CLUSTER MEMBERS14

with no alignment to the galactic coordinates as is done by BANYAN. They also included the observational uncertainties and the ability to deal with missing values, at least in parallax and radial velocities. When the parallaxes and radial velocities are not present, the estimated contamination rate ranges between 20% and 80% for a wide range (0.2-0.8) of probability cuts (see their Figure 5).

[Riedel et al. \(2017\)](#) developed a kinematic membership analysis code for LocAting Constituent mEmbers In Nearby Groups (LACeWING). Using only the spatial and kinematic information of stars, LACeWING, computes membership probabilities to 13 NYMGs. LACeWING computes what they call the goodness-of-fit value, which is the distance between each object observables and the value of the NYMG divided by the quadratic sum of the uncertainties. Then it draws synthetic stars, compute their goodness-of-fit values, and bin them. The membership probability of a real object correspond to the fraction of synthetic stars, in the same goodness-of-fit bin, that were generated as members of the moving group. These authors do not provide estimates of contamination and recovery rates on synthetic samples. Instead, they directly give the number of recovered and false positives returned by glslacewing in each NYMG. As mentioned by these authors, the recovery rates are similar to those of BANYAN and BANYAN-II.

[Krone-Martins & Moitinho \(2014\)](#) created the Unsupervised Photometric Membership Assignment in Stellar cluster (UPMASK) code. It establishes cluster membership probabilities in a frequentist approach using positions and photometry. It is an unsupervised and data driven iterative algorithm. Their methodology relies on clustering algorithms and the Principal Components Analysis (PCA). It establishes membership probabilities by randomly generating synthetic stars based on the individual uncertainties. The membership of an object is the fraction of randomly generated stars in which the object was classified as a cluster member. Although untested, the authors mention that their methodology is able to incorporate proper motions, deal with missing data and with different uncertainty distributions. Measured on synthetic samples (with typical sizes ranging from thousands to tens of thousand objects), these authors find that UPMASK delivers true positive (recovery) rates grater than 80% for a probability classification threshold of $p=0.9$ (they do not provide any reason for the use of this particular value). One of the great advantages of UPMASK is its ability to deal with superimposed clusters.

[Sarro et al. \(2014\)](#) created a Bayesian classifier to infer posterior membership probabilities based only on proper motions and photometry. Their cluster model is data driven and includes some parametric correlations (it is not a naive classifier like BANYAN or BANYAN-II). They construct the proper motions and photometric models of the field and cluster with clustering algorithms. However, the photometric model of the cluster is constructed using the principal curve analysis. Their treatment of uncertainties and missing values is consistent across observed features. They infer the best parameter values of both cluster and field models using a Maximum-Likelihood Estimator (MLE) algorithm,

but based only on completely observed objects (i.e. without missing entries). Afterwards, they assign membership probabilities to objects with missing entries. They found an optimal probability classification threshold at $p = 0.85$ using synthetic data sets of 2 million sources. At this threshold they measure a contamination rate of 4.5% and a true positive rate of 92.9%.

[Sampedro & Alfaro \(2016\)](#) created a Bayesian algorithm to estimate membership probabilities to open clusters. They compute the euclidean distance, in a multidimensional normalised space, of each object to the over-density of the cluster. Then, they assign membership probabilities according to this distance assuming univariate normal distribution for both cluster and field. Their methodology assumes that the cluster members are more densely concentrated than the field population. Since they use an euclidean metric to compute distances in a normalised space (normalised by the individual uncertainties), their methodology is highly affected by the heteroscedasticity of the presence of missing values in the observables. In an euclidean metric, objects with missing values have smaller, or at most equal, distances than those of objects with complete observations. They use a 0.5 probability classification threshold based on the Bayes minimum error rate, however, they do not provide error rates. On synthetic data sets of 500 objects they measure completeness and misclassification as a function of the similarity between the cluster and field univariate normal distributions. They do this varying i) the fraction of cluster members in the total data set size (from 20% to 80%), and ii) the number of variables (from among positions and proper motions). Their misclassification is in the range of 25% to 5% for two to four variables, while their completeness is better than 90%.

The previous methodologies perform well on the classification task, and successfully led to the identification of many new high probability members of nearby clusters and associations. However, key aspects still need to be tackled. These are

- Uncertainty of membership probabilities. These, as any other measurement, are uncertain. The previous authors report just the first moment of the object membership probability distributions.
- Treatment of objects with missing entries in their observables. In astronomy, measurements are strongly affected by the brightness of the source. The physical limits imposed by the dynamical range of detectors lead to non-uniform distributions of objects with missing entries. At the bright end, the excess of photons saturates the detector pixels and, most of the time, renders the measurements useless (however, see [Maíz-Apellániz 2003](#); [Olivares et al. 2013](#), for examples of high-precision astrometry and photometry on saturated images). At the faint end, sources with brightness below the limit of sensitivity are not detected. Furthermore, in a multi-wavelength data set the intrinsic stellar colours add another level of correlation between the sensitivity limits of different bands. The previous effects create a non-uniform distribution of objects with missing values. In addition, missing values can also

appear due to other non-random effects (e.g. proximity to a bright source), which will further affect any analysis that discards them. If the distribution of objects with missing entries will be uniform, then results based only on the completely observed (non-missing value) objects would be unbiased. However, the less uniform the distribution of missing-value objects is, the most biased the results are. See Chap. 8 of [Gelman et al. \(2013\)](#) for a discussion on missing at random and ignorability of the missing pattern. Objects with missing values have an important effect in the resulting samples of members. The cluster and field model are conditioned on the objects used to construct them. The previous works constructed their models based only on objects with completely observed entries, and some of them later applied these models to objects containing missing values. Thus, these completely-observed models could be biased.

- Heteroscedastic⁴ uncertainties. Each object in the cosmos is unique and distinct from others. Assuming that all of them are alike is useful in certain situations, though. However, the assumption of homoscedasticity in the uncertainties of a sample, which is often done for practical reasons, may lead to biases. For example, it is known that the performances of PCA (used by [Krone-Martins & Moitinho 2014](#)), and consequently of the Principal Curve Analysis (used by [Sarro et al. 2014](#)), are strongly affected by heteroscedastic uncertainties ([Hong et al. 2016](#)).
- Sampling bias. Using a probability classification threshold to select candidate members results in a trade-off between contamination and completeness. To keep contamination under reasonable levels samples are never complete. Therefore, any further statistical analysis resulting from them suffers from a sampling bias.
- Propagation of uncertainties. Uncertainties in the observables must be propagated until the very end of subsequent astrophysical analyses. Currently, once a list of candidate members have been obtained, luminosity functions and then mass functions are derived on the basis of poisson uncertainties. At best, the uncertainties include the photometric ones, but completely discard proper motion uncertainties and those of the model that generated the list of candidates.

The methodology presented in this work attempts to address the previous problems.

⁴In statistics, homoscedasticity is the property of random sample of variables whose variance is homogeneous. This is, any sub-population shows the same variance as that of the population. By contrast, heteroscedasticity is the absence of homoscedasticity.

1.5 A new intelligent system: the Bayesian Hierarchical Model

As mentioned before, this new IS steps ahead of the classification paradigm and focuses on a new one: *learning the kinematic and photometric distributions of the cluster populations*, both single and binary stars. This new IS addresses the aforementioned issues in the following way.

- Uncertainty of membership probabilities. Together with the kinematic and photometric distributions of the cluster population, it renders the cluster and equal-mass binaries (full) membership probability distributions, not just point estimates of them. Thanks to its Bayesian framework, it computes the probability distribution of the class, cluster vs field and single vs binary, given the object datum.
- Treatment of objects with missing entries in their observables. Thanks to its Bayesian framework, the new IS is able to include in its data set objects with missing entries in its observables. The missing values are treated as parameters which are marginalised with the aid of a prior. Currently, the model assumes that this prior is uniform (i.e. missing-at-random mechanism for the missing values), nevertheless, this assumption return less unbiased estimators than those obtained discarding objects with missing values (like the works mentioned in the previous Section). Upon availability, non-uniform priors for the missing value mechanism can be directly incorporated, provided that enough computer power is also available.
- Heteroscedastic uncertainties. In the new IS, it is assumed that objects uncertainties share the same family distribution, the multivariate normal. However, the values of the uncertainties are not assumed to be the same. The new IS incorporates the intrinsic heteroscedasticity of the data. It assumes that the observed data results from the addition of a noise process to the *true*⁵ data. The true intrinsic underlying relation is accessible after deconvolution of the observed uncertainties (see [Bovy et al. 2009](#), for another example of deconvolution).
- Sampling bias. The new IS avoids the bias associated to the use of only the high membership probability objects in the following way. It derives the kinematic and photometric distributions of the cluster populations taking into account each data set object proportionally to its cluster likelihood. Thus, there is no need of a probability classification threshold to obtain the clusters distributions.
- Propagation of uncertainties. Thanks to its Bayesian framework and the use of heteroscedastic uncertainties, the new IS is able to propagate the observational

⁵The true data is that which would be observed under negligible uncertainties.

uncertainties directly into the posterior distribution of the parameters of the cluster model. Then, the distributions of the parameters can be propagated into the luminosity and mass distributions. The resulting mass distribution incorporates not just the observational uncertainties of all the objects, but also the uncertainties associated with the cluster model.

The core of this new IS is the Bayesian framework. The latter demands the use of prior distributions for the value of its parameters. To avoid as much as possible the subjectivity of choosing them, the new IS uses the BHM methodology together with weakly informative priors (see [Gelman 2006](#); [Gelman et al. 2008](#); [Huang & Wand 2013](#); [Chung et al. 2015](#)). The works of [Jefferys et al. \(2007\)](#); [Shkedy et al. \(2007\)](#); [Hogg et al. \(2010b\)](#); [Sale \(2012\)](#); [Feeney et al. \(2013\)](#) are some examples of the use of BHMs in astrophysics. In the BHMs, the parameters of the prior distributions are given by other distributions in a hierarchical fashion. These parameters are also fitted from the data. Thus, BHM provide the most objective approach to the settling of prior distributions ([Gelman 2006](#)). However, it comes at a price: BHMs are computationally more expensive because they require far more parameters than standard approaches.

In such a way, the new IS learns the posterior distributions of the parameters in the BHM given the kinematic and photometric data. Due to the high dimension of the parametric space (the BHM has 85 parameters), the learning process demands a fast and reliable technique to obtain the posterior distributions of the parameters. Furthermore, the typical data set size for a cluster and the surrounding field is in the order of millions of sources. Thus the likelihood of the data must loop over all these millions of sources. The high dimensionality of the parametric space and the large data set size demand a technique that, on top of being fast and reliable, will also be compatible with parallel computing. Thus reducing to a minimum the computing time. The Markov Chain Monte Carlo techniques offer the demanded requirements. In specific, the *emcee* algorithm ([Foreman-Mackey et al. 2013](#)) was chosen due to its excellent performance properties and its ability to work in a parallel computing scheme.

The BHM presented in this work has been benchmarked on the Pleiades cluster. This reason roots in the following points. First, the Pleiades cluster together with the Orion Nebula Cluster are probably the most studied clusters in the history of astronomy. Thus, the current knowledge of Pleiades makes it ideal to benchmark any new tool or theory. Second, currently the DANCe project has processed the data of only three clusters: M35, CygOB2 and the Pleiades. CygOB2 and M35 are relatively poorly understood compared to the Pleiades, and are far from the sun (see Tables 1.1 and 1.2), which give them small proper motions values. Since the Pleiades is a well understood cluster, with well characterised lists of members (e.g [Stauffer et al. 2007](#); [Lodieu et al. 2012](#); [Sarro et al. 2014](#); [Bouy et al. 2015](#)) and precise and accurate measurements, it is the perfect case study for the development, testing and validating of the new IS described here.

The rest of this work is structured as follows. In Chapter 2, I do a compilation of the current knowledge on the Pleiades cluster. In particular, that concerning its distance, spatial, velocity, luminosity and mass distributions. Also I give details of the Pleiades DANCe Data Release 2 (DDR2) data set. The incredibly detailed knowledge of the Pleiades cluster and the high precision and carefully designed observations of the DANCe project are the main reasons for benchmarking the BHM on this cluster. Later, in Chapter 3, I give a brief introduction to probability theory and also present the details of the BHM methodology and of the techniques used to sample the statistical distributions of the cluster populations. Later, in Chapter 4, I give details of the analysis performed on synthetic data, of the comparison of the recovered candidate members with those from the literature, of the kinematic and photometric distributions, and of the present day system mass distribution. Finally, in Chapter 5, I present my conclusions and my point of view concerning the work that must be done in the near future to continue improving our knowledge of the star formation process.

Chapter 2

The Pleiades as a benchmark

2.1 Generalities

The ancient greeks named Pleiades to a crowded group of nine stars which they believed shared a common origin. These stars were the seven sisters, that together with their parents the titan Atlas and the nymph Pleione, were put in the sky by the god Zeus.

Today, we call the Pleiades cluster not just to the nine stars that made up the original Pleione family, but to a much larger group, which according to [Bouy et al. \(2015\)](#) adds up to ~ 2100 members. This cluster is fairly close to the sun, ~ 134 pc (with parallaxes of 7.44 ± 0.08 and 7.48 ± 0.03 according to [Galli et al. 2017](#); [Gaia Collaboration et al. 2017](#), respectively), and is also young in galactic scales, with only ~ 125 Myr ([Stauffer et al. 1998](#)). Since it is located in the solar neighbourhood, it has a distinctive angular velocity in the plane of the sky: about $-16 \text{ mas} \cdot \text{yr}^{-1}$ in right ascension and $20 \text{ mas} \cdot \text{yr}^{-1}$ in declination. It has a metallicity near to the solar one ($[\text{Fe}/\text{H}] \sim 0$, [Takeda et al. 2017](#)). Also, it has an almost null extinction of $A_v = 0.12$ mag ([Guthrie 1987](#)). These properties make the Pleiades one of the most studied clusters in the history of astronomy¹. Thus making it also the perfect test case of the methodology developed in this work.

As stated in the previous Chapter, the objective of the present study is to obtain the statistical distributions of the distance, position, velocity, luminosity and mass of the Pleiades cluster. Thus, in the following sections I will describe the current knowledge of the Pleiades, concerning these astrophysical quantities.

2.2 The distance to the Pleiades

2.2.1 Measuring distances

In astronomy, measuring distances is a complicated task. Techniques vary according to the distance scale that they aim to measure. The distance ladder is constructed from

¹Probably just after the Orion complex.

smaller to larger distances. The first step in this ladder is the distance to the sun. After that, the distance to the planets and then to the stars. This work deals only with nearby clusters, thus I only focus on measuring distances to these objects.

The most direct way to measure distance to nearby stars is by means of the trigonometric parallax. This is the maximum relative angular displacement, with respect to the far distant stars, that an object suffers in the course of a year. It is usually reported in milliarc seconds (mas). The relative displacement results from the movement of the Earth (thus of the observer) on its orbit around the sun. The relative displacement is maximal when measurements are taken at opposed points in the earth's orbit, when they are separated by six months. If the parallax were measured in seconds of arc and with infinite precision, then the distance to the object would be obtained by simply inverting its parallax. By doing so, the distance will be measured in parsecs. This unit gets its name from parallax-second. Thus an object located at a distance of one parsec from the sun shows a parallax of one arc second. The further the object is, the smaller the parallax gets.

As any measurement, parallaxes have uncertainties, which usually represent, or are a proxy for, the width of the distribution. The parallax distribution is also continuous and non-limited.

When transforming parallaxes into distances we may be tempted to take a summary of the distribution, the mean for example, and just invert it to obtain the distance. This only holds if the summary corresponds to the true value (i.e. the statistic is unbiased). The true value is that which would be observed in the presence of negligible uncertainties. However, because measurements have uncertainties, which almost always are not negligible, the inversion of the parallax not always renders an unbiased estimate of the distance. Assuming that the distribution of parallax measurements of an object is Gaussian, [Lutz & Kelker \(1973\)](#) found that the distance to the object can be reasonably recovered by just inverting the parallax if its relative uncertainty is below 0.15-0.20. However, the shape of the distribution of parallax measurements of an object (the second and higher order moments) plays also an important role. Transforming the parallax distribution into that of the distance require more than a simple inversion.

Several authors have proposed different approaches to the problem of distance determination using parallaxes, see for example [Lutz & Kelker \(1973\)](#); [Bailer-Jones \(2015\)](#); [Astraatmadja & Bailer-Jones \(2016a,b\)](#). The proper way, as [Bailer-Jones \(2015\)](#) points out, consists of inferring the true distances given the observed parallaxes. For that, a prior on the distance must be established. The authors mentioned before describe three different kinds of priors and the methodology needed to infer the true distances. However, going into deeper detail is beyond the scope of this work.

Now, I focus on the particular case of the distance to the Pleiades. One of the first measurements of the Pleiades distance using parallaxes from the space was done by [van Leeuwen & Hansen Ruiz \(1997\)](#) using *Hipparcos* data. Using the astrometric data of

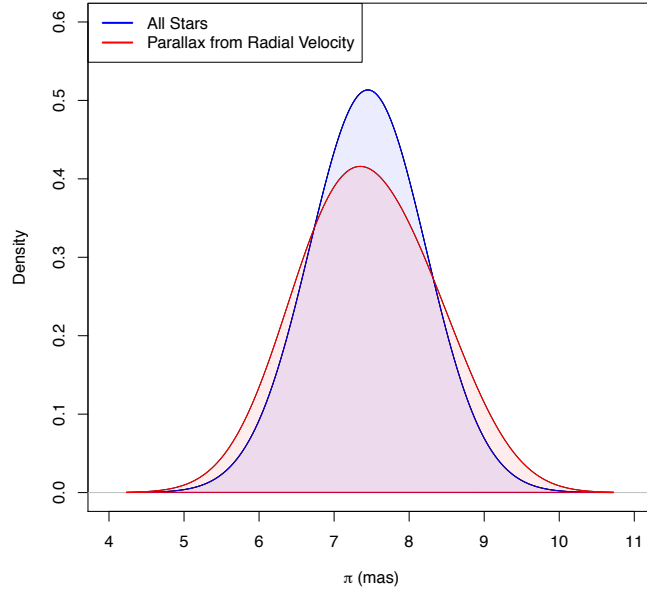
sample of 54 Pleiades members and the abscissae method (van Leeuwen 1997), these authors obtained a parallax distribution with a mode near 8.9 mas (113 pc, see Figure 2 of van Leeuwen & Hansen Ruiz 1997). Their parallax results was in considerable disagreement with previous (mainly photometric) determinations. Just to mention some of them, Eggen (1986) found ~ 135 pc (7.4 mas or 5.65 mag of distance modulus) using the lower main-sequence fitting method, Giannuzzi (1995) found ~ 133 pc (7.5 mas) using the parameters of a binary system, and O'dell et al. (1994) found ~ 135 pc (7.5 mas or 5.6 mag of distance modulus) using the periods, rotational velocities and angular diameters of a small sample of the late-type stars.

Later, (van Leeuwen 2009) refined his previous analysis and obtained an still discrepant value of 120 ± 1.9 pc. However, Gatewood et al. (2000) with parallax measurements of seven stars taken at the Allegheny Observatory, and later Soderblom et al. (2005) with the parallaxes of three stars measured with the Fine Guidance Sensors of the *Hubble Space Telescope*, derived distances of 130.9 ± 7.4 pc and 134.6 ± 3.1 pc, respectively. Finally, Melis et al. (2014) using very long baseline radio interferometric parallaxes of three stars obtained a distance of 136.2 ± 1.2 pc. There was a clear controversy between *Hipparcos* data and other parallax measurements. The current data release of the *Tycho-Gaia* Astrometric Solution (TGAS), gives a distance to the Pleiades of 133.7 ± 0.5 pc (from a parallax of 7.48 ± 0.03 mas Gaia Collaboration et al. 2017). This seems to indicate that the *Hipparcos* parallaxes were somehow biased.

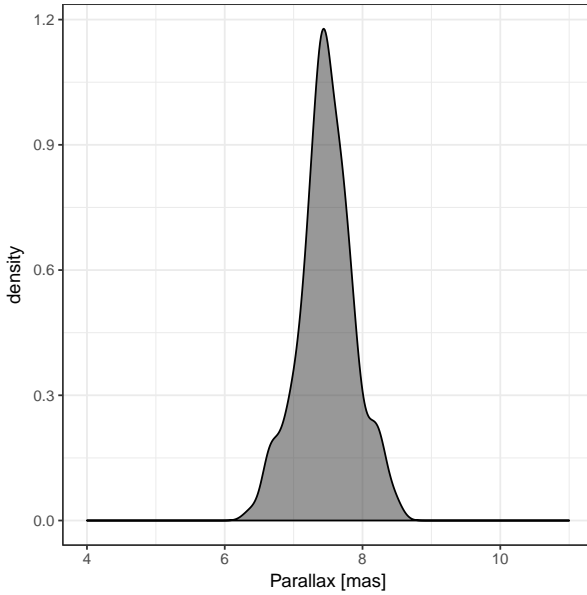
Our research group finds a distance to the Pleiades of $134.4_{-2.8}^{+2.9}$ pc (from a parallax of 7.44 ± 0.08 mas) (Galli et al. 2017), which is in good agreement with the one of TGAS. We found this distance using the kinematic parallaxes delivered by the moving cluster technique. This essentially exploits the fact that since clusters are bound, their members show a clear kinematic footprint: they seem to converge to a point in the sky (Blaauw 1964). Using this point and the velocity of the members (proper motion and radial velocities) it is possible to derive individual parallaxes. Furthermore, these individual parallaxes show a distribution which results from the dispersion of the cluster members distances along the line of sight. Figures 2.1a and 2.1b show the distribution of parallaxes for the Pleiades candidate members according to Galli et al. (2017) and Gaia Collaboration et al. (2017), respectively. As can be seen from these Figures, the results of both works agree on the mean of the parallax distribution. However, they recover different variances. This difference results from the discrepancy in the number of objects, 1210 in Galli et al. (2017) vs. 152 in Gaia Collaboration et al. (2017), and in the selection function of the two surveys. The TGAS sample is limited to the bright objects ($V \sim 11.5$ mag), whereas the DDR2 includes the faint end of the distribution ($i \sim 25$ mag). For these reasons, in the following I adopt the distance found by Galli et al. (2017).

Nevertheless, the distance distribution (measured uncertainties comprised) is only the depth component of the space distribution of the cluster, the other two components are

given by the projected spatial distribution.



(a) Parallaxes according to [Galli et al. \(2017\)](#). The red line shows all their candidate members (1210) while the blue one only those with known radial velocity (64). Reproduced from Figure 13 of [Galli et al. \(2017\)](#), *A revised moving cluster distance to the Pleiades open cluster*, A&A, Vol. 598.



(b) Parallaxes according to [Gaia Collaboration et al. \(2017\)](#). Only their 152 candidate members.

Figure 2.1: Distribution of parallaxes for the Pleiades members.

2.3 Projected spatial distribution

The Projected Spatial Distribution (PSD) is the two dimensional projection, in the plane of the sky (the one perpendicular to the line of sight), of the cluster three dimensional space distribution. In astronomy, object positions are commonly measured in what is

called the Equatorial Coordinate System². It can be thought as the projection of the geographical coordinates, latitude and longitude, into the sky. The Right Ascension (R.A.) coordinate, analogous to the longitude, gives the objects angle with the vernal equinox, measured in an eastward direction and along the celestial equator. The Declination (Dec.) coordinate, analogous to the latitude, gives the object angle perpendicular to the celestial equator, positive to the North and negative to the South. For more details of the Equatorial Coordinate System see for example [Smart & Green \(1977\)](#).

Stellar positions of an object are far more easily measured than its parallax. For this reason, just a small fraction of objects with stellar positions has also parallax measurements. In the case of the Pleiades, after cross-matching the *Hipparcos* catalogue ([Perryman et al. 1997](#)) with the candidate members of [Bouy et al. \(2015\)](#), I find that only 70 of the ~ 2100 candidates have parallaxes. As seen in the previous section, this figure is roughly doubled with the new TGAS ([Gaia Collaboration et al. 2016b](#)) data release. In addition to the scarcity of parallaxes, which is expected to be solved with future *Gaia* data releases, the relative uncertainties in R.A. and Dec. coordinates, measured in degrees, are far better ($\sim 10^{-5}$) than those of the parallaxes ($\sim 10^{-1}$), measured in mas. Transforming these relative precisions into parsecs, by means of the distance, it is seen that the position in the plane of the sky is 10^4 more precise than along the line of sight. These two are the main reasons, for which the Pleiades space distribution has been studied mainly through its PSD. The latter has been the subject of several studies.

One of the earliest results of the Pleiades PSD was done by [Limber \(1962\)](#). He used a mixture of four indices polytropic distribution, as was described in his earlier [Limber \(1961\)](#) work, to fit the PSD of the 246 candidate members of [Trumpler \(1921\)](#). These candidates were contained in a 3° radius around *Alcyone* (one of the central most massive stars of the Pleiades cluster).

Later, [Pinfield et al. \(1998\)](#) fitted King profiles ([King 1962](#)) to candidate members from the literature, which were contained in a 3° radius area. They fitted King profiles to objects within different mass ranges, their bins centred at $5.2, 1.65, 0.83$ and $0.3 M_\odot$. The tidal radius they found, 13.1 pc ($\sim 5.6^\circ$) contained 1194 candidate members. The total mass of these members amounted to $735 M_\odot$. These authors also estimated a mean individual stellar mass of $0.616 M_\odot$. They measured core radius in the 0.9 to 2.91 pc range for the King profiles fitted to their different mass bins.

On the same year [Raboud & Mermilliod \(1998\)](#) also fitted a King's profile ([King 1962](#)) to a list of 270 candidate members with masses in the range $0.74 - 7.04 M_\odot$, which were contained within a 5° radius area. They found a core radius of 1.5 pc and a tidal radius of 17.5 pc (7.5 degrees). Using different approaches, they derived a total mass within the range of $500 - 8000 M_\odot$. They also measured an ellipticity of $\epsilon = 0.17$, however they did not make any explicit mention on the position angle of the axis of the ellipse.

²Another common coordinate system is the Alt-Azimuth one (see [Smart & Green 1977](#)).

Later, [Adams et al. \(2001\)](#) also fitted a King profile to objects with membership probabilities $p > 0.3$ within a radius of 10° . They found a core radius of $2.35 - 3.0$ pc and a tidal radius of $13.6 - 16$ pc ($5.8 - 6.8^\circ$). They estimate a total mass of $\sim 800 M_\odot$, and their measured ellipticities are in the range $0.1 - 0.35$.

[Converse & Stahler \(2008\)](#) fit a King profile to a sample of 1245 candidate members from [Stauffer et al. \(2007\)](#) compilation. These objects have masses greater than $0.08 M_\odot$ and are contained within a 5° radius. They obtained a tidal radius of 18 pc (7.7 degrees) and a core radius of 1.3 pc. Later, [Converse & Stahler \(2010\)](#) refined their study and obtained a core radius of 2.0 ± 0.1 pc, a tidal radius of 19.5 ± 1.0 pc (~ 8.3 degrees) and a total mass of $870 \pm 35 M_\odot$. In Fig. 2.2a, I reproduce the surface density fit obtained by these authors.

The previous summary of results shows at least two interesting points. In the first place, King profile ([King 1962](#)) has been the preferred choice for the Pleiades cluster, although it was created to fit the PSD of globular clusters. Since globular clusters are farther away than open clusters and in a low density environment, usually the end of their PSD is well within the survey area. The second point concerns the increasing trend of the tidal radius with the size of the survey and the publication date, see Table 2.1. As the surveys increase in area the derived tidal radii increase as well. The exception is the work of [Adams et al. \(2001\)](#). Since these authors used low membership probability (≥ 0.3) objects, they may have also fitted the field. The surface density of a tidally truncated cluster should diminish with radius and eventually go to zero at the tidal radius. However, as can be seen in Figure 2.2b, where I reproduce Figure 8 of [Adams et al. \(2001\)](#), their surface density remains almost constant after 5° . This may be an indication of contamination in their sample. Furthermore, as those authors mention, they expect that the contamination dominates their sample outside the 5° radius.

The two points mentioned before are tightly related. With the exception of the work of [Adams et al. \(2001\)](#), the coverages of the rest of the surveys have not reached their estimated tidal radius. It indicates that the sample of members we currently have is spatially biased. It only contains objects from the inner parts of the cluster. Thus, estimates of the tidal radius may also be biased. Nevertheless, this issue will be addressed with the full sky coverage of *Gaia's* data.

2.4 Velocity Distribution

The three dimensional velocity distribution of the Pleiades has also been studied using its projections. One of them goes along the line of sight, it corresponds to the radial velocity. The other one is perpendicular to the previous one, lies in the plane of the sky, and corresponds to the transverse velocity. It is derived from proper motions. These are angular velocities obtained after measuring the angular displacement of the object

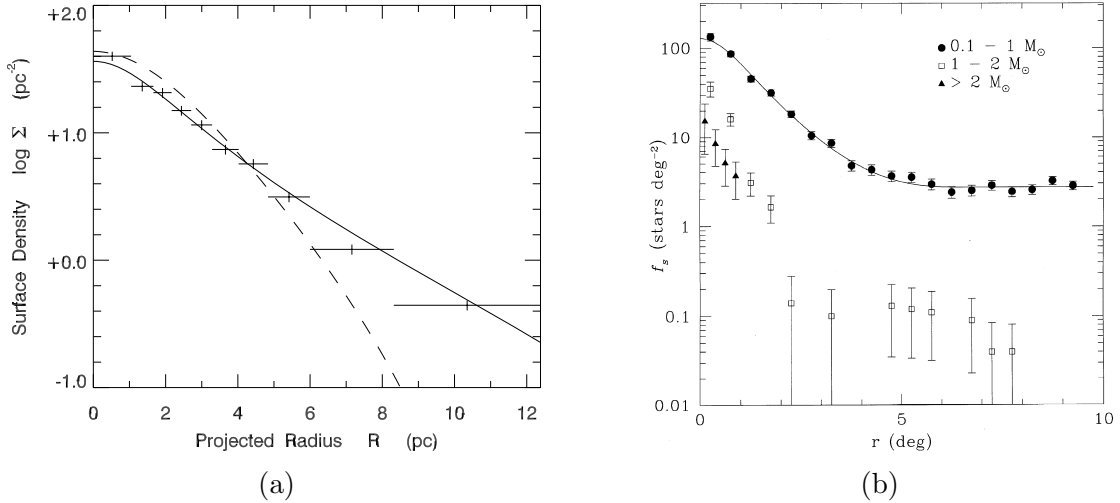


Figure 2.2: Projected spatial distribution of the Pleiades cluster. (a) Results from [Converse & Stahler \(2010\)](#). The crosses, and the dashed and solid lines represent the data and the fitted polytrope and King profile, respectively. Reproduced from Figure 1 of [Converse & Stahler \(2010\)](#), *The dynamical evolution of the Pleiades*, MNRAS, Vol. 405. (b) Results from [Adams et al. \(2001\)](#). The line shows the fitted King profile while the symbols are for different mass bins used. Reproduced from Figure 8 of [Adams et al. \(2001\)](#), *The Mass and Structure of the Pleiades Star Cluster from 2MASS*, AJ, Vol. 121.

Table 2.1: Survey, and derived core and tidal radius for recent studies in the literature.

Authors	Core radius (pc)	Tidal radius (pc)	Tidal radius (°)	Survey radius (°)
Pinfield et al. (1998)	0.9-2.91	13.1	5.6	3
Raboud & Mermilliod (1998)	1.5	17.5	7.5	5
Adams et al. (2001)	2.35-3.0	16	6.8	10
Converse & Stahler (2008)	1.3	18	7.7	5
Converse & Stahler (2010)	2.0	19.5	8.3	5

in at least two different epochs. Again, measuring the individual stellar position and its displacement over time is far easier than measuring radial velocities. These are measured using the Doppler shifted absorption lines in the spectre of the object. This shift is proportional to the object velocity relative to the observer along the line of sight.

Since radial velocities require the object spectrum, their obtention for all cluster members, and particularly for the fainter ones, will demand a large amount of observing time. On the other hand, wide field images have been available for quite a long time, thus allowing long time base lines to measure proper motions. Nevertheless, due to the Pleiades distance, radial velocities are often more precise than proper motion measurements, usually on the $1 \text{ km} \cdot \text{s}^{-1}$ regime. For these reasons, historically, the velocity distribution of the Pleiades cluster has been studied through the proper motions of its members.

Probably the first qualitative appreciation of the Transverse Velocity Distribution

(TVD) of the Pleiades is that of Pritchard (1884). Using archival data from Königsberg (1838-1841), Paris(1874) and Oxford (1878-1880) observatories, together with his own *Differential Micrometer* observations, he was able to observe the relative displacements of 40 Pleiades stars. According to him (Pritchard 1884): *the relative displacements of these distant suns, although not distinctly and accurately measurable in numerical extent, appear to vary both in direction and amount; indicating thereby the mutual influence of a group of gravitating bodies, and not simply that common motion of the whole which would necessarily arise simply from the translation of the solar system in space.* However, as he mentioned, the relative movements were of [...] so slight an amount, that their exact determination does not seem fully within the reach of the observations as yet extant [...].

Later, Trumpler (1921) used, for the first time, proper motion measurements to identify the members of the Pleiades cluster. He classified objects as candidate members according to the distance they show, in the proper motion space, to the mean proper motion of the cluster. This mean was previously calculated by Boss in his *Preliminary General Catalog* (Boss 1910). So far as my historic research went, Boss' work was the first measurement of a statistic of the TVD of the Pleiades.

Later Titus (1938), using Trumpler's data and archival compilations, was able to measure the dispersion of the proper motions distribution. He estimated it to be $0.79 \text{ mas} \cdot \text{yr}^{-1}$ ($0.65 \text{ km} \cdot \text{s}^{-1}$ at 136 pc). This was probably, the first measurement of the second moment of the spatial velocity distribution. From this value he then derived a total mass of 260 M_\odot .

In recent years Pinfield et al. (1998) used the velocity dispersion to probe that the cluster was in an state near to the virial equilibrium. Later, Loktin (2006) used the projected radial and tangential velocity components of the spatial velocity distribution of 340 members to claim the absence of evidence for rotation, expansion or compression of the cluster. Also, he found no evidence to support mass segregation. However, due to the scarcity and small area coverage of his sample of members (17% of the total number of Bouy et al. 2015, candidate members, and distributed in only the central 2°), together with his simplistic approach to select them (only using proper motions), may suggest that his data and methodology may not allow him to detect the mentioned effects.

Concerning the radial velocities, the first record for the Pleiades correspond to Adams (1904). He measured the radial velocities of the six brightest stars. After this seminal work, more than a dozen of works have been published. Among them are the works of Wells (1924); Smith & Struve (1944); Mermilliod (1979); Liu et al. (1991); Rosvick et al. (1992); Stauffer et al. (1994); Mermilliod et al. (1997); Martin et al. (1996); Terndrup et al. (2000); Loktin (2006); Wheeler (2009); Mermilliod et al. (2009), and Kordopatis et al. (2013). In previous studies, the typical number of Pleiades candidate members was below 100 objects, with the works of Wheeler (2009) and Mermilliod et al. (2009) reaching 269 and 275 objects, respectively. The latest compilation of radial velocities from the

literature is the one made by [Galli et al. \(2017\)](#). This list contains measurements for 394 objects. The distribution of these radial velocities is almost gaussian with a centre at $5.6 \text{ km} \cdot \text{s}^{-1}$. In [Galli et al. \(2017\)](#), we estimated a velocity dispersion of the $0.8 \text{ km} \cdot \text{s}^{-1}$ for the Pleiades candidate members.

Although, transverse and radial velocities are useful projections, the dynamical analysis of the cluster demands the three dimensional distribution. In [Galli et al. \(2017\)](#) we provide a list of 64 cluster members with full spatial velocities. The distributions of the three projections of these spatial velocities are shown in Figure 2.3.

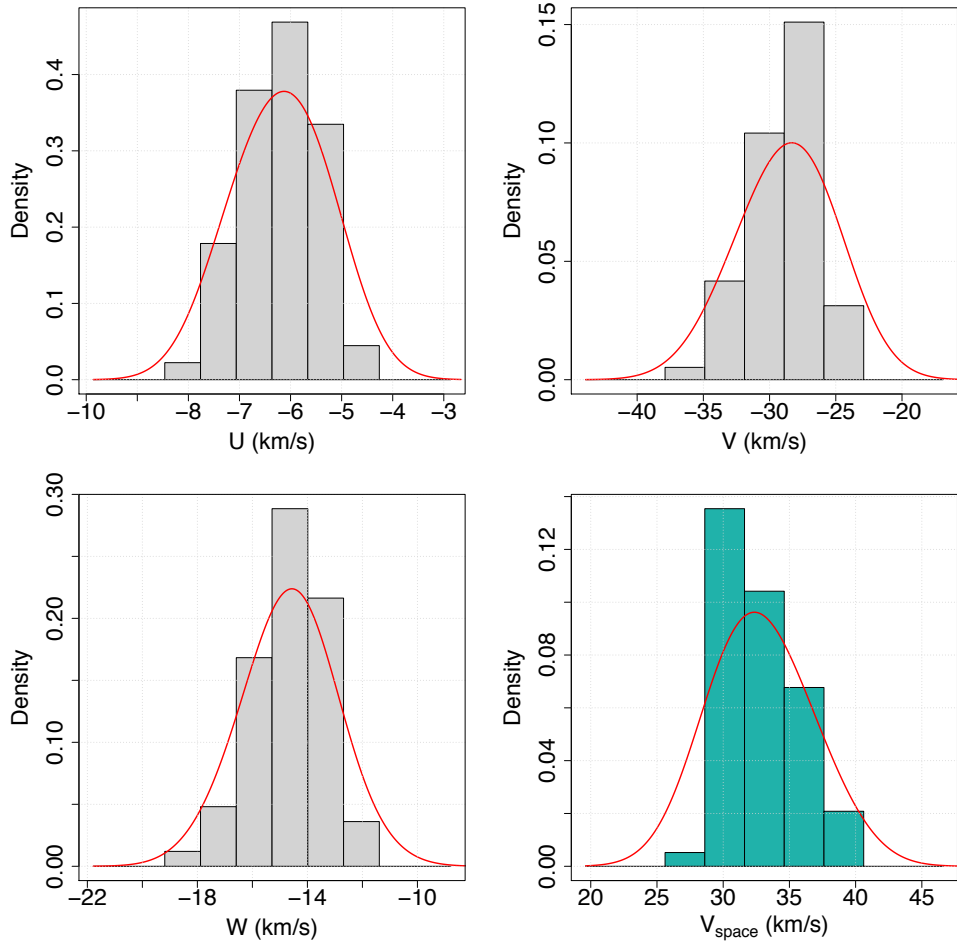


Figure 2.3: Histogram and kernel density estimation (red line) of the components (grey) and modulus (green) of the spatial velocity distribution of 64 candidate members of [Galli et al. \(2017\)](#) with radial velocities and parallaxes. Reproduced from Figure 11 of [Galli et al. \(2017\)](#), *A revised moving cluster distance to the Pleiades open cluster*, A&A, Vol. 598.

2.5 Luminosity Distribution

The luminosity distribution usually refers to the statistical probability distribution of the absolute³ magnitude of the cluster population. It can also refer to the distribution of apparent magnitudes. It can be thought as the spectrum of brightness of the cluster members. Its importance lies in the fact the the luminosity of a star, measured in absolute magnitudes, can be related to its mass by the mass-luminosity relation. Therefore, the luminosity distribution is a proxy for the mass distribution.

The study of the distribution of luminosities in the Pleiades started few years later than those of the positions and proper motions. The first record I found on the luminosity distribution is the one of [Trumpler \(1921\)](#) (see Fig. 2.4). He computed the number of stars in each magnitude bin for his two samples of candidate members, those comprising the objects within the central 1° , and those between 1° and 3° , referred as Tables I and II, respectively. The completeness of the inner and outer samples was estimated at 14.5 and 9.8 photographic magnitudes (roughly 14 and 9 in the visual band), respectively. He observed that the luminosity distributions of these two samples were not alike, with the inner sample being brighter than the outer one. He also noticed that the luminosity distribution is not smooth, and shows a local minimum at 9 magnitudes, then an abrupt rise. Both effects are present in the two samples.

Later, [Johnson & Mitchell \(1958\)](#) obtained the luminosity distribution using a sample of 289 candidate members. They assessed membership solely on photometry. Their luminosity distribution is shown in Fig. 2.5

Later, [Limber \(1962\)](#) compared the luminosity distributions derived from the data of [Trumpler \(1921\)](#), [Hertzsprung \(1947\)](#), and [Johnson & Mitchell \(1958\)](#), with the initial luminosity distribution that he derived ([Limber 1960](#)). The initial luminosity distribution corresponds to the distribution of luminosities that the cluster had at the moment of formation. [Limber \(1960\)](#) derived it mixing data of galactic clusters and the local neighbourhood, and later correcting it by effects of age. He noted that the Pleiades present day luminosity distribution starts to differ from the initial luminosity distribution at visual magnitude 5.5, see Fig. 2.6. Assuming that this difference is due to the fact that stars fainter than 5.5 have not yet had enough time for contraction, he derives an age of 50 Myr. As he mentions, this contraction time could be wrong by a factor of two. Currently, we know that a star of such magnitude has a luminosity of $0.5L_\odot$, which translates into a mass of $0.8 M_\odot$ and thus in a contraction time of roughly twice that assumed by Limber.

In recent years, the luminosity distribution has been described in the works of [Lodieu et al. \(2012\)](#) and [Bouy et al. \(2015\)](#). [Lodieu et al. \(2012\)](#), using the *UKIDSS DR9* survey for galactic clusters and a probabilistic membership selection method (see discussion in Chapter 1) based on proper motions only, and proper motions and photometry, found 8797

³The absolute magnitude M , is the brightness that an object of apparent magnitude m will show at a distance of 10 pc.

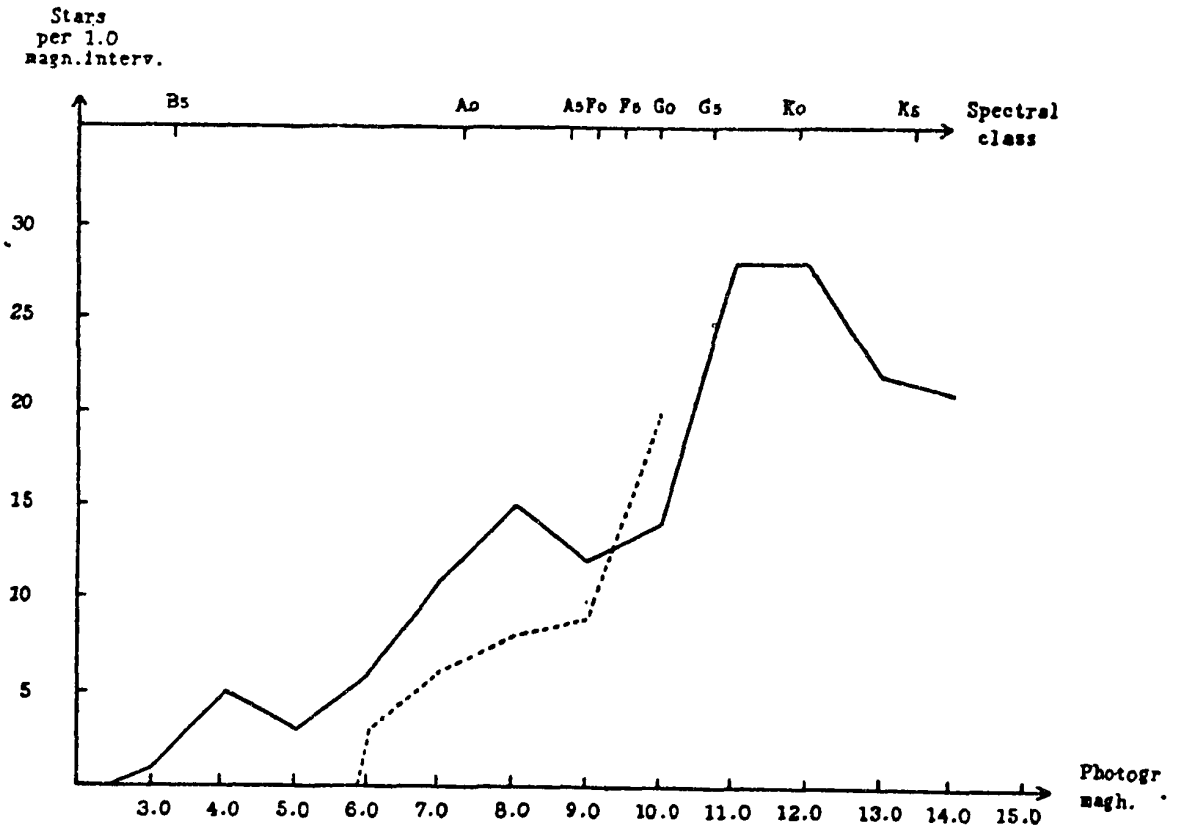


Figure 2.4: Luminosity distribution according to [Trumpler \(1921\)](#). The solid and dashed lines correspond to objects within 1° and within 1° , and 3° from the centre. Reproduced from Figure 2 of [Trumpler \(1921\)](#), *The physical members of the Pleiades group*, Lick Observatory Bulletin, Vol. 10.

and 1147 candidate members, respectively. However, they do not provide the contamination rate in their analysis. Using both lists, they provide their luminosity distributions in the Z band, which I show in Fig. 2.7.

In [Bouy et al. \(2015\)](#), we estimated the present day system luminosity distribution of 1378 candidate members contained within the central 3° region (with the centre at R.A.= 03 : 46 : 48 and Dec.= 24 : 10 : 17 J2000.0). It is called systemic because it has not been corrected for unresolved systems. An unresolved system is a group of stars (e.g. binaries) that due to its compactness appears as a single object. This distribution was computed for the K_s band and is sensitive up to $K_s \sim 20$ mag and complete until $K_s \sim 17$ mag. This luminosity distribution is reproduced in Fig. 2.8

The luminosity distribution of [Bouy et al. \(2015\)](#) is till date, the most extended and precise one from the literature. As can be seen from Fig. 2.8, it extends across 15 magnitudes (-4 to 11 mags, with a gap at $M_{Ks} \sim 4$) with a contamination rate of only $\sim 8\%$. In comparison the one from [Lodieu et al. \(2012\)](#) extends only 10 magnitudes (12 to 22) and with unknown contamination rate.

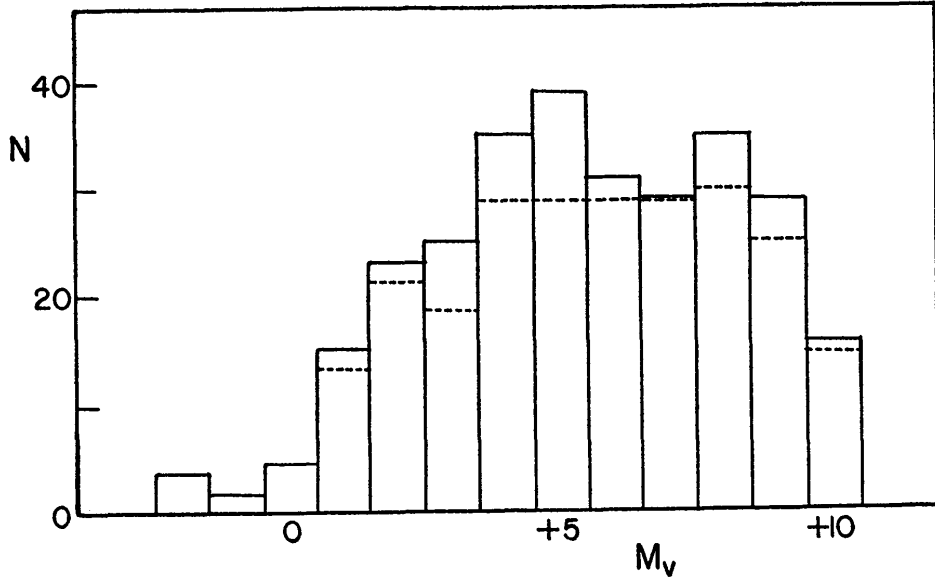


Figure 2.5: Luminosity distribution in the visual band according to [Johnson & Mitchell \(1958\)](#). The dotted line represent the counts of main sequence stars only. Reproduced from Figure 3 of [Johnson & Mitchell \(1958\)](#), *The Color-Magnitude Diagram of the Pleiades Cluster. II.*, ApJ, Vol. 128.

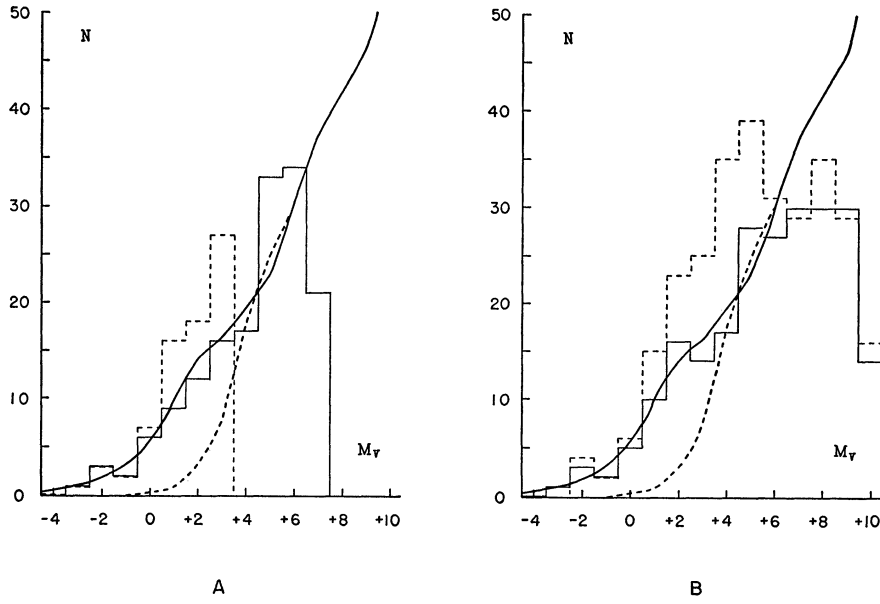


Figure 2.6: Luminosity distribution in the visual band according to [Limber \(1962\)](#). The solid and dashed histograms in: A correspond to [Trumpler \(1921\)](#) data from the Tables II and I, respectively, in B, correspond to the data from [Hertzsprung \(1947\)](#) and [Johnson & Mitchell \(1958\)](#), respectively. The solid and dashed curves line represent initial luminosity distribution and the present day luminosity distribution of the solar neighbourhood, respectively, both from [Limber \(1960\)](#). Reproduced from Figure 4 of [Limber \(1962\)](#), *The Dynamics of the Pleiades Cluster.*, ApJ, Vol. 135.

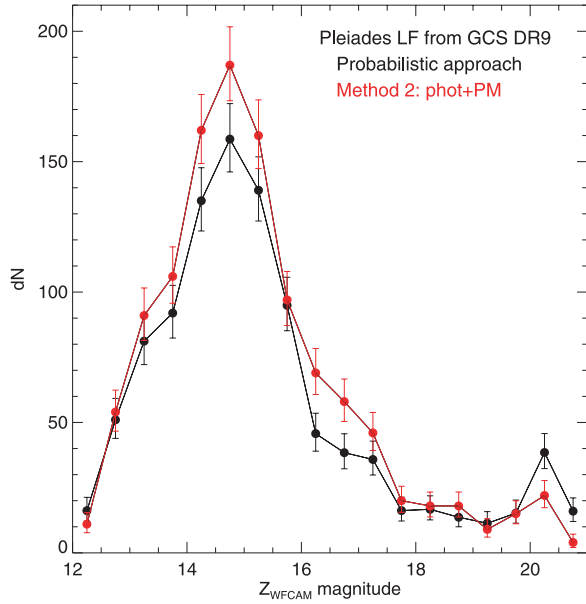


Figure 2.7: Luminosity distribution in the Z band according to [Lodieu et al. \(2012\)](#). The red and black lines correspond to the two different probabilistic methods. Reproduced from Figure 9 of [Lodieu et al. \(2012\)](#), *Astrometric and photometric initial mass functions from the UKIDSS Galactic Clusters Survey - I. The Pleiades*, MNRAS, Vol. 422.

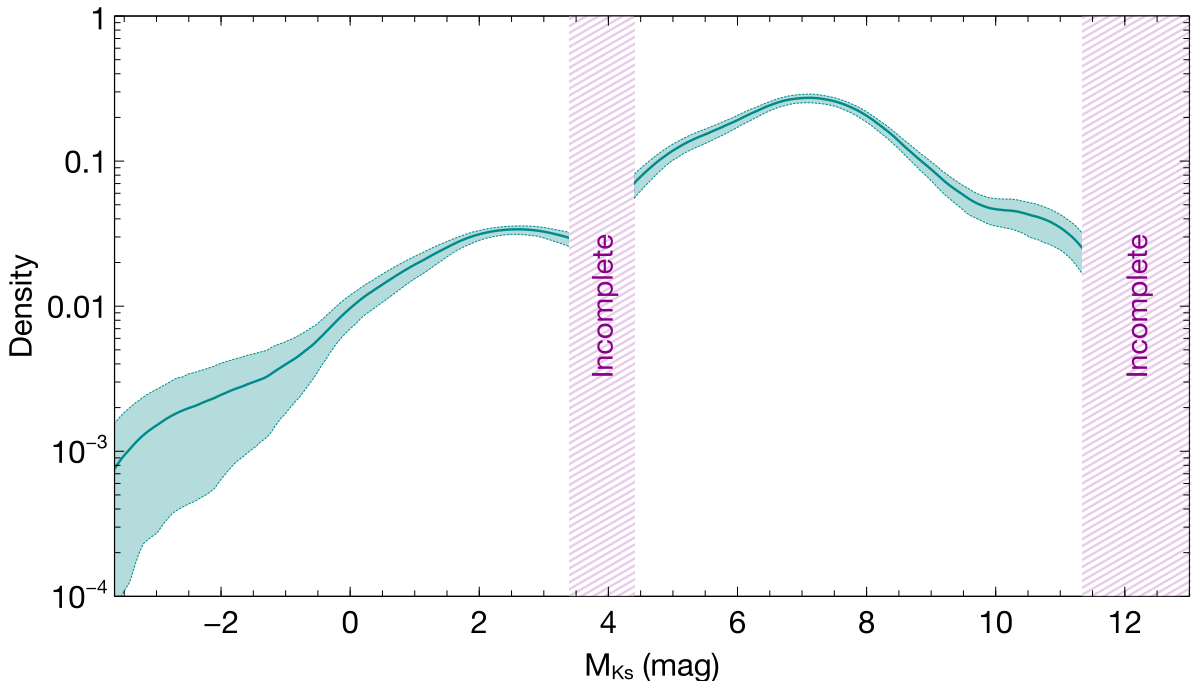


Figure 2.8: Luminosity distribution in the K_s band according to [Bouy et al. \(2015\)](#). The incompleteness regions are shaded. Reproduced from Figure 8 of [Bouy et al. \(2015\)](#), *The Seven Sisters DANCE. I. Empirical isochrones, luminosity, and mass functions of the Pleiades cluster*, A&A, Vol. 577.

2.6 Mass Distribution

In astrophysics, the mass distribution is a cornerstone in the understanding of the star formation process and the later evolution of stellar systems. Although the temporal evolution of these systems is mainly dominated by the gravitational potential, the initial conditions and an ongoing star formation process, if any, can contribute to the shape of the mass distribution. This last contains the fingerprints of past events in the history of the cluster and plays a key role in its future evolution. Indeed, the evolution of the mass distribution is an essential element in one of modern astrophysics' objectives: the determination of the role played by the initial conditions or the environment, in the temporal evolution of the stellar systems. The mass distribution at the moment of the cluster formation, which is known as the initial mass distribution evolves in time according to: i) stellar internal and atmospheric processes (e.g. contraction, mass loss, inflation, supernova events), ii) population dynamical interactions (e.g. three-body encounters, runaway stars, stellar evaporation), and iii) galactic dynamics (e.g. tidal effects, encounters with other clusters). For these reasons, the study of the initial mass function and its posterior evolution is a key element in the current understanding not just of open clusters but also of galactic and extragalactic populations.

The mass distribution of the Pleiades has been largely studied. The first work on the mass distribution is that of [Limber \(1962\)](#). Although he did not show any graphical or tabular representation of it, he gave the luminosity distribution and the mass-luminosity ratio. From these the mass distributions can be derived. Instead, he used them to obtain the total mass of the cluster ($760 M_{\odot}$, see next Section).

Most probably, the first work to present the mass distribution derived from luminosity distributions and a mass-luminosity relation from theoretical models was that of [Hambly & Jameson \(1991\)](#). Using R and I observations from the *United Kingdom Schmidt Telescope Unit* together with the mass-luminosity relation from theoretical isochrone models of Padova group, he was able to transform his luminosity distribution into a mass distribution. In Fig. 2.9, I reproduce his results.

From the year 2000 till date, several studies have been published in which the subject of analysis is the Pleiades mass distribution, e.g. [Hodgkin & Jameson \(2000\)](#); [Jameson et al. \(2002\)](#); [Moraux et al. \(2001, 2003, 2004\)](#); [Lodieu et al. \(2007\)](#). However, for the sake of simplicity, here I only analyse the two most recent works, those of [Lodieu et al. \(2012\)](#) and [Bouy et al. \(2015\)](#). The PDSMD derived from both these works are shown in Figs. 2.10 and 2.11. These works obtained first the luminosity distribution, and then transformed it into a mass distributions using mass-luminosity relations of theoretical isochrone models.

[Lodieu et al. \(2012\)](#) used a distance of 120.2 pc, an age of 120 Myr, and the *NEXTGEN* theoretical models of [Baraffe et al. \(1998\)](#) to transform the luminosity into the mass distribution. On the other hand, in [Bouy et al. \(2015\)](#) we use a distance of 136.2 pc an

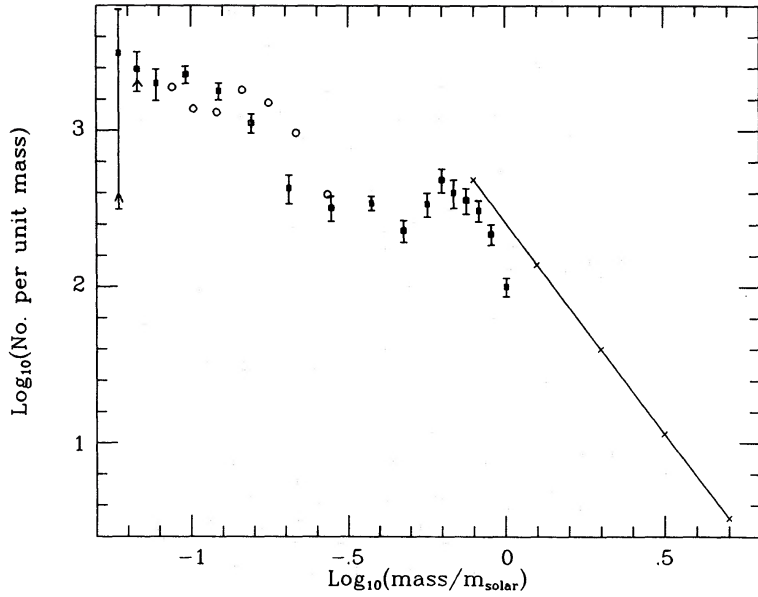


Figure 2.9: Mass distribution of Hambly & Jameson (1991) derived from luminosity distribution and theoretical isochrone models. The open circles result from assuming an older age of 200 Myr. The line represent the mass distribution of van Leeuwen (1980). Reproduced from Figure 11 of Hambly & Jameson (1991), *The luminosity and mass functions of the Pleiades - Low-mass stars and brown dwarfs*, MNRAS, Vol. 249.

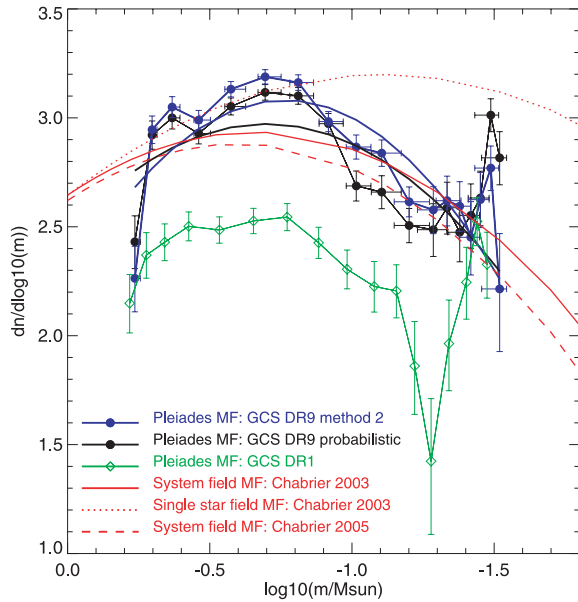


Figure 2.10: Pleiades present day mass distribution from Lodieu et al. (2012). GCS stands for Galactic Cluster Survey. The first and last two points must be treated with caution due to saturation and contamination at the bright and faint ends, respectively. Reproduced from Figure 9 of Lodieu et al. (2012), *Astrometric and photometric initial mass functions from the UKIDSS Galactic Clusters Survey - I. The Pleiades*, MNRAS, Vol. 422.

age of 120 Myr and the *BT-Settl* theoretical isochrone models of Allard (2014).

Both works found that their derived PDSMD are in general agreement with the IMF of

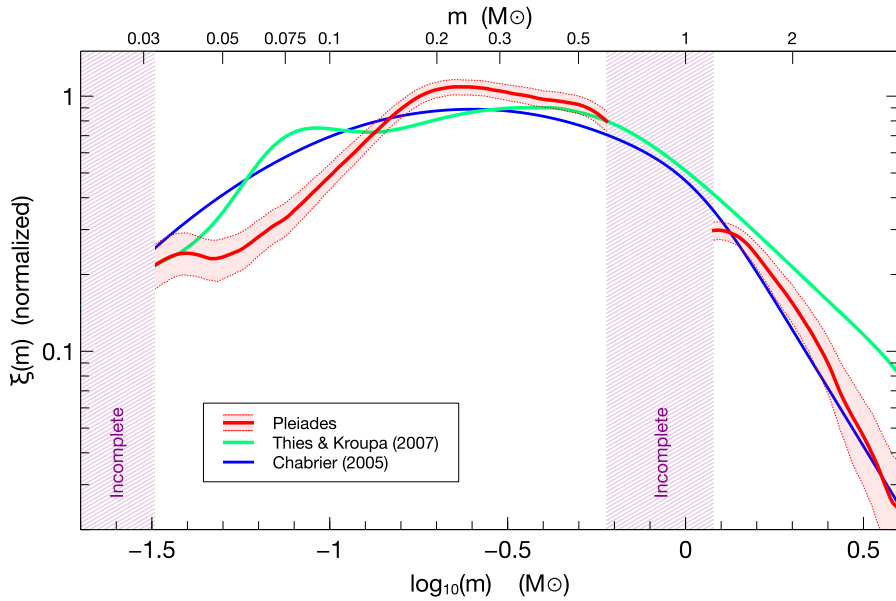


Figure 2.11: Pleiades present day mass distribution from Bouy et al. (2015) (red). IMFs from Chabrier (2005)(blue) and Thies & Kroupa (2007) (green) are also shown. Reproduced from Figure 9 of Bouy et al. (2015), *The Seven Sisters DANCE. I. Empirical isochrones, luminosity, and mass functions of the Pleiades cluster*, A&A, Vol. 577.

Chabrier (2005) for unresolved systems (see Section 1.1). However, in Bouy et al. (2015) we pointed out that, assuming that the theoretical mass-luminosity relation is correct, the IMFs of Chabrier (2005) and Thies & Kroupa (2007) predict too many low-mass stars and brown dwarfs in the range $0.04 - 0.1 M_\odot$.

The differences at the low mass regime between the PDSMD derived by Lodieu et al. (2012) and Bouy et al. (2015) (see Figs. 2.10 and 2.11) could arise from the different i) samples of members, ii) mass-luminosity relations, and iii) distances adopted by both works. To discard the last two points and clearly compare the different methodologies, I transformed the luminosity distribution of Lodieu et al. (2012) to the present day mass distribution using the same assumptions as in Bouy et al. (2015). The result of such transformation for both Lodieu et al. (2012) methods is shown in Fig. 2.12. Both works use the GCS of UKIRT Infrared Deep Sky Survey (UKIDSS) in the low-mass domain, thus, both are limited by the completeness of this survey (marked in grey, together with the high-mass domain of Bouy et al. 2015). As can be seen, both Lodieu et al. (2012) methods, the one based only on photometry and the one based on photometry and proper motions, result in a present day mass distribution which is in clear discrepancy with that of Bouy et al. (2015) in the low-mass range.

Concerning the differences between the lists of candidate members, Lodieu et al. (2012) do not provide (at least explicitly) any estimate of contamination rate. Furthermore, their membership methodology has draw backs (see Sarro et al. 2014) which may have biased their results. Therefore, the agreement that Lodieu et al. (2012) found between

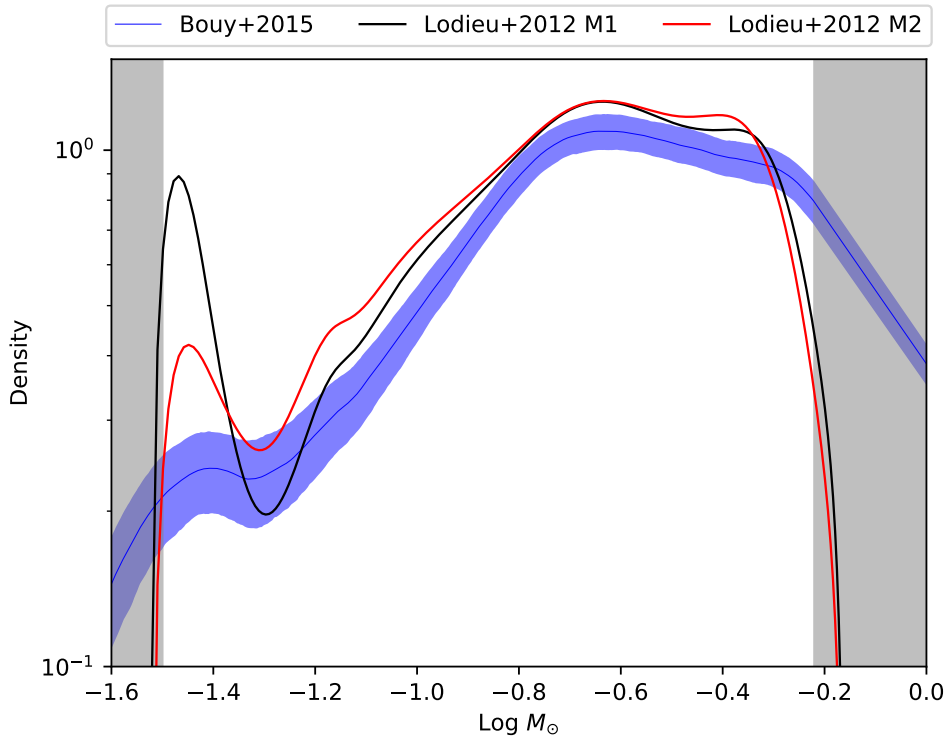


Figure 2.12: Pleiades present day mass distribution from [Bouy et al. \(2015\)](#) (blue line) and methods 1 (black line) and 2 (red line) of [Lodieu et al. \(2012\)](#). The grey areas mark the incompleteness regions in the work of [Bouy et al. \(2015\)](#), which in the low-mass end coincide with that of [Lodieu et al. \(2012\)](#).

their present day mass distribution and the IMF of [Chabrier \(2005\)](#), which models the field mass distribution, may be an indication that their sample of candidate members is contaminated by the field.

On the other hand, in [Bouy et al. \(2015\)](#) we estimated a contamination rate of 7%. However, we have no evidence for it to be non-homogeneous in mass. Even if the 7% contaminants were not homogeneously distributed in the mass range, this value is not able to account for the observed discrepancies (30 – 40% in the low-mass regime) between the IMF of [Chabrier \(2005\)](#) and our present day mass distribution.

Given the previous considerations, and in the light of the comparison shown in Fig. 2.12, the most probable scenario is that the methodologies used by [Lodieu et al. \(2012\)](#) result in list of candidate members that are contaminated in the low-mass domain.

The previous studies show that there is still work to do in the analysis of the Pleiades mass distribution, particularly at the low-mass regime where the IMFs show discrepancies with the observed present day mass distribution.

2.6.1 Total mass of the cluster

Before ending this section I present a (non exhaustive) summary of the studies that provided an estimate of the total mass of the cluster.

The first record I found of the cluster total mass is that of [Titus \(1938\)](#). He estimated a total mass of $260 M_{\odot}$ assuming virial equilibrium. He also computed $200 M_{\odot}$ using the Eddington's mass-luminosity relation for objects brighter than 15 mag in the visual band.

The subsequent works continue to report higher masses. [Woolley \(1956\)](#) estimated a total mass of $337 M_{\odot}$ using a polytrope model fitted to Hertzsprung's catalogue. He then mentions that taking into account Trumpler's data, the total mass should be about $500 M_{\odot}$.

[Limber \(1962\)](#) computed the total mass in two ways. In the first one he assumed the cluster was virialised and obtained a mass of $900 M_{\odot}$. Using the luminosity function he estimated the lower limit to the total mass in $760 M_{\odot}$.

[Jones \(1970\)](#) measured $470 M_{\odot}$ and $690 M_{\odot}$ using the luminosity distribution and the virial theorem, respectively.

Later, [van Leeuwen \(1980\)](#) determined a total mass of $2000 M_{\odot}$ using the virial theorem, a mean individual mass of $2 M_{\odot}$, and a velocity dispersion of $0.7 \text{ km} \cdot \text{s}^{-1}$ in each spatial direction.

[Lee & Sung \(1995\)](#) measured $700 M_{\odot}$ using the luminosity distribution and a mass-luminosity relation.

[Pinfield et al. \(1998\)](#) fitting a King profile to the PSD of the cluster members obtained $735 M_{\odot}$.

[Raboud & Merrilliod \(1998\)](#) estimate the total mass in three ways, using the: i) tidal radius, ii) virial theorem and, iii) mass function. For the tidal radius they assume that it corresponds to the Jacobi one, thus using the Oort's constants they obtain $1400^{+1500}_{-870} M_{\odot}$. For the virial theorem they use a velocity dispersion of 0.36 km s^{-1} , and an harmonic radius of 3.96 pc to derive a mass of $720^{+220}_{-210} M_{\odot}$. For the mass function they use a binary correction of 1.16 and obtain $950^{+200}_{-150} M_{\odot}$.

[Adams et al. \(2001\)](#) counting individual masses of candidate members within 5.5° obtained a total mass of $690 M_{\odot}$.

[Converse & Stahler \(2008\)](#) found $820 M_{\odot}$ after adding the individual masses of 1245 candidate members of [Stauffer et al. \(2007\)](#). To obtain these masses they transformed the K and $I - K$ magnitude and colour into masses using the mass-luminosity relation given by the theoretical isochrone models of [Baraffe et al. \(1998\)](#). Later, [Converse & Stahler \(2010\)](#) redid their analysis and found the total mass to be $870 \pm 35 M_{\odot}$.

As can be observed, the mass estimates derived from the mass distribution are consistently lower than those derived using dynamical assumptions. While the formers have a mean value of $750 \pm 155 M_{\odot}$, the latter have a mean value of $1140 \pm 560 M_{\odot}$. It is important to consider that estimates based on the mass function do not take into account neither the

planetary-mass objects nor all those laying beyond the survey coverage area, which judging by the tidal radius measurement of [Converse & Stahler \(2010\)](#), ~ 20 pc, seem to reach just half the cluster tidal radius. Therefore, the total mass estimates derived from the mass function can be thought as a lower limit to the total cluster mass. On the other hand, the dynamical estimates are based on over-simplistic assumptions that must probably overestimate the total mass. For example, assuming the tidal radius corresponds to the Jacobi radius, or that the measured velocity dispersion corresponds to the true velocity dispersion, leave aside effects of the cluster internal and environmental dynamics such as cluster internal rotation, galactic orbital eccentricity, tidal elongation, stellar ejections, tidal streams, etc. (see for example [Küpper et al. 2010b,a](#); [Binney & Tremaine 2008](#)). Therefore, the true value of the total cluster mass remains an elusive parameter that should be estimated in the light of new and precise data together with more comprehensive cluster models.

As shown by the brief summary presented in the previous Sections, although the Pleiades cluster is one of the most studied in the literature, its properties remain an active area of research.

2.7 The Pleiades DANCe DR2

The Pleiades DANCe Data Release 2 (DDR2) contains astrometric (stellar positions and proper motions) and photometric ($ugrizYJHK_s$) measurements for 1,972,245 objects. As explained in Chapter 1, the DANCe data set has an heterogenous origin, which can be observed in Fig. 2.13 where the patchy pattern arise from the combination of several surveys. The interested reader can find more the details of this data set and its processing in [Bouy et al. \(2013, 2015\)](#). Here, I briefly summarise its properties. Table 2.2 contains the basic statistics for the observables, while Table 2.3 does it for the uncertainties. As an example, Fig. 2.14 shows the proper motions uncertainties as a function of the i magnitude.

2.7.1 Selection of observables

The DDR2 contains the positions R.A., Dec. (in the following α and δ), proper motions, $\mu_{\text{R.A.}}, \mu_{\text{Dec.}}$, and photometric $ugrizYJHK_s$ bands, of almost two million sources on the vicinity of the Pleiades clusters. Although these 13 observables carry information valuable to discriminate cluster members from field objects, not all of them do it in the same way. [Sarro et al. \(2014\)](#) give a detailed analysis of the capacity of the previous observables (with the exception of the stellar positions) to discriminate between cluster members and field population. These authors use random forest to select the observables that were the most discriminant. They find that the proper motions ($\mu_{\text{R.A.}}, \mu_{\text{Dec.}}$) and the photometric bands $rizYJHK_s$ are the most discriminants.

KPNO/Mosaic1 **UKIRT/WFCAM** **Subaru/SuprimeCam** **CFHT/CFHT12K**
INT/WFC **CFHT/UH8K** **KPNO/NEWFIRM** **CTIO/MOSAIC2** **CFHT/MegaCam**

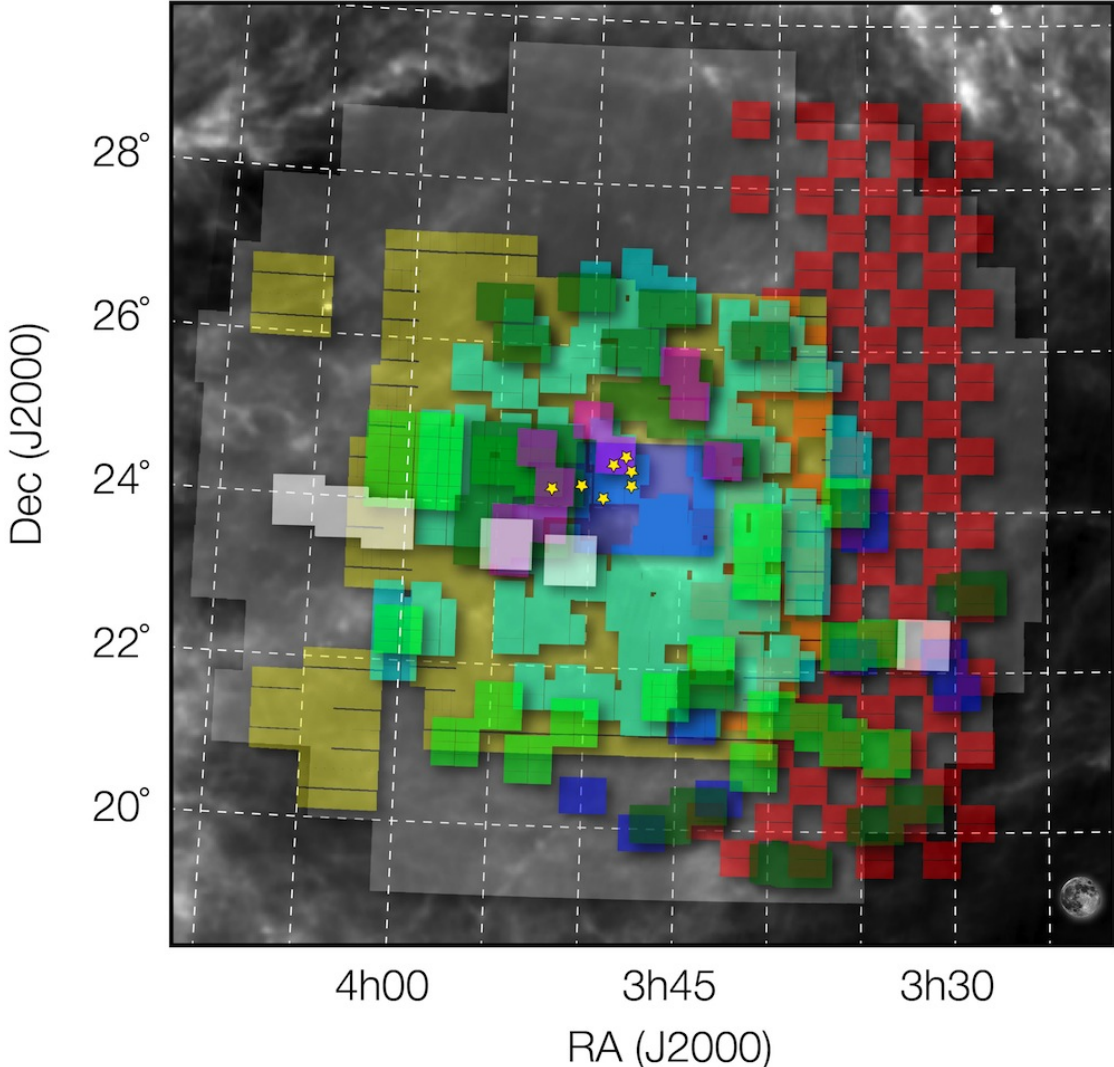


Figure 2.13: Patchy composition of the DDR2. The moon shows the scale, and the yellow stars correspond to the central brightest objects of the Pleiades cluster. As can be seen, the UKIDSS (UKIRT) survey provides the most homogeneous and extended coverage. Reproduced from Figure 1 of Bouy et al. (2013), *Dynamical analysis of nearby clusters. Automated astrometry from the ground: precision proper motions over a wide field*, A&A, Vol. 554.

Since most the objects with a missing r band occur at the faint end of the cluster sequence, Sarro et al. (2014) train their model (see Section 1.4) in two stages. In the first stage, they use all literature candidate members with observed r band. In the second stage, they discard the r band observations and continue training their model with objects in which the r band was missing. In a subsequent analysis using roughly the same methodology, Bouy et al. (2015) skipped the first training stage and worked only with the RF-2, which also excludes the z band.

Table 2.2: Summary of the DDR2.

Observable	Min.	1st. Qu.	Median	Mean	3rd. Qu.	Max.	NA's
RA [deg]	51.23	55.40	57.35	57.26	59.01	62.94	0
Dec. [deg]	19.12	22.47	24.32	24.27	25.95	29.69	0
$\mu_\alpha [mas \cdot yr^{-1}]$	-99.998	-6.060	-1.645	-1.240	3.401	99.996	0
$\mu_\delta [mas \cdot yr^{-1}]$	-99.997	-2.835	2.548	1.976	7.017	99.989	0
u [mag]	13.6	20.4	22.0	21.6	23.3	25.2	1756374
g [mag]	9.4	19.6	22.1	21.1	23.3	25.5	1492564
r [mag]	8.4	17.6	21.3	20.3	22.6	25.1	1222853
i [mag]	7.5	20.0	21.6	21.0	22.7	25.5	820861
z [mag]	11.2	17.9	19.3	18.9	20.2	25.0	697412
Y [mag]	8.3	17.2	18.5	18.1	19.4	24.2	688144
J [mag]	2.8	16.7	17.9	17.5	18.8	23.1	645469
H [mag]	2.0	16.1	17.3	16.9	18.1	20.9	653682
K_s [mag]	1.8	16.0	17.0	16.7	17.7	23.8	561745

Table 2.3: Uncertainties of the DDR2.

Observable	Min.	1st. Qu.	Median	3rd. Qu.	Max.	Mean
RA [deg]	8.900e-08	9.270e-07	1.933e-06	4.037e-06	2.156e-02	3.173e-06
Dec. [deg]	8.900e-08	9.270e-07	1.932e-06	4.037e-06	2.156e-02	3.173e-06
$\mu_\alpha [mas \cdot yr^{-1}]$	2.01e-01	1.89e+00	4.35e+00	1.00e+01	1.49e+22	3.99e+16
$\mu_\delta [mas \cdot yr^{-1}]$	1.92e-01	1.89e+00	4.35e+00	1.00e+01	4.71e+09	1.42e+04
u [mag]	3.73e-04	8.07e-03	3.06e-02	8.56e-02	2.17e-01	5.48e-02
g [mag]	1.72e-01	1.02e-02	3.90e-02	7.90e-02	1.82e+00	5.34e-02
r [mag]	2.83e-04	1.54e-02	4.88e-02	1.04e-01	1.42e+00	6.34e-02
i [mag]	4.04e-04	9.03e-03	2.73e-02	5.85e-02	2.40e+00	4.37e-02
z [mag]	6.49e-04	5.62e-02	9.16e-02	1.85e-01	3.12e+00	1.34e-01
Y [mag]	3.00e-02	5.21e-02	6.50e-02	1.03e-01	9.01e+00	8.56e-02
J [mag]	1.60e-02	5.24e-02	6.66e-02	1.04e-01	8.89e+00	8.57e-02
H [mag]	1.40e-02	5.28e-02	7.04e-02	1.10e-01	1.00e+01	8.85e-02
K_s [mag]	1.40e-02	5.75e-02	8.17e-02	1.32e-01	3.88e+01	1.04e-01

Therefore, in the present work I use as a reference set the the proper motions, μ_α, μ_δ , the photometric bands Y, J, H, K_s , and the colour index $i - K_s$, with the addition of the stellar positions α and δ . This decision roots in the following reasons.

- First, [Sarro et al. \(2014\)](#) prove that these observables (excluding the stellar positions) are amongst the most discriminant ones in the DDR2.
- Second, this set corresponds to the one used by [Bouy et al. \(2015\)](#), thus, it will enable us to perform a direct comparison and validation with their results. However, observables used by [Bouy et al. \(2015\)](#) and the ones use in the present work are

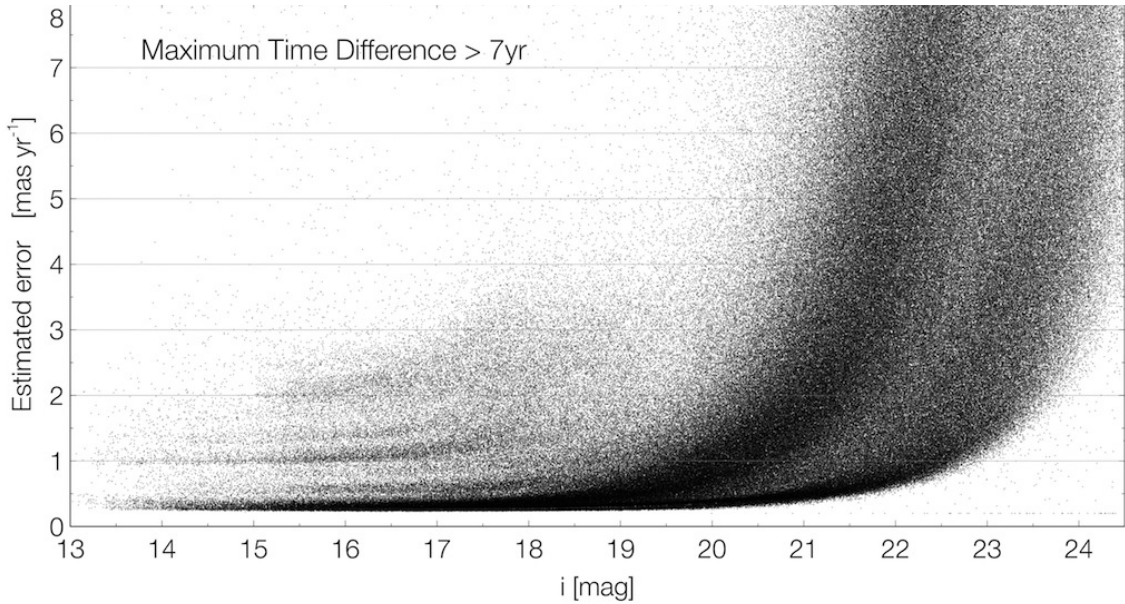


Figure 2.14: Proper motion uncertainty as a function of the photometric magnitude in the i band. Reproduced from Figure 12 of [Bouy et al. \(2013\)](#), *Dynamical analysis of nearby clusters. Automated astrometry from the ground: precision proper motions over a wide field*, A&A, Vol. 554.

not exactly alike. While here I use the Y band alone, [Bouy et al. \(2015\)](#) use the colour index $Y - J$. Originally, I tested the methodology with this $Y - J$ colour index but the contamination resulting from it was higher than that resulting from the use of the Y band. This is a consequence of how the intrinsic dispersion of the cluster photometric sequence is modelled. The details of it will be shown in Section 3.3.4. Here suffices to say that the photometric model describes the cluster sequence dispersion with a constant width across the $i - K_s$ colour index. The dispersion of the cluster sequence in the $Y - J$ vs. $i - K_s$ colour-colour diagram varies greatly across $i - K_s$ contrary to the elatively stable dispersion in the Y vs $i - K_s$ CMD. This effect can be observed in Figure 2.15, where the candidate members of [Bouy et al. \(2015\)](#) (blue dots) are depicted, together with the DDR2 density (black contour lines), in the colour-colour diagram $Y - J$ vs. $i - K_s$, and the CMD Y vs $i - K_s$. Therefore, the use of $Y - J$ results in larger contamination in those regions where the true clusters sequence is narrower than the average model. Future steps will be take to include more colour indices in the reference set of observables.

Concerning the stellar positions α and δ , neither [Bouy et al. \(2015\)](#) nor [Sarro et al. \(2014\)](#) use them in their analyses. Thus, I will independently analyse the: i) the kinematic and photometric distributions of the cluster population, and ii) the PSD. This decision roots in the following reasons.

- To fulfil the objective of the DANCe project (see Section 1.3), the inventory of kinematic and photometric distributions of the NYCs must be obtained with an

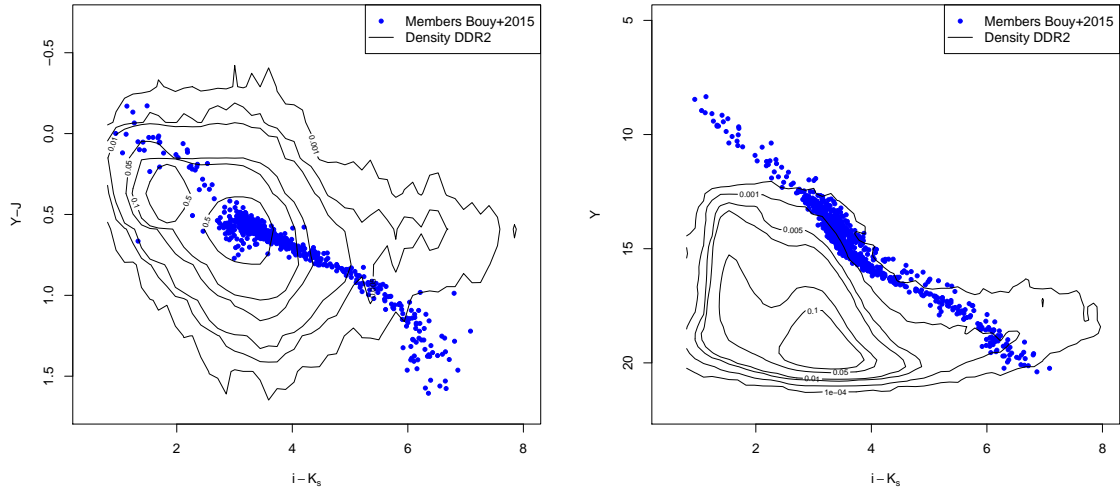


Figure 2.15: Candidate members of Bouy et al. (2015), blue dots, together with the density of the Restricted Pleiades DANCe Data Release 2 (RDDR2) data set, black contours, in the colour-colour diagram $Y - J$ vs. $i - K_s$ (left) and CMD Y vs $i - K_s$ (right).

homogenous methodology. The DANCe NYC targets (see Tables 1.1 and 1.2) do not share similar projected spatial density profiles; while Taurus, Ophiucus and the Trapezium are extended (see for example Simon 1997), the Pleiades is almost radially symmetric (Raboud & Mermilliod 1998). Thus, including the spatial information together with the proper motions and photometry would require completely different models for the PSD of different clusters. That would result in non-homogenous methodologies that would bias any comparison between the derived PDSMD of these clusters.

- To validate the results of the present work, which will be conducted in the Pleiades cluster, we must compare them with similar results under the most similar conditions. Since Bouy et al. (2015); Sarro et al. (2014) do not include the stellar positions in their observables, I do that as well.
- Almost all previous analyses of the Pleiades PSD use King profile (see Section 2.3) without providing any further reason beyond its physical interpretability, which nevertheless remains a good one. Thus, we decided to perform a Bayesian model selection analysis to compare how well the common surface density profiles, included the King's one, reproduce the Pleiades PSD. The results of this analysis have been submitted to the *A&A* journal.

As will be described in Section 3.3.4, the cluster photometric sequence, in each magnitude, is modelled by functions in which the parameter is the *true* Colour Index $i - K_s$ (CI) (details for this decision will be given in Section 3.3.4. Thus, our photometric

set of observables is made of the colour index $CI = i - K_s$ and the photometric bands Y, J, H and K_s .

2.7.2 Data preprocessing

Since both photometry and proper motions carry crucial information for the disentanglement of the cluster population, we restrict the data set to only those objects with observed proper motions, and also at least two photometric entries in our photometric set ($i - K_s, Y, J, H, K_s$). Objects with only one photometric entry, although theoretically could be included in the data set, are left aside due to computational reasons. Their treatment requires selection statements to choose between the univariate and multivariate computational libraries that proved to be computationally expensive.

The previous restrictions exclude 22 candidate members of [Bouy et al. \(2015\)](#), which have only one observed value in the photometry. For these particular objects, we compute their marginal proper motion membership probability a posteriori, once the parameters of the model were inferred. The mode and 16 and 84 percentiles of their membership probabilities are listed in Table 2.4. Only four of these 22 objects have membership probabilities below 0.5, which may indicate they are contaminants. Since these membership probabilities were computed using only the kinematic information, these four members could not be discarded as probable candidate members.

In the following, whenever I mention the Pleiades candidate members of [Bouy et al. \(2015\)](#), I refer to the 1988 objects in the DDR2 with [Bouy et al. \(2015\)](#) membership probabilities grater than 0.75, and with at least two observed values in the photometry.

Furthermore, we restrict the lower limit of the CI to the value of the brightest cluster member, $CI=0.8$ in the DDR2 data set (The actual value is $CI=0.93$, see Table 2.5, but 0.8 was chosen conservatively to include the uncertainty). We do not expect to find new bluer members in the bright part of the CMDs. In the Tycho+DANCe data set ([Bouy et al. 2015](#)), which also comprises the bright side of the cluster sequence, the bluer candidate member of [Bouy et al. \(2015\)](#) has a $CI=0.67$. This shows that the cut at 0.8 is reasonable for the fainter DDR2 data set.

Also, we set the upper limit of the CI to $CI=8$, which is one magnitude redder than the colour index of the reddest known cluster member. This value allows for possible new discoveries. Due to the sensitivity limits of the DDR2 survey in i and K_s bands, ($i \sim 23$ mag and $K_s \sim 18$ mag, see Appendix A of [Bouy et al. 2015](#)), the 262 objects with a CI grater than this limit have K_s magnitudes brighter than 16 mag. This combination of CI and K_s magnitude is clearly incompatible with the cluster sequence of [Bouy et al. \(2015\)](#) (see Fig. 2.16), which allows us to remove them from the data set.

Although formally these two cuts in the observed CI (and only in objects with observed CI) are not needed for the statistical analysis (which accounts for this truncation, see Section 3.3.4), they nevertheless improved significantly the computing time required for it.

Table 2.4: Membership probabilities of the 22 excluded candidate members of [Bouy et al. \(2015\)](#).

ID DANCe	P_{16}	Mode	P_{84}
J035106.55+211604.3	0.751182	0.7774335	0.785560
J035057.42+240630.8	0.792295	0.8090186	0.829541
J034704.76+252249.8	0.701193	0.7319624	0.750745
J034725.80+250832.7	0.789872	0.8169538	0.827954
J034437.44+250815.6	0.762013	0.7773114	0.798125
J035125.88+244738.6	0.883488	0.9007972	0.905823
J034235.64+215029.7	0.838538	0.8662402	0.871439
J034516.66+243432.1	0.862284	0.8666611	0.881004
J034926.12+235714.8	0.852537	0.8606685	0.866286
J034920.60+244635.9	0.923319	0.9270399	0.935532
J035300.63+233252.3	0.762996	0.7747163	0.781901
J034606.52+235020.2	0.928688	0.9333306	0.940772
J035040.89+245657.7	0.509435	0.5215143	0.530379
J034845.33+233124.8	0.260551	0.2650812	0.275513
J034713.67+234953.3	0.814689	0.8489593	0.855902
J034546.48+234743.0	0.897035	0.9098442	0.912059
J034548.95+235110.2	0.933892	0.9376429	0.945558
J035202.26+242148.1	0.248011	0.2649874	0.305949
J035313.22+235540.8	0.518388	0.5425345	0.553376
J034425.60+244052.5	0.581242	0.5902633	0.602096
J035518.38+245637.2	0.198074	0.2087989	0.252831
J035418.93+252944.0	0.366009	0.3760922	0.386213

If we were to include these objects, the resulting CI range ($\text{CI} \in [-6, 12.5]$) would have been 2.5 times larger than the $\text{CI} \in [0.8, 8]$. Thus, increasing in the same amount the computing time of the analysis (for more details, see Footnote 21 on page 100).

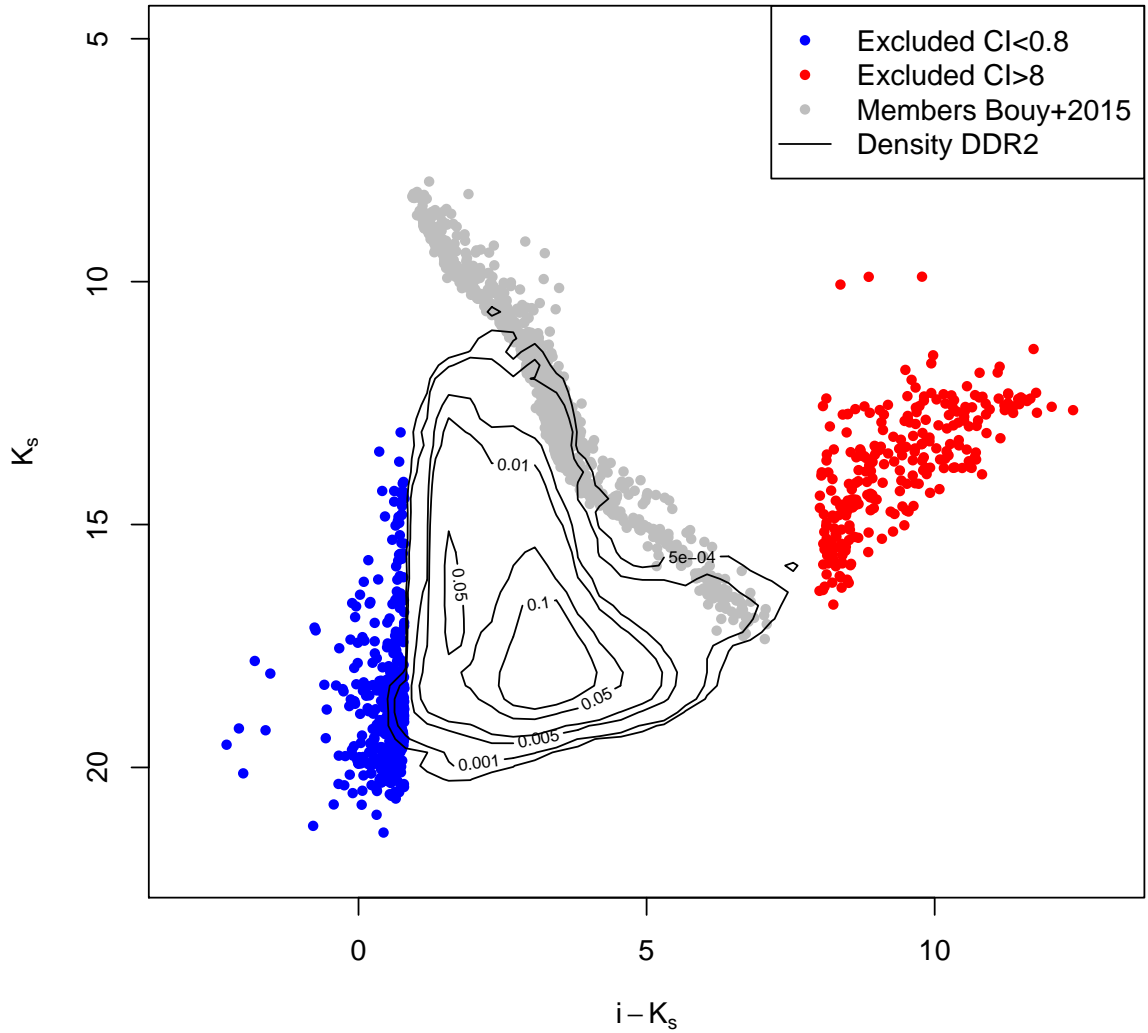


Figure 2.16: K_s vs CI CMD showing the density (black contour lines) of all objects (with observed entries in this CMD) in the DDR2. Also shown, the candidate members of [Bouy et al. \(2015\)](#) (grey dots), and the objects excluded by the cuts at $\text{CI}=0.8$ (blue dots) and $\text{CI}=8$ (red dots). See text for details.

With the previous restrictions, the number of sources in the DDR2 reduces to 1 424 893 objects, where the large number of rejected objects ($\sim 500\,000$) results from a completely missing photometry.

There is no selection of objects based on proper motions or sky positions besides those intrinsic to the catalogue. The latter are: i) the proper motions are truncated to $\mu_\alpha \leq 100$

mas yr^{-1} and $\mu_\alpha \leq 100 \text{ mas yr}^{-1}$, and ii) the sky positions have a patchy composition (see Fig. 2.13), which reaches its end with the spatial coverage of UKIDSS.

In the following sections I present two faces of an important element in any observational analysis: the non-observed data. One face corresponds to data from which no record exists. The second face corresponds to data in which some information is lost (i.e. the data is partially observed). For the first case I will estimate the region, in the observable space, where the data at hand (which comprises also the partially observed data) can be assumed as representative of the true population. For the second case, I will estimate the probability distributions of the partially observed data in each of the observables. These two elements will be useful for the statistical analysis presented in Chapter 3, and the results shown in Chapter 4.

2.7.3 Completeness

In the astronomical community, the completeness of a sample is defined as the percentage of the sources in the true population that are present in the sample. It is common to refer to a sample as complete if its completeness is 100%, otherwise, its completeness percentage or fraction is indicated. Thus, for example, a sample is said to be complete in volume, if it contains all the sources within a certain volume. Also, a sample is said to be complete until certain magnitude if it contains all objects up to certain limiting magnitude. The question then turns in knowing how many sources from the true population are within the limits we are interested in. This question has not a simple answer, and often a complex model have to be assumed.

Since one of the objectives of this work is to obtain the statistical distributions of the cluster population, it is important to establish these limits for all the observables.

The photometric completeness of the DDR2 is difficult to estimate due to its heterogeneous origin (e.g. see Figure 2.13). The variety of instruments, sensitivity in each of them, and integration times, makes this task overwhelming. Nevertheless, [Bouy et al. \(2015\)](#), in their Appendix A, give rough estimates of these limits for the i and K_s bands. To estimate these limits in all the bands, I make the simplistic assumption that the number of sources in the region of the sky occupied by the DDR2 grows as a power-law⁴ in the observed photometric magnitude. This assumption is of course very simplistic since the Pleiades cluster and the galaxy itself introduce inhomogeneities that prevent this model. In spite of that, as can be seen in Figure 2.17, which shows the distribution of sources in the DDR2 (resulting from the restrictions of the previous section) as a function of the photometric magnitudes, this assumption is correct in most of the photometric domain. However, at certain points, the power-law behaviour stops and the number of sources rapidly falls. In

⁴The brightness of an object vanishes proportionally the square of its distance. Thus, under the assumption that sources are uniformly distributed in space, the number of observed sources is expected to grow quadratically with brightness.

the following, I will assume that the survey is whenever its distribution of sources follows that of the power-law.

In addition, [Bouy et al. \(2015\)](#) mention that, due to the heterogeneous origins of the DDR2 data set, the spatial coverage is also not homogeneous. To remedy this issue, they identify a region with complete spatial coverage. They assume it to be the inner three degrees of the cluster (see Fig. 2.13). Then, they restricted their photometric analysis to this spatially complete region. Doing so, results in a sample of candidate members that is spatially biased. If any dynamical process has been set on the cluster such that the mass distribution of its members is not uniformly distributed in the space, then a spatial cut in a sample of candidate members will result in a bias on the mass distribution. One of such dynamical process is the mass segregation, which, as suggested by several authors ([Adams et al. 2001](#); [Converse & Stahler 2008, 2010](#), including the present work) occurs in the Pleiades.

Thus, to avoid such spatial restriction, in the following I assume that the UKIDSS survey ([Lawrence et al. 2007](#)), which is the most photometrically sensitive and spatially extended from among those that contribute to the DDR2 data set, provides homogeneous spatial and sensitivity coverage at faint magnitudes (see Fig. 2.13, and [Bouy et al. 2013](#)). According to [Lawrence et al. \(2007\)](#), the completeness limits of the UKIDSS survey are: $Y \sim 20.16$, $J \sim 19.56$, $H \sim 18.81$, and $K \sim 18.19$ magnitudes. In the i band, which is not present in UKIDSS, [Bouy et al. \(2015\)](#) estimate that the completeness limit is $i \sim 23$ mag. Figure 2.17 shows the previous limits as vertical dotted lines. As can be seen, these limits are optimistic for the DDR2. Thus, after re-estimating them, I find the following values: $i \sim 21.13$, $Y \sim 19.25$, $J \sim 18.6$, $H \sim 18$, and $K \sim 17.4$ magnitudes, which are also shown in Figure 2.17 as the vertical dashed lines.

It is important to notice that, although avoiding the truncation to the central three degrees prevents the biases introduced in the sample of [Bouy et al. \(2015\)](#), the DDR2 is nevertheless still biased by the truncation resulting from the spatial coverage of UKIDSS.

The DDR2 is also incomplete in the bright end. The bright stars can saturate the detectors (i.e collect more photons than those allowed by the analogical to digital converters), and thus prevent to collect a complete sample of the bright sources. As stated in the Appendix A of [Bouy et al. \(2015\)](#) the DDR2 JHK photometry is perfectly covered by the dynamics range of Two Micron All-Sky Survey (2MASS) and UKIDSS. Thus, I will assume that the DDR2 is complete in the bright end of these bands. On the other hand, the Y and i bands show effects of saturation. This is perfectly seen in Figure 2.17, where the Y distribution falls abruptly below $Y \sim 13$. However, the case of the i band is more intricate. This band comes from two main surveys: AAVSO Photometric All-Sky Survey (APASS) in the bright end (with completeness limit $i \sim 15.5$ mag., see bump in Figure 2.17), and CFHT/MegaCam (yellow pattern in Figure 2.13) at the mid and low ends (with completeness limit at $i \sim 21.2$). However, while APASS covers 100% of the

DDR2 sky area and its detectors do not saturates at the bright end (at least within the range covered by the DDR2 values), the detectors of CFHT/MegaCam, which covers just the central 3° area, saturate at $i \sim 13$, as indicated by Bouy et al. (2015). This intricate pattern prevents an homogeneous completeness coverage. Thus, I make the conservative assumption that the i band in the DDR2 is complete within the limits of $i \in [13, 21.2]$ mag given by CFHT/MegaCam.

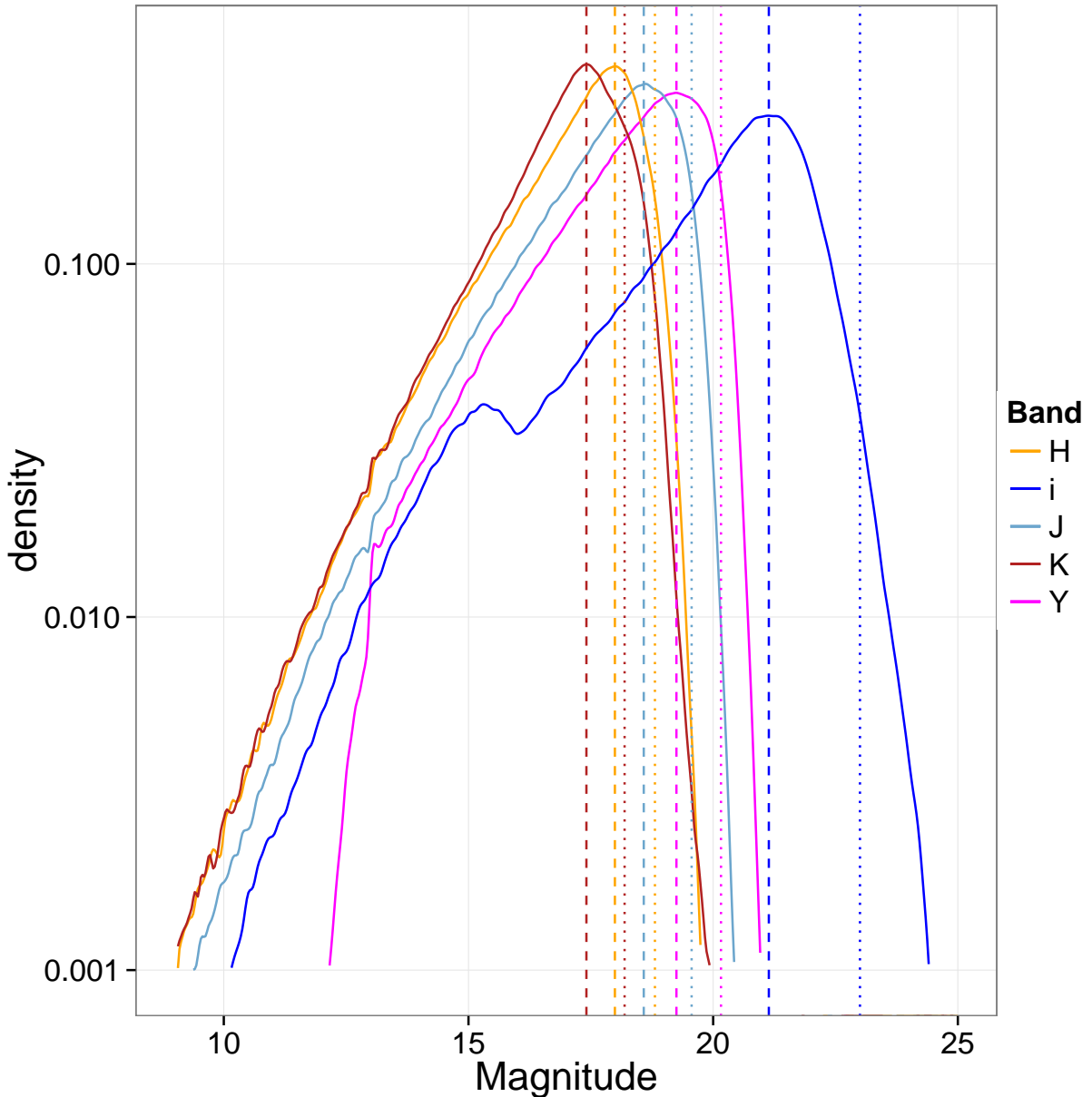


Figure 2.17: Density of all DDR2 sources as a function of the observed magnitudes. The vertical dotted and dashed lines correspond to the completeness limits of the literature, and to those derived as the mode of the densities, respectively. The bump in the i distribution at 15.5 mag corresponds to the completeness limits of the APASS survey. See text and Bouy et al. (2015) for more details.

In terms of proper motions, given that no selection has been performed based on these

quantities, and that I assume independence between proper motions and photometry⁵, I take it for granted that the survey is complete within the limits $|\mu_\alpha|, |\mu_\delta| < 100 \text{ mas yr}^{-1}$ imposed by the authors of the catalogue. Nevertheless, as we will see in Section 3.3.3, the field model accounts for this truncation.

As mentioned in Section 2.7.1, we will independently analyse the cluster PSD and the kinematic and photometric distributions. Nevertheless, here I gauge possible photometric incompletenesses caused by the spatial coverage of the DDR2 data. To do it I assume that the true population of sources in the sky area covered by the DDR2 is homogeneously distributed. This is a simplistic assumption that discards inhomogeneities introduced by the cluster and the galaxy. Nevertheless, it suffices to roughly quantify the completeness. Figure 2.18 shows the spatial completeness, in each photometric band, as a function of the maximum magnitude of the sources contained within the given limiting radius. The latter is measured from the cluster centre (R.A. = 56.65° , Dec. = 24.13° [Bouy et al. 2015](#)). The completeness is measured as the ratio of the observed to expected density of sources, where the expected density is computed from two million synthetic sources uniformly distributed within a radius of 6° . As can be seen from this Figure, the spatial and photometric completeness of the Y, J, H and K_s bands drops near the limits imposed by the sky coverage and limiting magnitudes of UKIDSS. However, the i band is only partially complete. The latter arise due to the different spatial coverage and limiting magnitudes of the APASS and CFHT/MegaCam date sets.

2.7.4 Missing values

As can be verified from Table 2.2, the amount of DDR2 sources with missing values is not negligible. However, objects with at least one observable marked as a missing value⁶ occur only in the photometric measurements (see Table 2.2), with the bluer bands being the most affected. As expected, the probability distribution of sources with missing values is not uniform. Missing values occur with higher probability at the faintest end of the photometric distributions (~ 18 mag in J, H and K_s bands). Figure 2.19 shows the distribution of objects in the DDR2 (resulting after the restrictions mentioned in previous sections) having at least one missing entry in one band, as a function of the band that is actually observed. The vast majority of these objects occur at the faint end, close to the sensitivity limits of the survey, which coincide with those of the the UKIDSS Galactic Cluster Survey ($Y \sim 20.3$, $J \sim 19.5$, $H \sim K_s \sim 18.6$ according to [Lawrence et al. 2007](#), and shown in Figure 2.19 with vertical dotted lines). In this Figure, the bumps at the bright and middle ranges arise due to the mixing of surveys. The first bump corresponds

⁵During the summer of 2017, I co-supervised the stage of a master student who investigated the validity of this assumption. Briefly, he found only a mild correlation between the proper motions and the photometry. Once the proper motions are transformed to galactic coordinates the correlation is only present, but still negligible, along the galactic plane.

⁶Usually marked as Not Available (NA) or Not A Number (NAN).

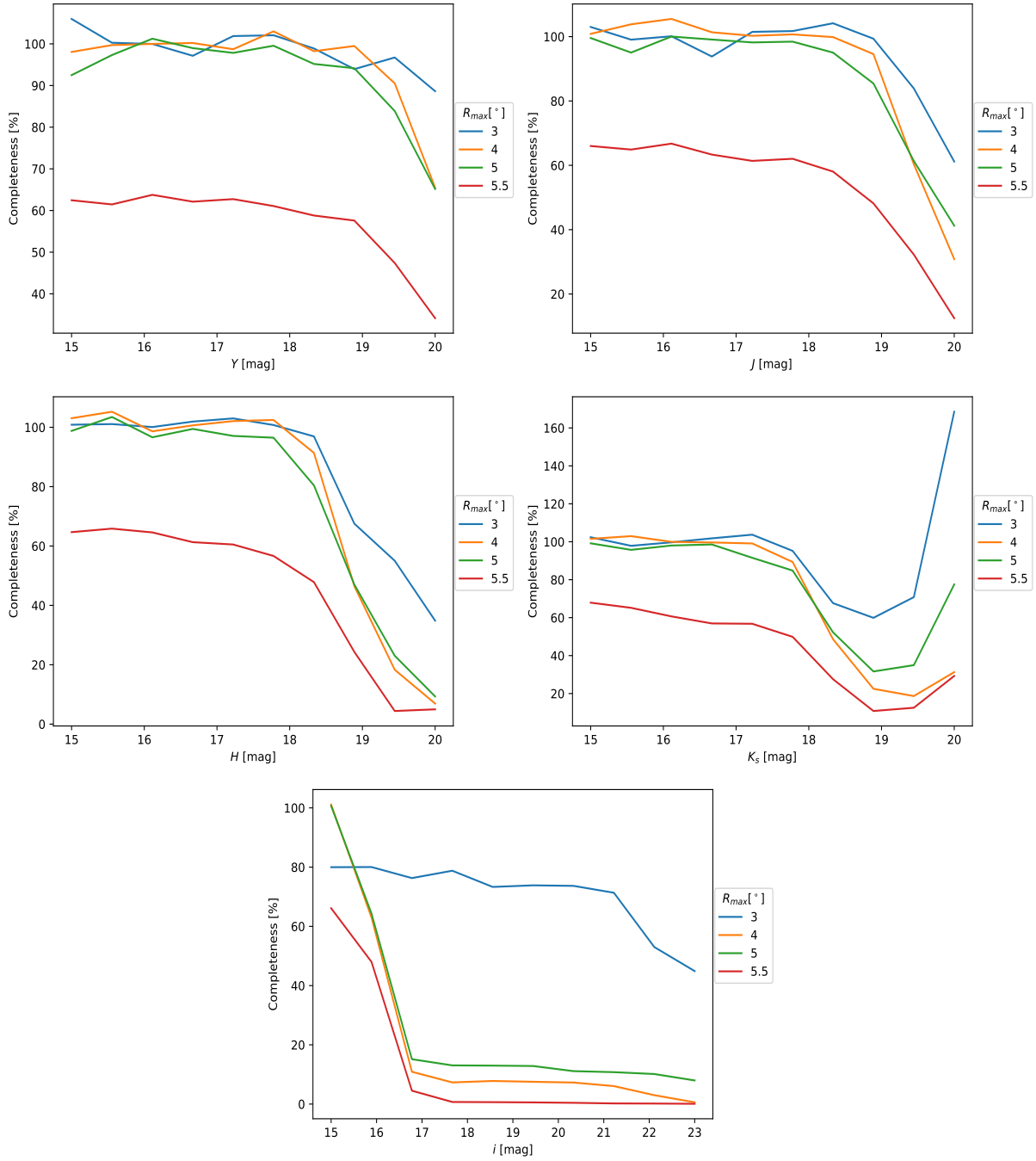


Figure 2.18: Spatial and photometric completeness of the DDR2 as a function of limiting magnitude and maximum radius of sky coverage.

to the survey carried out by Bouy et al. (2015). As mentioned in their Appendix A, due to saturation, the Y band photometry was limited to objects fainter than ~ 13 magnitude. Thus, they complemented the Pleiades DANCe catalogue with shallow Y band photometry in the magnitude range of 8 to 14 magnitudes but only for 40 candidate members of Stauffer et al. (2007) and their surrounding objects (see Bouy et al. 2015, for more details). Thus, the large amount of missing Y values in the 8 to 14 mag range of Fig. 2.19 come from those objects not observed by these authors. The second bump at the middle range

is slightly fainter than the sensitivity limits of the 2MASS survey ($J \sim 16.4$, $H \sim 15.5$ and $K_s \sim 14.8$, see Section 6.2 of the Explanatory Supplement to the 2MASS All Sky Data Release⁷), which indicates that it comes from the mixing of the 2MASS and UKIDSS surveys. Due to the different spatial resolutions, some objects are detected in 2MASS and not in UKIDSS (e.g. pairs that are resolved in the former but unresolved in the latter).

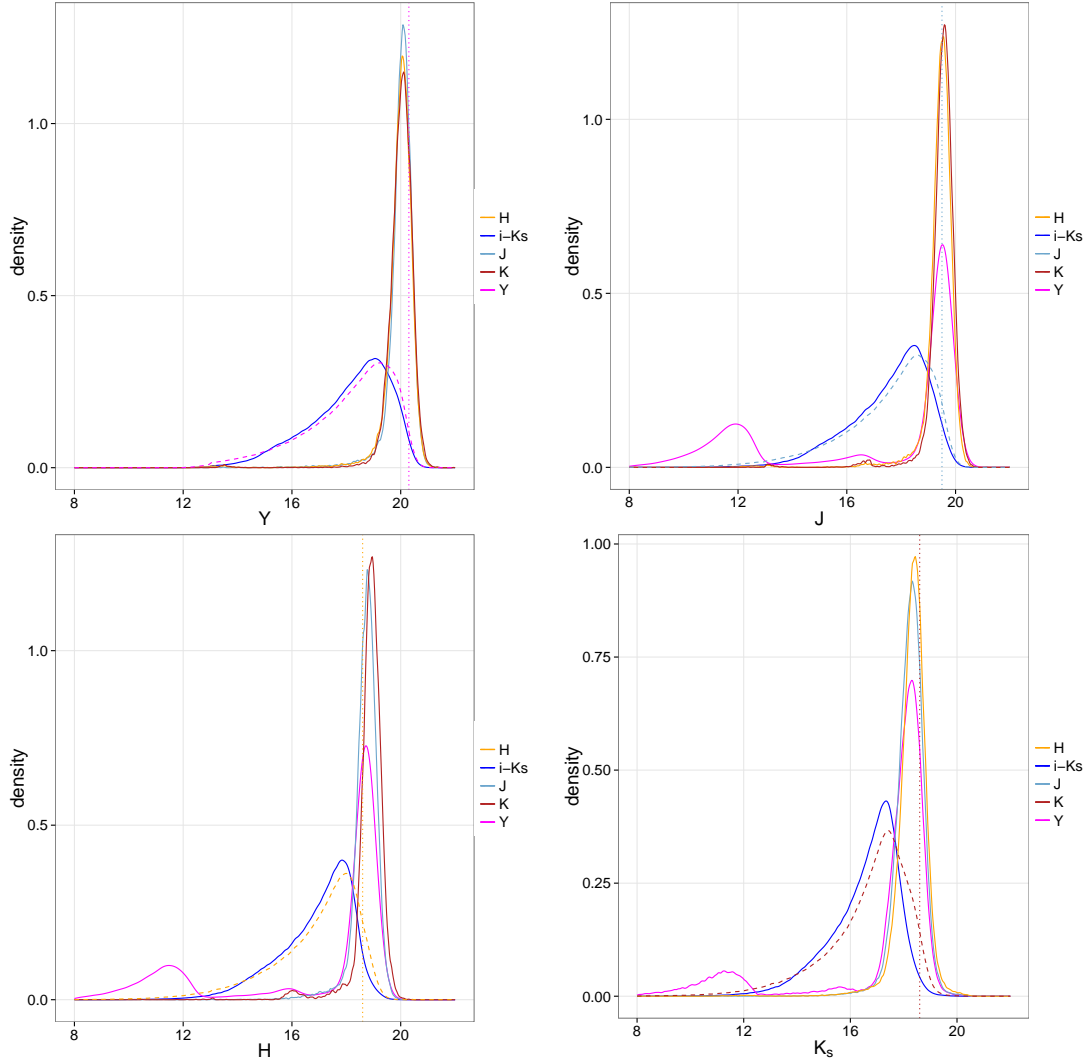


Figure 2.19: Density distributions in Y , J , H and K_s bands for DDR2 objects with missing values in the other bands. For comparison, the distribution of observed objects is also shown with a dashed line. The majority of the missing value objects are located at the faint end of the magnitude distributions, which roughly correspond to the sensitivity limits of UKIDSS: $Y \sim 20$, $J \sim 19$, $H \sim 18.5$, and $K_s \sim 18$, which are marked by vertical dotted lines. A non negligible fraction of missing Y band photometry is at the bright end ($J, H, K_s \sim 8 - 14$ mag), and in the middle range of 13 to 16 magnitudes. See text for details.

⁷https://www.ipac.caltech.edu/2mass/releases/allsky/doc/sec6_2.html

2.8 The Restricted DANCe Data Release 2 (RDDR2)

As I will show in Section 3.2, the methodology developed in this work is computationally demanding. This, in addition to our computational constraints (see Section 3.6.4), prevented us to apply it in the entire DDR2 described in the previous sections. However, the precision of our methodology, as that of any statistical analysis, increases with the number of independent observations. Therefore, we are forced to find a balance between sample size and computing time spent on analysing it. Proceeding in an heuristic way, we find that a size of 10^5 , which nevertheless takes four weeks to be analysed (see Section 3.6 for details on the computing facilities), represents a reasonable compromise between size and computing time.

Although a smaller data set produces faster results (within days), it also renders a less precise and potentially more biased model of the field. The latter results in a more contaminated model of the cluster. To restrict the size of the data set we decided to select objects based on its membership probability to the cluster. This decision is based upon the following premises.

- Our main objective is to characterise the cluster population.
- Computational time is expensive and limited.

By selecting objects based on membership probability, we ensure ourselves to avoid expending expensive and limited computing time in objects that most likely belong to the field, and thus fall outside our objective. Thus, we restrict theDDR2 to the 10^5 objects with highest membership probabilities according to [Bouy et al. \(2015\)](#). This selection is equivalent to set a probability threshold at membership probability of $p = 1.05 \times 10^{-11}$. In the following I will refer to this data set as the RDDR2. Performing this selection has two important consequences.

Since the field objects within the RDDR2 are no longer a representative sample of the field population, the field model should be constructed using this sample.

Since the probability of leaving a cluster member out of the RDDR2 is less than $p = 1.05 \times 10^{-11}$, we can safely assume that the completeness limits of the DDR2 (estimated in Section 2.7.3) apply to the cluster population present in the RDDR2, and only to it. This selection of objects depends deeply on the membership probabilities estimated by [Bouy et al. \(2015\)](#). However, the large size of the RDDR2 data set (10^5), compared to the cluster population (~ 2000), and the lower value of the membership probability threshold ($p = 1.05 \times 10^{-11}$), ensure that leaving out a true cluster members is highly unlikely. This assumption will be corroborated in Section 4.2, where membership probabilities for all the objects in the DDR2 are estimated *a posteriori*, once the cluster

model is learnt from the RDDR2. Here, I anticipate that no cluster member is found outside the RDDR2, which confirm this assumption.

Tables 2.5 and 2.6 show summaries of the observables and uncertainties for the 98012 field and 1988 cluster objects in the RDDR2, respectively. This classification is based on the membership probabilities and probability threshold ($p = 0.75$) derived by [Bouy et al. \(2015\)](#).

Table 2.5: Summary of the 1988 candidate members of [Bouy et al. \(2015\)](#) in the DDR2.

Observable	Min.	1st. Qu.	Median	Mean	3rd. Qu.	Max.	NA's
$\mu_\alpha [mas \cdot yr^{-1}]$	-81.64	14.45	16.24	16.30	18.14	90.32	0
$\mu_\delta [mas \cdot yr^{-1}]$	-81.88	-42.09	-39.85	-39.62	-37.45	82.59	0
i - K_s [mag]	0.934	3.002	3.364	3.396	3.678	7.085	713
Y [mag]	8.284	13.700	14.450	14.690	15.400	20.390	518
J [mag]	6.545	11.950	13.400	13.160	14.380	19.310	6
H [mag]	6.587	11.330	12.850	12.610	13.840	18.300	13
K_s [mag]	6.514	11.090	12.530	12.300	13.500	17.360	1

Uncertainties

Observable	Min.	1st. Qu.	Median	Mean	3rd. Qu.	Max.	NA's
$\mu_\alpha [mas \cdot yr^{-1}]$	0.08	0.25	0.76	0.5201	2.02	1e+5	0
$\mu_\delta [mas \cdot yr^{-1}]$	0.08	0.25	0.76	0.52	2.02	1e+5	0
i [mag]	0.0200	0.0200	0.0200	0.0351	0.0202	2.1610	713
Y [mag]	0.0300	0.0500	0.0501	0.0569	0.0503	0.2392	518
J [mag]	0.02000	0.02700	0.05005	0.04270	0.05014	0.15990	6
H [mag]	0.02000	0.02700	0.04009	0.03994	0.05010	0.14340	13
K_s [mag]	0.02000	0.05003	0.05045	0.05278	0.06001	9.99500	1

2.8.1 Missing values

Since the RDDR2 is not a random sample of the DDR2, the distributions of objects containing missing values are not the same as those shown in Section 2.7.4. Thus, Fig. 2.20 shows the distribution of objects containing missing entries in one band as a function of magnitude in the other bands.

In addition, Fig 2.21 shows the magnitude distributions of completely observed objects (without missing values) compared to those of all objects, including those with missing entries. This Figure shows that the distributions of objects with completely observed photometry is highly discrepant from that of the entire population. Thus probing that our analysis can not be based only on objects with completely observed photometry, and that the treatment of missing values is of paramount importance (more details will be given in Section 3.3.1).

Table 2.6: Summary of the 98012 filed objects in the RDDR2.

Observable	Min.	1st. Qu.	Median	Mean	3rd. Qu.	Max.	NA's
$\mu_\alpha [mas \cdot yr^{-1}]$	-99.980	-11.730	1.803	1.307	15.050	99.910	0
$\mu_\delta [mas \cdot yr^{-1}]$	-99.990	-17.980	-4.820	-4.088	9.189	99.980	0
i - K_s [mag]	1.04	3.49	5.13	4.81	5.81	7.99	95628
Y [mag]	9.97	18.70	19.45	18.83	19.93	22.23	21988
J [mag]	3.954	17.790	18.660	17.880	19.160	20.620	7305
H [mag]	2.969	16.950	17.750	17.020	18.210	20.270	7655
K_s [mag]	2.598	16.260	16.960	16.360	17.370	21.020	5013

Uncertainties							
Observable	Min.	1st. Qu.	Median	Mean	3rd. Qu.	Max.	NA's
$\mu_\alpha [mas \cdot yr^{-1}]$	0.08	8.65	14.94	23.50	25.60	1.0e+05	0
$\mu_\delta [mas \cdot yr^{-1}]$	0.085	8.652	14.940	20.710	25.600	1.86e+04	0
i [mag]	0.02	0.02	0.07	0.08	0.12	0.66	95628
Y [mag]	0.030	0.068	0.103	0.112	0.148	0.938	21988
J [mag]	0.020	0.065	0.097	0.104	0.136	0.403	7305
H [mag]	0.020	0.065	0.093	0.099	0.124	9.998	7655
K_s [mag]	0.020	0.060	0.079	0.087	0.101	9.998	5013

2.9 The Tycho+DANCe candidate members

As mentioned in Section 2.7.1, we will independently analyse the cluster PSD and the kinematic and photometric distributions. Thus, here I describe the data set used for the analysis of the Pleiades PSD. It comprises, for the middle and faint luminosities, the High Membership Probability Sample (HMPS) of candidate members recovered by the BHM, described in Section 4.2, and summarised in Table 2.7, and for the high luminosities, the Tycho+DANCe candidate members of [Bouy et al. \(2015\)](#), summarised in Table 2.8. This data set is the largest and less contaminated list of Pleiades candidate members to date.

This joint data set contains the positions, in equatorial coordinates R.A. and Dec. (in the following α and δ), proper motions, photometry, and membership probabilities of 2060 unique candidate members. For the analysis of the PSD we work only with the positions, membership probabilities, and J photometric band. The latter is the bluest most available photometric band for this list of members. It will be used as a proxy for the mass, and to explore evidence of mass segregation.

2.9.1 Contamination and completeness

In Section 4.1, we estimate a contamination rate of $4.3 \pm 0.2\%$ in the HMPS, which would amount to 84 of the 1967 candidate members. Also, [Sarro et al. \(2014\)](#) estimate that the contamination rate of their methodology is $11.0 \pm 2.0\%$ for a probability threshold of $p = 0.5$, as the one used by [Bouy et al. \(2015\)](#) to classify the candidate members of their

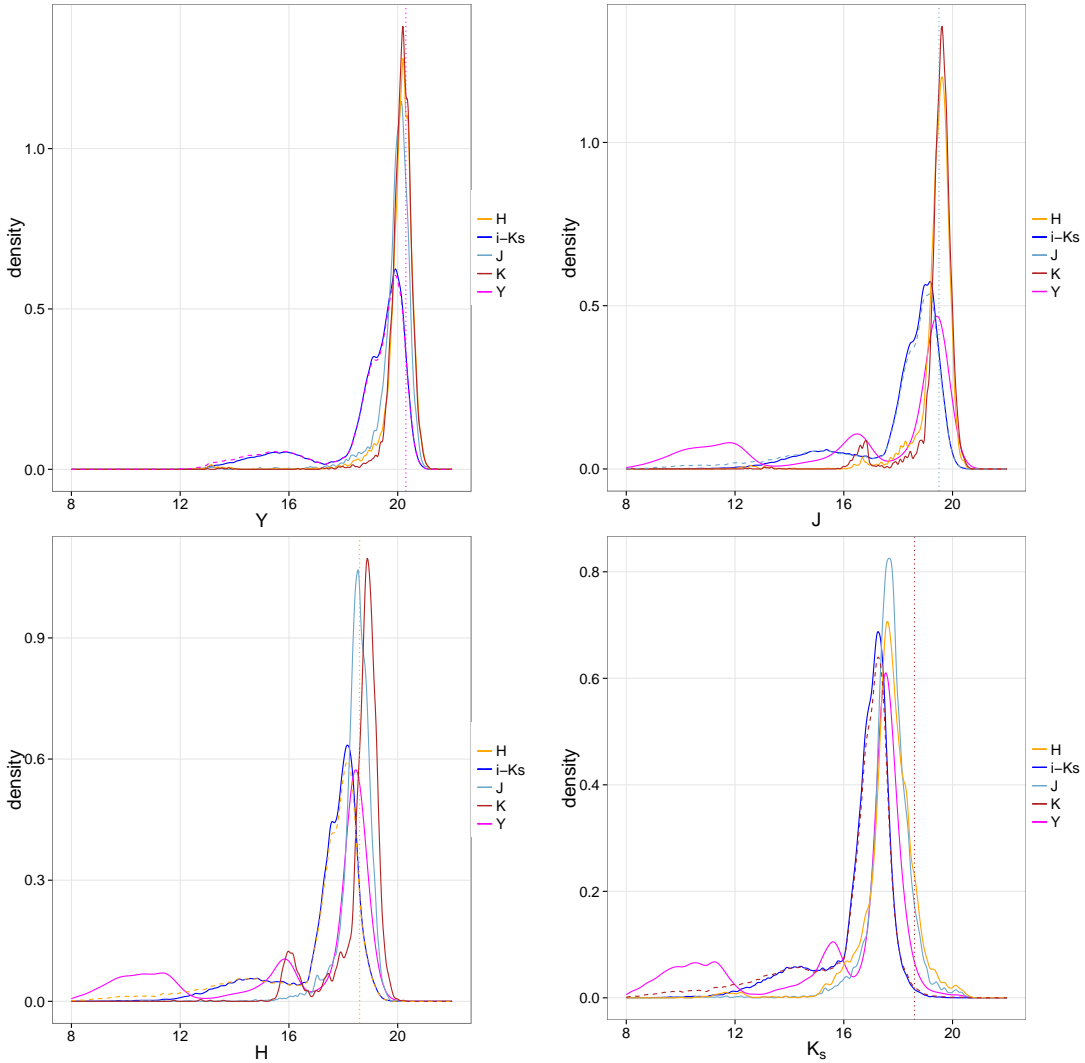


Figure 2.20: Density distributions in Y , J , H and K_s bands of RDDR2 for objects with missing values in the other bands. For comparison, the distribution of observed objects is also shown with a dashed line. The features are similar to those in Fig. 2.19. The small differences between the two figures come from the fact that the RDDR2 is not a random sample of the DDR2.

Tycho2+DANCe (T+D) data set. Thus, in our combined T+D list of candidate members, we acknowledge a mean contamination rate of $\sim 8\%$. We would expect these contaminating sources to be uniformly distributed in right ascension and declination because the position on the sky was explicitly removed from the calculation of membership probabilities.

We estimate the completeness of our list of candidate members, in terms of the J band luminosity and spatial coverage, by assessing the completeness of the joint T+D survey. In Fig. 2.22 we show the distribution of the number of sources in the combined T+D catalogue as a function of the radial position for different limiting magnitudes in the J band. The radial position is computed assuming a distance of 134.4 pc to the Pleiades cluster (Galli et al. 2017) and a centre at $\alpha, \delta = [56.65, 24.13]$. Distances are corrected by geometric distortions of large angles (using Eqs. 3.82 and 3.83). As can be seen from

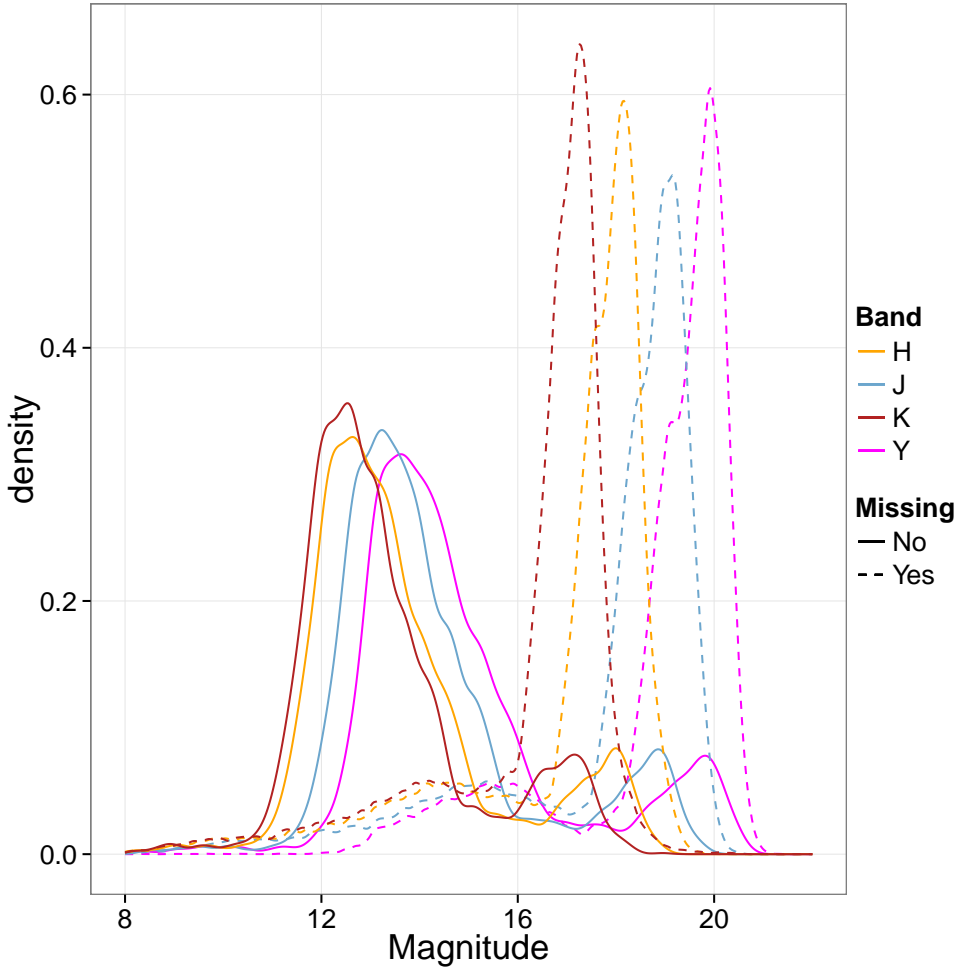


Figure 2.21: Density distributions in Y , J , H and K_s bands of RDDR2 for objects with: a) at least one missing entry (dashed lines), and b) no-missing entries (solid line).

Table 2.7: Summary of the 1967 objects classified as members by the BHM.

Observable	Min.	1st. Qu.	Median	Mean	3rd. Qu.	Max.	NA's
RA [deg]	51.42	55.67	56.69	56.76	57.81	62.81	0
Dec. [deg]	19.13	23.11	24.10	24.13	25.22	29.56	0
$\mu_\alpha [mas \cdot yr^{-1}]$	-23.34	14.59	16.32	16.73	18.37	53.84	0
$\mu_\delta [mas \cdot yr^{-1}]$	-81.370	-42.410	-40.130	-40.480	-37.760	-2.016	0
$i - K_s$ [mag]	0.934	2.979	3.357	3.325	3.648	6.662	643
Y [mag]	8.284	13.660	14.360	14.590	15.310	20.100	467
J [mag]	7.058	12.060	13.370	13.180	14.290	18.570	5
H [mag]	7.009	11.430	12.810	12.620	13.750	17.480	9
K_s [mag]	7.008	11.190	12.500	12.320	13.410	16.740	0

this figure, the T+D catalogue is complete until magnitude $J \sim 19$ and radial distance of 11.5 pc ($\sim 5^\circ$). We notice that the latter corresponds roughly with the sky coverage of the UKIDSS survey (Lawrence et al. 2007). Hence, we restrict our list of candidate members to those with: i) J band observed and less than 19 mag., and ii) radial distances less than

Table 2.8: Summary of the 207 objects from the Tycho2+DANCe data set classified as Pleiades candidate members ($P > 0.48$) by [Bouy et al. \(2015\)](#).

Observable	Min.	1st. Qu.	Median	Mean	3rd. Qu.	Max.	NA's
RA [°]	52.05	55.89	56.46	56.55	57.30	62.49	0
Dec. [°]	18.56	23.13	24.08	23.99	24.88	29.89	0
μ_α [mas · yr $^{-1}$]	9.7	18.9	20.1	20.0	21.1	26.7	0
μ_δ [mas · yr $^{-1}$]	-55.10	-46.60	-45.10	-45.19	-43.70	-37.70	0
i [mag]	7.910	9.321	10.21	10.04	10.76	12.960	72
J [mag]	3.800	7.588	8.638	8.451	9.575	10.590	0
H [mag]	3.864	7.535	8.463	8.236	9.209	10.030	0
K_s [mag]	3.879	7.478	8.373	8.167	9.113	9.929	0

11.5 pc. This results in 1964 candidate members, which represents more than 50% more candidate members than those of [Converse & Stahler \(2010\)](#), who did the latest analysis of the Pleiades PSD.

Nevertheless, we remind the reader that the inhomogeneities (e.g. spatial resolutions, gaps in luminosity) of the T+D data set are so complex (and some of them only partially understood) that can indeed bias the sample of candidate members in unknown ways. For example, the gap in luminosity coverage between the faint end of Tycho-2 catalogue and the bright end of the DANCe survey (see in Fig. 8 of [Bouy et al. 2015](#)) may result in undetected sources, therefore unmeasured proper motions and finally an incomplete list of candidate members.

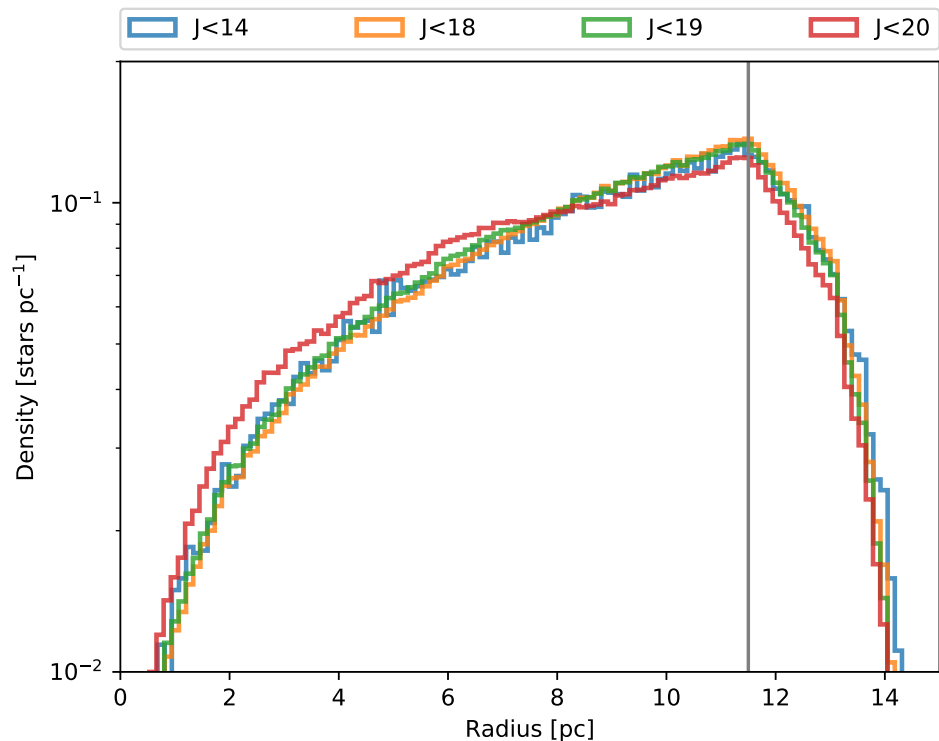


Figure 2.22: Density of sources in the combined T+D catalogue as a function of the radial distance to the cluster centre and limiting magnitude in the J band. The vertical grey line marks the limit of spatial completeness, 11.5 pc.

Chapter 3

Bayesian formalism

This chapter provides a general introduction to probability theory and its application to parametric inference. The objective of this work is to infer the probability distributions of the cluster properties (e.g. luminosity and velocity). Bayes' theorem provides the proper probabilistic framework for the inference of the parameters governing these distributions. The Bayesian framework demands, though, the setting up of prior beliefs about the parameters values. Thus, later in this chapter, I describe the reason why the Bayesian Hierarchical Models are the least subjective to establish priors. Once the posterior distribution of the parameters in the model has been analytically described, I proceed to describe the Markov Chain Monte Carlo (MCMC) techniques and the particular one I use to sample the posterior distribution.

In the Sections ahead I also provide the details on the assumptions I make to model the data, and to choose the parameters of the prior distributions. The two final sections focus on the practical issues related to the sampling of the posterior distributions, and the description of the codes I adopted and/or developed.

Partial results of the work presented here have been submitted to the journal A&A as [Olivares et al. \(2017\)](#). In the following, I use both pronouns *we* and *I* to refer the investigation done by collaborators of the DANCe team (see Chapter 1).

3.1 Introduction to probability theory.

The probability is the reasonable degree of confidence and is not identical with the number used to express it.

— Jeffreys, Theory of Probability

Probability, and the number used to express it, represent our degree of confidence in the occurrence of a proposition or phenomenon. That confidence could be informed, for example by making measurements, or can be simply an *a priori*. Every measurement has an

associated confidence interval or uncertainty, otherwise it is not a complete measurement¹. The term uncertainty must not be confused with the term error, which refers to the difference between the measured value of the quantity and its *true* value² ([JCGM 2008](#)). It is commonly accepted that probability can be mathematically expressed³. If it is referred for a discrete (taking a finite set of values) variable, a for example, then its probability is called probability mass function. On the other hand, if a is continuous (with an infinite set of values), then its probability is called Probability Density Function (PDF). Throughout the text, I refer to the probability distribution function of a random variable as its probability distribution or simply its distribution.

Any probability distribution satisfies the following properties:

Property 1 It has units, those of the inverse of a .

Property 2 $p(a) \geq 0 \quad \forall a \in S_a$, with S_a the support of a .

Property 3 $1 = \int_{S_a} p(a)da$.

If a is a discrete variable, then the integral, in the last property, change to the sum of all possible values of $p(a)$.

These properties hold regardless of the dimension of a . Furthermore, they also hold for conditional probability distributions. A conditional probability distribution results from the knowledge about the particular value of one or several variables of the probability distribution. For example, be $p(\alpha, \delta, \tau)$ the joint probability distribution of sky positions α, δ and time τ of an object. Then, at the particular moment $\tau = \tau_0$ (with $\tau_0 \in S_\tau$) the object will have a probability distribution for its sky positions given by the conditional probability distribution $p(\alpha, \delta | \tau_0)$. Since, $p(\alpha, \delta | \tau_0)$ is still a probability distribution on α and δ , it must also satisfy:

- It has units of $\alpha^{-1}\delta^{-1}$.
- $p(\alpha, \delta | \tau_0) \geq 0 \quad \forall \alpha \in S_\alpha, \delta \in S_\delta$.
- $1 = \int_{S_\alpha} \int_{S_\delta} p(\alpha, \delta | \tau_0) d\alpha \cdot d\delta$.

The link between joint and conditioned probabilities is given by the following symmetric definition:

$$\begin{aligned} p(a, b) &= p(a|b) \cdot p(b). \\ p(a, b) &= p(b|a) \cdot p(a), \end{aligned} \tag{3.1}$$

¹Upper and lower limits are examples of incomplete measurements.

²The true value is that which ideally results when the uncertainty tends to zero.

³In the same way that it is commonly accepted that humans have names which represent them. In the same way that our names are not identical to us, the probability *is not identical with the number used to express it*.

which can be further conditioned on c to obtain:

$$\begin{aligned} p(a, b|c) &= p(a|b, c) \cdot p(b|c), \\ p(a, b|c) &= p(b|a, c) \cdot p(a|c). \end{aligned} \quad (3.2)$$

If the joint probability of a and b can be factorised, this is

$$p(a, b) = p(a) \cdot p(b), \quad (3.3)$$

then a and b are say to be *independent*. An alternative option is to say that a and b are *independent* if the conditional probability of a on b is $p(a|b) = p(a)$.

Property 3 establishes that the amount of probability density⁴ (or mass if a is discrete) spread over the volume of the support, adds to one, thus keeping the integrals of PDFs bounded. Two important operations using these bounded integrals are the following.

The *marginalisation* of *nuisance* parameters. These are parameters that, although are necessary in the model, lack interest for the research. The classical example of a nuisance parameters is the standard deviation, σ , of a normal distribution when the interest lies solely in the mean, μ . This nuisance parameter can be marginalised from the joint PDF of the parameters, $p(\mu, \sigma)$, in the following way,

$$p(\mu) = \int_0^\infty p(\mu, \sigma) \cdot d\sigma. \quad (3.4)$$

The computing of *expected values*. The expected value of a , $E(a)$, corresponds to the mean of a once we have drawn many realisations from its probability distribution. To compute it, we add all the possible values of a weighted by their probability. This is,

$$E(a) = \int_a^\infty a \cdot p(a) \cdot da. \quad (3.5)$$

Once again, these last two equations (3.4 and 3.5) hold if the distributions are conditioned on any other measurement.

It is important to recall that the term measurement, and its unavoidable uncertainty, refer not just to directly measured quantities, like the photons (counts) and pixels in a CCD, but also to indirect measurements. Stellar magnitudes and positions in the sky, for example, are indirect measurements derived from the direct measurement of photons, pixels and telescope arrangements. This generalisation also applies to the measurement of parameters in any physical or statistical model.

This Section ends with a brief description of the procedure that is generally applied

⁴Which could be infinite, like in Dirac's delta.

when we want to transform a probability distribution into another probability distribution, under a nonlinear transformation (for more details see for example [Bishop 2006](#), pages 18 and 19).

Let f be a probability distribution on $x \subset \mathbb{R}$, with support on $a < x < b$, then

$$\int_a^b f(x)dx = 1$$

Let $y = g(x)$ be the nonlinear transformation, with g a function of x with inverse g^{-1} , continuous and with continuous derivative, so that $x = g^{-1}(y)$, with $y \subset \mathbb{R}$. Then, the following is true,

$$\int_a^b f(x)dx = \int_{g(a)}^{g(b)} f(g^{-1}(y)) \cdot \left| \frac{dg^{-1}(y)}{dy} \right| dy. \quad (3.6)$$

3.1.1 Bayes theorem

The definition of conditioned probability (Eq. 3.2) leads to Bayes' theorem:

$$p(a|b, c) = \frac{p(b|a, c) \cdot p(a|c)}{p(b|c)}. \quad (3.7)$$

Integrating on a we find that,

$$\begin{aligned} p(b|c) \cdot \int_a p(a|b, c) \cdot da &= \int_a p(b|a, c) \cdot p(a|c) \cdot da \\ p(b|c) &= \int_a p(b|a, c) \cdot p(a|c) \cdot da. \end{aligned} \quad (3.8)$$

This Equation illustrates that $p(b|c)$ is a normalisation constant which can be evaluated once $p(b|a, c)$ and $p(a|c)$ are known. This turns out to be very useful, since it tells us that $p(a|b, c) \propto p(b|a, c) \cdot p(a|c)$.

Models and parametric inference

In a broad sense, models are representations or abstractions of the knowledge someone has about something. Sometimes this knowledge is also shared by others. Models are everywhere in our daily life: from the words we speak every day, to the evolution of the species and the general relativity; from a kid's drawing to cosmological models. In science, however, the concept of model is restricted to a mathematical representation of the relations (the knowledge) among the entities that the model attempts to describe: the observables (i.e. the data). If the model contains variables that through the different values they take reproduce in some extent the observables, then model is called parametric and the variables the parameters.

Parametric statistical models, like the ones I use in this work, assume that the underlying population of interest, from which the observed data is just a sample, can be described by parametric probability distribution functions. The act of finding the parameters governing these distributions is called parametric inference. This last can focus either on the entire PDFs of the parameters, or just on some summary of them (e.g. the Maximum A Posteriori (MAP), or the mean and variance).

The proper way to obtain the entire probability distribution of the parameters in a model, given the data, is through Bayes' theorem. Thus it is called Bayesian inference. Another example of parametric inference is the maximum likelihood approach, where the likelihood, which is seen as a function of the parameters, is maximised. Despite that it obtains the parameter values that make the model to resemble the data, it does not return their probability distribution. Formally, the likelihood is a probability distribution for the data, and just a function of the parameters. Thus, to obtain the probability distribution of the parameters, the likelihood must be multiplied by the priors and the product normalised. This is what Bayes' theorem does.

In this context, Bayes' theorem is:

$$p(\boldsymbol{\theta}|\mathbf{D}, \mathcal{M}) = \frac{p(\mathbf{D}|\boldsymbol{\theta}, \mathcal{M}) \cdot p(\boldsymbol{\theta}|\mathcal{M})}{p(\mathbf{D}|\mathcal{M})}. \quad (3.9)$$

where $\boldsymbol{\theta}$, \mathbf{D} and \mathcal{M} correspond, respectively, to the parameters in the model, the data which the model tries to describe, and the model itself.

The term on the left-hand side is called the posterior probability distribution of the parameters, $\boldsymbol{\theta}$ given the data \mathbf{D} , and the model \mathcal{M} . On the right hand side, the two terms in the numerator are called the *likelihood* for the data, $p(\mathbf{D}|\boldsymbol{\theta}, \mathcal{M})$ and the *prior* of the parameters, $p(\boldsymbol{\theta}|\mathcal{M})$. The denominator, $p(\mathbf{D}|\mathcal{M})$, is called the *evidence*, and results from

$$Z \equiv p(\mathbf{D}|\mathcal{M}) = \int_{\boldsymbol{\theta}} p(\mathbf{D}|\boldsymbol{\theta}, \mathcal{M}) \cdot p(\boldsymbol{\theta}|\mathcal{M}) \cdot d\boldsymbol{\theta} \quad (3.10)$$

Formally, the likelihood and the prior are probability distributions for the data \mathbf{D} and of parameters $\boldsymbol{\theta}$, respectively. However, for the posterior to be a probability distribution of the parameters, it only suffices that the product of the likelihood times the prior does not vanish everywhere or be negative anywhere⁵. If these are not probability distributions, they are called *improper* priors or *improper* likelihoods. In the extreme case that their product vanishes everywhere, which may be the case if the prior is terribly specified or if the likelihood does not take proper account of extreme data, the posterior will not be a probability distribution due to a division by zero. Nevertheless, it makes no sense to try to estimate the parameters of a model with zero evidence.

As mentioned before, the likelihood is a probability distribution for the data, given

⁵See Property 2. Although negative probabilities may have sense in quantum mechanics. See for example [Dirac \(1942\)](#)

the parameters, regardless of the size of it. Almost always the data is a collection of measurements of several objects, but it could also be made up of just one object. The collection of measurements of one or several quantities of a single object follows a probability distribution, which is usually summarised by two statistics. It is often assumed that this probability distribution is normal (univariate or multivariate), which then is summarised by the mean and the standard deviation. These two are commonly known as the datum and its uncertainty, respectively. A data set is then composed of the collection of summary statistics of one or several objects. To compute the likelihood for this collection of statistics (i.e. the data), some assumption must be made.

When measuring the properties of objects, it is often assumed that the probability distribution obtained from the collection of measurements of a single object, is independent from that of another object. For example, if we were to measure the weight of a group of persons, we usually assume that the PDF of the weight of one person, is independent of that of another person. It means that measuring the weight of one person has no effect at all in the weight of another person.

In this work it is always assumed that the PDFs of the measured quantities of individual objects are independent amongst them. Nevertheless, in the following, I give an example where this assumption may not be entirely right. Obtaining stellar positions in celestial coordinates often requires what is called an astrometric solution. This solution is a map from the raw data, like pixel positions in the detectors and observing epoch, to the celestial coordinates (e.g. right ascension, declination and epoch). This astrometric solution often needs large collections of measurements of the same objects, so that they can be robustly estimated. Since this mapping is computed from the data (e.g. using maximum-likelihood estimates) and then applied to the same data, then it is common to observe correlations among the uncertainties of different objects (see for example [Holl et al. 2010](#); [Gaia Collaboration et al. 2017](#)). If the correlation in the uncertainties is significative, then their PDFs are probably not independent⁶.

Let \mathbf{D} be the data, i.e. the collection of statistics of the N objects, and $p_n(\mathbf{d}_n)$ be the probability distribution rendered by several measurements of object n . If these $\{p_n(\mathbf{d}_n)\}_{n=1}^N$ are assumed to be independent, then

$$p(\mathbf{D}) = \prod_{n=1}^N p_n(\mathbf{d}_n), \quad (3.11)$$

with p_n explicitly stating that the individual probability distributions are distinct.

Similarly, if the likelihood of the data, $p(\mathbf{D}|\boldsymbol{\theta}, \mathcal{M})$ is assumed to be independent for

⁶Independent PDFs produce uncorrelated samples, however, uncorrelated samples do not imply independence between the PDFs of their underlying populations.

each object, then

$$p(\mathbf{D}|\boldsymbol{\theta}, \mathcal{M}) = \prod_{n=1}^N p(\mathbf{d}_n|\boldsymbol{\theta}, \mathcal{M}). \quad (3.12)$$

The term $p(\mathbf{d}_n|\boldsymbol{\theta}, \mathcal{M})$ is the likelihood of datum \mathbf{d}_n . This is also called the *generative* model, since it contains the necessary information to generate the data.

To take into account the uncertainty process for object n , we model the datum \mathbf{d}_n as resulting from the addition of the true value, \mathbf{x}_n , which is given by the model, with a random variable, \mathbf{e}_n , given by the uncertainty process. This is

$$\mathbf{d}_n = \mathbf{x}_n + \mathbf{e}_n.$$

In general, if the model does not contain any intrinsic dispersion, then its likelihood can be thought of as a Dirac δ function, which is centred at the *true* value \mathbf{x}_n . Then, it can be added (i.e. convolved⁷) to the distribution of the uncertainty process. However, it is customary to also include an intrinsic dispersion in the model to account for over-simplistic assumptions or underestimated uncertainties.

In particular, it can be assumed that both the uncertainty process of datum \mathbf{d}_n , and the likelihood of the model are normally distributed with variances Σ_n^2 and Σ^2 , respectively,

$$\begin{aligned} p(\mathbf{e}_n|\Sigma_n^2) &= \mathcal{N}(\mathbf{e}_n|0, \Sigma_n^2), \\ p(\mathbf{x}_n|\boldsymbol{\theta}, \mathcal{M}, \Sigma^2) &= \mathcal{N}(\mathbf{x}_n|\boldsymbol{\theta}, \mathcal{M}, \Sigma^2). \end{aligned}$$

Formally, Σ^2 is part of the set of model parameters, $\boldsymbol{\theta}$, but I explicitly leave it outside to exemplify the process.

Then the addition of these two normally distributed random variables results in another normally distributed random variable⁸. Thus,

$$p(\mathbf{x}_n|\boldsymbol{\theta}, \mathcal{M}, \Sigma^2) * p(\mathbf{e}_n|\Sigma_n^2) = \mathcal{N}(\mathbf{d}_n|\boldsymbol{\theta}, \mathcal{M}, \Sigma_n^2 + \Sigma^2). \quad (3.13)$$

Therefore, Eq. 3.12, can be expressed in general as,

$$p(\mathbf{D}|\boldsymbol{\theta}, \mathcal{M}) = \prod_{n=1}^N p(\mathbf{d}_n|\boldsymbol{\theta}, \mathcal{M}, \mathbf{u}_n), \quad (3.14)$$

where \mathbf{u}_n is the uncertainty of datum \mathbf{d}_n .

Bayes' theorem can be interpreted as the probabilistic way to update the state of knowledge. To me, it embodies the process of knowledge improvement once we recognise that knowledge is uncertain. Even when its uncertainty is negligible under the evidence

⁷The addition of two random variables results in another random variable. This is analogous to the convolution, denoted $*$, of their PDFs.

⁸The convolution of two Gaussian PDFs is another Gaussian PDF.

that supports it. Bayes' theorem helps us update our prior beliefs once we multiply it by the likelihood of the data. Then, the posterior probabilities, become our new state of knowledge.

Furthermore, Bayes' theorem also provides the objective way to compare two models or hypothesis, and update the *a priori* knowledge used to construct them. This is called model selection, which I briefly explain in the next section.

3.1.2 Model Selection

Whenever we have a data set and two or more models that attempt to describe these data, the most straightforward thing to do is to compare these models. Almost always, we want to select the *best* model. Obviously the term *best* depends on the objective of the research. For example, imagine that our data set consists of the positions of an object as function of time. If we were interested in reproducing exactly the same points in the data set, the *best* model would be a polynomial with degree equal to the number of points. This polynomial will pass through all the points. However, once we recognise the unavoidable uncertainty of the data, we realise that an exact representation of the data may be of no use since it fits also the noise.

In general, we are interested in the predictive capabilities of a model, its ability to predict future observations rather than to replicate the ones we currently have. Thus, an exact representation of the observed data (an over-fitted model as in the previous example), will poorly describe any new data. In this sense, an over-fitted model *memorises* the data rather than *learns* from it.

A model that *learns* from the data is that which recovers the *true* underlying relation embedded in the data. This *true* underlying relation is the one that produces the *true* data. The observed data results once the uncertainty is added.

Nevertheless, we still need to select among different learning models.

We can draw some help from the commonly known Ockham's razor or principle⁹. It says:

Among competing hypotheses, the one with the fewest assumptions should be selected.

Here, hypotheses can be identified with models. Thus, this principle tells us we should choose the model that makes the fewest assumptions. I classify the assumptions of a model in two groups: fixed and free ones. The fixed assumptions belong to what I previously described as the *a priori* knowledge used to construct the model. These may render the model more interpretable in the physical or statistical sense, or even give it coherence

⁹The origin of this motto and its exact phrasing is beyond the scope of this work. I just mention that paradoxically, an ancient formulation is attributed to Ptolomey: “We consider it a good principle to explain the phenomena by the simplest hypothesis possible” ([Franklin 2002](#))

within the corpus of a theory. The free assumptions on the other hand, correspond directly to the parameters in the model. They give it flexibility when fitting the data¹⁰. For example, in the case of a straight line model, the fact that the data is linearly related can be considered as a fixed assumption. The free assumptions correspond to the slope and ordinate at the origin.

When comparing a linear model to a quadratic one in which the constant term has been fixed, we see that they have the same number of free parameters, two, but clearly the second one has an extra fixed assumption. Therefore, choosing the model with fewer free parameters does not necessarily mean choosing the model with the fewest assumptions.

One of the great advantages of the Bayesian methodology is that it incorporates directly Ockham's principle. Suppose that we want to compare two models, \mathcal{M}_1 and \mathcal{M}_2 , which we assume describe the data set, \mathbf{D} . Each model has prior Probability Mass Function (PMF)¹¹, $P(\mathcal{M}_k)$, and likelihoods $p(\mathbf{D}|\mathcal{M}_k)$ (with $k = 1, 2$). Notice that now, I use Bayes' theorem for models and not for parameters within a model. So, the prior probabilities of the models reflect our beliefs about the fixed assumptions within each model. On the other hand, the likelihood of the data, given the model, is related to the parameters (the free assumptions) and their prior probabilities, both within a model. This likelihood of the data given the model corresponds to the *evidence* of the model (Eq. 3.10). This evidence, written in terms of the model parameters, $\boldsymbol{\theta}_k$, is now

$$p(\mathbf{D}|\mathcal{M}_k) = \int_{\boldsymbol{\theta}_k} p(\mathbf{D}|\boldsymbol{\theta}_k, \mathcal{M}_k) \cdot p(\boldsymbol{\theta}_k|\mathcal{M}_k) \cdot d\boldsymbol{\theta}_k. \quad (3.15)$$

Bayes' theorem applied to models, instead of individual parameters as illustrated above, tells us that

$$P(\mathcal{M}_k|\mathbf{D}) = \frac{p(\mathbf{D}|\mathcal{M}_k) \cdot P(\mathcal{M}_k)}{p(\mathbf{D})}, \quad (3.16)$$

with $k = 1, 2$. Notice that $P(\mathcal{M}_k|\mathbf{D})$ can be defined without problem because the joint probability $p(\mathcal{M}_k, \mathbf{D})$ is a generalised¹² PDF.

Since there are only two models, their prior probabilities are related by $P(\mathcal{M}_1) =$

¹⁰However, they can also introduce degeneracy in the parametric space.

¹¹Since the number of models is in principle discrete, their probabilities do not define a continuous PDF, but a discrete probability function which is called PMF. Thus, the capital P is used to differentiate it from a PDF.

¹²The generalised PDF of a mixed random variable is defined as,

$$f_X(x) = \sum_k a_k \cdot \delta(x - x_k) + g(x),$$

where $a_k = P(X = x_k)$, δ is the Dirac delta, and $g(x)$ is a continuous PDF, with no Dirac deltas. By definition,

$$1 = \int f_X(x) dx = \sum_k a_k + \int g(x) dx.$$

For further details see https://www.probabilitycourse.com/chapter4/4_3_1_mixed.php.

$1 - P(\mathcal{M}_2)$. Therefore,

$$P(\mathcal{M}_k|\mathbf{D}) = \frac{p(\mathbf{D}|\mathcal{M}_k) \cdot P(\mathcal{M}_k)}{p(\mathbf{D}|\mathcal{M}_1) \cdot P(\mathcal{M}_1) + p(\mathbf{D}|\mathcal{M}_2) \cdot P(\mathcal{M}_2)}. \quad (3.17)$$

From this last Equation, the ratio of the posterior distributions is:

$$\frac{P(\mathcal{M}_1|\mathbf{D})}{P(\mathcal{M}_2|\mathbf{D})} = \frac{p(\mathbf{D}|\mathcal{M}_1) \cdot P(\mathcal{M}_1)}{p(\mathbf{D}|\mathcal{M}_2) \cdot P(\mathcal{M}_2)}. \quad (3.18)$$

This ratio provides an objective measure of how better the model \mathcal{M}_1 is when compared to model \mathcal{M}_2 , under the measure provided by the data \mathbf{D} by means of the evidence. When both prior probabilities $P(\mathcal{M}_1)$ and $P(\mathcal{M}_2)$ are set alike, the ratio of posteriors equals the ratio of likelihoods. This is known as the *Bayes factor* (for a similar derivation and some examples of its application see [Kass & Raftery 1995](#)).

Even when the priors for the models are set alike, the evidences themselves (Eq. 3.15) embody Ockham's principle. The evidence is the integral, in parametric space, of the prior times the likelihood, with the likelihood acting as a weight to the priors. Thus, Eq. 3.15 provides the measure of the available evidence supporting a model. It is important to notice that the evidence integral does not penalises models with parameters unconstrained by the data ([Trotta 2008](#)). There is simply no evidence for such parameters.

As explained in this section, the paramount importance of Bayes' theorem comes from the fact that it is the proper probabilistic way to update knowledge based on the statistical evidence.

3.1.3 Membership probability

In the previous Section we derived the ratio of the probabilities of two competing models \mathcal{M}_1 and \mathcal{M}_2 , given the data \mathbf{D} . In this Section, I describe a similar problem: the probability of two competing models given the two likelihoods for a single datum, \mathbf{d} . It also can be interpreted as the probability that the datum \mathbf{d} was generated by model \mathcal{M}_k . This probability is commonly known as the membership probability of the datum \mathbf{d} to belong to model or class, \mathcal{M}_k ($k = 1, 2$).

Bayes' theorem for this particular case is,

$$P(\mathcal{M}_k|\mathbf{d}) = \frac{p(\mathbf{d}|\mathcal{M}_k) \cdot P(\mathcal{M}_k)}{\sum_{k=1}^2 p(\mathbf{d}|\mathcal{M}_k) \cdot P(\mathcal{M}_k)}, \quad (3.19)$$

where $p(\mathbf{d}|\mathcal{M}_k)$ is the likelihood of datum \mathbf{d} and, $p(\mathcal{M}_k)$ is the prior probability that object \mathbf{d} was generated by model \mathcal{M}_k , with $\sum_{k=1}^2 P(\mathcal{M}_k) = 1$.

3.2 Bayesian Hierarchical Models

3.2.1 Generalities

The Bayesian formalism requires the establishment of priors. These represent the beliefs the user of the model has about the possible values that parameters of the model can take before new data are observed. This is indeed subjective. This subjectivity is the main source of criticism from the non-Bayesian community¹³.

Bayesian Hierarchical Model (BHM) are classified within the Empirical Bayes methods. On these methods, the prior distributions are inferred from the data rather than being directly specified, as it is done in common Bayesian methods. In BHM the priors are specified by parametric distributions whose parameters are also drawn from another parametric distribution in a hierarchical fashion. For this reason, hierarchical models are also called multilevel models. A full-BHM is that in which the parameters at the higher hierarchy level are drawn from a non-parametric distribution. In a non full-BHM the settlement of parameters stops at some level. These end-level parameters are called hyper-parameters.

Given their properties, BHMs represent the most objective way to the establishment of prior distributions (Gelman 2006). Regardless of the level of the BHM, for it to be effective, the family, or class, of prior distributions must be carefully chosen. These families must allow the *true* value of the parameter of interest (Morris 1983). If the likelihood parametric support is not fully contained in the prior (for example when the likelihood, as a function of the parameters, has a maximum outside the domain of a truncated prior), then the inferred posterior can be biased. For this reason, inspecting the prior knowledge is an important step in any Bayesian study.

Despite their theoretical advantages, BHMs are difficult to evaluate since they require far more parameters than standard Bayesian methods. Furthermore, their hierarchy (levels) must stop at some point. There are at least two approaches to stop this hierarchy. The first one uses a non-parametric distribution for the parameters at the higher level. This renders, as previously noted, a full-BHM. However, it demands an a priori knowledge of the non-parametric distribution, which, most of the time, is not the case. The second option is to give a point estimate, usually the mean or the mode, for the distribution of the parameter at the top of the hierarchy.

Although in BHMs the parameters of the prior distributions are inferred from data, the user of the model has the important task of specifying the family of distributions to be used for them. Selecting these families continues to be an active area of research. The most common approaches are the following.

- Conjugate priors. In this kind of priors the posterior distribution, which results of

¹³See Gelman (2012) for a discussion on the ethical use of prior information

the product of the prior times the likelihood, is also in the same family distribution of the prior.

- Default priors. These priors are used when there is insufficient information to set the prior and are supposed to be the default choice in the absence of any other information.
- Reference priors. Formally, a reference prior is permissible and maximise the missing information. See [Berger et al. \(2009\)](#) and references therein.
- Non-informative priors. This kind of priors intentionally discards all information on the phenomenon.
- Weakly informative priors. These provide intentionally weaker information than what actually is.

The default and non-informative approaches are discarded since for the Pleiades, which is one of the most studied cluster in the literature, there is already reliable information which must be used. Conjugate priors do not always agree with the previous knowledge. Reference priors, although an interesting approach, require complicated derivations which are hard to implement and thus computationally expensive.

From the previous options, I choose the weakly-informative approach. These are recommended by [Gelman \(2006\)](#); [Gelman et al. \(2008\)](#); [Huang & Wand \(2013\)](#) and [Chung et al. \(2015\)](#), since they show better computational performance when compared to non-informative priors.

Whatever family used for the prior distribution, we must always analyse the priors in terms of the posterior distribution, and check if the late makes sense ([Gelman 2006](#); [Gelman et al. 2013](#), Chap. 6).

3.2.2 Examples

Since BHMs usually need more parameters than standard techniques, its use was restricted until fast computers were widely available. The concept of BHM was already present in the 1960s. However, it was not until the 1970s that they were used to infer parameters of normal distributions and linear models (see [Good 1980](#), for an historical perspective of BHMs). In modern days, BHMs have a wide range of applications. Just to cite some examples, [Gelman & Hill \(2007\)](#) use them in the social sciences, [Fei-Fei & Perona \(2005\)](#) applies them for vision recognition and, [Diard & Bessiere \(2008\)](#) for robot navigation.

BHMs are also widely applied in astrophysics. Although, originally its use was mainly in the domain of inference of cosmological parameters (see for example the works of [Feeney et al. 2013](#); [March et al. 2014](#); [Anderes et al. 2015](#); [Shariff et al. 2016](#); [Alsing et al. 2017](#)),

they were rapidly adopted in other domains. For example, they have been used to study the eccentricity distribution of binary stars Hogg et al. (2010b), the Cepheids (Barnes et al. 2004) and RR Lyrae distances (Jefferys et al. 2007), the chemical composition (Wolfgang & Lopez 2015) and albedos of exoplanets (Demory 2014), extinction maps (Sale 2012), stellar parameters (Shkedy et al. 2007), and the present day mass distribution (Tapiador et al. 2017).

3.2.3 Graphical representation.

Probabilistic Graphical Model (PGM) provide the background to graphically depict BHMs. PGMs are graphs that portray the conditional relations among the elements in a probabilistic model. These elements can be constants or stochastic variables that interact by means of conditional relations, which can in turn be deterministic or stochastic.

In PGMs, stochastic variables are represented with circles and constants with squares. If the variable is known, as in the case of the data, it is represented with a filled symbol, otherwise with an empty symbol. Stochastic and deterministic relations are depicted with solid and dashed lines, respectively. If there is no line between two given elements, it indicates that they are assumed to be independent. Variables that repeat together, as in the case of the data, are grouped within a plate. The number of repetitions is indicated in one corner of the plate. For more details on PGMs see for example the book of Koller & Friedman (2009).

To exemplify the use of PGMs, Figure 3.1 shows the PGM for the BHM that infers the parameters in a Gaussian Mixture Model (GMM). In this model the parameters are the means μ_k , variances σ_k^2 and fractions ϕ_k of each of the K gaussian distributions in the mixture. Then $\mu_0, \sigma_0^2, \lambda, \nu$ and β are the hyper-parameters, while x_i represent the data, and z_i the categorical latent variable that indicates the parent gaussian for datum x_i . The squiggly line ending in T indicates that z_i is switch, which selects the gaussian at which x_i belongs.

3.3 The BHM for the Pleiades DANCe data set

Creating a model is a complex task. As previously mentioned, a model is a mathematical representation of the knowledge about a certain phenomenon. Thus, constructing a model demands gathering and arranging the *a priori* knowledge of the phenomenon. However, the model is not a isolated entity, in the sense that having a model alone, besides its pure mathematical interest, is almost useless without a data set into which apply it. The data set and the model conform an entity able to produce knowledge, this entity is the likelihood. For this knowledge to be accurate the likelihood must incorporate the information of the data collection mechanism, particularly if the latter is non-ignorable.

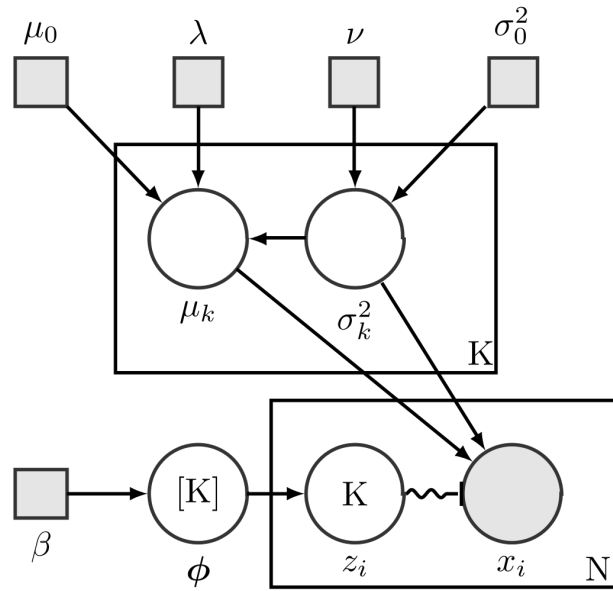


Figure 3.1: PGM representing the parametric inference of a Gaussian Mixture, see text for details. Figure by Benwing, license: Creative Commons BY-3.0

The *a priori* knowledge of the Pleiades cluster together with the description of the data collection mechanism of the DDR2 data set are summarised in Chapter 2. Here, I describe how this information is assembled to create the BHM.

Once the *a priori* knowledge has been gathered, the creation of the model becomes an iterative and continuous process. Assembling the knowledge into a coherent system demands continuous iterations of decision making, test, and analysis of preliminary results. This Section provides a snapshot of this process: the state of the model once the article [Olivares et al. \(2017\)](#) was submitted.

The following is a brief description of the BHM. Probabilistic models (likelihoods) are created for the field and cluster populations. These models, together with the data set, are used to infer both the posterior distributions of the cluster parameters, and the cluster membership probabilities of objects in the data set. Both cluster and field models are assumed to be independent in photometry and proper motions. The proper motions and photometric elements of the field model are described using GMMs. The cluster population is additionally modelled as the joint population of single stars and Equal-Mass Binaries (EMB). Both cluster proper motion models, for singles and EMB, are described using GMM. The photometric models of both single and EMB consist of multivariate normal distributions whose means and covariances are parameters of the model. The means of these multivariate normal distributions are parameterised by means of spline functions. In turn, these are parameterised by the *true* CI of each star, which is marginalised using the *true* colour distribution. Later, this *true* CI distribution will be used, in combination with the splines parameters, to derive the distributions of the magnitudes, and from them the luminosity distributions.

The details are explained in the following Sections. First, Section 3.3.1, explains the statistical procedure to deal with one of the crucial aspects of the DDR2 data set: the missing information. Later, Section 3.3.2 provides details of how the relevant knowledge about the Pleiades cluster and field populations are embedded in the generative model of the data. Finally, Sections 3.3.3 and 3.3.4 deal with the explanation of the field and cluster model, respectively.

3.3.1 Treatment of missing information

Missing information refers to at least two forms of absent values. In one hand, there are the data completely lost and from which the data set contains no information at all (except perhaps for the number of lost objects). On the other hand, there are the data that has been partially observed, and thus contains missing entries in some of its observables, but not in all of them.

A missing entry or missing value refers to a non-measured or non-available value in the vector of measurements of an object. It can arise due to different statistical or physical processes.

From the physical perspective, missing values occur due to faint or bright sources that produce counts values outside the dynamical range of the detector. They can also emerge due to detector malfunctions (e.g. electronic failures), or to random effects (e.g. cosmic rays).

From the statistical perspective, it is important to know if the origin of the missing information, called the missing process, is deterministic or stochastic. In the former, they occur only above or below a certain hard limit, while in the latter, they follow a probability distribution. If its origin is deterministic, there are two possible scenarios: censoring and truncation.

Truncation occurs when the data set contains measures of the population but until a certain limit. All information of the population above this limit is lost. Thus, the data set does not contain records, neither of the measured value nor of the number of measurements, for objects whose measured quantity lies outside the truncation limits. On the other hand, censoring happens when the data set contains only partial information about the actual value of the measured quantity. This information is the number of objects with missing values and the threshold limit upon which they appear. Basically, censoring happens when the value lies outside the upper or lower limits of the measuring instrument, and the number of these objects become the only available record.

In the DDR2, the proper motions are truncated to lay within the limits of -100 mas yr^{-1} and 100 mas yr^{-1} in both R.A. and Dec., see Section 2.7. However, due to its heterogenous origin, it does not posses unique truncation or censoring limits in its photometry. Although these limits could also be inferred from the data, the large number of DDR2 sources (not just surveys, but instruments and detectors) prohibits this task.

To account for the missing information the likelihood of the data must be modified. In truncation, the likelihood is renormalised to integrate to one within the observed limits, while in censoring this renormalisation account for the number of censored data. However, if the missing process is stochastic a more detailed treatment is needed.

However, in the DDR2 missing values not only occur because of censoring or truncation. Other sources of missing values include but are not restricted to cosmic rays, hot pixels, halos of bright stars, diffraction patterns and cross-matching failures. The statistical treatment of missing values originating from each of these sources lies beyond the scope of this work.

In terms of probability, there is no distinction between missing values and parameters. Therefore, when computing the likelihood $p(\mathbf{d}|\boldsymbol{\theta})$, where \mathbf{d} is the datum with a missing entry, and $\boldsymbol{\theta}$ is the set of likelihood parameters, we can marginalise the missing values as we do with any other nuisance parameter: with the aid of a prior. In this case, the prior sets the probability of finding a missing value within the domain of the observable. This prior probability can also be conditioned on extra information that may or not be available. For example, it can be conditioned on other observations (usually called covariates, e.g. the proper motions or sky positions), in the value of the observed (non-missing) entries \mathbf{d}_{obs} , or in parameters of the missing data collection mechanism, which can also be inferred from the data in hierarchical fashion.

The interested reader can find, in Chapter 8 of [Gelman et al. \(2013\)](#), a detailed description of the variety of schemes to account for the data collection mechanism, including the special cases of censoring and truncation. In general, the missing data mechanism can be accounted for by expressing the missing values entries with index I (a matrix of dimensions equal to those of the data, with ones in the entries corresponding to the observed entries in the data and zeros in the missing ones) and modifying the likelihood to account for the missing information.

The likelihood of the complete datum, which comprises not just the observed and missing datum $\mathbf{d} = \{\mathbf{d}_{obs}, \mathbf{d}_{mis}\}$, but also the index I , conditioned on the model parameters $\boldsymbol{\theta}$, is

$$p(\mathbf{d}, I|\boldsymbol{\theta}) = p(I|\mathbf{d}, \boldsymbol{\theta}) \cdot p(\mathbf{d}|\boldsymbol{\theta}),$$

with $p(I|\mathbf{d}, \boldsymbol{\theta})$ the missingness probability.

However, the actual information available in the datum is (\mathbf{d}_{obs}, I) . Thus, the observed-datum likelihood can be expressed as

$$p(\mathbf{d}_{obs}, I|\boldsymbol{\theta}) = \int p(\mathbf{d}|\boldsymbol{\theta})p(I|\mathbf{d}, \boldsymbol{\theta})d\mathbf{d}_{mis}, \quad (3.20)$$

where the missing values have been marginalised with the aid the prior $p(I|\mathbf{d}, \boldsymbol{\theta})$.

The probability $p(I|\mathbf{d})$ can be assumed to be uniform, which results in what is called the *ignorability* of the data collection mechanism. The result of this assumption is that $p(\mathbf{d}_{obs}, I|\boldsymbol{\theta}) = p(\mathbf{d}_{obs}|\boldsymbol{\theta})$, which is equivalent to ignore the missing mechanism. This assumption is incorrect because, as shown in Section 2.7, missing values are most probable at the faint photometric ends.

The probability $p(I|\mathbf{d}, \boldsymbol{\theta})$ is formally not known because DDR2 is a compilation of data from a variety of surveys. Thus the data collection mechanism is neither homogeneous nor totally understood¹⁴. In spite of that, it can also be assumed that the collection mechanism depends only on the observed values, \mathbf{d}_{obs} . Such assumption is called *missing at random* (Gelman et al. 2013, p. 450) because the distribution of the missing-data mechanism does not depend on the missing values. This assumption is still incorrect because, as shown in Section 2.7, the probability of detecting an object depends on its brightness. However, under this assumption, $p(I|\mathbf{d}, \boldsymbol{\theta}) = p(I|\mathbf{d}_{obs})$. Thus, Equation 3.20 reduces to,

$$\begin{aligned} p(\mathbf{d}_{obs}, I|\boldsymbol{\theta}) &= \int p(\mathbf{d}|\boldsymbol{\theta}) \cdot p(I|\mathbf{d}_{obs}) d\mathbf{d}_{mis} \\ &= p(I|\mathbf{d}_{obs}) \cdot \int p(\mathbf{d}_{mis}, \mathbf{d}_{obs}, |\boldsymbol{\theta}) d\mathbf{d}_{mis} \\ &= p(I|\mathbf{d}_{obs}) \cdot p(\mathbf{d}_{obs}|\boldsymbol{\theta}). \end{aligned} \quad (3.21)$$

This approach is similar to the use of the so called *selection function* (see for example Andreon & Hurn 2013). Indeed, the probability $p(I|\mathbf{d}_{obs})$, is the probability of including the object with observables \mathbf{d}_{obs} in the data set under analysis. Thus we can call it *selection probability*.

As kindly suggested by Stefano Andreon (one of the referees of this work), another possibility to compute the likelihood function based on the observed data is given by Equation 30 of Andreon & Hurn (2013). In the latter,

$$p(y_i^{obs}|I_i = 1, y_i, \theta) = \frac{f(I_i = 1|y_i) \cdot p(y_i^{obs}|y_i, \theta)}{\int f(I_i = 1|z) \cdot p(z|y_i, \theta), dz} \quad (3.22)$$

where y_i and y_i^{obs} are the true and observed values, respectively, $f(I_i = 1|y_i)$ is the *selection function*, and $p(y_i^{obs}|y_i, \theta)$ is the likelihood of the observed data given the true data and the parameters θ .

However, in the BHM the previous approach can not be used because of the following reasons. First, the DDR2 has a *selection function* which is almost impossible to estimate given that objects are selected based on their membership probability to the cluster. Even if a simpler selection function could be used instead (like cuts in the observable space), the

¹⁴ The DANCe team is currently working on the assessing of the missingness process. In particular, we are interested in the detection probability as a function of signal-to-noise and sky position. The latter is of paramount importance in the vicinity of bright sources where halos and artefacts have the largest impact.

resulting one will be the *selection function* conditioned on the observed values, and not in the true ones, as required by Eq. 3.22. Furthermore, this approach is computationally expensive due to the integral in the denominator of Eq. 3.22, and using it will result in an even larger computing time.

As it will be shown in the next section, the likelihood of the data (Eq. 3.20) will be partitioned in the likelihoods of the cluster and field (Eq. 3.27). Since the objects in the RDDR2 were selected based on their cluster membership probability, then, under the assumption of *missing at random*, the cluster *selection probability* is $p(I|\mathbf{d}_{obs}) = 1 - 10^{-11}$, where 10^{-11} is the probability of leaving one cluster member out of the RDDR2 (see Section 2.8). Therefore, we can safely assume that the cluster *selection probability* is one. Thus from Eq. 3.21, $p(\mathbf{d}_{obs}, I|\boldsymbol{\theta}) = p(\mathbf{d}_{obs}|\boldsymbol{\theta})$.

Summarising, in the treatment of missing values I make the following assumptions.

- The cluster data collection mechanism is *missing at random* with *selection probability* $p(I|\mathbf{d}_{obs}) = 1$.
- The field data collection mechanism is *ignorable* with $p(I|\mathbf{d})$ uniform.

This assumptions, although incorrect, are taken because of the following reasons.

First, the $p(I|\mathbf{d}, \boldsymbol{\theta})$ for the formal treatment of missing values in Eq. 3.20 is not known.

Second, even if the probability $p(I|\mathbf{d}, \boldsymbol{\theta})$ would be available (or an approximation of it), the current computational capabilities will not allow to numerically evaluate the integral of Eq. 3.20. The use of a uniform probability enable us to analytically evaluate this integral thus avoiding the high computational burden of computing it for each object and missing value in the data set and at each step in the MCMC chain.

Therefore, although the *ignorability* assumption is not correct, it currently provides the simplest and straight forward option to perform the expensive integral of Eq. 3.20. Since this assumption is incorrect, and therefore results in biased estimators of the true population parameters, in the following section I quantify this biases.

Validity of the *ignorability* assumption.

In this Section, I present the quantification of the bias introduced by assuming the *ignorability* of the missing mechanism. In addition, I also quantify the bias introduced by assuming that the true population parameters can be recovered using only completely observed objects and discarding those with missing entries. The latter, which here I call the *naivety* assumption, is common practice in the literature (at least in the works mentioned in Section 1.4. Notice that these two assumptions, *naivety* and *ignorability* are undistinguishable in the absence of correlations amongst observables. Therefore, the bias must be quantified in a data set with similar correlations to those in the RDDR2.

To quantify the biases rendered by these assumptions, I proceed as follows.

First, I assume to know the parameter values of the true population. Thus, I use the parameter values of the GMM describing the photometry of the field population contained in the RDDR2 data set. In specific, I assume that these true parameter values are those inferred in Section 3.3.3.

Second, using these true parameter values I generate a synthetic data set with 10^4 objects.

Third, using the real data from the RDDR2, I mask as missing entries the photometric entries in the synthetic data. The masking procedure is the following.

Given that the K_s photometric band is the most observed one in the RDDR2, I use it as covariate, and to obtain the probability of having a missing value. Thus,

$$p(I_x = 0|K_s) = \frac{p(K_s|I_x = 0) \cdot p(I_x = 0)}{p(K_s)},$$

where $I_x = 0$ stands for the probability that the photometric band x which can be $\{i - K_s, Y, J, H\}$ is missing, $p(K_s|I_x = 0)$ is the probability of K_s given that the band x is missing, $p(K_s)$ is the probability of all observed values of K_s , and $p(I_x = 0)$ is the fraction of objects with missing entries in the x band. Then, I create a synthetic random matrix R of size equal to that of the synthetic data. The entries in this matrix are drawn from a uniform probability distribution between zero and one. Then, objects in the synthetic data set are masked as missing if and only if

$$\begin{cases} R_{i,x} > p(I_x = 0|K_s) & \text{for } x \in \{i - K_s, Y, J, H\} \\ R_{i,x} > p(I_x = 0) & \text{for } x = K_s \end{cases} \quad (3.23)$$

with $p(I_{K_s} = 0)$ the fraction of objects with missing values in K_s . The latter assumes that missing values in K_s are uniformly distributed.

Thus, I now have three synthetic data sets. The original one, with completely observed entries (hereafter Complete), the one with missing values (hereafter Missing), and, the one resulting from taking only the completely observed objects from the one with missing values (hereafter Observed). Figure 3.2 shows the distribution of objects in these data sets as a function of the photometric magnitude for each magnitude. These densities are similar to the corresponding ones in the RDDR2, as expected (see Fig. 2.21). To each of these data sets, I apply the GMM algorithm (the one described in Section 3.6.3) and recover the fractions, means and covariance matrices of the GMM. I call these set of parameters and the densities they produce Complete, Missing, and Observed, in accordance to the data set from which they were obtained.

By means of these three set of parameters, I can quantify the bias induced by the *ignorability* and *naivety* assumptions. The first is given by the Missing data set and the parameters derived from it, while the later by the Observed data set and its derived parameters. Furthermore, to minimise the effects of the sample size, instead of comparing

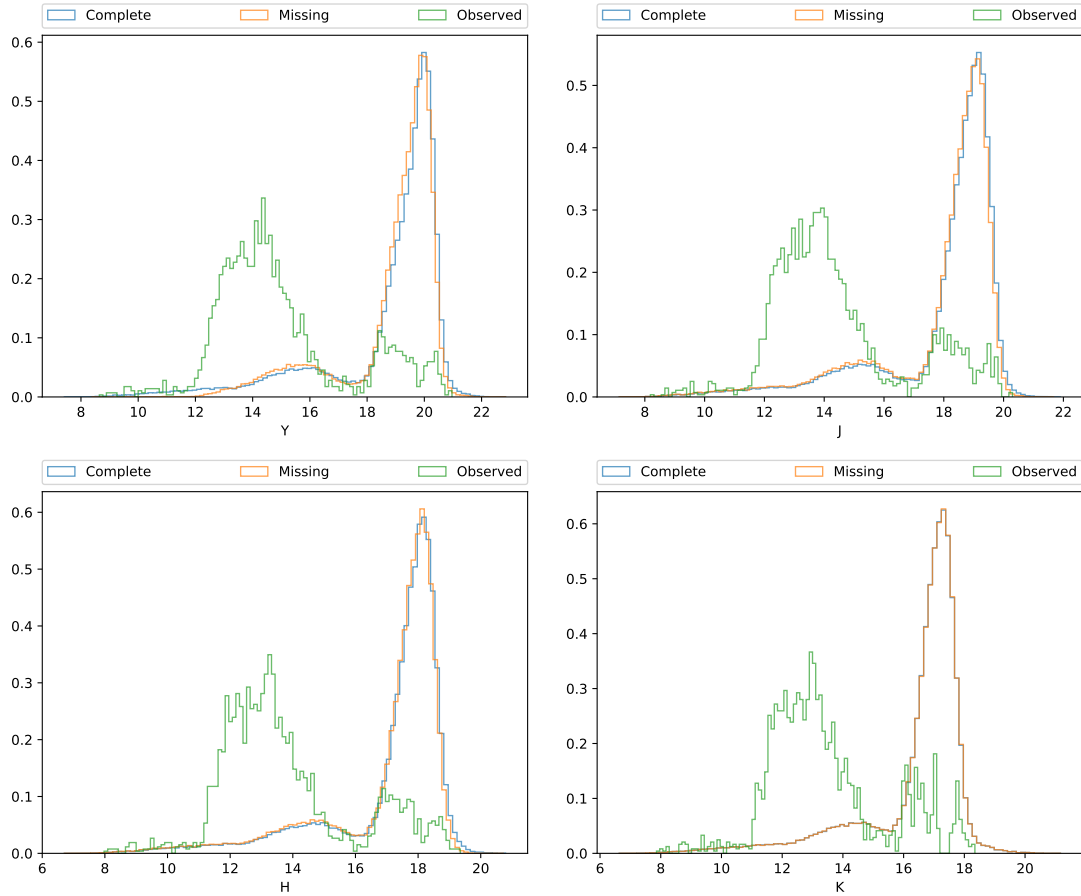


Figure 3.2: Density distributions in Y, J, H and K_s bands of the synthetic objects in the Complete, Missing and, Observed data sets. See text.

the Missing and Observed set of parameters to the true one, I compare them to the Complete set of parameters. To quantify differences, I use the Root Mean Square Relative Deviation, which is defined as,

$$RMSRD = \sqrt{\frac{\sum_i^n \left(\frac{x_i - y_i}{y_i} \right)^2}{n}},$$

where x_i is the density given by the either the Missing or the Observed GMMs, and y_i is the density given by the Complete GMM.

The densities of the Complete, Missing and Observed GMMs are evaluated in grids (with n total points separated by 0.05 mag) in each of the Y, J, H, K_s vs CI CMDs. The RMSRDs are computed just for those points in the grids where the Complete density is higher than 10^{-3} , which avoids the regions far from the cluster sequence where the density vanishes. The mean RMSRD of the Observed and Missing GMMs in the four CMDs are 0.78 ± 0.38 and 0.21 ± 0.4 , respectively. Uncertainties are the standard deviation of the four RMSRDs.

In addition, the mean absolute relative difference of the Missing and Observed set of parameters when compared to the Complete ones are 0.42 ± 2.5 and 1.5 ± 3.2 , respectively.

The previous values indicate that the Missing and Observed GMMs resulting from the *ignorability* and *naivety* assumptions, respectively, are indeed biased. However, as these values demonstrate, the bias introduced by the *naivety* assumption is 3.5 times larger than that introduced by the *ignorability* assumption.

Figure 3.3 shows the (absolute) differences of the Missing and Observed GMMs when compared to the Complete one. As can be seen, the *naivety* assumption (Observed GMM) leads to: i) overestimated field densities in the central regions corresponding $CI = 3.5$, and, ii) underestimated field densities in the bright and faintest regions $CI \sim [2, 5, 6.5]$. On the other hand, the *ignorability* assumption (Missing GMM) leads to field densities similar to the Complete ones across the CMDs, except at the very faint ends $CI > 5$.

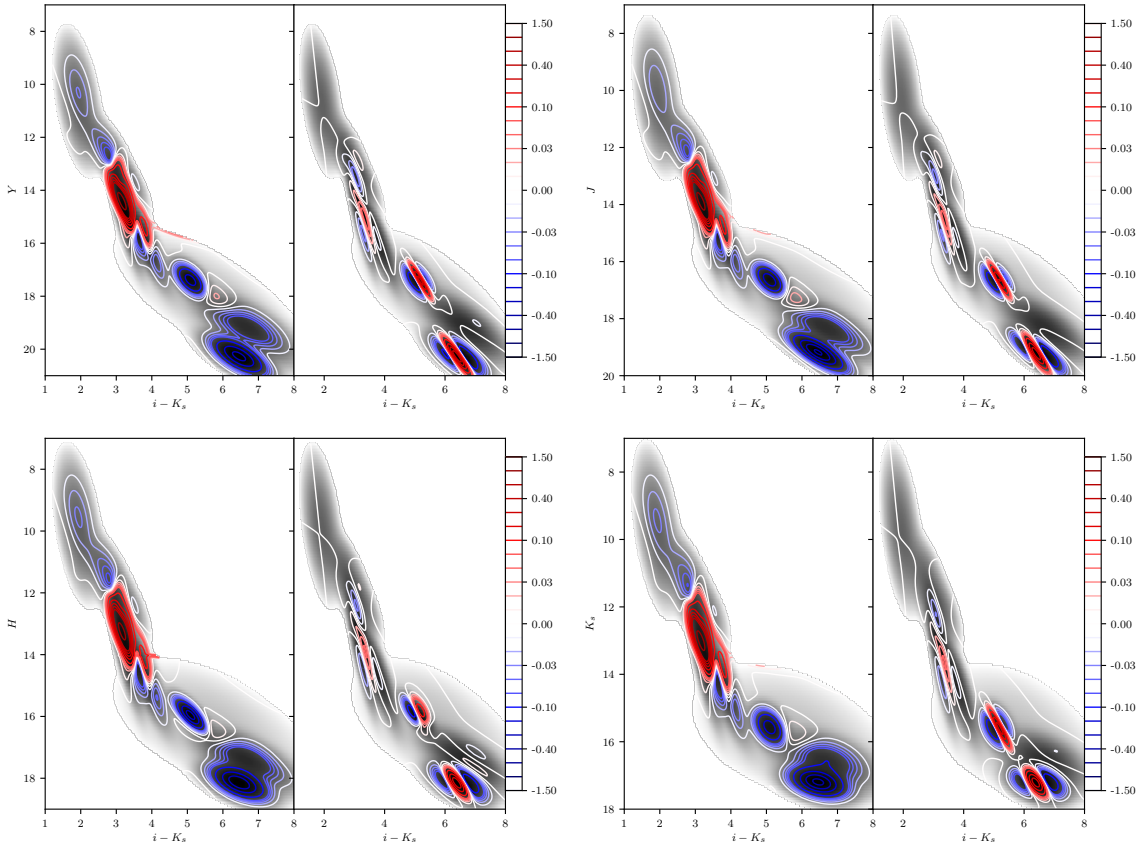


Figure 3.3: Contours comparing the deviations in the density (in units of mag^{-2}) of the Observed (left panels) and Missing (right panels) GMMs when compared to the Complete GMM (in grey scale at the background), projected in each of the CMDs used in this work. Regions where the density of the Complete model goes below 10^{-3} are not shown.

In spite of the incorrectness of the *ignorability* assumption, which nevertheless enable us to analytically perform the marginalisation integral (Eq. 3.20) and reduce the computing time, it renders better estimates of the true population parameters than the commonly spread *naivety* assumption used by the previous works from the literature (see Section 1.4).

3.3.2 The generative model

In the DDR2 data set, cluster stars and field sources are mixed. Their probabilistic disentanglement requires probabilistic models for each population, i.e. their likelihoods. The true values of these two likelihoods, field and cluster, will be given by parametric relations embodying the state of knowledge of NYC (i.e. the models of cluster and field). Using these likelihoods, the individual cluster membership probability of each object in the data set is computed (by means of Eq. 3.19). These PDFs together with a probability classification threshold, allow individual objects to be separated into cluster and field populations.

The inference process demands a set of N binary integers \mathbf{q} , one q_n for each object. The two possible values of these binary integers represent one of the two mutually exclusive possibilities: the object belongs to the cluster ($q_n = 1$) or to the field population ($q_n = 0$).

Let $\boldsymbol{\theta}$ and $\boldsymbol{\phi}$ be the parameters of the cluster and field models, and p_c and p_f their likelihoods, respectively. Then, the likelihood of the data, \mathbf{D} , is,

$$p(\mathbf{D}|\mathbf{q}, \boldsymbol{\theta}, \boldsymbol{\phi}) = \prod_{n=1}^N p_c(\mathbf{d}_n|\boldsymbol{\theta})^{q_n} \cdot p_f(\mathbf{d}_n|\boldsymbol{\phi})^{(1-q_n)}. \quad (3.24)$$

The inference of these N binary integers will demand a computing power that is outside the current possibilities. Thus, instead of inferring them, I marginalise them using a prior probability, which is set in terms of a new and unique parameter π . It represents the *prior* probability that an object belongs to the field. Thus, the prior probability of \mathbf{q} is

$$p(\mathbf{q}|\pi) = \prod_{n=1}^N (1 - \pi)^{q_n} \cdot \pi^{(1-q_n)}. \quad (3.25)$$

Since the entries in \mathbf{q} can only take as value zero or one, the marginalisation integral is indeed a sum. Furthermore, the domain of this sum is the 2^N possible ways to combine the binary variables q_n . Thus, the marginalisation sum over all these 2^N possible states results in,

$$\begin{aligned}
p(\mathbf{D}|\pi, \boldsymbol{\theta}, \phi) &= \sum_{\mathbf{q}} p(\mathbf{D}, \mathbf{q}|\pi, \boldsymbol{\theta}, \phi) \\
&= \sum_{\mathbf{q}} p(\mathbf{D}|\mathbf{q}, \pi, \boldsymbol{\theta}, \phi) \cdot p(\mathbf{q}|\pi) \\
&= \sum_{\mathbf{q}} \prod_{n=1}^N p_c(\mathbf{d}_n|\boldsymbol{\theta})^{q_n} \cdot p_f(\mathbf{d}_n|\phi)^{(1-q_n)} \cdot \prod_{n=1}^N (1-\pi)^{q_n} \cdot \pi^{(1-q_n)} \\
&= \sum_{\mathbf{q}} \prod_{n=1}^N [(1-\pi) \cdot p_c(\mathbf{d}_n|\boldsymbol{\theta})]^{q_n} \cdot [\pi \cdot p_f(\mathbf{d}_n|\phi)]^{(1-q_n)} \\
&= \prod_{n=1}^N (1-\pi) \cdot p_c(\mathbf{d}_n|\boldsymbol{\theta}) + \pi \cdot p_f(\mathbf{d}_n|\phi).
\end{aligned} \tag{3.26}$$

This last equality is a rather complicated derivation which can be found in Press (1997), and in Hogg et al. (2010a) for p_c and p_f in the exponential family. Also, a general derivation of this expression is given by Jaynes (2003). He obtains it assuming individual unknown probabilities p_n instead of q_n and marginalising over them with the aid of a prior.

Thus, the *generative model* or likelihood of the datum \mathbf{d}_n is

$$p(\mathbf{d}_n|\pi, \boldsymbol{\theta}_c, \boldsymbol{\theta}_f, \mathbf{u}_n) = \pi \cdot p_f(\mathbf{d}_n|\boldsymbol{\theta}_f, \mathbf{u}_n) + (1-\pi) \cdot p_c(\mathbf{d}_n|\boldsymbol{\theta}_c, \mathbf{u}_n), \tag{3.27}$$

where $\boldsymbol{\theta}_f$ and $\boldsymbol{\theta}_c$ indicate the cluster and field parameters, while \mathbf{u}_n refers to the datum uncertainty. The probabilities $p_f(\mathbf{d}_n|\boldsymbol{\theta}_f, \mathbf{u}_n)$ and $p_c(\mathbf{d}_n|\boldsymbol{\theta}_c, \mathbf{u}_n)$ are the field and cluster models, respectively. These models are explained in detail in the next two sections.

The cluster membership probability of each object in our data set are computed from the elements in Eq. 3.27, by means of Eq. 3.19. Thus, the cluster membership probability is given by,

$$p(\mathcal{M}_c|\mathbf{d}_n) = \frac{p_c(\mathbf{d}_n|\boldsymbol{\theta}_c, \mathbf{u}_n) \cdot (1-\pi)}{\pi \cdot p_f(\mathbf{d}_n|\boldsymbol{\theta}_f, \mathbf{u}_n) + (1-\pi) \cdot p_c(\mathbf{d}_n|\boldsymbol{\theta}_c, \mathbf{u}_n)}, \tag{3.28}$$

In Eq. 3.19, the probabilities $P(\mathcal{M}_k|\mathbf{d})$ are PMF because the probabilities $P(\mathcal{M}_k)$ are themselves PMF. However, in Eq. 3.28, by setting the prior probability π as a random variable ($\pi \in [0, 1]$), which is itself inferred from the data in a hierarchical way and with prior PDF given by a Dirichlet distribution $Dir(\boldsymbol{\alpha})$ (with $\boldsymbol{\alpha}$ its hyper-parameter), then $p(\mathcal{M}_c|\mathbf{d}_n)$ also follows a probability distribution. To demonstrate this, let

$$\begin{aligned}
y &= p(\mathcal{M}_c|\mathbf{d}_n), \\
g(\pi) &= \frac{p_c(\mathbf{d}_n|\boldsymbol{\theta}_c, \mathbf{u}_n) \cdot (1-\pi)}{\pi \cdot p_f(\mathbf{d}_n|\boldsymbol{\theta}_f, \mathbf{u}_n) + (1-\pi) \cdot p_c(\mathbf{d}_n|\boldsymbol{\theta}_c, \mathbf{u}_n)}, \\
\pi &\sim p(\pi),
\end{aligned}$$

with $p(\pi)$ the probability distribution of the random variable π , and $g(\pi)$ a linear transformation of π . Then, by definition $y \equiv g(\pi)$, and y follows the probability distribution given by $y = g(p(\pi))$. Since the parameter π is also inferred from the data, then each cluster membership probability determined in this work is itself a PDF.

In the following, I assume that the observed quantities result from the convolution of the model likelihood, given the *true* quantities, with the uncertainty process (see Section 3.1.1). The latter could be different for each object, thus resulting in different individual uncertainties. Thus, the model allows heteroscedastic uncertainties. Although these uncertainties are not assumed to have the same values, I assume that all of them are multivariate normal. This assumption is standard practice and is also supported by the large and heterogeneous origins of the DDR2 data set.

3.3.3 The field population

To model the field population, I assume that the joint seven-dimensional probability distribution of the field can be factorised into the probability distributions of proper motions and photometry. Thus, the field likelihood of the proper motions and the photometry are assumed to be independent. Also, I assume that both distributions are described by GMM. The flexibility of GMMs to fit a variety of distribution geometries makes them a suitable model to describe the field density of the heterogeneous DDR2 data set.

A GMM is a probability distribution resulting from the linear combination of M Gaussian distributions,

$$p_{GMM}(x|\boldsymbol{\pi}, \boldsymbol{\mu}, \boldsymbol{\Sigma}) = \sum_{m=1}^M \pi_m \cdot \mathcal{N}(\boldsymbol{\mu}_m, \boldsymbol{\Sigma}_m), \quad (3.29)$$

where π_m is the fraction of the m th Gaussian, $\boldsymbol{\mu}_m$ its mean and, $\boldsymbol{\Sigma}_m$ its covariance matrix. The m fractions must add to one.

Notice that the number of Gaussians in the mixture is not formally speaking a parameter, but rather it implies a collection of parameters. The number of these parameters increases linearly with the number of Gaussians and quadratically with the dimension.

According to [Bouy et al. \(2015\)](#), the number of Pleiades candidate members in the DDR2 data set is 2010 (going up to 2109 in the combined Tycho+DDR2) from a total of 1,972,245 sources. It means that the number of field objects dominates (99.9%) the DDR2 data set. Even in our restricted 10^5 objects data set, RDDR2 (see Sect. 2.8), the field still dominates with a 0.98 fraction. Thus, it can be assumed that any classification of candidate members will have a negligible impact on this figure. Therefore, it seems reasonable to assume that the GMM describing the field population can be frozen (fixed) during the process of cluster parameters inference. I elaborate more on this assumption.

The objects that [Bouy et al. \(2015\)](#) classified as belonging to the field are those

whose cluster membership probabilities are lower than 0.75. This probability threshold corresponds to the one found by [Sarro et al. \(2014\)](#) after analysing the performance of their methodology when applied to synthetic data sets. In [Sarro et al. \(2014\)](#) the authors report that, at a probability threshold $p = 0.75$, the contamination and true positive rates are $\sim 8\%$ and $\sim 96\%$ respectively. Assuming that these values are correct, the real number of field objects would change by approximately 4% of the cluster members (adding the 8% of contaminants and subtracting the 4% of missed members), thus ~ 80 objects. This value is negligible compared to the size of the data set (10^5 objects in the RDDR2). It represents the negligible fraction of 8×10^{-4} .

It can be further assumed that these hypothetically misclassified objects are spread in the space of observables. Indeed, these misclassified objects can be thought to have membership probabilities near the classification threshold. Thus, they may lay in the entanglement regions which corresponds, in proper motions, to a halo around the cluster centre, and in photometry, to a region around the cluster sequence. For example, these objects could have photometry that agrees with the cluster sequence but proper motions that are far from it. There are several combinations of observables values which may render these intermediate membership probabilities. The observable regions that these objects may populate allows us to assume that they are spread over the observable space.

If the misclassified objects are a few and spread over the observable space, then their contribution to the parameters of the GMM describing the field population can be neglected. Thus, the parameters of the GMM can remain fixed and out of the inference process.

The previous assumption is of paramount importance due to practical reasons, but because the field parameters remain fixed, their uncertainty is not propagated to cluster parameters and neither to membership probabilities. If I were to simultaneously infer the parameters of both cluster and field models, even only those of the field proper motions GMM, the required computing time would be excessive. The number of parameters in the field GMM goes up to ~ 300 , more than twice that of the cluster model (85 parameters). Even inferring only the 42 parameters of the field proper motions GMM would represent, at least, a 50% increase in the computing time. Instead, I first fit the parameters of the field GMM using the field objects in the RDDR2 (the $\sim 98,000$ objects with membership probabilities below 0.75) and then I keep these parameters fixed in the inference process.

The number of gaussians for the proper motions and photometric GMM is found using the Bayesian Information Criterion (BIC) introduced by [Schwarz \(1978\)](#). The BIC is a model selection criterium that aims at avoiding over-fitting. It represents a compromise between the likelihood, \mathcal{L} , of the n data points, and the number of parameters, k . This is,

$$BIC = \ln n \cdot k - 2 \ln \mathcal{L}. \quad (3.30)$$

To estimate the parameters of the GMM we use the Expectation Maximisation (EM) algorithm. However, the missing values in the photometry prevent the use of the standard

form of the algorithm (see for example Chapter 9 of [Bishop 2006](#)). Instead, I estimated these parameters with the modified version of the EM algorithm for GMM found by [McMichael \(1996\)](#) and rediscovered by me (see Section 3.6.3). On this version, objects with missing values also contribute to the MLE of the parameters. The distribution of missing values though is also assumed uniform (i.e. it assumes the ignorability of the missing-value process). I applied this algorithm to the five dimensional photometric observables of the 98,010 objects (from the RDDR2) with membership probabilities below 0.75 according to [Bouy et al. \(2015\)](#). I tested GMMs whose number of components ranged from 1 to 20. The optimal number of components suggested by the BIC is 14. Figures 3.4 and 3.5 show two dimensional projections of the 14 components in the five dimensional GMM. It is important to notice that only $\sim 1\%$ of these 98,010 objects have completely observed photometry (i.e. no missing values in any observable). For this reason, some of the Gaussians appear empty in Fig. 3.4. However, Fig. 3.5 shows projections of the same 14 component and five dimensional GMM in the magnitude-magnitude diagrams, where the percentage of completeness is above 80%. As a consequence, there are no empty Gaussians in this Figure, as shown by the log scale density. If we were to work only with the completely observed objects and discarded 99% of the data set, our derived parameters would be severely biased (see Section 3.3.1).

In the case of proper motions, since they do not contain missing values, I computed the GMM parameters with the standard EM algorithm. The BIC finds a model with 15 components, the majority of them with large variances and small fractions (see Fig. 3.6a). These small-fraction Gaussians fit an extended component of the proper motions distributions, which is clearly non-Gaussian. For this reason, we decided modify the mixture of Gaussians by adding a uniform distribution $\mathcal{U}(\mathbf{d}_{pm}|S_{\mu_\alpha}, S_{\mu_\delta})$, with S_{μ_α} and S_{μ_δ} the support of the proper motions in Right Ascension and Declination, respectively (see Table 2.2). I changed the EM algorithm to properly account for this modification. The BIC applied to this new mixture renders more reasonable results (see Fig. 3.6b), with an eight components mixture distribution: seven Gaussians plus the uniform. This modification improves the GMM while simultaneously reduces the number of parameters.

Finally, the field likelihood $p_f(\mathbf{d}|\boldsymbol{\theta}_f, \mathbf{u})$ of an object with measurements \mathbf{d} , given its standard uncertainties \mathbf{u} and the field parameters, $\boldsymbol{\theta}_f$, is

$$p_f(\mathbf{d}|\boldsymbol{\theta}_f, \mathbf{u}) = \left[\pi_{f,pm,0} \cdot \mathcal{U}(\mathbf{d}_{pm}|S_{\mu_\alpha}, S_{\mu_\delta}) + \sum_{i=1}^7 \pi_{f,pm,i} \cdot \mathcal{N}(\mathbf{d}_{pm}|\boldsymbol{\mu}_{f,pm,i}, \boldsymbol{\Sigma}_{f,pm,i} + \mathbf{u}_{pm}) \right] \cdot \left[\sum_{i=1}^{14} \pi_{f,ph,i} \cdot \mathcal{N}(\mathbf{d}_{ph}|\boldsymbol{\mu}_{f,ph,i}, \boldsymbol{\Sigma}_{f,ph,i} + \mathbf{u}_{ph}) \right]. \quad (3.31)$$

The first and second brackets represent the proper motion (subindex pm) and photometric (subindex ph) models, respectively, with $\boldsymbol{\pi}_f, \boldsymbol{\mu}_f, \boldsymbol{\Sigma}_f$ their fractions, means and covariance matrices, respectively. The first term of the proper motion model is the uniform distribution,

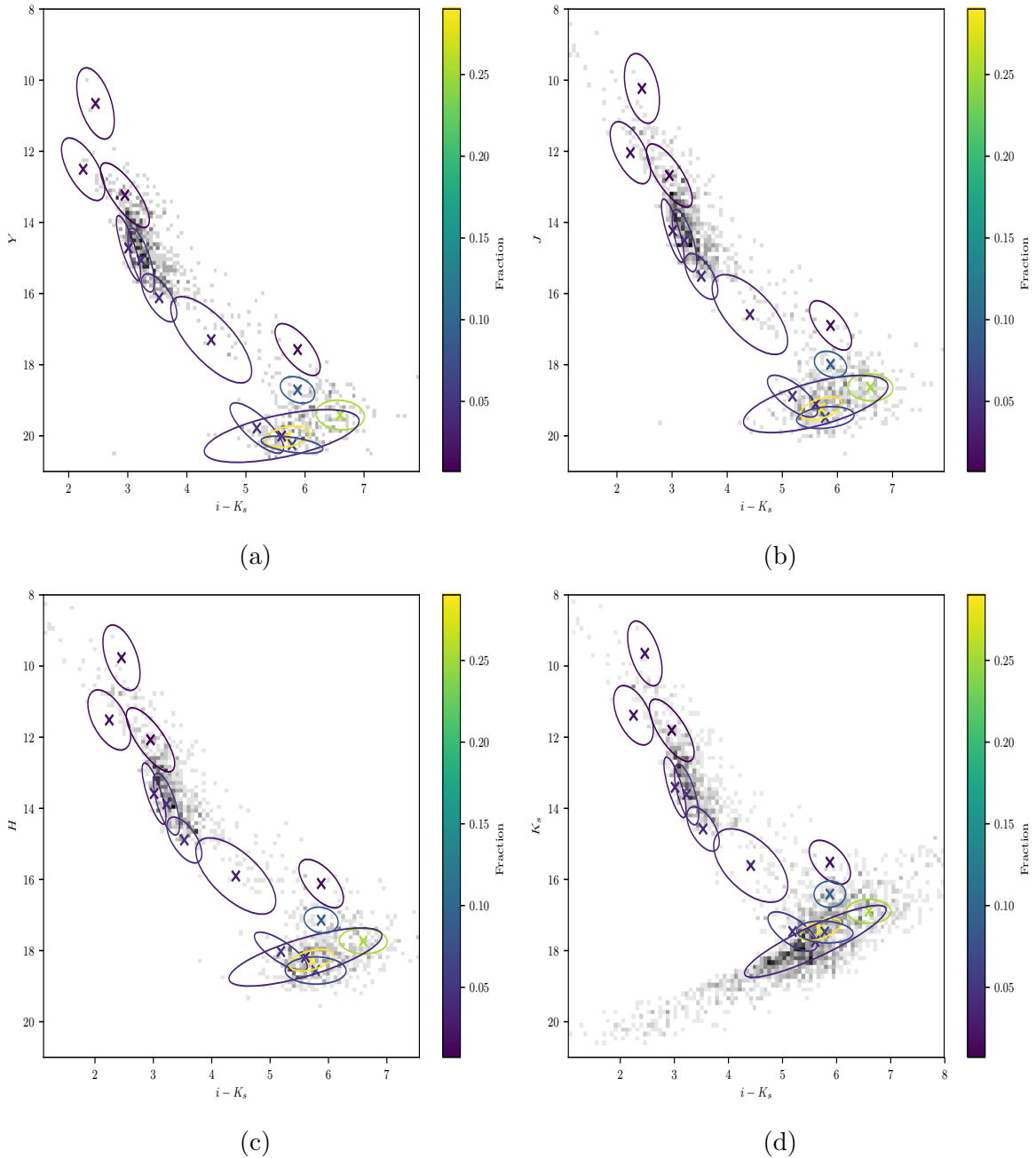


Figure 3.4: CMDs showing projections of the 14 components in the GMM (ellipses for the covariance matrix and crosses for the mean) used in the model the field photometry. The density of field objects with $p < 0.75$ (according to Bouy et al. 2015, there are 98010 field objects) is shown in grey scale. Notice that only $\sim 2.4\%$ of these field objects have complete observations in these projections. For this reason, some of the Gaussians appear almost empty. The ellipses shown in Fig. 4.16 represent this GMM.

with $\pi_{f,pm,0}$ its fraction. The uncertainty process is convolved (see Section 3.1) with the assumed models using the individual proper motions (\mathbf{u}_{pm}) and photometric (\mathbf{u}_{ph}) uncertainties.

Table 3.1 lists the groups (proper motions or photometry), symbols, dimension, and meanings of all the field parameters θ_f (see Eq. 3.27) described in

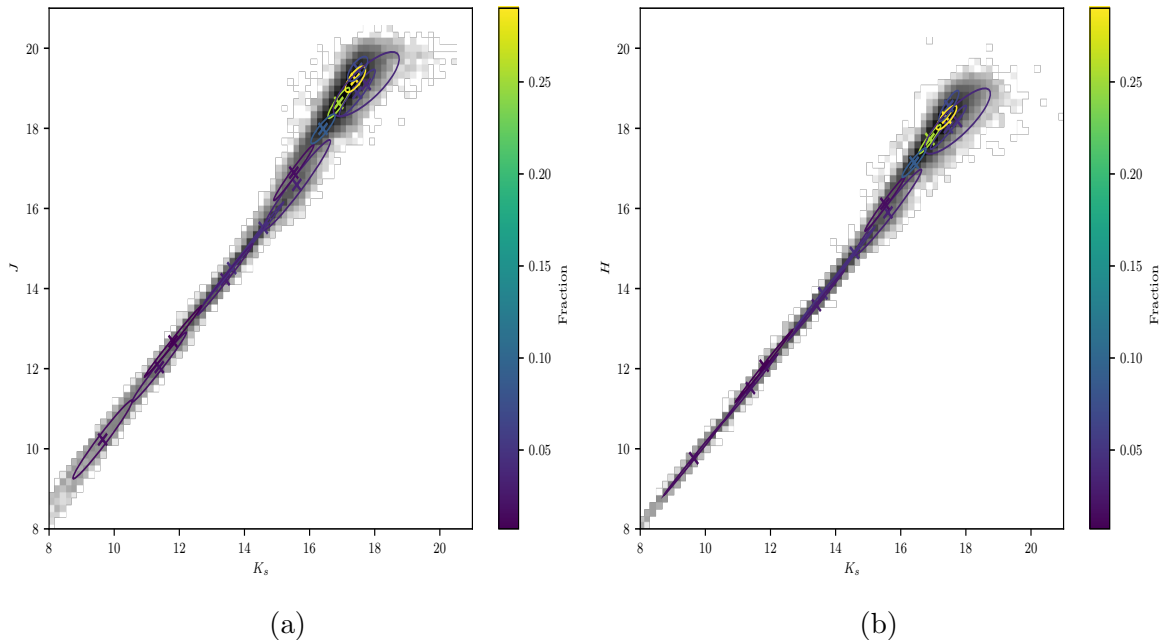


Figure 3.5: Magnitude-magnitude diagrams showing projections of the 14 components in the GMM (ellipses and crosses) used in the model the field photometry, and the logarithm of the density (grey) of field objects with $p < 0.75$ (according to [Bouy et al. 2015](#), there are 98010 field objects). Notice that $\sim 85\%$ of these field objects have complete observations in the projections shown.

this Section. These parameters are derived from the RDDR2 objects whose cluster membership probability is lower than 0.75 according to Bouy et al. (2015). As stated earlier, these field parameters remain fixed through the inference process of the cluster parameters θ_c (see Eq. 3.27). Thus, there is no need to establish priors for them.

Table 3.1: Field parameters. Listed are the groups, symbols, dimensions and descriptions of the field parameters derived from the field objects of the RDDR2 data set.

Group	Symbol	Dimension	Description
Proper Motions	$\pi_{f,pm,0}$	1	Fraction of the uniform distribution
	S_{μ_α}	2	Support of the uniform distribution in R.A
	S_{μ_δ}	2	Support of the uniform distribution in Dec.
	$\pi_{f,pm}$	7	Fractions of Gaussians in the mixture
	$\mu_{f,pm}$	7×2	Means of Gaussians in the mixture
	$\Sigma_{f,pm}$	7×4	Covariance matrices of Gaussians in the mixture
Photometry	$\pi_{f,ph}$	14	Fractions of Gaussians in the mixture
	$\mu_{f,ph}$	14×5	Means of Gaussians in the mixture
	$\Sigma_{f,ph}$	14×25	Covariance matrices of Gaussians in the mixture

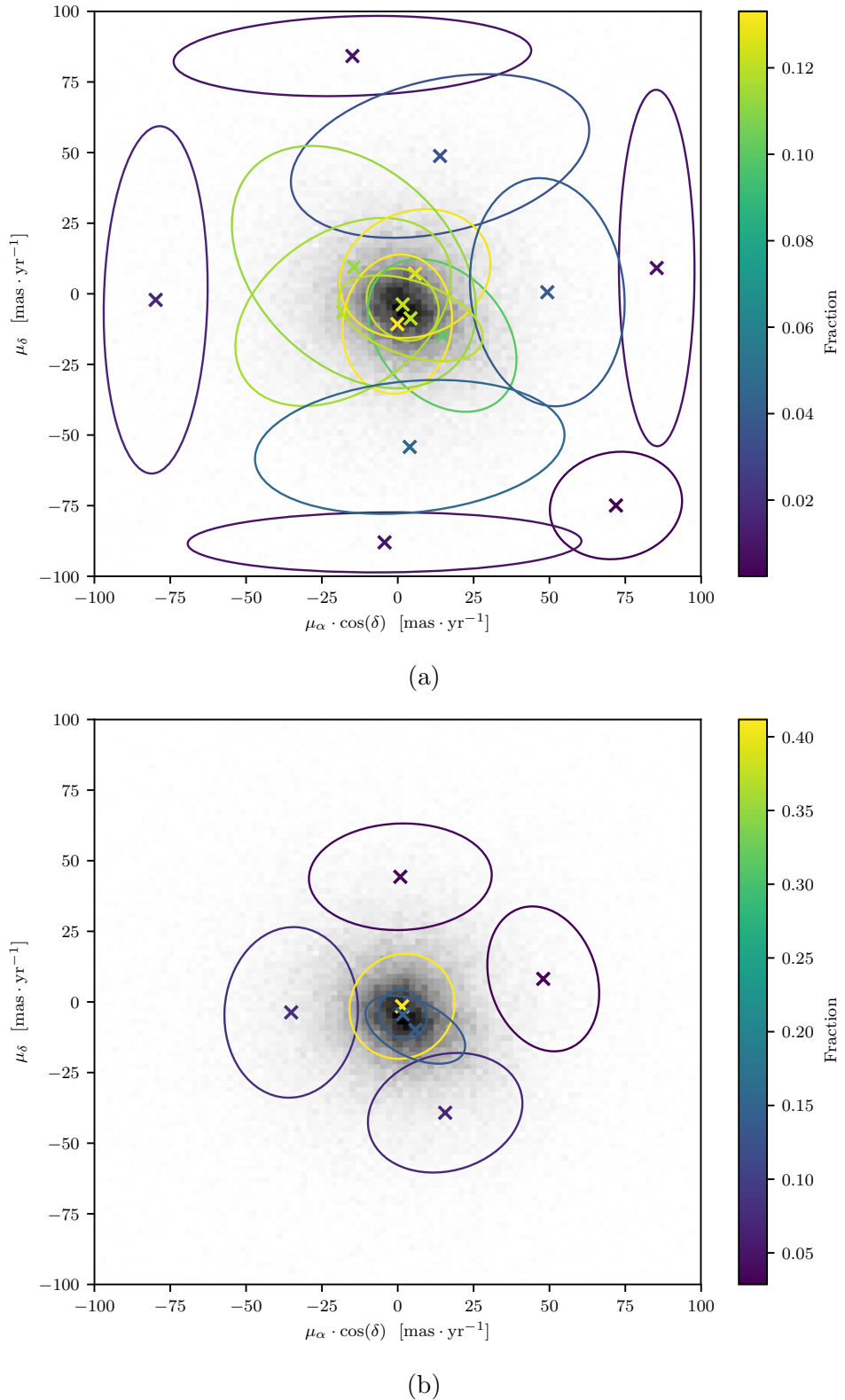


Figure 3.6: Gaussian (a) and Modified (b) Mixture Models fitted to the proper motions of the field objects in the RDDR2 data set (density in grey scale). The crosses and ellipses indicate the means and the one- σ covariance matrices, respectively. The colour code indicates the value of the fraction in the mixture. Uniform distribution not shown in (b). The ellipses in Fig. 4.23 show the Modified Mixture Model of this figure.

3.3.4 The cluster population

Similarly to what I assume for the field population model, I also assume that the cluster model or likelihood can be factorised into the product of the proper motions distribution times the photometric distribution. Thus, I assume these two models are independent.

It is known that unresolved systems of stars (groups of stars that, given the spatial resolution of the telescope, are seen as an individual object) have an increased brightness proportional to the multiplicity of the system. In particular, if an unresolved system is made of two equally luminous objects, then its magnitude is 0.752 times brighter than that of an individual object. This happens for equal mass binaries.

Since the pioneer work of [Trumpler \(1921\)](#), we know that some of the Pleiades members are double systems. Recently, [Sarro et al. \(2014\)](#) show evidence that some of these double systems lie in an EMB sequence. Those authors model the EMB sequence assuming that its number of objects is 20% of the total number of cluster members. In the present work, we also model objects in this displaced EMB sequence but we do not assume that its proportion is fixed; we infer it from the data.

Unresolved multiple systems, binary systems particularly, have an impact on the cluster proper motions distribution. In stellar clusters, the massive objects are expected to be preferentially located at the centre of the gravitational potential as a consequence of primordial mass segregation, violent relaxation¹⁵ and/or two-body relaxation¹⁶ ([Parker et al. 2016](#)). Since binaries and multiple systems are typically more massive than the average object, they are expected to be prominently at the cluster centre.

From an astrometric point of view, an unresolved system shifts the photo-centre of its images when compared to that of a single object. Given the previous considerations, we decide to model the EMB as an independent population in the proper motions. Furthermore, we pair this proper motions model to its photometric counterpart. This more comprehensive statistical model allows us to directly compare the kinematic and photometric properties of the EMB population with those of the rest of the cluster.

Furthermore, our model of cluster and EMB also include an intrinsic dispersion of the photometric sequences. This intrinsic dispersion allows to include as candidate members true cluster members that are displaced from the infinitely narrow sequence due to variations in the average properties (e.g. distance). One of these properties is the mass ratio, but notice that due to the degeneracies, we can not disentangle binaries of low mass ratio from single stars that are closer than the average. In a similar way, the sequence of EMB, due to its width, contains also binaries of mass ratio similar to one. However, for the sake of simplicity, in the following whenever I refer to the photometric or proper motions model of the EMBs and stars of mass ratio similar to one, I call it the EMB

¹⁵Violent relaxation changes the stellar energies as a consequence of a gravitational potential that varies in time. However, it is independent of the stellar mass. See p. 380-381 of [Binney & Tremaine \(2008\)](#)

¹⁶Two body relaxation is a process that diffuses the velocity of a star into the system due to cumulative effect of thousands of two-body encounters, see p. 36 of [Binney & Tremaine \(2008\)](#)

sequence model (with the subindex *Bs*). Likewise, whenever I refer to the model of the single stars, which include binaries with mass ratio similar to zero, I call it the cluster sequence or the single star sequence. Despite that this is an abuse of the terminology, it keeps the text more readable.

Photometric model of single and EMB stars

One of the corner stones of stellar physics is the Hertzsprung–Russell diagram (HRD) (Fig. 3.7). On it, the luminosity of stars and brown dwarfs is shown against their temperature. As this diagram exhibits, the luminosities and temperatures of stars and brown dwarfs are heavily correlated and occupy very specific loci. Since the beginning of their life, stars and brown dwarfs start to migrate to a narrow sequence called the main sequence, where they live most of their life times. Later (at roughly the ages shown by the green arrows), they start to migrate off the main sequence, and to the regions of giants, supergiants and white dwarfs. The stellar evolution models, like those of Baraffe et al. (1998); Allard et al. (2013); Allard (2014) provide a physical description about how the properties (e.g. temperature, luminosity) of stars and brown dwarfs evolve along their life time.

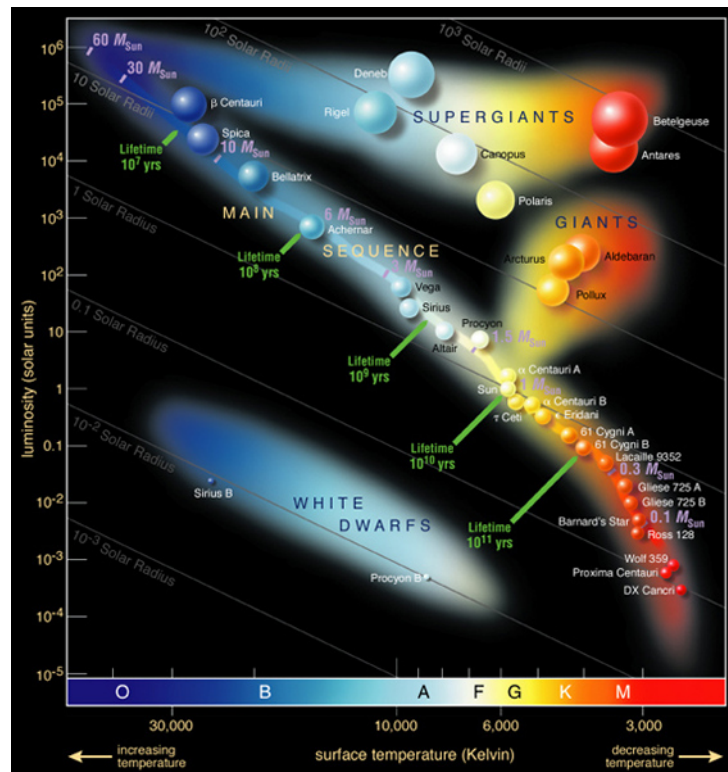


Figure 3.7: Hertzsprung-Russell Diagram identifying many well known stars in the Milky Way galaxy. Image by ESO <https://www.eso.org/public/images/eso0728c/>, CC BY 4.0 <https://commons.wikimedia.org/w/index.php?curid=19915788>

In star clusters, stars and brown dwarfs are born almost simultaneously (although the

birth of the most massive stars might trigger the birth of less massive stars and brown dwarfs), share similar metallicities and are located at similar distances from the observer (assuming that the cluster is smaller compared to the distance to the observer). Thus, the stellar clusters provide the very opportunity to observe, in the space of photometric observables (i.e. apparent magnitudes), the main sequence, which otherwise is blurred by the different ages, metallicities and distances of the objects. Stellar clusters are therefore the very laboratory where the stellar evolutionary models can be tested. Figure 3.8 shows the luminosity L_\odot , in solar units, predicted by the BT-Settl evolutionary models of (Allard 2014) for the Pleiades cluster (120 Myr and solar metalliclicity), as function of the effective temperature T_{eff} . For comparison, Figure 3.8 also shows the K vs. $i - K$ CMD of Bouy et al. (2015) Pleiades candidate members.

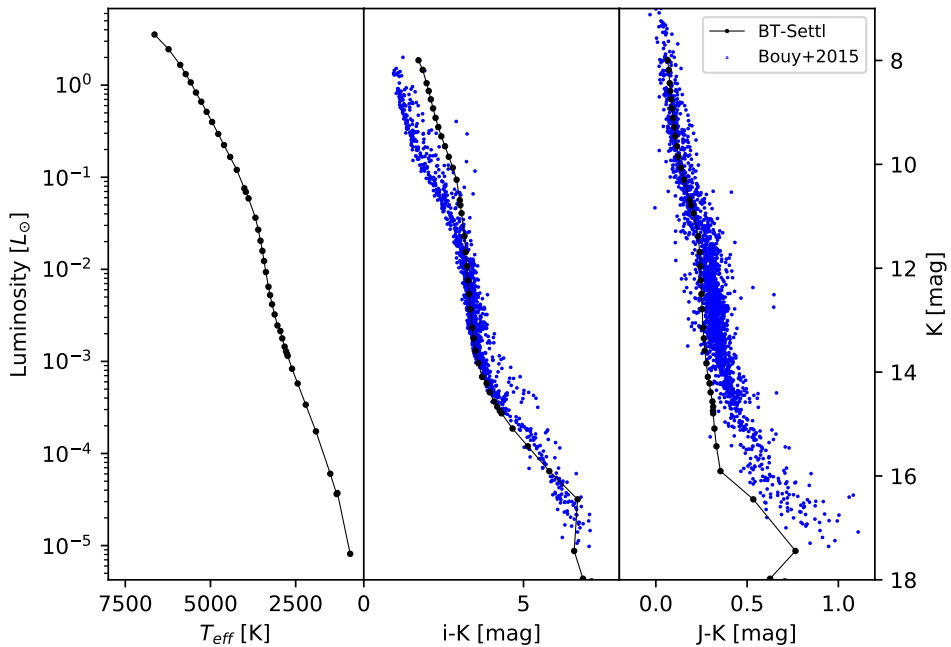


Figure 3.8: HRD (left), K vs. $i - K$ (middle) and K_s vs $J - K_s$ (right) CMDs. The black dots and lines are the Pleiades isochrone given by the BT-Settl models of (Allard 2014). The blue dots are the Pleiades candidate members of Bouy et al. (2015). In the middle panel the i band has been shifted 0.7 mag.

Besides the close and almost deterministic relation between the luminosity of stars and brown dwarfs and its effective temperature, the later also determines the bulk of the spectral energy distribution in which the luminosity is emitted. The stars radiative energy is emitted in a distribution of frequencies (or wavelengths) that roughly corresponds to that of a black body (or grey body with emissivity less than one in absorption lines and larger than one in emission lines). The spectral energy distribution of a black body is parametrised by its temperature by means of Planck's law¹⁷.

¹⁷ Planck's law describes the amount of radiative energy B_λ , that a body of temperature T gives off at

In the ideal model of a star, its luminosity and spectral energy distribution are prescribed by its effective temperature¹⁸ and radius.

Because of the previous reasons, the photometric observables can be roughly¹⁹ estimated as the combined outcome of the radius and effective temperature of stars and brown dwarfs (although the opacity of their atmospheres plays an important part). Given the importance of the effective temperature, it seems reasonable to find proxies for it in the combination of direct observables. If we were to use of the effective temperature (or the mass) of the star as the parameter to model the photometry, its determination would have require the use of a stellar structure model (like the BT-Settl described before). The simple black body approximation is not precise enough. Although the stellar structure models are one of the greatest achievements of modern astrophysics, they still fail to reproduce, at the level of precision required in this work, the observed photometry of low-mass stars and brown dwarfs (see Fig. 3.8, and for example [Bouy et al. 2015](#)). Thus, instead of modelling the photometry by means of a non-observed parameter, we opt to use a combination of observables. Colour indices are good proxies of the effective temperature. Defined as the difference of two photometric bands, they provide a proxy for the slope of the spectral energy distribution and therefore for the effective temperature. However, the quality of the index as an estimator of the effective temperature depends on the value of the latter.

As mentioned by [Bessell et al. \(1998\)](#), the colour index I-K is a good indicator of the effective temperature of M dwarfs. In the light of new theoretical evolutionary models of [Allard \(2014\)](#), I decided to investigate which of the magnitudes or colour indices available in our set of observables provides the best proxy for the effective temperature.

Figure 3.9 shows the effective temperature, given by the 120 Myr isochrone of the BT-Settl models ([Allard 2014](#)), as a function of the absolute magnitudes and colour indices available in our set of observables. As it can be seen, given the typical uncertainty of 0.1 mag in the photometric bands, the Colour Index $i - K_s$ (CI) provides the best estimator of the effective temperature from within the available colour indices.

Therefore, to model the observed photometric bands, we use function and I choose the *true* CI to be the parameter of these functions. As shown in Figures 3.10 and 3.11, this colour allows the most one-to-one relation with the photometric band K_s (this effect is similar for the rest of the bands). This one-to-one relation, which basically enable us to model the magnitudes as functions of the CI, is crucial to avoid degeneracies. Without it, two magnitudes could be described by the same colour index, as it occurs with colour index

each wave length λ . Its formulation is

$$B_\lambda(\lambda, T) = \frac{2hc^2}{\lambda^5} \frac{1}{e^{hc/\lambda k_B T} - 1}$$

where, h , k_B and c are Planck's and Boltzmann's constants and the speed of light, respectively.

¹⁸The definition of effective temperature is that of a black body that yields the same luminosity per surface area as the star

¹⁹This is a very idealised scenario in which the metallicity, variability, magnetic fields, rotation, and other properties have been left aside.

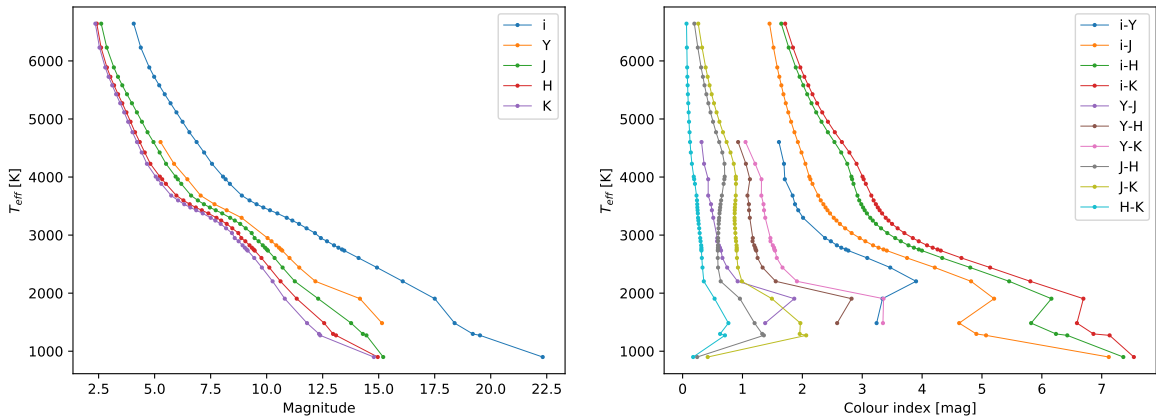


Figure 3.9: Effective temperature as a function of the photometric bands and colour indices within the photometric observables of the RF-2 set. Derived from the BT-Settl models ([Allard 2014](#)) using an age of 120 Myr.

$J - K_s$ at values ~ 0.9 (see right panel of Fig. 3.9 and panel b of Fig. 3.11). Therefore a simple monotonic relation between colour index and magnitude would not be valid, an injective²⁰ function is needed.

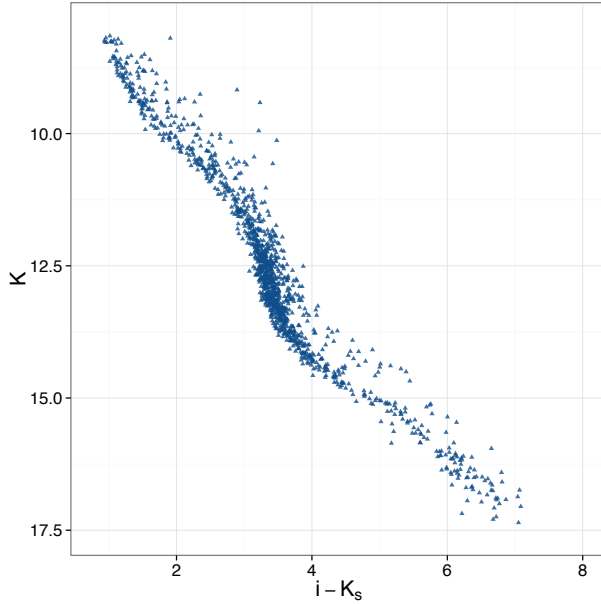


Figure 3.10: K_s vs $i - K_s$ CMD for the Pleiades candidate members of [Bouy et al. \(2015\)](#) with membership probability > 0.75 .

It is important to notice that if a photometric band, like K_s for example, would be used to parametrise the rest of the photometric bands and the CI. Then, the resulting magnitude-magnitude diagrams would provide no information to discriminate between cluster members and field objects.

²⁰An injective function is a one-to-one function that maps each element in its domain to one and only one in its codomain.

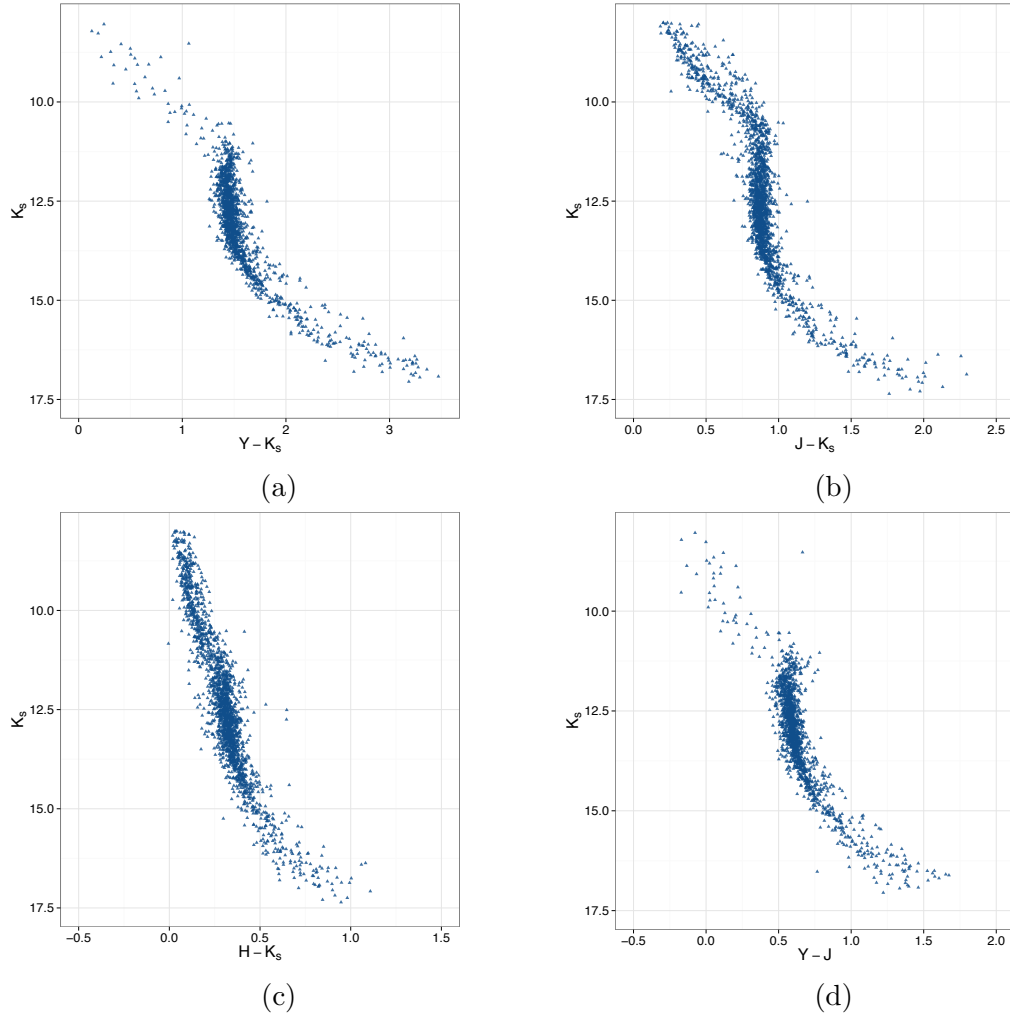


Figure 3.11: CMD for the Pleiades candidate members of [Bouy et al. \(2015\)](#) with membership probability > 0.75 . The magnitude K_s is shown versus the colour indices: $Y - K_s$ (a), $J - K_s$ (b), $H - K_s$ (c), and $Y - J$ (d).

After testing several functions, including the monic, Laguerre, Hermite, and Chebyshev polynomial bases, I decided to use cubic splines to model the cluster photometric sequence. Splines are piece-wise polynomial functions with more flexibility than common polynomial bases. In specific, they provide a better fit of the cluster sequence in region around $CI \sim 3$ where other polynomial bases fail due to the high slope.

Despite their superior flexibility when compared to the tested polynomials bases, spline series require more parameters than the latter. In addition to the coefficients of the series, they need a set of points, within their domain and in non-descending order, which are called knots. These knots represent the starting and ending points of the segments in which each piece of the pice-wise function is defined.

In addition, any spline function can be uniquely represented in terms of Basis-splines (B-splines). By definition, a B-spline of order n is a piece-wise polynomial function of order $n - 1$ in its parameter, in this case the CI. For a given set of knots $\mathbf{t} = \{t_0, t_1, \dots, t_n\}$, there is one and only one B-spline representation of the spline, thus the name Basis-spline

(B-spline). In particular, any cubic spline can be represented as,

$$S_3(CI|\beta, \mathbf{t}) = \sum_i \beta_i \cdot B_{i,3}(CI|\mathbf{t}). \quad (3.32)$$

Where $B_{i,3}$ are the cubic B-splines given by the Cox-de Boor recursive formula, and β are the coefficients of the series. For more details on splines and the Cox-de Boor formula see De Boor (1978).

Despite their fitting properties, B-splines present a problem when simultaneously inferring their coefficients and knots: there is multi-modality in the parametric space (Lindstrom 1999). It means that at least more than one combination of parameters produces the same solution. To avoid this multi-modality, I decided to keep the knots fixed throughout the inference. Although this decision reduces the flexibility of the splines, it allows a still better fit than that of the tested functions (i.e. the polynomial bases). To obtain the MLE of the knots I use the algorithm of Spiriti et al. (2013). This algorithm, implemented in the *freetknotsplines* R package, allows to simultaneously obtain the knots and the best truncation value for the spline series. It uses the BIC to select among competing models. In order to obtain both the truncation of the series and the value of the knots, I use the candidate members of Bouy et al. (2015). The BIC indicates that seven coefficients is the best number of components for the B-splines series, with the knots at $\mathbf{t} = \{0.8, 3.22, 3.22, 5.17, 8.0\}$. I tested different number of knots, ranging from two to nine, with five the best configuration given by the BIC. Figure 3.12 show the spline fits to the RDDR2 candidate members of Bouy et al. (2015), resulting from the previous knots. In this fit, EMBs are excluded (see Section 3.4 for details of how they are removed). The positions of the knots are indicated by vertical lines.

In general, the continuity of a spline function is C^{p-k} , with p the degree of the spline, and k the highest multiplicity of the knots (De Boor 1978). In our case, since the knot at 3.22 has a multiplicity of two, then the resulting spline has lost one degree of continuity. It is now C^1 continuous. It means that the spline and its derivative are continuous, thus ensuring a smooth²¹ function. Furthermore, due to their pice-wise properties, B-splines will enable us to model more complicated photometric sequences in which the turn-off point of the sequence may be present.

As I mentioned in the introduction to this Section, we assume that the observed photometric quantities are drawn from a distribution resulting from the convolution of the observed uncertainties, with the likelihood of the model prescribed by the *true* quantities. We also assume that the model has an intrinsic dispersion that addresses photometric variations resulting from astrophysical phenomena not treated by our model (see Section

²¹In Section 4.6, the B-spline will be used to transform the *true* CI distribution into the magnitude distributions. Since the spline and its derivative are both continuous, no further treatment is needed. If this were not the case, the *true* CI distribution should have to be transformed in the intervals in which the splines and its derivative are both continuous.

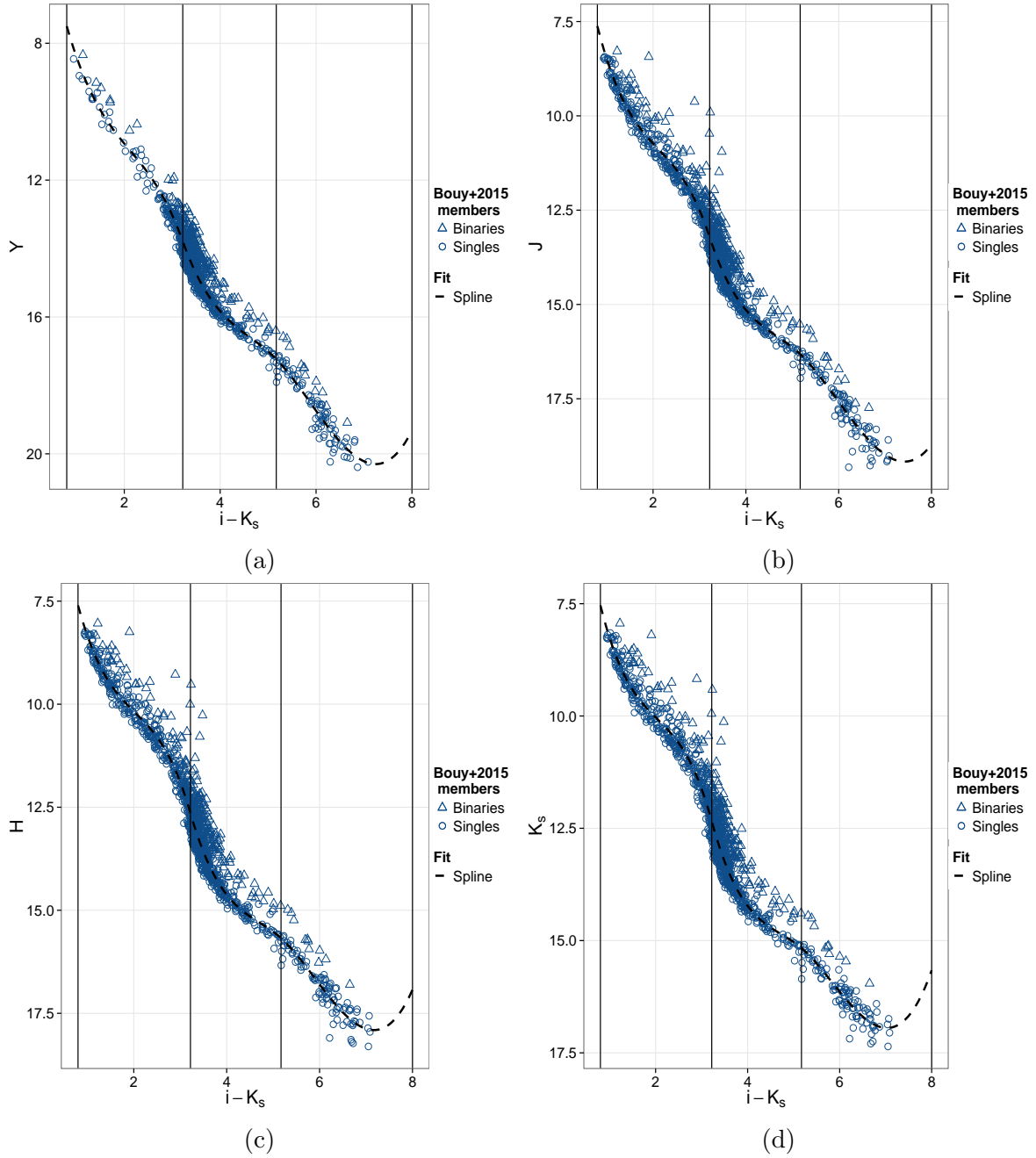


Figure 3.12: Spline fits (dashed lines) to the single stars candidate members of [Bouy et al. \(2015\)](#) (blue circles) resulting from the use of the knots, $\mathbf{t} = \{0.8, 3.22, 3.22, 5.17, 8.0\}$, (vertical lines).

3.1.1). These phenomena include, but are not limited to, age, metallicity and distance dispersions, unresolved systems (other than EMB), variability, and transits. If we were to assume no *true* intrinsic dispersion, then any deviation from the *true* quantities would have to be explained *only* on the basis of the observational uncertainties. Thus it would result in an over-simplistic model, which would underestimate the likelihood of hypothetical true cluster members.

This photometric dispersion shows an skewed distribution (see Figure 2 of [Hillenbrand et al. 2008](#), which I reproduce in Fig. 3.13), which we model with a multivariate Closed

Skewed Normal (CSN) distribution; see for example [González-Farias et al. \(2004\)](#); [Gupta et al. \(2004\)](#). Despite the fact that the CSN requires only five parameters more than a multivariate normal distribution, the computing of its density takes $\sim 50\%$ more Central Processing Unit (CPU) time than that of the multivariate normal distribution. Due to computational constraints, we decided to postpone the results of the CSN until our computational resources allow it.

Instead of using the CSN, we model the intrinsic photometric dispersion of both the cluster and EMB sequences with two multivariate normal distributions, one for the single stars sequence and other for the EMB sequence. Each of them has five dimensions corresponding to our photometric reference set: CI, Y, J, H, K_s . The B-splines model the *true* photometric quantities, both for the cluster sequence, $\mathbf{t}_{ph;Cs}$, and the EMB, $\mathbf{t}_{ph;Bs}$. The latter is displaced 0.75 into the bright side of the cluster sequence. In the following, the matrix Σ_{clus} , represents the covariance matrix of these two multivariate normal distribution. Since we have no reasons to believe that the intrinsic dispersion of EMB and single stars is different, we use only one Σ_{clus} for both of them. By definition, covariance matrices are symmetric and positive semi-definite. Therefore, from the 25 entries in Σ_{clus} , only 15 are unique. These are also inferred from the data set.

Thus, the *true* photometry is given by,

$$\begin{aligned}\mathbf{t}_{ph;Cs} &= \{CI, Y, J, H, K_s\}, \\ \mathbf{t}_{ph;Bs} &= \{CI, Y - 0.75, J - 0.75, H - 0.75, K_s - 0.75\},\end{aligned}$$

where

$$Y = \mathcal{S}_Y(CI, \hat{\beta}_Y), \quad (3.33)$$

$$J = \mathcal{S}_J(CI, \hat{\beta}_J), \quad (3.34)$$

$$H = \mathcal{S}_H(CI, \hat{\beta}_H), \quad (3.35)$$

$$K_s = \mathcal{S}_{K_s}(CI, \hat{\beta}_{K_s}), \quad (3.36)$$

with $\hat{\beta}_i, i \in \{Y, J, H, K_s\}$ the vectors of seven coefficients of the B-splines for the Y, J, H, K_s bands. For the sake of simplicity I denote this 4×7 coefficients matrix as $\boldsymbol{\beta}$.

Since the photometry of the EMB is a linear transformation, T_{Bs} , of the mean *true* photometry of cluster sequence, no extra parameters are required. Therefore,

$$\mathbf{t}_{ph;Cs} = \mathcal{S}(CI, \boldsymbol{\beta}) \quad (3.37)$$

$$\mathbf{t}_{ph;Bs} = T_{Bs}(\mathcal{S}(CI, \boldsymbol{\beta})). \quad (3.38)$$

Thus, cluster and EMB likelihoods of an object with photometric measurements \mathbf{d}_{ph} ,

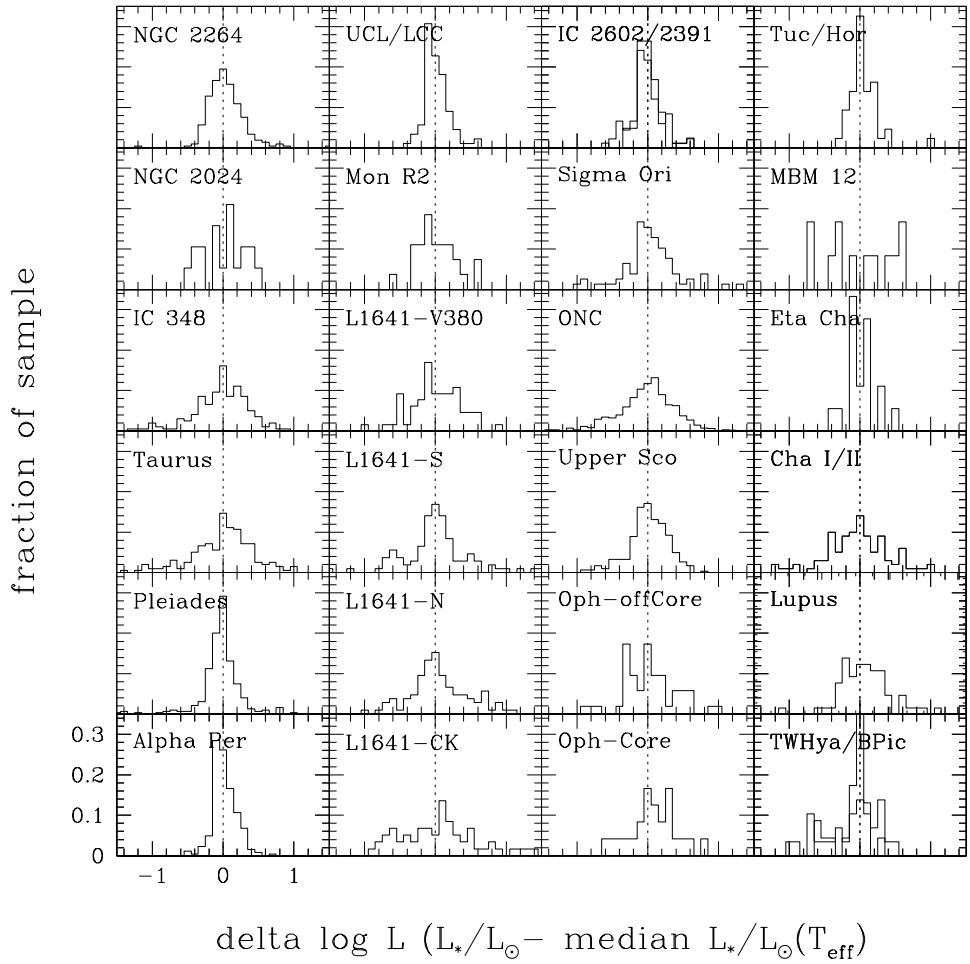


Figure 3.13: Histogram of luminosity dispersion for young clusters. Reproduced from Figure 2 of Hillenbrand et al. (2008), *An Assessment of HR Diagram Constraints on Ages and Age Spreads in Star-Forming Regions and Young Clusters*, Astronomical Society of the Pacific Conference Series, Vol. 384.

and standard uncertainties \mathbf{u}_{ph} , are:

$$\begin{aligned} p_{Cs}(\mathbf{d}_{ph}|CI, \boldsymbol{\beta}, \Sigma_{clus}, \mathbf{u}_{ph}) &= \mathcal{N}(\mathbf{d}_{ph}|\mathbf{t}_{ph;Cs}, \mathbf{u}_{ph} + \Sigma_{clus}), \\ p_{Bs}(\mathbf{d}_{ph}|CI, \boldsymbol{\beta}, \Sigma_{clus}, \mathbf{u}_{ph}) &= \mathcal{N}(\mathbf{d}_{ph}|\mathbf{t}_{ph;Bs}, \mathbf{u}_{ph} + \Sigma_{clus}), \end{aligned} \quad (3.39)$$

where $\mathbf{t}_{ph;Cs}$ and $\mathbf{t}_{ph;Bs}$ are given by Equations 3.37 and 3.38, respectively.

Since the splines are parametrised by the true CI of each object, we have more parameters than objects in our data set ²². This *true* CI is unknown even if its observed value is not missing. We solve this problem (it is a computational problem!) by marginalising these nuisance parameters.

To marginalise these CIs we need a prior, which we provide in a hierarchical way (thus the name Bayesian Hierarchical model). This marginalisation leaves behind a precise

²²Although this sounds crazy, the rules of probability calculus do not discard this possibility.

estimate of the parameters of the prior distribution. Paradoxically, all objects, even those without a measurement of the CI, contribute to this estimate. Here lays the force of the BHM .

We model the prior of the *true* CI as a truncated ($0.8 \leq CI \leq 8$) univariate GMM with five components, whose parameters are also inferred from the data. We choose five components as suggested by the BIC computed from the EM algorithm for GMM applied to the RDDR2 candidate members of Bouy et al. (2015) with observed CIs. I tested larger number of components in the mixture (up to ten), but the posterior distribution did not changed significantly, thus indicating that the BIC value was a proper assumption. **Figure 3.14 shows the fit of this five component univariate GMM to the RDDR2 candidate members of Bouy et al. (2015) with observed CIs.** Notice that these fits are only performed to obtain the best number of components in the GMM.

The GMM modelling the prior of the *true* CI is

$$p(CI|\boldsymbol{\pi}_{CI}, \boldsymbol{\mu}_{CI}, \boldsymbol{\sigma}_{CI}) = \sum_{i=1}^5 \pi_{CI,i} \cdot \mathcal{N}_t(CI|\mu_{CI,i}, \sigma_{CI,i}). \quad (3.40)$$

In this last Equation, the symbol \mathcal{N}_t stands for the truncated ($0.8 < CI < 8$) univariate normal distribution.

Then, the marginalisation of CI runs as follows:

$$\begin{aligned} p_{Cs}(\mathbf{d}_{ph}|\boldsymbol{\theta}_c, \mathbf{u}_{ph}) &= \int p_{Cs}(\mathbf{d}_{ph}, CI|\boldsymbol{\theta}_c, \mathbf{u}_{ph}) \cdot dCI \\ &= \int p_{Cs}(\mathbf{d}_{ph}|CI, \boldsymbol{\theta}_c, \mathbf{u}_{ph}) \cdot p_{Cs}(CI|\boldsymbol{\theta}_c, \mathbf{u}_{ph}) \cdot dCI \end{aligned} \quad (3.41)$$

$$\begin{aligned} p_{Bs}(\mathbf{d}_{ph}|\boldsymbol{\theta}_c, \mathbf{u}_{ph}) &= \int p_{Bs}(\mathbf{d}_{ph}, CI|\boldsymbol{\theta}_c, \mathbf{u}_{ph}) \cdot dCI \\ &= \int p_{Bs}(\mathbf{d}_{ph}|CI, \boldsymbol{\theta}_c, \mathbf{u}_{ph}) \cdot p_{Bs}(CI|\boldsymbol{\theta}_c, \mathbf{u}_{ph}) \cdot dCI. \end{aligned} \quad (3.42)$$

In these Equations, $\boldsymbol{\theta}_c$ stands for all cluster parameters related to photometry, and the first and second terms of the integrals in the last equalities correspond to Equations 3.39 and 3.40, respectively. The distribution of CI depends only on $\boldsymbol{\pi}_{CI}, \boldsymbol{\mu}_{CI}, \boldsymbol{\sigma}_{CI}$, thus, the

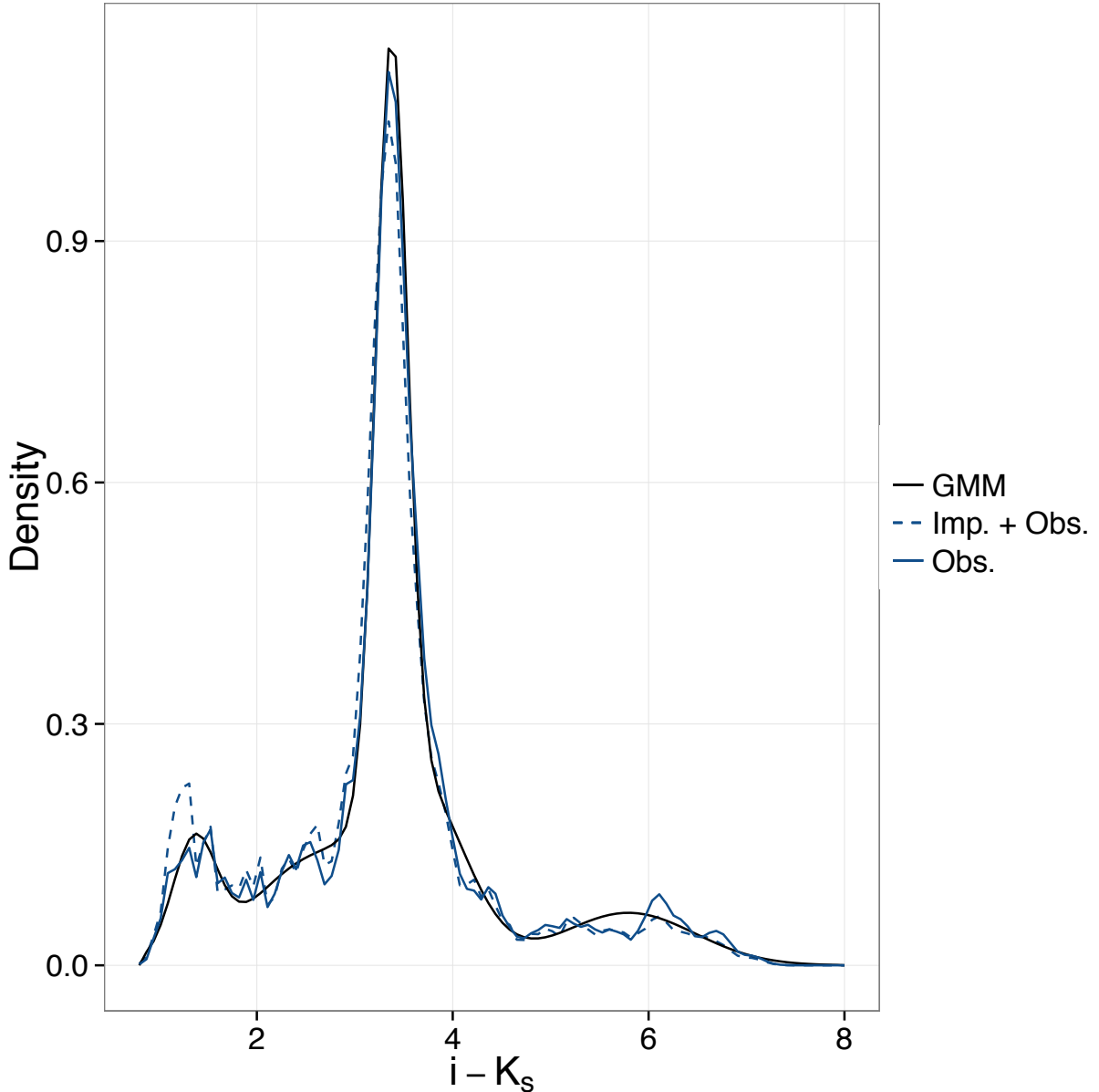


Figure 3.14: Distribution of observed CIs of the candidate members of Bouy et al. (2015) (solid blue line). The uncertainties are taken into account by performing a KDE in which each object kernel is Gaussian with bandwidth equal to its observed uncertainty. Also shown is the five components GMM fitted to this data (solid black line). For the sake of completeness, I also show the distribution of imputed and observed CIs for all candidate members of Bouy et al. (2015) (dashed blue line). Missing CIs where imputed with those of the closest Euclidean neighbour in the five dimensional space.

cluster and equal-mass binaries likelihoods of datum \mathbf{d}_{ph} are

$$\begin{aligned}
 p_{Cs}(\mathbf{d}_{ph} | \boldsymbol{\pi}_{CI}, \boldsymbol{\mu}_{CI}, \boldsymbol{\sigma}_{CI}, \boldsymbol{\beta}, \Sigma_{clus}, \mathbf{u}_{ph}) \\
 = \int \mathcal{N}(\mathbf{d}_{ph} | \mathcal{S}(CI, \boldsymbol{\beta}), \mathbf{u}_{ph} + \Sigma_{clus}) \cdot \sum_{i=1}^5 \pi_{CI,i} \cdot \mathcal{N}_t(CI | \mu_{CI,i}, \sigma_{CI,i}) \cdot dCI \\
 p_{Bs}(\mathbf{d}_{ph} | \boldsymbol{\pi}_{CI}, \boldsymbol{\mu}_{CI}, \boldsymbol{\sigma}_{CI}, \boldsymbol{\beta}, \Sigma_{clus}, \mathbf{u}_{ph}) \\
 = \int \mathcal{N}(\mathbf{d}_{ph} | T_{Bs}(\mathcal{S}(CI, \boldsymbol{\beta})), \mathbf{u}_{ph} + \Sigma_{clus}) \cdot \sum_{i=1}^5 \pi_{CI,i} \cdot \mathcal{N}_t(CI | \mu_{CI,i}, \sigma_{CI,i}) \cdot dCI. \quad (3.43)
 \end{aligned}$$

The observed CI and magnitudes help us to reduce the computing time of the marginalisation integral. We use them to discard regions of the integral in which the argument is almost zero (i.e. far from the measured values). Although we allow the nuisance parameters CIs to have all their possible values, the data, by means of the likelihood, give us information about the distribution of these individual nuisance parameters. To use this information, we proceed as follows. First, we compare the observed photometry to the true one (i.e. the cluster sequence given by the splines). For it we use a grid of 300 points uniformly distributed in the domain of CI ($0.8 < CI < 8$)²³. Then, we find the point, p , of the grid that is closest to the vector of the observed photometry. Distance is computed under the Mahalanobis metric. This metric takes into account the observational uncertainty, \mathbf{u}_{ph} , and the intrinsic dispersion of the cluster sequence, Σ_{clus} . Finally, the limits of the marginalisation integral are defined as those given by a ball of 3.5 Mahalanobis distances around point p . Contributions outside this ball are negligible to the integral ($< 4 \times 10^{-4}$).

Proper motion model of EMB and single stars

As mentioned before, we assume that the cluster population has two subpopulations: single and EMB stars. We model the proper motions of these two subpopulations with independent GMM. If the cluster is virialised (see Chapter 2), we can assume that the distribution of its velocity modulus is almost Maxwellian (Maxwell-Boltzman distribution). Therefore a GMM is a reasonable approximation. Furthermore, in the absence of external forces, a virialised system is expected to have spherical symmetry both in its spatial and velocity distributions. Thus we can safely assume that the gaussians within each GMM are concentric, thus they share the same mean. However we allow independent means for both single and EMB subpopulations. The assumption of spherical symmetry may be a weak one in the presence of the galactic potential. It can perturb the cluster and deviate its spatial and velocity distribution from spherical symmetry. Furthermore, the ellipticity of the spatial distribution, which has been reported to be no-negligible ($\epsilon = 0.17$, according to [Raboud & Mermilliod 1998](#)), can be due to projection effects that further deviate the observed velocity distribution profile from spherical symmetry. Nevertheless, since we model the covariance matrices of the GMM of both single and EMB, as full covariance matrices, any departure from the spherical symmetry in the velocity distribution can still be modelled by the non-diagonal entries of these matrices.

We infer the parameters of these GMMs as part of our Bayesian hierarchical model. However we set a priori the number of gaussians in each GMM. Not doing so will demand a technique in which the model parameters can be augmented. Although such techniques

²³As explained in Section 2.8, if this CI range will have covered that of all the objects in the DDR2 data set, the marginalisation integral would have to be computed over the extended CI range. Therefore, the computing time of the BHM would have also increased proportionally to the number of extra points in this integral.

already exist, they are still under computational development (see [Fan & Sisson 2011](#), for a review of reversible jump MCMC).

Using the EM algorithm for GMM and the proper motions of the RDDR2 candidate members of [Bouy et al. \(2015\)](#), I obtained the MLEs for the GMM likelihoods. I did this for configurations of GMM ranging from one to six components. The BIC (Eq. 3.30) suggested four and two components for the cluster and EMB GMMs, respectively. **Figures 3.15 and 3.16 show the Gaussians fitted, and the marginal densities.** Notice that this fit is only illustrative of the number of components used for these GMMs. Since covariance matrices are always symmetric, only three parameters are needed to fully specify the covariance matrices of these bivariate normal distributions.

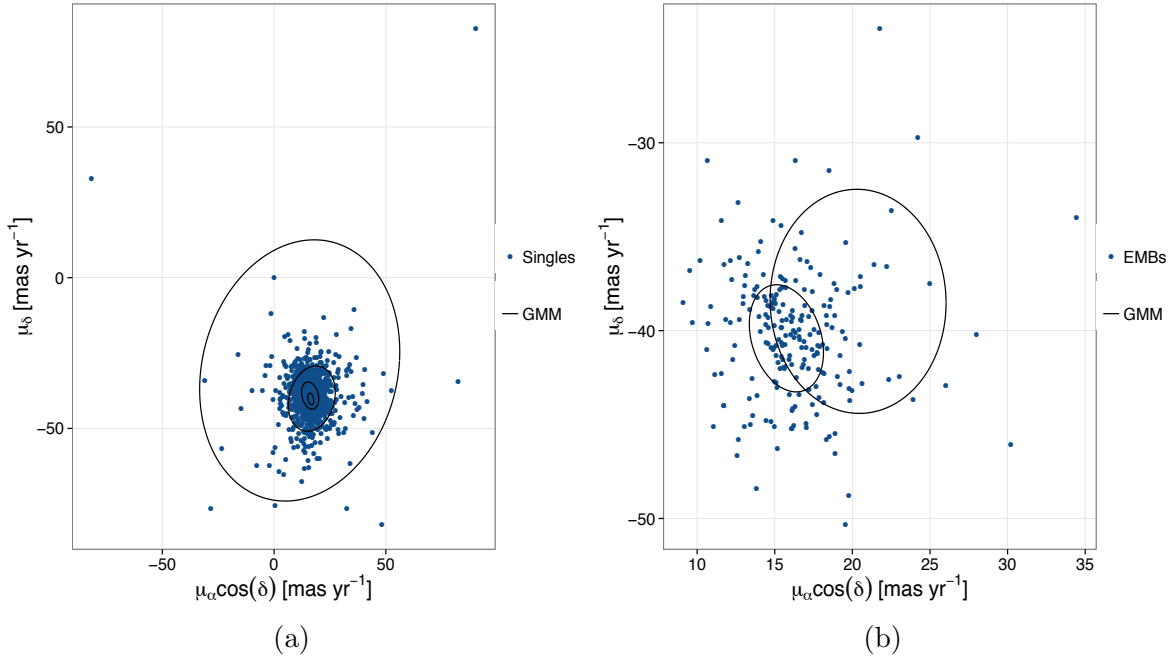


Figure 3.15: Single stars (a) and EMBs (b) members of [Bouy et al. \(2015\)](#) (blue circles) in the RDDR2. Also shown the fitted GMMs with four and two components according to the BIC.

The cluster (subindex C_s) and EMB (subindex B_s) likelihoods of an object with proper motions measurements \mathbf{d}_{pm} , and uncertainties \mathbf{u}_{pm} , are

$$p_{Cs}(\mathbf{d}_{pm} | \boldsymbol{\pi}_{Cs}, \boldsymbol{\mu}_{Cs}, \boldsymbol{\Sigma}_{Cs}, \mathbf{u}_{pm}) = \sum_{i=1}^4 \pi_{Cs,i} \cdot \mathcal{N}(\mathbf{d}_{pm} | \boldsymbol{\mu}_{Cs}, \boldsymbol{\Sigma}_{Cs,i} + \mathbf{u}_{pm}) \quad (3.44)$$

$$p_{Bs}(\mathbf{d}_{pm} | \boldsymbol{\pi}_{Bs}, \boldsymbol{\mu}_{Bs}, \boldsymbol{\Sigma}_{Bs}, \mathbf{u}_{pm}) = \sum_{i=1}^2 \pi_{Bs,i} \cdot \mathcal{N}(\mathbf{d}_{pm} | \boldsymbol{\mu}_{Bs}, \boldsymbol{\Sigma}_{Bs,i} + \mathbf{u}_{pm}). \quad (3.45)$$

Finally, combining the proper motions and photometric models, the total cluster likelihood of an object with measurement \mathbf{d} , and uncertainties \mathbf{u} , is

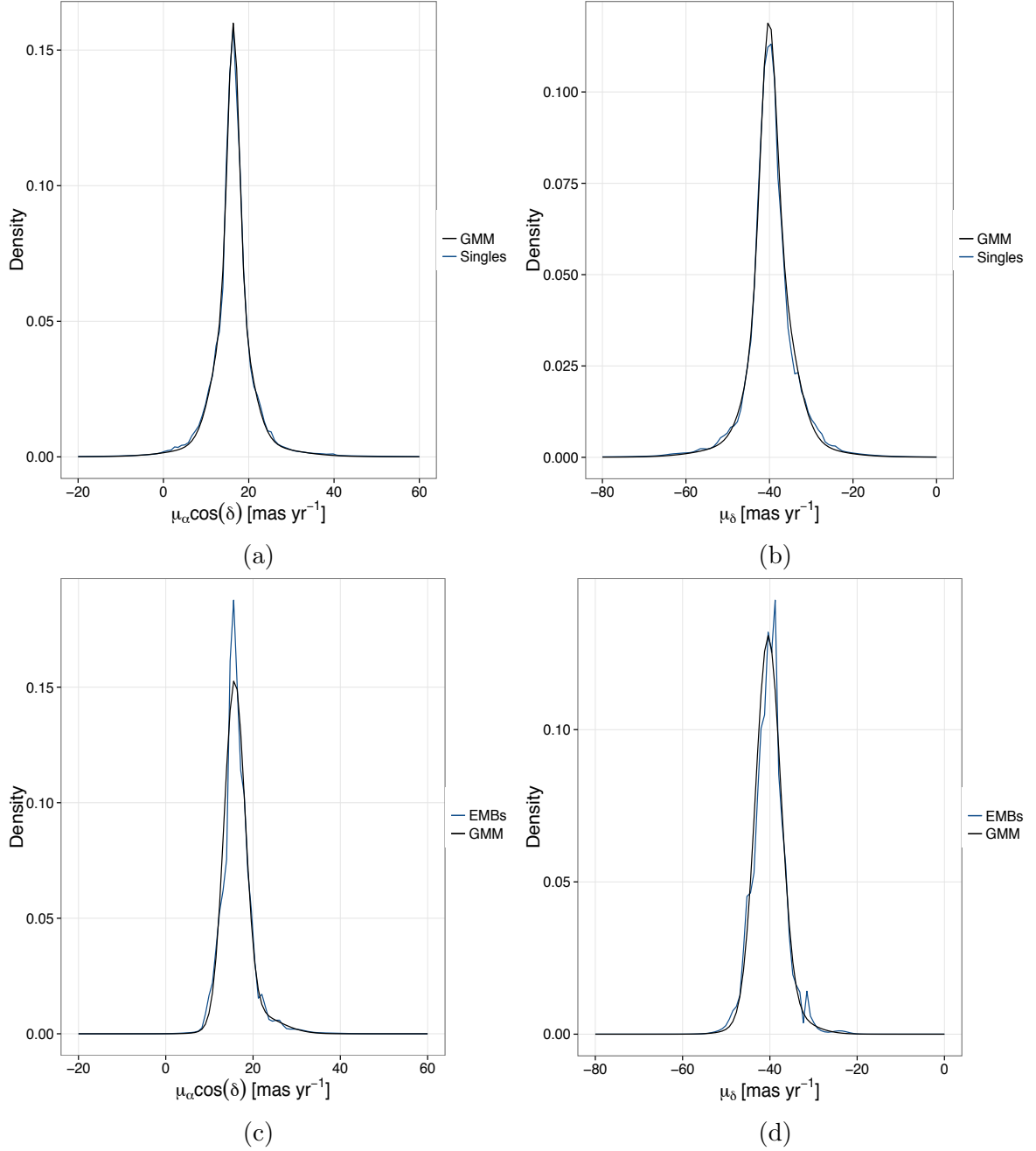


Figure 3.16: Marginal distributions of the single stars (a and b) and EMBs (c and d) candidate members of Bouy et al. (2015) in the RDDR2 (blue lines). The densities result of a KDE with gaussian kernel and bandwidth equal to the individual uncertainties. Also shown the marginal distribution resulting from the fitted GMMs of Fig. 3.15 (black lines).

$$\begin{aligned}
p_c(\mathbf{d}|\boldsymbol{\theta}_c, \mathbf{u}) = & \pi_{CB} \cdot p_{Cs}(\mathbf{d}_{pm}|\boldsymbol{\pi}_{Cs}, \boldsymbol{\mu}_{Cs}, \boldsymbol{\Sigma}_{Cs}, \mathbf{u}_{pm}) \cdot p_{Cs}(\mathbf{d}_{ph}|\boldsymbol{\pi}_{CI}, \boldsymbol{\mu}_{CI}, \boldsymbol{\sigma}_{CI}, \boldsymbol{\beta}, \boldsymbol{\Sigma}_{clus}, \mathbf{u}_{ph}) \\
& + (1 - \pi_{CB}) \cdot p_{Bs}(\mathbf{d}_{pm}|\boldsymbol{\pi}_{Bs}, \boldsymbol{\mu}_{Bs}, \boldsymbol{\Sigma}_{Bs}, \mathbf{u}_{pm}) \cdot p_{Bs}(\mathbf{d}_{ph}|\boldsymbol{\pi}_{CI}, \boldsymbol{\mu}_{CI}, \boldsymbol{\sigma}_{CI}, \boldsymbol{\beta}, \boldsymbol{\Sigma}_{clus}, \mathbf{u}_{ph}),
\end{aligned} \tag{3.46}$$

where π_{CB} is the parameter representing the proportion or fraction of single cluster

sequence stars in the single-EMB mixture model. The photometric and proper motions likelihoods are given by Equations 3.43, and 3.44 and 3.45, respectively.

Before ending this Section, in Table 3.2, I list the groups (proper motions of photometry), symbols, dimensions and meanings of the cluster parameters. Furthermore, Table 3.3 lists all parameters in the BHM (field and cluster) together with their symbols, status (i.e. if they are free or fixed, and the sample from which their values were derived, in case they are fixed), a brief description of their meaning, and the Section and Equation in which they are explained. Finally, Fig. 3.17 gives the graphical representation of the BHM in the form of a PGM.

Table 3.2: Cluster parameters. Listed are the groups, symbols, dimensions and descriptions of the cluster parameters.

Group	Symbol	Dimension	Description
Proper Motions	π_{CB}	2	Fractions of single and EMB stars.
	π_{Cs}	4	Fractions of GMM for the proper motions of single stars.
	μ_{Cs}	2	Mean of GMM for the proper motions of single stars.
	Σ_{Cs}	4×4	Cov. matrices of GMM for the proper motions of single stars.
	π_{Bs}	2	Fractions of GMM for the proper motions of EMB stars.
	μ_{Bs}	2	Mean of GMM for the proper motions of single EMB.
Photometry	Σ_{Bs}	2×4	Cov. matrices of GMM for the proper motions of EMB.
	π_{CI}	5	Fractions of GMM for the <i>true</i> CI.
	μ_{CI}	5	Means of GMM for the <i>true</i> CI.
	σ_{CI}	5	Standard deviations of GMM for the <i>true</i> CI.
	Σ_{clus}	5×5	Cov. matrix representing the intrinsic photometric dispersion.
	$\hat{\beta}_Y$	7	Coefficients of the B-splines for Y band.
	$\hat{\beta}_J$	7	Coefficients of the B-splines for J band.
	$\hat{\beta}_H$	7	Coefficients of the B-splines for H band.
	$\hat{\beta}_{K_s}$	7	Coefficients of the B-splines for K_s band.
	t	5	Knots of the B-splines.

3.4 Priors

The Bayesian formalism is characterised by the use of priors. These represent the objective way to establish the subjective beliefs that the user of the model may have about the distribution of the parameter values. Although the beliefs themselves remain subjective, the way to establish them is measurable and reproducible. For example, by stating that I use a normal distribution as the prior for certain parameter, I provide a measure of my subjective beliefs, its PDF, that others can reproduce.

In the following, I describe the information used to establish both the family of the prior distribution as well as its hyper-parameters (the parameters at the top hierarchy of the BHM). As mentioned before, these families are chosen to fall, whenever possible,

Table 3.3: Parameters of the BHM. Listed are the groups (cluster or field), symbols, status (whether they are free or fixed in the inference process, and the sample from which the fixed ones are derived), a brief description, and a reference to the Section and Equations were they are introduced. See also Tables 3.1 and 3.2 for more details.

Group	Symbol	Status	Description	Section	Equation
Cluster	π	Free	Fraction of field objects in the data.	3.3.2	3.27
	$\boldsymbol{\pi}_{Cs}$	Free	Fractions of GMM for the proper motions of single stars.	3.3.4	3.44
	$\boldsymbol{\mu}_{Cs}$	Free	Mean of GMM for the proper motions of single stars.	3.3.4	3.44
	$\boldsymbol{\Sigma}_{Cs}$	Free	Cov. matrices of GMM for the proper motions of single stars.	3.3.4	3.44
	$\boldsymbol{\pi}_{Bs}$	Free	Fractions of GMM for the proper motions of EMB stars.	3.3.4	3.45
	$\boldsymbol{\mu}_{Bs}$	Free	Mean of GMM for the proper motions of single EMB.	3.3.4	3.45
	$\boldsymbol{\Sigma}_{Bs}$	Free	Cov. matrices of GMM for the proper motions of EMB.	3.3.4	3.45
	$\boldsymbol{\pi}_{CI}$	Free	Fractions of GMM for the <i>true</i> CI.	3.3.4	3.40
	$\boldsymbol{\mu}_{CI}$	Free	Means of GMM for the <i>true</i> CI.	3.3.4	3.40
	$\boldsymbol{\sigma}_{CI}$	Free	Standard deviations of GMM for the <i>true</i> CI.	3.3.4	3.40
	$\boldsymbol{\Sigma}_{dus}$	Free	Cov. matrix representing the intrinsic photometric dispersion.	3.3.4	3.39,3.43
	$\hat{\beta}_Y$	Free	Coefficients of the B-splines for Y band.	3.3.4	3.33
	$\hat{\beta}_J$	Free	Coefficients of the B-splines for J band.	3.3.4	3.34
	$\hat{\beta}_H$	Free	Coefficients of the B-splines for H band.	3.3.4	3.35
	$\hat{\beta}_{K_s}$	Free	Coefficients of the B-splines for K_s band.	3.3.4	3.36
	\mathbf{t}	Fixed ^a	Knots of the B-splines.	3.3.4	3.32
Field	$\pi_{f,pm,0}$	Fixed ^b	Fraction of the uniform distribution	3.3.3	3.31
	S_{μ_α}	Fixed ^b	Support of the uniform distribution in R.A	3.3.3	3.31
	S_{μ_δ}	Fixed ^b	Support of the uniform distribution in Dec.	3.3.3	3.31
	$\boldsymbol{\pi}_{f,pm}$	Fixed ^b	Fractions of GMM of field proper motions	3.3.3	3.31
	$\boldsymbol{\mu}_{f,pm}$	Fixed ^b	Means of GMM of field proper motions	3.3.3	3.31
	$\boldsymbol{\Sigma}_{f,pm}$	Fixed ^b	Cov. matrices of GMM of field proper motions	3.3.3	3.31
	$\boldsymbol{\pi}_{f,ph}$	Fixed ^b	Fractions of GMM of field photometry	3.3.3	3.31
	$\boldsymbol{\mu}_{f,ph}$	Fixed ^b	Means of GMM of field photometry	3.3.3	3.31
	$\boldsymbol{\Sigma}_{f,ph}$	Fixed ^b	Cov. matrices of GMM of field photometry	3.3.3	3.31

^aDerived from objects in the RDDR2 (Sect. 2.8) with probability $p > 0.75$ according to Bouy et al. (2015).

^bDerived from objects in the RDDR2 (Sect. 2.8) with probability $p < 0.75$ according to Bouy et al. (2015).

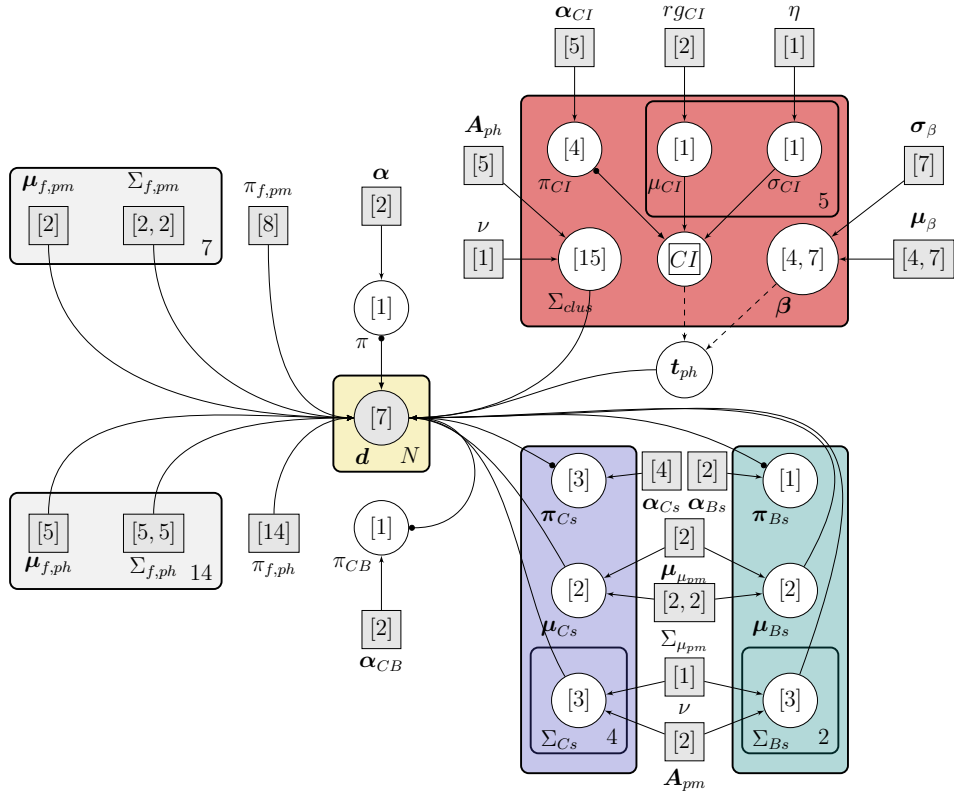


Figure 3.17: Probabilistic graphical model representing the BHM . The left grey plates show the field model. The middle yellow plate shows the node where the likelihood is computed for each datum, \mathbf{d} . The right plates describe the relations among parameters in the cluster model. The photometric cluster model (red) is on top, while the proper motions cluster (blue) and equal-mass binaries (green) are at the bottom left and right, respectively. See Section 3.2.3 for more details. Reproduced from Figure 19 of Olivares et al. (2017), *The Seven sisters DANCE III: Hierarchical Bayesian model*, A&A, Vol. submitted.

in the category of weakly informative priors. **All the free parameters of the BHM together together with their priors and symbols are listed in Table 3.4.**

The priors in the BHM can be grouped into three main categories. The first one correspond to priors for parameters representing fractions in mixture models. The second and third categories correspond to parameters in the proper motions and photometric models.

In the BHM, there are different types of mixtures: the GMMs of the proper motions, the cluster-field mixture, and the singles-EMB mixture. At each mixture, the fractions quantify the contribution of each element in the mixture to the probability distribution. Fractions must add to one and be bounded by the $[0, 1]$ interval. We choose the Dirichlet distribution to be the family of all fraction parameters. This decision roots in the fact that this distribution is the multivariate generalisation of the beta distribution. The latter is commonly used to model the probability of success of an event.

The Dirichlet distribution, $Dir(\mathbf{x}|\boldsymbol{\alpha})$, of dimension n ($\{\mathbf{x}, \boldsymbol{\alpha}\} \subset \mathcal{R}^n$) has support in $[0, 1]$ for each entry x_k of \mathbf{x} , and is parametrised by $\boldsymbol{\alpha}$. Each α_k gives the concentration of

Table 3.4: Parameters names, symbols, and priors.

Name	Symbol	Prior	Name	Symbol	Prior
Field fraction	π	Dirichlet(α)	Coefficient [1,1]	$\beta_{Y,1}$	Normal(μ_β, σ_β)
Cs fraction	π_{CB}	Dirichlet(α_{Cs})	Coefficient [1,2]	$\beta_{Y,2}$	Normal(μ_β, σ_β)
Cs PM fraction 1	$\pi_{Cs,1}$	Dirichlet(α_{Cs})	Coefficient [1,3]	$\beta_{Y,3}$	Normal(μ_β, σ_β)
Cs PM fraction 2	$\pi_{Cs,2}$	Dirichlet(α_{Cs})	Coefficient [1,4]	$\beta_{Y,4}$	Normal(μ_β, σ_β)
Cs PM fraction 3	$\pi_{Cs,3}$	Dirichlet(α_{Cs})	Coefficient [1,5]	$\beta_{Y,5}$	Normal(μ_β, σ_β)
Bs PM fraction 1	$\pi_{Bs,1}$	Dirichlet(α_{Bs})	Coefficient [1,6]	$\beta_{Y,6}$	Normal(μ_β, σ_β)
Color fraction 1	$\pi_{CI,1}$	Dirichlet(α_{CI})	Coefficient [1,7]	$\beta_{Y,7}$	Normal(μ_β, σ_β)
Color fraction 2	$\pi_{CI,2}$	Dirichlet(α_{CI})	Coefficient [2,1]	$\beta_{J,1}$	Normal(μ_β, σ_β)
Color fraction 3	$\pi_{CI,3}$	Dirichlet(α_{CI})	Coefficient [2,2]	$\beta_{J,2}$	Normal(μ_β, σ_β)
Color fraction 4	$\pi_{CI,4}$	Dirichlet(α_{CI})	Coefficient [2,3]	$\beta_{J,3}$	Normal(μ_β, σ_β)
Mean color 1	$\mu_{CI,1}$	Unifrom(rg_{CI})	Coefficient [2,4]	$\beta_{J,4}$	Normal(μ_β, σ_β)
Mean color 2	$\mu_{CI,2}$	Unifrom(rg_{CI})	Coefficient [2,5]	$\beta_{J,5}$	Normal(μ_β, σ_β)
Mean color 3	$\mu_{CI,3}$	Unifrom(rg_{CI})	Coefficient [2,6]	$\beta_{J,6}$	Normal(μ_β, σ_β)
Mean color 4	$\mu_{CI,4}$	Unifrom(rg_{CI})	Coefficient [2,7]	$\beta_{J,7}$	Normal(μ_β, σ_β)
Mean color 5	$\mu_{CI,5}$	Unifrom(rg_{CI})	Coefficient [3,1]	$\beta_{H,1}$	Normal(μ_β, σ_β)
Variance color 1	$\sigma_{CI,1}$	HalfCauchy(0, η)	Coefficient [3,2]	$\beta_{H,2}$	Normal(μ_β, σ_β)
Variance color 2	$\sigma_{CI,2}$	HalfCauchy(0, η)	Coefficient [3,3]	$\beta_{H,3}$	Normal(μ_β, σ_β)
Variance color 3	$\sigma_{CI,3}$	HalfCauchy(0, η)	Coefficient [3,4]	$\beta_{H,4}$	Normal(μ_β, σ_β)
Variance color 4	$\sigma_{CI,4}$	HalfCauchy(0, η)	Coefficient [3,5]	$\beta_{H,5}$	Normal(μ_β, σ_β)
Variance color 5	$\sigma_{CI,5}$	HalfCauchy(0, η)	Coefficient [3,6]	$\beta_{H,6}$	Normal(μ_β, σ_β)
Mean PM Cs[1,1]	$\mu_{Cs,1}$	Normal($\mu_{\mu_{pm}}, \Sigma_{\mu_{pm}}$)	Coefficient [3,7]	$\beta_{H,7}$	Normal(μ_β, σ_β)
Mean PM Cs[1,2]	$\mu_{Cs,2}$	Normal($\mu_{\mu_{pm}}, \Sigma_{\mu_{pm}}$)	Coefficient [4,1]	$\beta_{K,1}$	Normal(μ_β, σ_β)
Variance Cs[1,1]	$\Sigma_{Cs,1,1}$	Half-t(ν, A_{pm})	Coefficient [4,2]	$\beta_{K,2}$	Normal(μ_β, σ_β)
Variance Cs[1,2]	$\Sigma_{Cs,1,2}$	Half-t(ν, A_{pm})	Coefficient [4,3]	$\beta_{K,3}$	Normal(μ_β, σ_β)
Variance Cs[1,3]	$\Sigma_{Cs,1,3}$	Half-t(ν, A_{pm})	Coefficient [4,4]	$\beta_{K,4}$	Normal(μ_β, σ_β)
Variance Cs[2,1]	$\Sigma_{Cs,2,1}$	Half-t(ν, A_{pm})	Coefficient [4,5]	$\beta_{K,5}$	Normal(μ_β, σ_β)
Variance Cs[2,2]	$\Sigma_{Cs,2,2}$	Half-t(ν, A_{pm})	Coefficient [4,6]	$\beta_{K,6}$	Normal(μ_β, σ_β)
Variance Cs[2,3]	$\Sigma_{Cs,2,3}$	Half-t(ν, A_{pm})	Coefficient [4,7]	$\beta_{K,7}$	Normal(μ_β, σ_β)
Variance Cs[3,1]	$\Sigma_{Cs,3,1}$	Half-t(ν, A_{pm})	Covariance Phot[1]	$\Sigma_{clus}[1]$	Half-t(ν, A_{ph})
Variance Cs[3,2]	$\Sigma_{Cs,3,2}$	Half-t(ν, A_{pm})	Covariance Phot[2]	$\Sigma_{clus}[2]$	Half-t(ν, A_{ph})
Variance Cs[3,3]	$\Sigma_{Cs,3,3}$	Half-t(ν, A_{pm})	Covariance Phot[3]	$\Sigma_{clus}[3]$	Half-t(ν, A_{ph})
Variance Cs[4,1]	$\Sigma_{Cs,4,1}$	Half-t(ν, A_{pm})	Covariance Phot[4]	$\Sigma_{clus}[4]$	Half-t(ν, A_{ph})
Variance Cs[4,2]	$\Sigma_{Cs,4,2}$	Half-t(ν, A_{pm})	Covariance Phot[5]	$\Sigma_{clus}[5]$	Half-t(ν, A_{ph})
Variance Cs[4,3]	$\Sigma_{Cs,4,3}$	Half-t(ν, A_{pm})	Covariance Phot[6]	$\Sigma_{clus}[6]$	Half-t(ν, A_{ph})
Mean PM Bs[1,1]	$\mu_{Bs,1}$	Normal($\mu_{\mu_{pm}}, \Sigma_{\mu_{pm}}$)	Covariance Phot[7]	$\Sigma_{clus}[7]$	Half-t(ν, A_{ph})
Mean PM Bs[1,2]	$\mu_{Bs,2}$	Normal($\mu_{\mu_{pm}}, \Sigma_{\mu_{pm}}$)	Covariance Phot[8]	$\Sigma_{clus}[8]$	Half-t(ν, A_{ph})
Variance Bs[1,1]	$\Sigma_{Bs,1,1}$	Half-t(ν, A_{pm})	Covariance Phot[9]	$\Sigma_{clus}[9]$	Half-t(ν, A_{ph})
Variance Bs[1,2]	$\Sigma_{Bs,1,2}$	Half-t(ν, A_{pm})	Covariance Phot[10]	$\Sigma_{clus}[10]$	Half-t(ν, A_{ph})
Variance Bs[1,3]	$\Sigma_{Bs,1,3}$	Half-t(ν, A_{pm})	Covariance Phot[11]	$\Sigma_{clus}[11]$	Half-t(ν, A_{ph})
Variance Bs[2,1]	$\Sigma_{Bs,2,1}$	Half-t(ν, A_{pm})	Covariance Phot[12]	$\Sigma_{clus}[12]$	Half-t(ν, A_{ph})
Variance Bs[2,2]	$\Sigma_{Bs,2,2}$	Half-t(ν, A_{pm})	Covariance Phot[13]	$\Sigma_{clus}[13]$	Half-t(ν, A_{ph})
Variance Bs[2,3]	$\Sigma_{Bs,2,3}$	Half-t(ν, A_{pm})	Covariance Phot[14]	$\Sigma_{clus}[14]$	Half-t(ν, A_{ph})
			Covariance Phot[15]	$\Sigma_{clus}[15]$	Half-t(ν, A_{ph})

the resulting PDF for entry x_k . The means and variances of these latter are given by,

$$E[x_k] = \frac{\alpha_k}{\sum_k \alpha_k}, \quad (3.47)$$

$$Var[x_k] = \frac{-\alpha_k \cdot (\alpha_k - \sum_k \alpha_k)}{(\sum_k \alpha_k)^2 \cdot (1 + \sum_k \alpha_k)}. \quad (3.48)$$

For the field-cluster mixture we set the hyper-parameters to $\boldsymbol{\alpha} = \{98, 2\}$. We expect a mean 98% of field objects and a 2% of cluster objects with little variance. These figures correspond to the existing prior knowledge, that is the fraction of field and cluster candidate members of [Bouy et al. \(2015\)](#) contained in the RDDR2. For the single-EMB mixture we use an hyper-parameter value, $\boldsymbol{\alpha}_{CB} = \{8, 2\}$. We expect a mean 20% of EMB, as suggested by [Bouy et al. \(2015\)](#). For fractions in the proper motions GMM, hyper-parameter are $\boldsymbol{\alpha}_{Cs} = \{1, 1, 5, 5\}$ and $\boldsymbol{\alpha}_{Bs} = \{1.2, 8.8\}$. These values induce fraction distributions whose means are similar to the fractions recovered after fitting a GMM to the candidate members of [Bouy et al. \(2015\)](#) (**see Fig. 3.15 and 3.16**). For the fraction in the GMM of the CI distribution, the hyper-parameter were set all to 1, ($\boldsymbol{\alpha}_{CI} = \{1, 1, 1, 1, 1\}$), which results in equal means and large variances for all components in the mixture.

In the previous cases, with exception of the cluster-field mixture, the hyper parameters are chosen so that the resulting fraction distributions have large variances, see Fig.3.18. The narrow variance in the cluster-field mixture expresses our prior belief about the number (fraction) of candidate members within our large RDDR2 data set.

For the priors of the means in the proper motions GMM, both of single stars and EMB, we choose the bivariate normal distribution. We set the hyper-parameters of this bivariate normal to those found after fitting a bivariate normal to the proper motions of the candidate members of [Bouy et al. \(2015\)](#) in the RDDR2. **Figure 3.19 shows the proper motions of these objects and the fitted Gaussian. The parameters of the latter are**

$$\boldsymbol{\mu}_{\mu_{pm}} = (16.30, -39.62) \text{ mas} \cdot \text{yr}^{-1},$$

and

$$\Sigma_{\mu_{pm}} = \begin{pmatrix} 36.84 & 1.18 \\ 1.18 & 40.71 \end{pmatrix} \text{ mas}^2 \cdot \text{yr}^{-2}.$$

As prior for the covariance matrices of both single stars and EMB proper motions we use the Half- $t(\nu, \mathbf{A})$ distribution. It is parametrised by a scalar ν and a vector \mathbf{A} . As shown by [Huang & Wand \(2013\)](#), this distribution family leads to more accurate estimations of covariance matrices than the traditional Inverse-Wishart distribution. In specific, the marginal correlation parameters, ρ , have the following distribution,

$$p(\rho) \propto (1 - \rho^2)^{\frac{\nu}{2} - 1}. \quad (3.49)$$

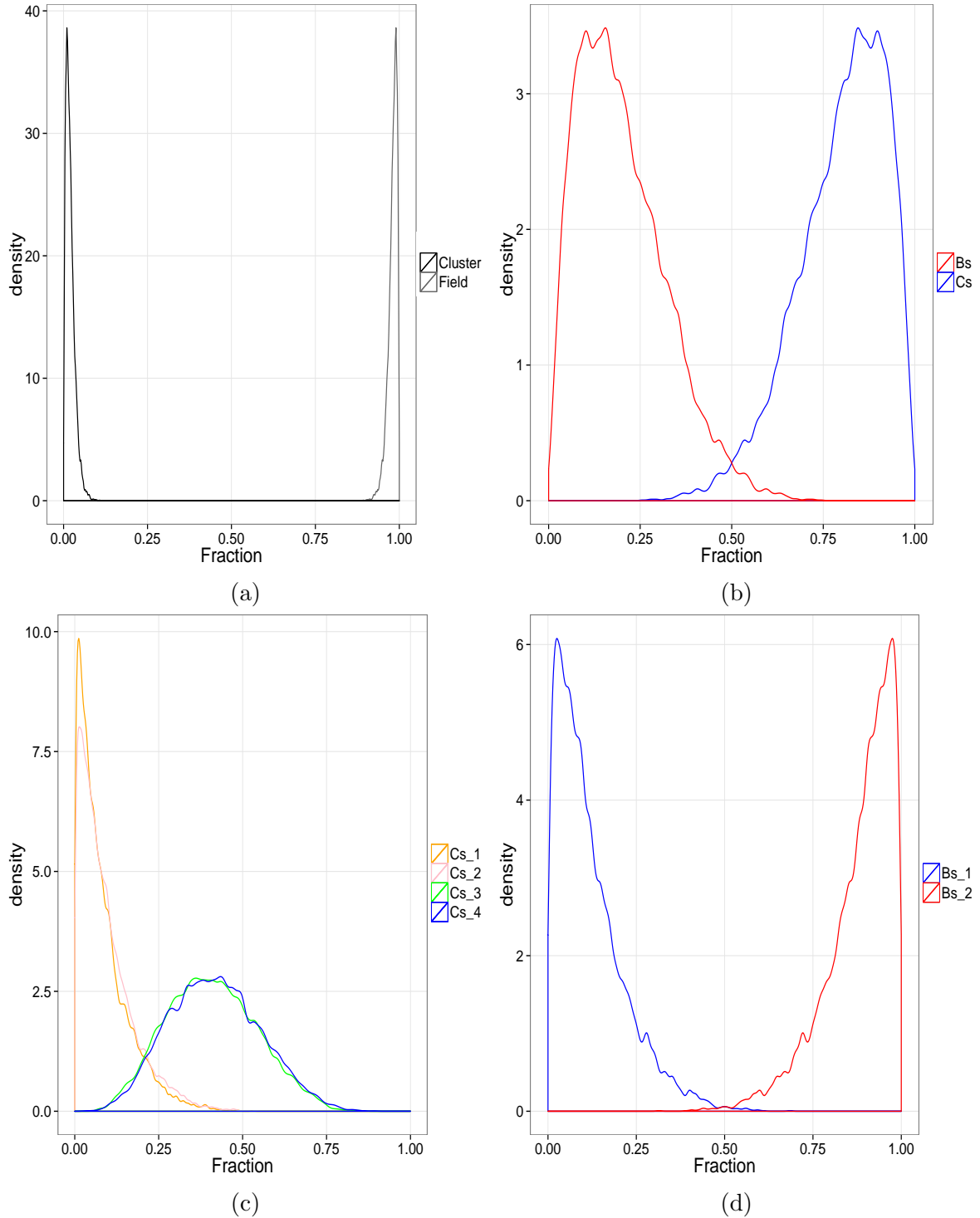


Figure 3.18: KDE of 10⁴ realisations of the prior distributions of fraction parameters. Distributions of: (a) The field fraction π , (b) The EMB fraction, $1 - \pi_{CB}$, (c) the proper motions cluster fractions, π_{Cs} , and (d) the proper motions equal-mass binaries fractions π_{Bs} .

The standard deviation term σ_k , associated to entry k , is distributed according to Half- $t(\nu, A_k)$. We set the hyper-parameters to $\nu = 3$ and $A_{pm} = \{10^5, 10^5\} \text{ mas} \cdot \text{yr}^{-1}$. According to Huang & Wand (2013), arbitrarily large values of A lead to arbitrarily weakly informative priors on the corresponding standard deviation terms.

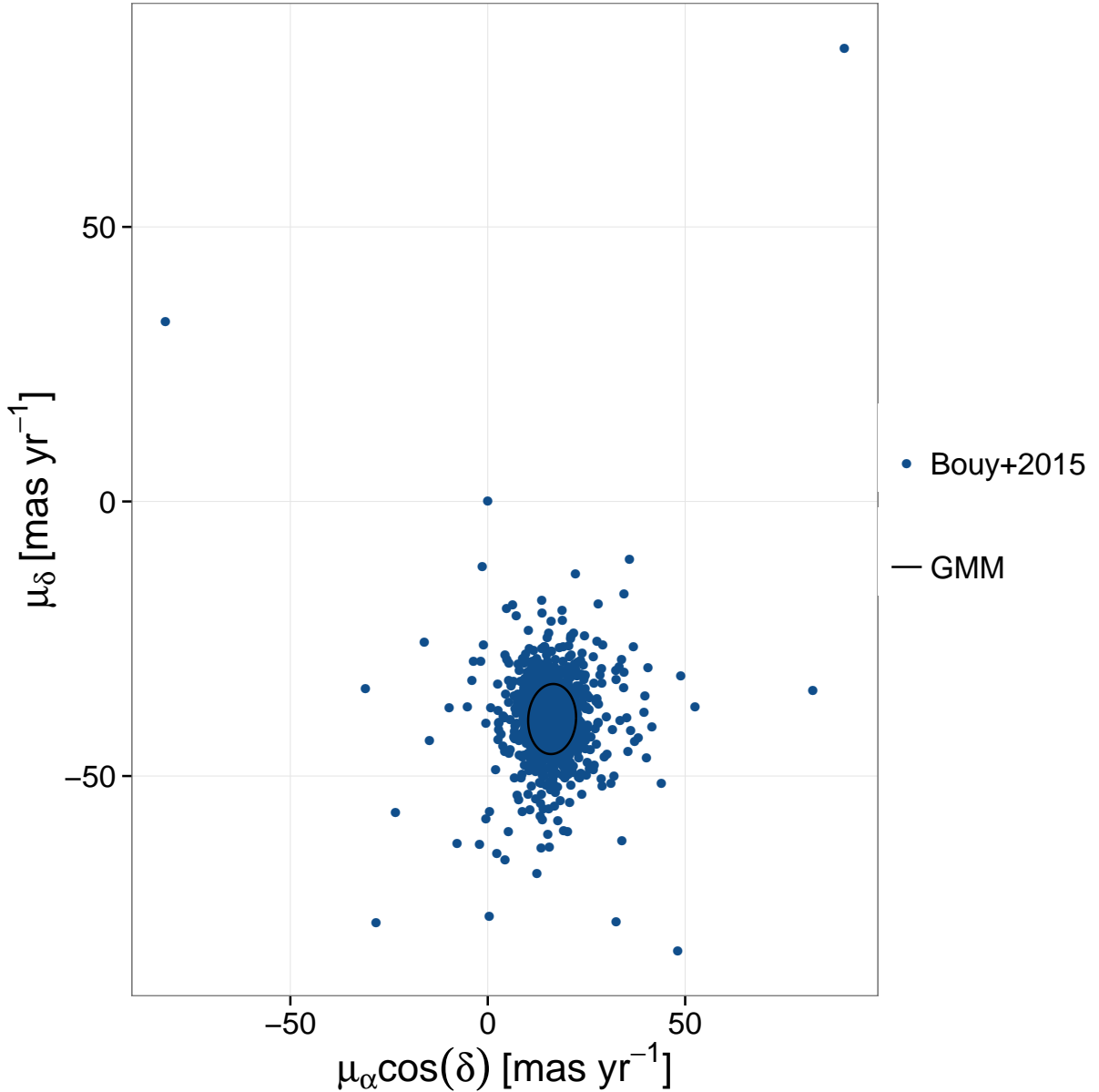


Figure 3.19: Proper motions of the candidate members of [Bouy et al. \(2015\)](#) in the RDDR2 (blue dots), and fitted Gaussian (black line).

Concerning the photometric priors, they can be grouped in three categories: (i) priors for the the *true* CI, (ii) priors for the splines coefficients, and (iii) priors for the cluster sequence intrinsic dispersion.

For the means in the univariate GMM of the *true* CI, I choose a uniform distribution in the range $(0.8 \leq CI \leq 8)$. For the standard deviations I choose the Half-Cauchy($0, \eta$) distribution as suggested by [Gelman \(2006\)](#). The value of η is set to an arbitrarily large value, $\eta = 100$. Figure 3.20 shows the KDE of 10^3 realisations from the prior distributions for the fractions, means, and variances of the parameters in the *true* CI GMM. Additonally, the lower right panel of this Fig. shows the resulting prior in the CI space. Notice that values in this latter panel are truncated in the range of the observed CI.

For the coefficients in the spline series we set the priors as univariate normal distributions.

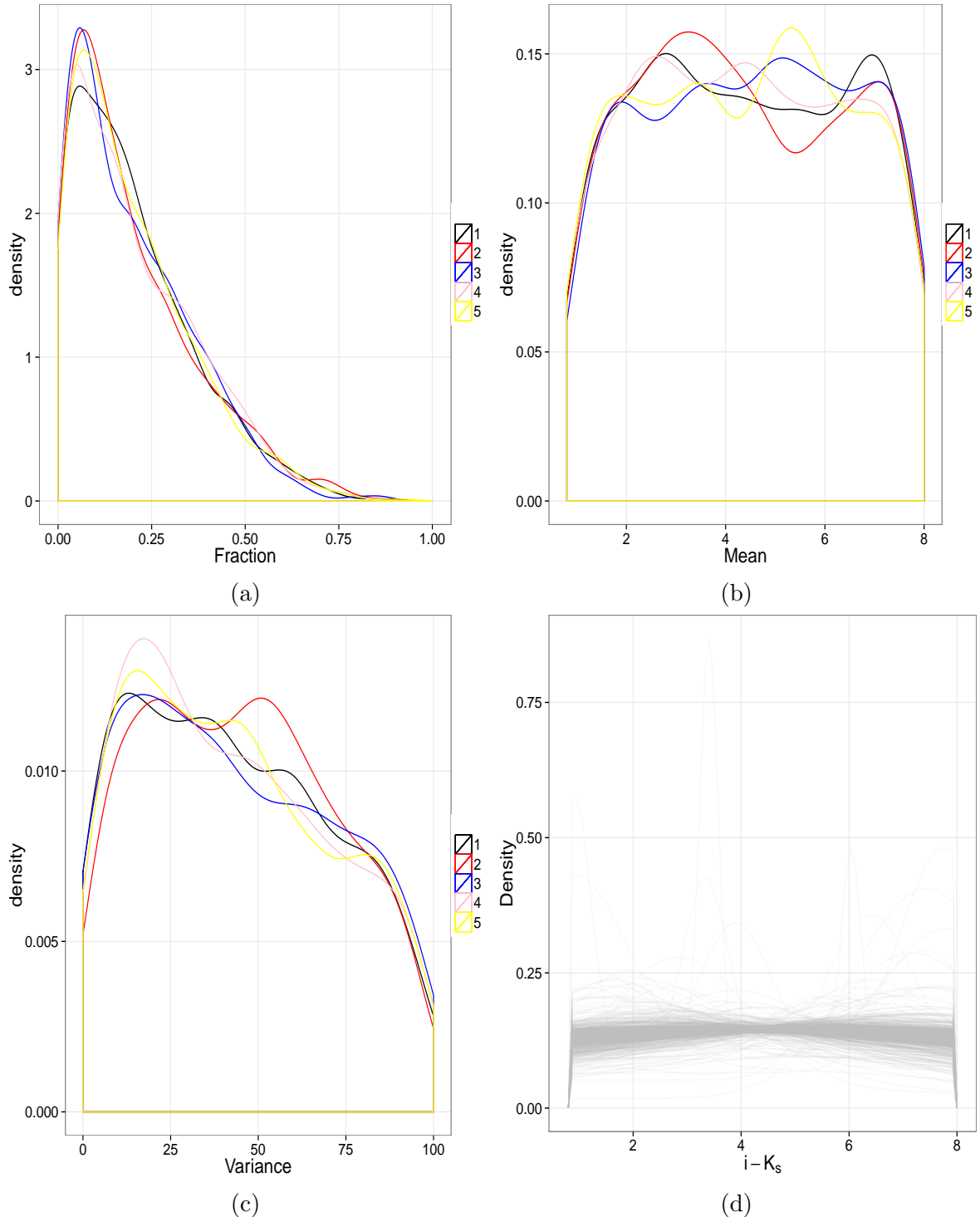


Figure 3.20: KDE of 10⁴ realisations of the prior distributions of parameters in the *true* CI GMM. Distributions of: (a) The field fraction π , (b) The EMB fraction, $1 - \pi_{CB}$, (c) the proper motions cluster fractions, π_{Cs} , and (d) the proper motions equal-mass binaries fractions π_{Bs} .

To find the mean and variance of these distributions we proceed as follows. First, we remove the EMB from the list of candidate members of Bouy et al. (2015). To do this, I performed an iterative fit of the cluster sequence, at each iteration I removed those objects whose photometry was as bright as that of the EMB. In the region of $CI > 7$

there are no candidate members of [Bouy et al. \(2015\)](#) or of any other source, see Fig 3.12. Thus, to provide a prior we complement our list of candidate members with the brown-dwarfs from the [Faherty et al. \(2012\)](#) sample. We choose only those objects observed in the same photometric bands of our data set. Finally, we fit the splines, and use the coefficients of this fit as the means, μ_β of the univariate normal distributions. **Figure 3.21 shows the four cubic B-splines fitted to our four CMDs complemented with the BDs of Faherty et al. (2012).** The standard deviation terms were set to $\sigma_\beta = \{1, 1, 1, 1, 1, 0.5, 0.1\}$ mag. These values provide a reasonable compromise between cluster sequences compatible with the previously known candidates, and those far away or with exotic shapes. We show a sample of these priors in Fig. 3.22. This Figure shows also the brown-dwarfs from [Faherty et al. \(2012\)](#) and the sequence (dashed line) we use to provide the means of the univariate normal distributions.

Again, I choose again the Half-t(ν, \mathbf{A}) distribution to set the prior for the parameters of the cluster intrinsic dispersion, Σ_{clus} . However, this time I use $\mathbf{A}_{ph} = \{10, 10, 10, 10, 10\}$ mag. These values are large when compared to the standard deviation terms of the observed uncertainties. Therefore, they provide a weakly informative prior on the marginal standard deviation terms of the Σ_{clus} covariance matrix.

Table 3.5 shows a summary all the hyper-parameter values used for the prior distributions. Since the majority of these values come from the work of [Bouy et al. \(2015\)](#), it is reasonable to question the influence that this particular work has on the results of the present one.

The methodology of the Bayesian Hierarchical Models, the one chosen here, has been specifically designed to avoid as much as possible the subjectivity of the chosen priors ([Gelman 2006](#)). Thus, by using the results of [Bouy et al. \(2015\)](#) to set only the hyper-parameter values of the prior distributions we avoid much of the subjectivity of choosing that particular work. On top of that, the use of the weakly informative priors (see Section 3.2.1) further decreases the impact of the prior information on the recovered posterior distributions.

Despite the weakly informative priors and the BHM methodology, the work of [Bouy et al. \(2015\)](#) may have influence our results in a similar way as it was influenced by previous works. There is an unavoidable influence from the past into the present. In this work, we aim at keeping this influence at minimum by using the least subjective approaches to the inference process under a Bayesian framework.

Furthermore, as mentioned at the end of Section 3.2.1, the prior information must be analysed in terms of the posterior distribution and verify if they make sense ([Gelman 2006; Gelman et al. 2013](#)). Details of this analysis will be presented in Section 4.9.

The quantitative analysis of the influence that the work of [Bouy et al. \(2015\)](#) may have in the present one should wait until further evidence (the application of the present methodology to other star clusters) is collected.

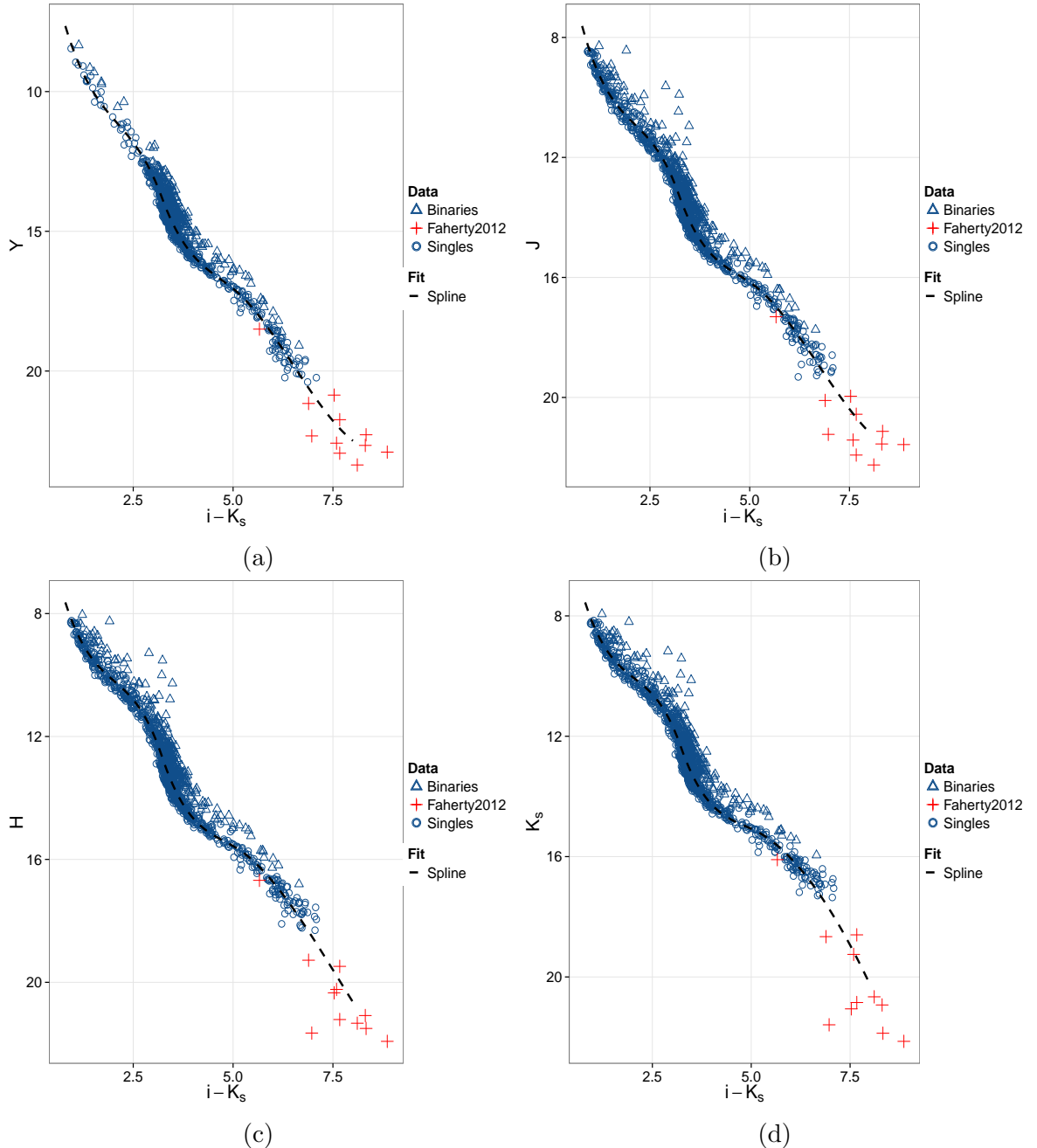


Figure 3.21: Spline fits (dashed lines) to the single stars candidate members of Bouy et al. (2015) (blue circles) and the BDs of Faherty et al. (2012) (red crosses).

Table 3.5: Hyper-parameters for different blocks of the BHM and the way in which they were derived. The upper and middle blocks correspond, respectively, to hyper-parameters of the proper motions and photometric models. The lower block to hyper-parameters shared by both models.

Hp.	Value	Derived from
α_{Cs}	{1, 1, 5, 5}	RDDR2 ($p > 0.75$)
α_{Bs}	{1.2, 8.8}	RDDR2 ($p > 0.75$)
A_{pm}	{ 10^5 , 10^5 }	Weakly-informative criterium
$\mu_{\mu_{pm}}$	{16.30, -39.62}	RDDR2 ($p > 0.75$)
$\Sigma_{\mu_{pm}}$	{36.84, 1.18, 40.71}	RDDR2 ($p > 0.75$)
α_{CI}	{1, 1, 1, 1, 1}	Weakly-informative criterium
	{0.8, 8}	RDDR2

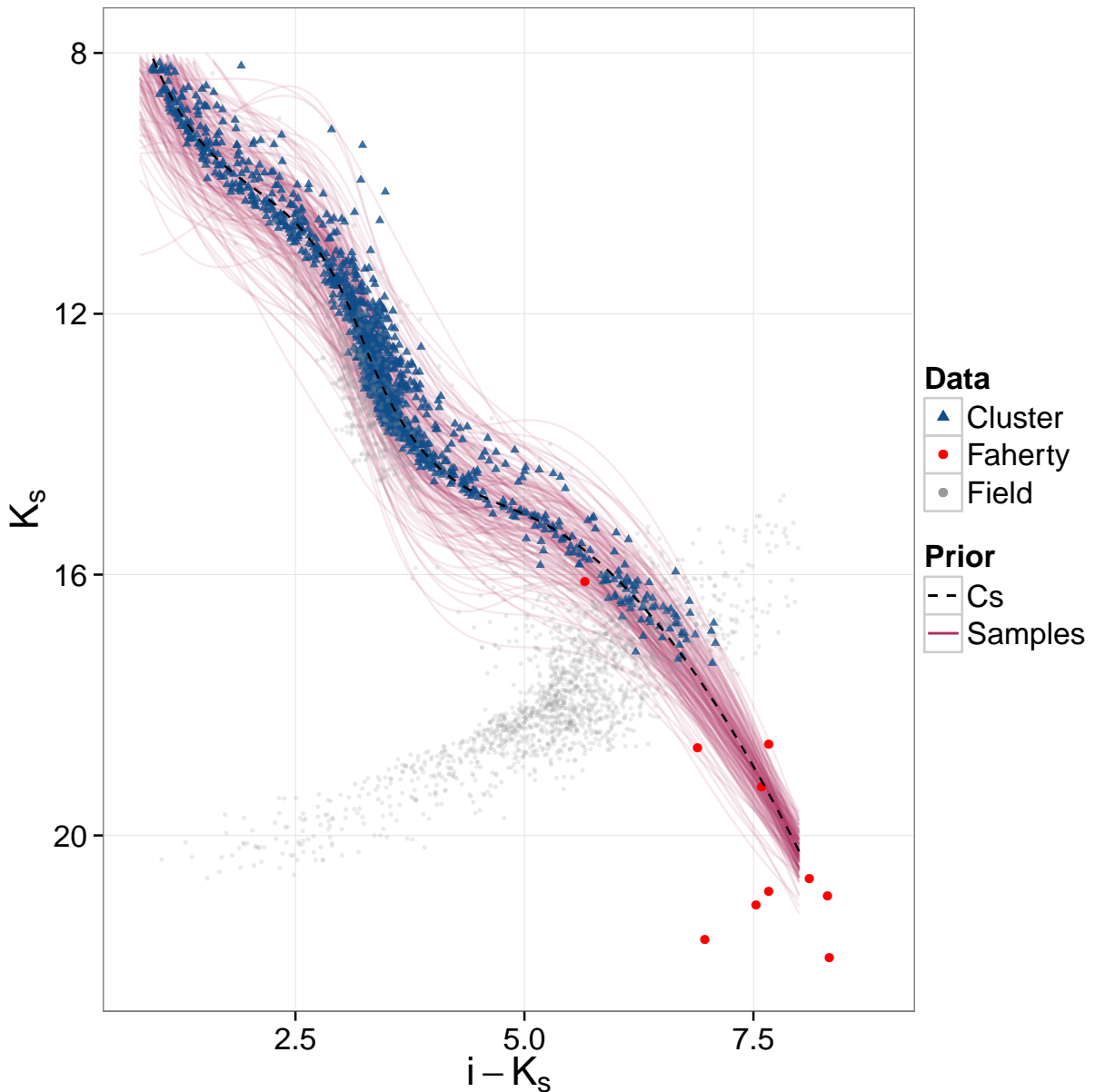


Figure 3.22: CMD K_s vs. $i - K_s$ showing a sample (100 elements) of the prior for the coefficients in the splines series. Also shown are the brown-dwarfs from Faherty et al. (2012) sample (red dots), the cluster sequence (dashed line) used as mean for the priors, the candidate members of Bouy et al. (2015) (blue triangles), and a sample of the field (grey dots).

3.5 Sampling the posterior distribution

Theoretically, there are at least three possible approaches to obtain the posterior distributions of the parameters in our model. One of these options is the analytical approach. The computing of the posterior distribution will become intractable given the size of the data set and the high dimensionality of the parametric space; the BHM has 85 parameters. The second option is the use of a grid in the parametric space. The likelihood

and the prior must be evaluated at each point in this grid and then multiplied. This approach is reasonable when the parametric space is of moderate dimension (≤ 5). It requires the evaluation of the posterior distribution q^p times, with q the number of grid points in one dimension, and p the dimension of the parametric space. The number of parameters in our model is 85, which immediately rules out this possibility. The third and so far only feasible approach is the use of MCMC sampling methods. Although these methods provide a solution in a reasonable time, nevertheless, the bottle neck of computing time is due to the evaluation of the likelihood, which grows linearly with the size of the data set.

This Section is structured as follows. First, I introduce an heuristic technique to perform a fast search of the maximum a posteriori of our target distribution. Then, I describe the MCMC techniques available in the literature. In particular, I focus on the one technique we choose, and the reasons of this decision. The Section ends detailing the convergence assessment of the MCMC.

3.5.1 PSO

The likelihood of the data is the product of the individual likelihoods of each datum (Eq. 3.12). Therefore, the number of operations needed to evaluate the likelihood grows proportionally to the size of the data. As I will explain in Section 3.5.2, the burn-in phase of MCMC techniques allows them to reach the target distribution. However, once the MCMC reaches this target distribution, the burn-in computations are discarded. Since the evaluation of the likelihood, and therefore of the posterior, is computationally expensive, I decided to reduce as much as possible the burn-in phase. To do so, I provide MCMC with a set of initial solutions which are close to the MAP of the target (posterior) distribution. These near-MAP solutions must not be too crowded on the MAP, or otherwise the MCMC will spend too much time expanding them to reach the entire distribution. Here, there is a trade-off between the crowdedness of the solutions and its proximity to the MAP. Since we aim at obtaining a representative sample of the posterior distribution and not just an estimate of it, then the initial set of solution for the MCMC must be carefully chosen to minimise the computing time. This section provides the details of this procedure.

In Section 3.5.2, I will also show that the MCMC flavour more suitable to our objective belongs to the family of *ensemble* MCMC. This flavour works with particles in the parametric space. To make the transition between the initial near-MAP solutions and the MCMC particles as efficient as possible, I choose the Particle Swarm Optimiser (PSO) of [Kennedy & Eberhart \(1995\)](#), which is a function optimiser that also works with particles. It provides a heuristic cheap-and-fast approach to the MAP solution. The PSO works with an ensemble of particles which move through the parametric space. These particles use the collective and individual past and present information to update their position. This information is specified by the score function, which in our case is the posterior

distribution. The particles update their position iteratively according to their velocity. This velocity has a random but restricted magnitude. However, its direction is determined by the particle position, and the individual and collective positions with maximum score. [Kennedy & Eberhart \(1995\)](#) show detailed description of the original algorithm, while a more efficient version is given by ([Clerc & Kennedy 2002](#)).

Although the PSO is a simple and rather efficient solution to the MAP approximation, it is far from perfect. Due to its heuristic origin, there is no theory behind its formulation. Furthermore, it does not guarantee the finding of the global maximum (for a convergence guaranteed version see [Patel et al. 2013](#)). Although, this issue does not affect our results (as we will see MCMC does guarantee the finding of the target distribution once it has converged), it impacts the computing time. If the global maximum is not found in the PSO stage, then the MCMC will take longer to arrive to the target distribution.

On the other hand, the PSO stops its computations once the mean of the particles scores lies within a user defined tolerance. If this tolerance is too large, the PSO may stop far from the MAP. If it is too small, it may converge to the MAP but deliver solutions highly concentrated around it. This poses a problem to the following MCMC stage. For it to explore the full posterior distribution, the MCMC will need more iterations, thus more time, to expand the initially concentrated positions. The optimal value for the relative tolerance is 10^{-7} . I found it after several trials and errors. It was a time consuming exercise that will be avoided in the analyses of other clusters.

To overcome the problem of crowdedness, I decide to use the charged PSO ([Blackwell & Bentley 2002](#)). Originally designed to optimise a time varying score function, the charged PSO maintains its exploratory capabilities due to an electrostatic force that repels particles when they get closer than a certain distance ([Blackwell & Bentley 2002](#)). Thanks to this electrostatic force the charged PSO avoids the over-crowding of particles around local best values.

The algorithm of [Blackwell & Bentley \(2002\)](#) computes distances in the entire parametric space. I find this approach unsuitable for our problem, thus I modified it. This modified version and the values chosen for its parameters are described with more detail in Section 3.6, together with the rest of the developed codes.

3.5.2 MCMC

Generalities

Markov Chain Monte Carlo (MCMC) is the generic name for a series of algorithms whose objective is the sampling of probability distributions. As their name indicates, the MCMC generates a chain (or a group of them) of Monte Carlo realisations that fulfil the Markov property. Monte Carlo realisations can be understood, broadly speaking, as continuous random realisations. Since it is an iterative algorithm, the chain is a process

that refers to the joint of all random Monte Carlo steps. The Markov property indicates the probabilistic independence between steps in the chain that are separated more than one iteration. Thus, in a Markov chain, the probability of a future step depends only on the present step, and not in the past steps.

[Andrieu et al. \(2003\)](#) provides a brief and interesting summary of the history of the MCMC methods. In the following I use their work to describe the fundaments of MCMC. For more details, see the aforementioned authors and the book of [Brooks et al. \(2011\)](#).

A stochastic process is defined as a sequence $\{\theta_1, \dots, \theta_n\}$ of random elements. On it, each element $\theta_i \subset \mathbb{R}^k$, with k the dimension of the *state space*.

A stochastic process, $\boldsymbol{\theta} = \{\theta_0, \theta_1, \dots, \theta_n, \theta_{n+1}\}$ is called a Markov chain if

$$p(\theta_{n+1} | \theta_0, \theta_1, \dots, \theta_n) = p(\theta_{n+1} | \theta_n).$$

A Markov chain has two important distributions, the initial distribution and the transition distribution. The initial distribution is the marginal distribution of θ_0 , $p(\theta_0)$. The transition distribution is the conditional probability $p(\theta_{n+1} | \theta_n)$. The latter is called stationary or homogeneous if it does not depend on n .

If this transition is irreducible and aperiodic, then there is an *invariant* or *equilibrium* distribution to which the chain converges, regardless of the initial distribution. Here, aperiodic means that the chain does not have loops, while it is irreducible if the probability of exploring all other states is not zero.

If we want to have $p(\theta)$ as the invariant distribution, then it suffices that the transition distribution $p_t(\cdot | \cdot)$ satisfies the detailed balance condition,

$$p(\theta_n) \cdot p_t(\theta_{n-1} | \theta_n) = p(\theta_{n-1}) \cdot p_t(\theta_n | \theta_{n-1}). \quad (3.50)$$

Thus, MCMC are Markov chains that satisfy the detailed balance condition, and have their invariant distribution as the target distribution. The large variety of MCMC algorithms arises from the efficiencies with which they arrive to the target distribution.

In the following I will review three of the MCMC categories: Metropolis-Hastings (MH), Hamiltonian Monte Carlo (HMC) and affine invariant samplers. The MH category comprises the classic MH algorithm but also contain particular cases like the Gibbs sampler ([Geman & Geman 1984](#)). I describe MH only for completeness and explanatory reasons. Later, I will focus on the particular cases of HMC, and affine invariant for ensemble samplers. Finally, I will briefly describe Nested Sampling, an algorithm that uses MCMC to numerically compute the Bayesian evidence and simultaneously generate samples of the posterior distribution.

Metropolis-Hastings

By far, the most popular MCMC algorithm is Metropolis-Hastings ([Metropolis et al. 1953](#); [Hastings 1970](#)). Once the Markov chain has been initialised in the state space, given the current θ and the proposed $\hat{\theta}$ positions, the chain moves from θ to $\hat{\theta}$ with acceptance probability:

$$\mathcal{A}(\hat{\theta}|\theta) = \min \left\{ 1, \frac{p(\hat{\theta}) \cdot q(\theta|\hat{\theta})}{p(\theta) \cdot q(\hat{\theta}|\theta)} \right\}, \quad (3.51)$$

where q is the transition probability. Since the algorithm allows rejection, it is aperiodic, and to ensure irreducibility, the support of q must include that of p ([Andrieu et al. 2003](#)). The popularity of MH lies in its simplicity. Nevertheless it requires a careful tuning of the transition probability. Usually, this probability is given by a normal distribution. It works well for relatively low dimensions of the parametric space (≤ 5). However, once the dimension goes higher, the MH algorithm spends a great amount of time tuning the parameters of this multivariate normal distribution. In particular, those of its covariance matrix.

Hamiltonian Monte Carlo

The Hamiltonian Monte Carlo (HMC) algorithms ([Duane et al. 1987](#); [Neal 1996](#)), as their name suggest²⁴, use Hamiltonian dynamics to express the target distribution as the potential distribution of a hamiltonian system of particles. In such systems the total energy is the sum of the potential and kinetic energies. The potential distribution depends only on position, whereas the kinetic one on momentum. HMC introduces a momentum to the particles in order to use their positions as a sample of the target distribution. To update the particles positions, HMC uses the Hamilton equations, which contain information about the gradient of the potential. Once HMC has tuned the momentum distribution, the proposed positions are more likely in terms of the target distribution. Therefore, using the information about the gradient of the target distribution, HMC is able to improve the acceptance ratio of the proposed steps. A detailed description of HMC can be found in Chapter 5 of [Brooks et al. \(2011\)](#). The package *Stan* ([Carpenter et al. 2017](#)) provides an efficient implementation of HMC.

Affine invariant

Affine invariant MCMC samplers use many particles, the ensemble, to sample the target distribution with a performance that is independent of its shape in the parametric space. Affine invariant MCMC does not need the tuning the transition probability. For

²⁴Originally called Hybrid Monte Carlo by ([Duane et al. 1987](#))

this reason, these samplers are faster than standard MCMC ([Goodman & Weare 2010](#)). In the following I use the derivation of [Goodman & Weare \(2010\)](#).

An ensemble $\boldsymbol{\theta}$ is a set of L particles $\theta_l \subset \mathbb{R}^k$. It lives in state space \mathbb{R}^{kL} , and the positions of it particles are independently drawn from the target distribution π . Therefore,

$$\Pi(\boldsymbol{\theta}) = \pi(\theta_1) \cdot \pi(\theta_2) \dots \pi(\theta_L).$$

Thus, an ensemble MCMC is a Markov chain in the state space of ensembles. An ensemble MCMC preserves the equilibrium distribution without the individual particles sequence, $\theta_1(1), \theta_1(2), \dots, \theta_1(t)$, being Markov or even independent. However, to update the particles positions, the detailed balance condition (Eq. 3.50) must be fulfilled. [Goodman & Weare \(2010\)](#) use partial resampling to ensure this. In partial resampling, the transition probability preserves the target (invariant) distribution if the single particle steps preserve the conditional distribution of the particle position given the complementary ensemble (the rest of the particles). Using the affine invariant *stretch move* (see below), these authors are able to define a Markov chain, in the state space of ensembles, that satisfies the detailed balance condition.

The stretch move $\theta_k(t) \rightarrow \hat{\theta}$ is defined as,

$$\hat{\theta} = \theta_j(t) + z \cdot (\theta_k(t) - \theta_j(t)),$$

where $\theta_j(t)$ is the current position of a particle in the complementary ensemble, and z is the stretching factor. It produces a symmetric transition, $p(\theta_k(t) \rightarrow \hat{\theta}) = p(\theta_k(t) \leftarrow \hat{\theta})$, if its density $g(z)$ satisfies the symmetry condition

$$g\left(\frac{1}{z}\right) = z \cdot g(z).$$

Finally, [Goodman & Weare \(2010\)](#) define their affine invariant MCMC using the following distribution for $g(z)$,

$$g(z) \propto \begin{cases} \frac{1}{\sqrt{z}} & \text{for } z \in [1/a, a] \\ 0 & \text{for } z \notin [1/a, a] \end{cases} \quad (3.52)$$

and the acceptance probability,

$$\mathcal{A}(\hat{\theta}|\theta) = \min \left\{ 1, z^{n-1} \cdot \frac{p(\hat{\theta})}{p(\theta)} \right\}. \quad (3.53)$$

The parameter a , which must be greater than one, improves the performance of the sampler ([Goodman & Weare 2010](#)). The acceptance fraction of the proposed transitions depends both on the ratio of probabilities $p(\hat{\theta})/p(\theta)$ and on the value of z^{n-1} . The support of the latter depends on the parameter a . Given $g(z)$ and certain dimension of the

parametric space, increasing a results in more probable smaller values of z , thus in smaller acceptance probabilities.

One of the great advantages of MCMC ensemble samplers is its possibility of parallelisation. Since they work with particles, these particles can be distributed among cores in a computer cluster, therefore reducing the computing time when compared to non ensemble MCMC. [Foreman-Mackey et al. \(2013\)](#) implemented the affine invariant stretch move of [Goodman & Weare \(2010\)](#) in the Python package *emcee*.

Nested sampling

Nested sampling ([Skilling 2004, 2006](#)) is an algorithm designed to numerically integrate the evidence (Eq. 3.15). As a by-product, it also delivers a sample of the posterior distribution.

To compute the evidence integral, it uses N particles whose positions, in the parametric space, are sampled from the prior. Then, at each subsequent step i the algorithm computes the likelihoods of the N particles. The particle with lowest likelihood is stored as x_i together with its likelihood L_i . The weight w_i is computed as

$$w_i = e^{-\frac{(i-1)}{N}} - e^{-\frac{i}{N}}.$$

The particle x_i is replaced with a new draw from the prior, on the condition that its likelihood is greater than L_i .

Once certain number of iterations have been done, the evidence integral is approximated by

$$z \leftarrow \sum_i w_i \cdot L_i. \quad (3.54)$$

The original algorithm was designed to compute the evidence of a unimodal distribution. However, an improved version of the original algorithm was implemented in *MultiNest* ([Feroz et al. 2009](#)). This version allows the sampling and computing of evidence in the even more difficult multimodal posteriors.

3.5.3 Implementation and convergence: PSO and MCMC

To sample the posterior distribution in our problem, we choose *emcee* due to the following properties: i) the affine invariance allows a faster convergence over common and skewed distributions (see [Goodman & Weare 2010; Foreman-Mackey et al. 2013](#), for details), ii) it can be run in parallel by distributing particles over the nodes of a computer cluster, which reduces considerably the computing time; and iii) it requires the hand-tuning of only two constants: the number of particles, and the parameter a of the $g(z)$ distribution(Eq. 3.52). I choose a ratio of particles to parameters of two, that results in 170 particles. This is the minimum ratio recommended by [Foreman-Mackey](#)

et al. (2013), which still allows a reasonable computing time. After trial and error, I fix the value of the a parameter to $a = 1.3$. As mentioned by Goodman & Weare (2010), this parameter can be tuned to improve performance of the sampler. This value keeps the acceptance fraction in the range $0.2 - 0.5$, as recommended by Foreman-Mackey et al. (2013).

As a front-end of *emcee*, and to handle the input and output of data, I use a modified version of the *emcee* handler known as *Cosmo Hammer* (Akeret et al. 2013). The next Section provides the details of these modifications.

As mentioned earlier, the PSO does not guarantee the finding of the global maximum of the score function. Therefore, I implement an iterative approach that minimises the risk of the PSO getting stuck in local maxima. To do so, I iteratively run PSO and 50 iterations of *emcee* (with the same number of particles as the PSO) until the relative difference between means of consecutive iterations is lower than 10^{-7} . The iterations of *emcee* spread the PSO solution without moving away from the target distribution.

Neither scheme, PSO alone or PSO-*emcee*, guarantees finding the global maximum. The solution this scheme provides could indeed be biased. However, we use them to obtain only a fast estimate of the global maximum, or at least, of points in its vicinity. If the initial solution provided by this scheme is indeed biased, the final *emcee* run erases, during the burning phase, any dependance on the initial solutions. After the convergence of the PSO-*emcee* scheme, I run *emcee* alone until it converges.

Convergence to the target distribution occurs when each parameter enters into the stationary equilibrium or normal state. The Central Limit Theorem ensures that this state exists. See Roberts & Rosenthal (2004) for guaranteeing conditions and Goodman & Weare (2010) for *irreducibility* of the *emcee* stretch move. The stationary or normal state is reached when, in at least 95% of the iterations, the sample mean is bounded by two standard deviations of the sample, and the variance by the two standard deviation of the variance²⁵. Fig. 3.23 shows the mean and variance of the ensemble of *emcee* particles for the last 4000 iterations before stoping the sampling. Both the mean and variances are normalised to the value of the last iteration.

²⁵ $sd(\sigma^2) = \sigma^2 \sqrt{\kappa/n + 2/(n-1)}$ with κ the kurtosis and n the sample size.

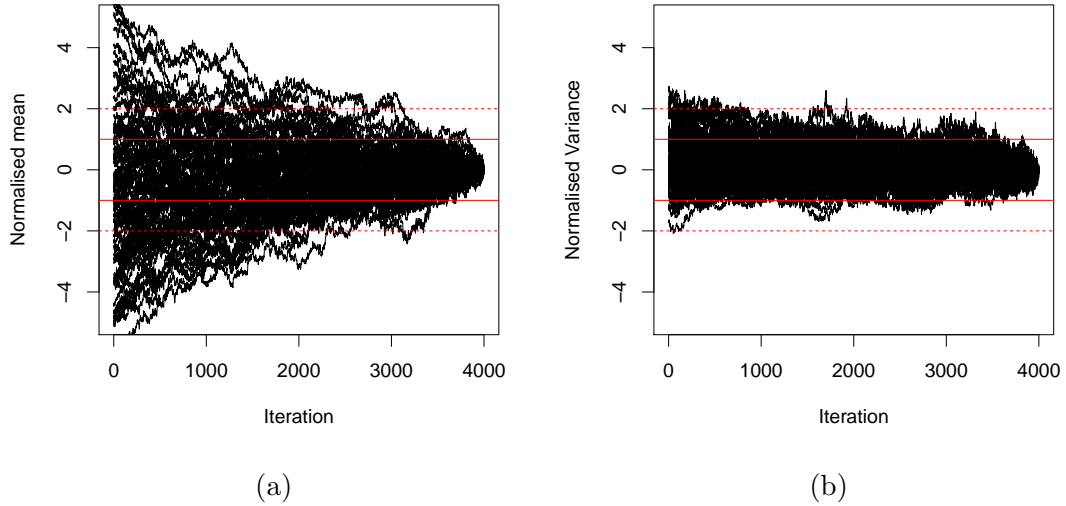


Figure 3.23: Normalised mean (a) and variance (b) of each parameter in BHM model as functions of iterations. The normalisation values are the mean and variance of the ensemble of particles positions at the last iteration. Red lines show one and two sigma levels of these normalisation values. Only shown the last 4000 iterations previous to stopping the algorithm.

I stop the *emcee* sampling once all parameters have entered the equilibrium state and the criterium of [Gong & Flegal \(2016\)](#)²⁶ is fulfilled. We choose this criterium because it was developed for high-dimensional problems and tested on Hierarchical Bayesian Models, as in the present work. In this criterium, the MCMC chain stops once its Effective Sample Size (ESS) is larger than a minimum sample size. This minimum is computed using the required accuracy, v , for each parameter confidence interval $(1 - \delta) \cdot 100\%$. The ESS is the size that an independent and identically distributed sample must have to provide the desired accuracy on the parametric inference.

The *emcee* run stops once the ESS of the ensemble of walkers is greater than the minimum sample size needed for the required accuracy $\epsilon = 0.05$ on the 68% confidence interval ($\delta = 0.32$) of each parameter.

3.6 Codes

This Section sets out the details about the code I developed to perform the computation described throughout this chapter. First, I give a brief chronological description of the model development. Later, I will describe the details on the implementation of the charged PSO, the modified *emcee*, and the GMM used to describe the field population. Finally, I will end this Section detailing the hybrid High-Performance Computing (HPC) code developed to minimise the computing time of the posterior distribution in the BHM.

²⁶Implemented in the R package *mcmcse* ([Flegal et al. 2016](#))

The first version of the Bayesian Hierarchical Model was implemented by Ángel Berihuete in the package *Stan* (Carpenter et al. 2017). It comprised a Bayesian model of the MLE model of Sarro et al. (2014). The proper motions were modelled using a single mixture of gaussians. The photometry was modelled with a Chebyshev polynomial parametrised by the length along the sequence. This length was found using a principal curve analysis and lacked physical interpretation.

I took this version and modified it in the following aspects. I included the photometric and proper motions EMB sequence, the uncertainties both in proper motion and in the photometry, and the width of the sequence modelled as the multivariate gaussian. Then, we realised that the principal curve analysis is not compatible with the deconvolution methodology. The principal curve analysis finds the dominant curve in the observed data, and not the *true* underlying relation that generates the observed data once the individual noise process for each object is accounted for. For this reason, the principal curve analysis is affected by individual uncertainties (see Hong et al. 2016, for the negative impact of heteroscedastic data on the related principal component analysis). Instead, we decided to model the intrinsic *true* underlying photometric relation with polynomials. We use as parameter for these polynomials the *true* colour CI, which is a more interpretable parameter than the distance along the principal curve, which was used in the previous version. Since we have one *true* CI for each object, the number of parameters is equal to the number of objects. We marginalised all these nuisance parameters with the aid of a prior. For this prior we introduced a probability distribution modelled by a GMM.

Previous to the introduction of the marginalisation of the nuisance parameters, the model worked fine on samples of a few hundreds of stars. Once the marginalisation was introduced, the computing time of the model increased dramatically, rendering its application to higher data sizes impractical. At this point we decided to port the existing *Stan* code into *Python*²⁷ so that we could work with the parallel *emcee* code. *emcee* proved to be of great use. Due to its parallelisation capabilities we were able to increase the data size from 2000 to 10,000 objects. Since the computing of the likelihood was the highest computational challenge, I developed my own routines to perform it in parallel. However, *CosmoHammer* (Akeret et al. 2013) turned out to be more efficient in distributing the parallel loads. I ported the BHM code into *CosmoHammer* and modified the latter. The modifications ranged from data files and log entries to the introduction of priors and the handling of a Hybrid-HPC scheme using both Message Passing Interface (MPI) and multithreading. Despite the Hybrid-HPC scheme, the computing of the likelihood of a data set with 10^5 objects seemed unreachable. At this point, I performed two tasks: the first was to strip the code of all auxiliary libraries calls, and the second was the vectorisation of the majority of the operations. Since the parameters of the field were held fixed, the field likelihood was computed externally for each object. The code was then fed with the

²⁷<https://www.python.org>

data set, the field likelihood, and all the auxiliary computations reduced to a minimum. Among the reduced computation there are, for example, the Cholesky decompositions and matrix inversions of the covariance matrices of the uncertainty. Instead of doing these computation inside the code, the code was fed with the precomputed values. This further reduced the computing time.

Introducing PSO and later the charged PSO further reduced the computing time. At this point the code was able to run on a data set with 10^5 objects. However, convergence of the MCMC still required several weeks of computations. Once the approximation to the marginalisation integral (Eqs. 3.41 and 3.42) was introduced, the computing time reduced far more. Finally, the tuning of the *emcee* parameters allowed us to increase the acceptance fraction, and reach convergence within four weeks of full computing time with an 80 cores computer cluster. It is indeed a very long time. However it is reasonable compared with our original estimates of approximately 2 years of computing time²⁸.

3.6.1 The modified charged PSO

As explained before, the charged PSO of [Blackwell & Bentley \(2002\)](#) was inappropriate to our objective. The metric of the parametric space of our problem is not isotropic because parameters have different length scales. For example, while fractions are constrained in the $[0, 1]$ interval, proper motions parameters are allowed in the range of proper motion measurements $[-99, 99] \text{ mas} \cdot \text{yr}^{-1}$. Therefore, the use of an isotropic metric results in a solution which is crowded in some parameters while is over-dispersed in others. To solve this issue, I modified the charged PSO by measuring distance between particles and applying the electrostatic force independently on each parameter. In such a way, the electrostatic force plays a role only when the relative distance between particles in any given parameter is smaller than 10^{-10} . I found this value heuristically.

In the original version of [Blackwell & Bentley \(2002\)](#), each particle is subject to the acceleration,

$$\mathbf{a} = \sum_{i \neq j} \frac{q_i \cdot q_j}{r_{ij}^3} \cdot \mathbf{r}_{ij}, \quad p_{\text{core}} < r_{ij} < p \quad (3.55)$$

where q_i and q_j are the charges of particles i and j , and r_{ij} is the distance between them. The distances p_{core} and p indicate the minimum and maximum distances at which the electrostatic force comes into action. Outside this range, the electrostatic force is zero. In this equation, $\mathbf{r}_{ij} = \mathbf{x}_i - \mathbf{x}_j$, where $\mathbf{x}_i, \mathbf{x}_j$ are the positions of particles i and j . Also, $\mathbf{r}_{ij}, \mathbf{x}_i, \mathbf{x}_j \subset \mathbb{R}^d$, with d the dimension of the space.

In the modified version, the distance is measured independently in each dimension of the parametric space. Thus, $\mathbf{r}_{ij} = \{x_{1,i} - x_{1,j}, x_{2,i} - x_{2,j}, \dots, x_{d,i} - x_{d,j}\}$. Also the

²⁸Today, the DANCe team is working on a Graphics Processing Unit (GPU) version of the code which computes the same amount of calculations in a couple of days.

acceleration has the form,

$$\mathbf{a} = \sum_{i \neq j} \frac{\mathbf{q}_i \cdot \mathbf{q}_j}{r_{ij}^2} \cdot \mathbf{r}_{ij}, \quad 10^{-50} < \frac{r_{ij}}{r_{eq}} < \epsilon \quad (3.56)$$

and it is now applied over each dimension of the parametric space. The distance r_{eq} is that at which the velocity caused by the acceleration equals the mean velocity caused by the common PSO. ϵ is a free parameter which, as said previously, was set heuristically to 10^{-10} .

3.6.2 Improvements of emcee

The modification I introduced in *emcee*, although very simple, improved the acceptance fraction and mixing of the particles. To allow the parallelisation, [Foreman-Mackey et al. \(2013\)](#) divide the ensemble of particles in two ensembles. In the original version, the particles in one ensemble use one and the same particle in the complementary ensemble to compute their positions according to Eq. 3.52. In the modified version, particles from one ensemble update their positions using a particle from the complementary ensemble. However, this particle is chosen randomly at each iteration.

In a private communication with Daniel Foreman-Mackey, the developer of *emcee*, he mentions that a similar modification was already introduced in a beta version of the *emcee* code.

3.6.3 GMM for the field population

As mentioned earlier in this Chapter, the field population is modelled by means of two independent photometric and proper motion distributions. The MLE of the parameters of these distributions were found using the EM algorithm. The conventional EM algorithm for GMM ([Dempster et al. 1977](#)) for a mixture of M gaussians goes as follows. Given a set of parameters $\theta = \{w_i, \boldsymbol{\mu}_i, \boldsymbol{\Sigma}_i\}_{i=1}^M$, where w_i , $\boldsymbol{\mu}_i$, and $\boldsymbol{\Sigma}_i$ are the fraction, mean and covariance matrix of gaussian component i , the likelihood of the data is,

$$p(\{\mathbf{y}_n\}_{n=1}^N | \theta) = \prod_{n=1}^N \sum_{i=1}^M w_i \cdot \mathcal{N}(\mathbf{y}_n | \boldsymbol{\mu}_i, \boldsymbol{\Sigma}_i). \quad (3.57)$$

To solve the problem, the EM algorithm requires a set of N variables, $\{\mathbf{z}_n\}_{n=1}^N$, of dimension M . The variable $z_{n,i}$ represent the probability that observation y_n was drawn from gaussian i . Therefore,

$$1 = \sum_{i=1}^M z_{n,i}. \quad (3.58)$$

These \mathbf{z} latent variables are found as

$$z_{n,i} = \frac{w_i \cdot \mathcal{N}(\mathbf{y}_n | \boldsymbol{\mu}_i, \boldsymbol{\Sigma}_i)}{\sum_{i=1}^M w_i \cdot \mathcal{N}(\mathbf{y}_n | \boldsymbol{\mu}_i, \boldsymbol{\Sigma}_i)}. \quad (3.59)$$

The EM works, as its name indicates, by maximising the expected value of the likelihood. The latter is given by

$$E[p(\{\mathbf{y}_n\}_{n=1}^N | \theta)] = \prod_{n=1}^N \sum_{i=1}^M z_{n,i} \cdot w_i \cdot \mathcal{N}(\mathbf{y}_n | \boldsymbol{\mu}_i, \boldsymbol{\Sigma}_i). \quad (3.60)$$

The previous expectation is maximal when,

$$w_i = \frac{1}{N} \sum_{n=1}^N z_{n,i}, \quad (3.61)$$

$$\boldsymbol{\mu}_i = \frac{1}{\sum_{n=1}^N z_{n,i}} \sum_{n=1}^N z_{n,i} \cdot \mathbf{y}_n, \quad (3.62)$$

$$\boldsymbol{\Sigma}_i = \frac{1}{\sum_{n=1}^N z_{n,i}} \sum_{n=1}^N z_{n,i} \cdot (\mathbf{y}_n - \boldsymbol{\mu}_i) \times (\mathbf{y}_n - \boldsymbol{\mu}_i)^T. \quad (3.63)$$

The modified version of the GMM, which includes a uniform distribution, is now a particular case of the GMM. This can be viewed as a gaussian distribution with fixed parameters and a constant probability c given by the uniform distribution. The new expectation is then,

$$E[p(\{\mathbf{y}_n\}_{n=1}^N | \theta)] = \prod_{n=1}^N \left[z_{n,0} \cdot w_0 \cdot c + \sum_{i=1}^M z_{n,i} \cdot w_i \cdot \mathcal{N}(\mathbf{y}_n | \boldsymbol{\mu}_i, \boldsymbol{\Sigma}_i) \right]. \quad (3.64)$$

The maximisation step remains identical except for the indices. There are now $M + 1$ fractions w_i , with $i = 0, 1, \dots, M$, and the means and covariances run from $i = 1, \dots, M$.

Regarding the photometric GMM of the field, and given that the photometry has missing values, we use the EM algorithm of [McMichael \(1996\)](#). This algorithm was developed to obtain the MLE of data sets containing objects with missing values. A recent and faster version was developed by [Lin et al. \(2006\)](#). Although this new version is faster, its mean absolute relative error is in the range 0.02-0.2 (see Tables 2 and 3 of the mentioned authors). In [McMichael \(1996\)](#) algorithm this indicator is lower, at least for fractions and means (see Fig. 3.24).

In the algorithm of [McMichael \(1996\)](#), there is a set of N gain matrices, one for each datum. Each M_n matrix is an identity matrix in which the rows of the corresponding

missing value have been deleted. Thus, the expected value of the likelihood is now,

$$E[p(\{\mathbf{y}_n\}_{n=1}^N | \theta)] = \prod_{n=1}^N \sum_{i=1}^M z_{n,i} \cdot w_i \cdot \mathcal{N}(\mathbf{y}_n | M_n \boldsymbol{\mu}_i, M_n \boldsymbol{\Sigma}_i M_n). \quad (3.65)$$

The maximisation step is now,

$$w_i = \frac{1}{N} \sum_{n=1}^N z_{n,i}, \quad (3.66)$$

$$\boldsymbol{\mu}_i = \frac{\sum_{n=1}^N z_{n,i} \cdot H_n \mathbf{y}_n}{\sum_{n=1}^N z_{n,i} H_n M_n} \quad (3.67)$$

with

$$H_i = M_i^T (M \boldsymbol{\Sigma}_i M^T)^{-1} \quad (3.68)$$

The maximisation step has no analytical solution for the covariance matrix. Therefore, a modified steepest descent is used

$$\boldsymbol{\Sigma}_i \leftarrow \boldsymbol{\Sigma}_i + \frac{\rho}{2} \cdot \boldsymbol{\Sigma}_i \Delta_i \boldsymbol{\Sigma}_i, \quad (3.69)$$

with Δ_i given by

$$\Delta_i = \frac{1}{\sum_{n=1}^N z_{n,i}} \cdot \sum_{n=1}^N z_{n,i} \cdot [H_n (\mathbf{y}_n - M_n \boldsymbol{\mu}_i) \times (\mathbf{y}_n - M_n \boldsymbol{\mu}_i)^T H_n^T - H_n I]. \quad (3.70)$$

This algorithm preserves the monotonic convergence of the conventional EM, and returns positive definite matrices provided that $\rho < 2$. For details and validation of this algorithm see [McMichael \(1996\)](#). Nevertheless, I tested the validity of this algorithm on synthetic data sets. I created them using the parameters of the photometric model presented in Section 3.3.3. Figure 3.24 shows the mean absolute relative differences between each of the input and recovered parameters in the GMM. The panels are separated by the kind of parameter: fractions, means and covariance matrices. The mean absolute relative differences are shown as a function of the sample size and the fraction of objects with missing values. The latter were randomly chosen, with missing entries in three of the five observables. As can be seen from this figure, the algorithm performs reasonably well in the explored range of sample sizes and missing fractions.

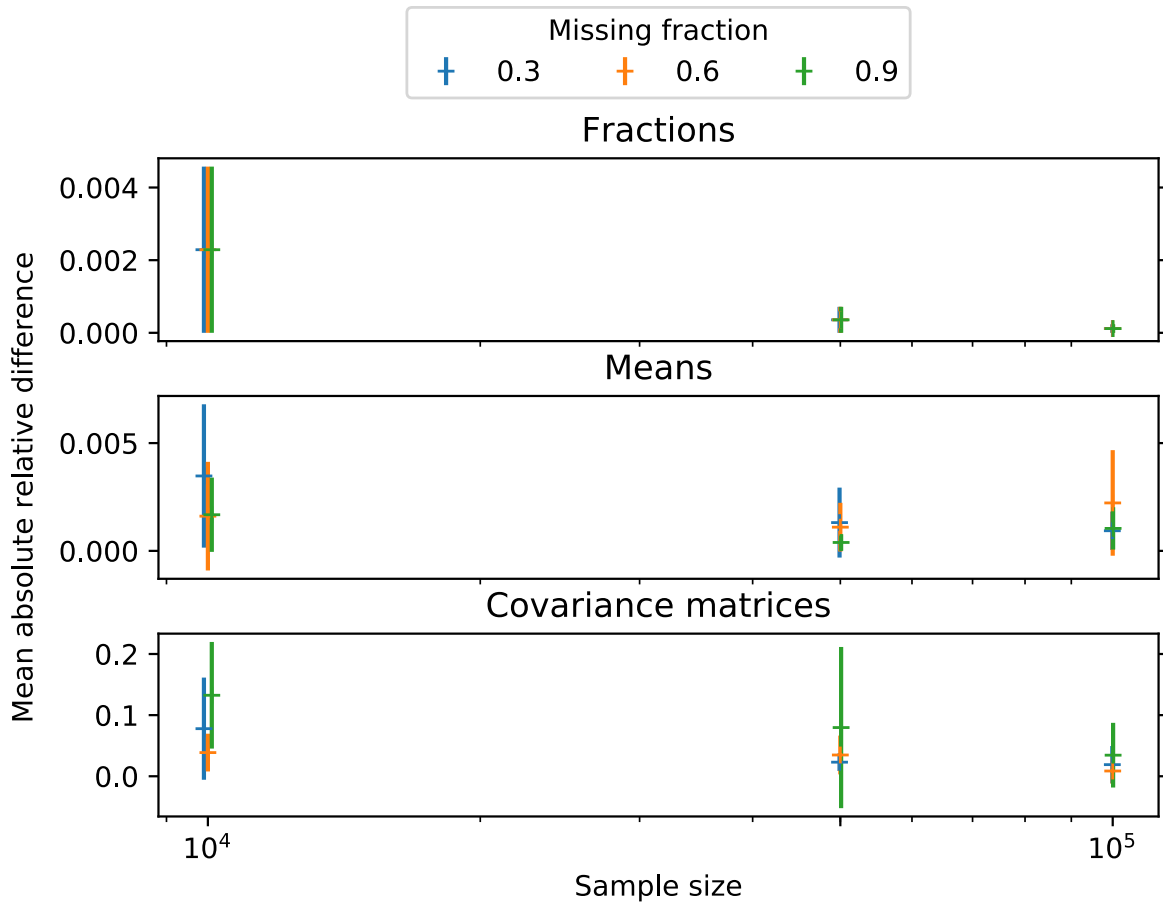


Figure 3.24: Mean of the relative difference between the input parameters and the recovered ones as a function of the sample size and the fraction of objects with missing values.

3.6.4 Hybrid-HPC implementations

As I outlined before, the parallel computing approach was an unavoidable step. Once the code was ported to *Python* and *CosmoHammer*, I modified the latter to better fit our needs. The modifications were mainly on the management of input and output files and the python *multiprocessing* package for the multithreaded computing of likelihoods. Also, I striped some of its original functions to reduce memory usage and implemented some others, like the use of initial positions for the particles.

In the Hybrid-HPC approach, the particles of *emcee* are distributed on the nodes of the computing cluster by means of the MPI protocol. Then, each core in the node computes the likelihood of one fraction of the objects in the data set. This Hybrid-HPC code was implemented and tested in different computing cluster architectures. For the cluster at the Centre of Astrobiology (Villanueva de la cañada, Madrid, Spain), I used a configuration of 6 nodes each with 12 cores. For the cluster at the University of Cádiz, (Andalucía, Spain) I used a configuration of 5 nodes each with 16 cores.

However, the Hybrid-HPC approach was not the best solution at the Infrastructure de

Calcul Intensif et de Donées²⁹ of the University of Grenoble Alpes. At the Froggy³⁰ cluster, the code continuously render errors of communication. For this reason, I implemented a MPI-only version of the code. In this version, the multithreading approach is left aside. Instead, the totality of the available cores is fully dedicated to the computing of the likelihood. Each of the n cores computes the likelihood of the n th fraction of the objects in the data set. Once the likelihood of all particles has been computed, the master node evaluates the new positions of the particles.

I finish this chapter with a brief description of the difficulties faced in the development and testing of the BHM code. As the code evolved in complexity, my computational skills were compelled to evolve as well. I started by learning R and solving some toy problems on it. Later, when the dimensionality of the posterior increased I learned *Stan*. When the data set increased in size, we faced the parallelisation, so I learned Python and MPI. Once these versions were operable, I was forced to deal with libraries, from the common, numpy, scipy and numba, to the linking of modules and libraries. Finally, when dealing with several clusters I learned the queue languages Condor, slurm and OAR. Currently, I am working on the improvement (memory allocation and data distribution) of the GPU implementation of the BHM code.

3.7 The methodology for the analysis of the PSD

In this Section, I present the methodology used to investigate the Projected Spatial Distribution (PSD) of the Pleiades. As explained in Section 2.7.1, we do an independent analysis of the PSD and the photometric and kinematic (proper motions) distributions (the reasons for this decision are detailed in the mentioned section). The data set for this analysis is the one called the T+D, which is described in Section 2.9. Here suffices to mention that it comprises the largest and less contaminated sample of Pleiades candidate members to date. Although the analysis of the PSD uses the membership probabilities inferred by the BHM (at Chapter 4), and those derived by Bouy et al. (2015) for the Tycho-2 sample, it is independent of them because in both analyses the sky positions are explicitly removed.

The generative model of the PSD is similar to that of the BHM (Eq. 3.27). However, instead of inferring the fraction of field objects in the data set (which would be similar to the estimated contamination rate, see Section 2.9.1), each object contributes to the cluster model proportionally to its cluster membership probability, P . Thus the generative model of the PSD for object n is

$$p(\mathbf{d}_n, P_n | \boldsymbol{\theta}_c, \boldsymbol{\theta}_f) = (1 - P_n) \cdot p_f(\mathbf{d}_n | \boldsymbol{\theta}_f) + P_n \cdot p_c(\mathbf{d}_n | \boldsymbol{\theta}_c), \quad (3.71)$$

²⁹<https://gricad.univ-grenoble-alpes.fr>

³⁰<https://ciment.ujf-grenoble.fr/wiki-pub/index.php/Hardware:Froggy>

with \mathbf{d}_n the vector of observations, comprising the sky positions (α and δ), the photometric band J , and P_n the cluster membership probability. The terms $p_f(\mathbf{d}_n|\boldsymbol{\theta}_f)$ and $p_c(\mathbf{d}_n|\boldsymbol{\theta}_c)$ are the field and cluster likelihood, respectively, of the datum \mathbf{d}_n given the field, $\boldsymbol{\theta}_f$ and cluster, $\boldsymbol{\theta}_c$, parameters. Since all objects in the T+D have R.A. and Dec. uncertainties which are symmetric, almost identical (homoscedastic uncertainties), and negligible ($\sim 2 \times 10^{-6}$ deg) compared to the size of the cluster ($\sim 7^\circ$), we can safely assume that: i) the data are independent and identically distributed, and ii) the observed positions correspond to the *true* ones. Thus, the uncertainties are not included in the generative model.

We assume that the contaminants ($\sim 8\%$, see Section 2.9) in the T+D are uniformly distributed in the plane of the sky. We assume this because the sky position was explicitly removed from the calculation of membership probabilities. Hence, we model these contaminants with a uniform spatial distribution \mathcal{U} . In this way, the contribution of these hypothetical contaminants will not bias our inference of the cluster parameters.

In the following subsections, I will describe the PSD models that we include in our model selection analysis. I will start with the classical radially symmetric profiles, then I will allow for biaxial (elliptic) symmetry, and finally, those with luminosity segregation (a proxy for mass segregation). The radially symmetric ones are classic in the literature. The biaxially symmetric ones have proven to be useful to describe the ellipticity of the Pleiades (Raboud & Mermilliod 1998). The luminosity segregated ones will allow us to put a solid statistical background to the assumption of mass segregation in the Pleiades cluster (see for example Moraux et al. 2004; Converse & Stahler 2010) without relying on mass-luminosity transformations for individual objects.

Finally, I will conclude this Section giving details of the kind of priors used for the parameters in the different density profiles.

3.7.1 Models with radial symmetry

The first alternative is King's profile (King 1962), which has been widely used in the Pleiades (see Section 2.3) and to describe open clusters (see Alonso-Santiago et al. 2017; Panwar et al. 2017, for recent applications), globular clusters (Myeong et al. 2017) and even to study galaxies (Robotham et al. 2017), halo substructure (Sohn et al. 2007) and the dark matter distribution (Jiang & van den Bosch 2016).

The analytical description of the surface number density of stars counts n is given by

$$\rho(R) = k \cdot \left(\frac{1}{\sqrt{1 + (R/r_c)^2}} - \frac{1}{\sqrt{1 + (r_t/r_c)^2}} \right)^2 \quad (3.72)$$

where r_c , the core radius, is a scale factor, r_t is the tidal radius, and k is a constant related (but not equal) to the central surface density. In the following we use R instead of r (as is often commonly done in the literature) to refer to the distance from the system centre

projected on the celestial sphere. Also, we use ρ to denote the surface number density of stars.

We have also considered the model proposed by Elson et al. (1987), henceforth Elson, Fall and Freeman (EFF), to describe young open clusters in the Large Magellanic Cloud. Their surface density (in star counts per solid angle) is given by

$$\rho(R) = \rho(0) \cdot (1 + (R/r_c)^2)^{\frac{\gamma}{2}}, \quad (3.73)$$

with r_c the core radius, and γ the slope of the profile at radii much larger than the core radius.

Finally, we analyse a more general parameterisation introduced in Lauer et al. (1995), Byun et al. (1996) and Zhao (1997), where the projected mass density is given as

$$\rho(R) = \frac{k'}{(R/r_c)^\gamma \cdot (1 + (R/r_c)^{1/\alpha})^{(\gamma-\beta)\alpha}}. \quad (3.74)$$

Equation 3.74 represents a double power law, with r_c the so called core or break radius, γ and β the exponents of the inner and outer regions, respectively, α the width of the transition region, and k' a scale constant. Meaningful values of these parameters fulfil the following conditions: $\alpha > 0$ and $0 \leq \gamma \leq \beta$. In purity, the aforementioned works assume this functional form for both the projected surface brightness, the projected mass density ρ_{mass} , and for the volume density v , although the latter two are related by integration:

$$\rho_{mass}(R) = \int_0^{\infty} v(r) \cdot dz \quad (3.75)$$

where z is the distance along the line of sight corresponding to the radial distance, R projected onto the plane of the sky.

In this work we will assume that the analytical expression in Eq. 3.74 is correctly stated in terms of the projected number density and not of projected mass density.

This model is a more general analytical expression, thus we call it generalised density profile³¹, here after the Generalised Density Profile (GDP), that comprises many simpler models each of which represent particular choices of the model parameters. For example, the model put forward by Plummer (1911) to describe the projected spatial density corresponds to the general model with $\alpha = 1/2$, $\beta = 5$ and $\gamma = 0$. Several density profiles proposed to describe galaxies can be grouped by particular choices of the parameters. For example, $\alpha = 1$ includes models by Navarro et al. (1997), Hernquist (1990), Jaffe (1983), and Moore et al. (1999), and $\alpha = 1/2$, $\gamma = 0$ includes the aforementioned model by Plummer (1911), and also models by Sackett & Sparke (1990) and de Zeeuw (1985). King's profile, however, cannot be cast into this general model unless the tidal radius R_t is fixed at infinity.

In the three aforementioned formulations we have use similar names for parameters r_c

³¹Although it is also called Nuker profile by Küpper et al. (2010a).

and γ . However, these parameters do no not share the meaning amongst models. The latter is distinctively specified by each model relation \mathcal{M} .

To avoid the use of bins and to properly infer the parameters of these models, we need to convert the projected stellar densities (number of stars per unit solid angle) into probability density functions that describe the probability of finding a star between R and $R + dR$, under the assumption of spherical symmetry. The probability density function $p(R)$ is constructed from the definition:

$$p(R) \cdot dR = \frac{2\pi \cdot R \cdot \rho(R) \cdot dR}{N}, \quad (3.76)$$

where N is the total number of stars in the system. This probability is renormalised to integrate to unity at the truncation radius R_{max} , which in our data set correspond to 11.5 pc (see Section 2.9).

Applying Equation 3.76 to King's profile, we obtain

$$p(R) = \frac{k \cdot 2\pi}{N} \cdot R \cdot \left(\frac{1}{\sqrt{1 + (R/r_c)^2}} - \frac{1}{\sqrt{1 + (r_t/r_c)^2}} \right)^2 \quad (3.77)$$

Actually, in probabilistic inference we write this probability function as:

$$p(R|r_c, r_t, k_1, I, \mathcal{M}_1) = k_1 \cdot R \cdot \left(\frac{1}{\sqrt{1 + (R/r_c)^2}} - \frac{1}{\sqrt{1 + (r_c/r_t)^2}} \right)^2 \quad (3.78)$$

where we have defined a new constant $k_1 = \frac{k \cdot 2\pi}{N}$, and made explicit the dependence of the probability on the underlying analytical expression (\mathcal{M}_1), and the values of the parameter set (k_1, r_c , and r_t). In practice k_1 is treated as a normalisation constant (to enforce unit integral) and there is no need to know the total number of stars in the system. This PDF corresponds to the cluster model of *likelihood*.

Likewise, the expression for the EFF model is

$$p(R|r_c, \gamma, k_2, I, \mathcal{M}_2) = k_2 \cdot R \cdot (1 + (R/r_c)^2)^{\frac{\gamma}{2}}. \quad (3.79)$$

And finally, the GDP model will be given by

$$p(R|r_c, \alpha, \beta, \gamma, k_3, I, \mathcal{M}_3) = \frac{k_3 \cdot R}{(R/r_c)^\gamma \cdot (1 + (R/r_c)^{1/\alpha})^{(\gamma-\beta)\alpha}}. \quad (3.80)$$

In all three cases, the R coordinate is defined with respect to the origin of a coordinate system. The actual values of R then depend on this choice of this origin (see Sect. 3.7.1).

Extensions of the classical profiles

In addition to the classical profiles we have tested two extensions of the King's profile, and one variant of the GDP. Let us describe them in order.

We define the General King's Profile (GKing) as the classical King's profile without fixing the exponents of the analytical expression. Instead of Equation 3.78, we have

$$\begin{aligned} p(R|r_c, r_t, \alpha, \beta, k_1, \mathcal{M}_1) = \\ k_1 \cdot R \cdot \left[\left(1 + (R/r_c)^{\frac{1}{\alpha}} \right)^{-\alpha} - \left(1 + (r_t/r_c)^{\frac{1}{\alpha}} \right)^{-\alpha} \right]^{\beta} \end{aligned} \quad (3.81)$$

where the classical King's profile is recovered for $\alpha = 0.5$ and $\beta = 2$. To the best of our knowledge, only in the work of [Robotham et al. \(2017\)](#) a similarly modified King's profile has been used. However, the profile used by those authors is more restrictive than the one presented here, requiring that $\beta = \alpha^{-1}$, and that both terms (r/r_c) , and (r_t/r_c) are at the power of 2.

The Optimised General King's Profile (OGKing) is the General King's Profile (GKing) profile with the values of α and β fixed at the MAP values of the GKing parameters. This maximises the evidence and reduces the dimensionality of the parameter space.

Finally, the Restricted Generalised Density Profile (RGDP) corresponds to the generalised profile with the value γ fixed at 0.

Central symmetry constraint

So far, we have defined a set of three models (King, EFF and the GDP) and their extensions. Each has a different set of parameters. King's model depends on two parameters (r_c and r_t); EFF's model depends on two parameters (r_c and γ); the generalised profile depends on four parameters (α , β , γ and r_c).

In reality, there are always two more parameters that do not appear explicitly in any of the classical analytical formulations of the King, EFF or generalised profiles. These are the cluster centre coordinates from which all radial distances R_i are measured. It is not a minor question because the problem is degenerate, and there is a maximum likelihood solution for each choice of the cluster centre. In principle, one could even choose a poor cluster centre estimate that renders the angular distribution of members asymmetric, and obtain a maximum likelihood fit better than those obtained with a better centre estimate. The models assume central symmetry, but this can only be ensured approximately. There is a region of non-negligible extent, where the cluster centre may be, and any particular choice of its position will influence the posterior distribution inferred. Thus, in order to propagate appropriately this uncertainty about the cluster centre position in our posterior inferences, we have included the two cluster centre coordinates, α_c and δ_c , as further parameters of our models.

For any given choice of the central coordinates, we calculate the radial distance, R , and

the position angle θ of each star in our data set. To avoid biases introduced by projection effects of objects located far from the cluster centre, we project each object coordinates into the plane of the sky along the line-of-sight vector (see for example, Eq. 1 of [van de Ven et al. 2006](#)).

These projected coordinates are

$$\begin{aligned}\tilde{x} &= \sin(\alpha - \alpha_c) \cdot \cos(\delta) \\ \tilde{y} &= \cos(\delta_c) \cdot \sin(\delta) - \sin(\delta_c) \cdot \cos(\delta) \cdot \cos(\alpha - \alpha_c)\end{aligned}\quad (3.82)$$

From these projected coordinates, the radial distance, R , and the position angle, θ , are computed as

$$\begin{aligned}R &= \sqrt{\tilde{x}^2 + \tilde{y}^2}, \\ \theta &= \arctan 2(\tilde{x}, \tilde{y}) + 2\pi \pmod{2\pi}\end{aligned}\quad (3.83)$$

The requirement of central symmetry is enforced by the inclusion of a multiplicative term in the likelihood. For a given set of parameters values of α_c, δ_c we divide the computed polar angles of individual stars θ , into four symmetric quadrants (divisions at $[0, \pi/2, \pi, 3\pi/2]$) and require that the number of stars in each quadrant be Poisson distributed with a mean rate given by $N_q = N_{tot}/4$. Under this model, the likelihood of any given proposal for the models parameters (α_c, δ_c) will be

$$\begin{aligned}\mathcal{L} &= p(N_1, N_2, N_3, N_4 | \alpha_c, \delta_c) \\ &= \mathcal{P}(N_1 | N_q) \cdot \mathcal{P}(N_2 | N_q) \cdot \mathcal{P}(N_3 | N_q) \cdot \mathcal{P}(N_4 | N_q)s\end{aligned}\quad (3.84)$$

where $N_i, i = 1, 2, 3, 4$ is the number of sources in each quadrant, and $\mathcal{P}(N_i | N_q)$ is the Poisson distribution with mean rate $N_{tot}/4$ evaluated at N_i .

3.7.2 Models with biaxial symmetry

In this Section we extend the previous models to allow for deviations from radial symmetry. We do this by allowing variations of the radial profile that depend on the angular coordinate but still maintain biaxial symmetry. This can be done in many ways. In this work we focus in the simplest one: the analytical expression of the radial profile is maintained along any radial direction but the profile parameters (r_c an r_t for example in the King profile) have an ellipse-like dependence on the angular coordinate.

This requires the definition of a coordinate system centred at the cluster centre and potentially rotated from the RA-Dec system of axes. We thus include in the set of

parameters the angle ϕ between the principal axis of the ellipse and RA-Dec system. The coordinates \tilde{x} and \tilde{y} of Eq. 3.82 are rotated by this angle ϕ , to obtain coordinates x and y . Then, R and θ are computed from the latter by means of Eq. 3.83.

The radially symmetric parameters of the previous Section have now an angular dependancy (thus are different for each star), which is expressed by means of the characteristic radii at the semi-major and semi-minors axes (denoted by subscript a and b , respectively). These new radii are expressed as

$$r(\theta) = \frac{r_a \cdot r_b}{\sqrt{(r_a \sin(\theta))^2 + r_b \cos(\theta))^2}}. \quad (3.85)$$

where θ is the position angle of each star, which is measured from the semi-major axis, and r_a and r_b are the parameters representing the characteristic radius at the semi-major and -minor axis, respectively.

We illustrate this new biaxial dependancy in the King's profile. For it, the likelihood term now is defined as

$$p(R, \theta | \phi, r_{ca}, r_{cb}, r_{ta}, r_{tb}, k_1, \mathcal{M}_1) = k_1 \cdot R \cdot \left(\frac{1}{\sqrt{1 + (R/r_c(\theta))^2}} - \frac{1}{\sqrt{1 + (r_t(\theta)/r_c(\theta))^2}} \right)^2 \quad (3.86)$$

where r_c and r_t are obtained from Eq. 3.85. Explicitly they are,

$$r_c(\theta) = \frac{r_{ca} \cdot r_{cb}}{\sqrt{(r_{ca} \sin(\theta))^2 + r_{cb} \cos(\theta))^2}}, \quad (3.87)$$

$$r_t(\theta) = \frac{r_{ta} \cdot r_{tb}}{\sqrt{(r_{ta} \sin(\theta))^2 + r_{tb} \cos(\theta))^2}} \quad (3.88)$$

r_{ca} and r_{tb} are the core and tidal radius at the semi-major axis of the ellipse, and r_{cb} and r_{tb} are the corresponding ones of the semi-minor axis. In these models, all the cluster members share the same $r_{ca}, r_{cb}, r_{ta}, r_{tb}$ parameters, but each individual member have different r_t and r_c . Notice that we do not constrain the two ellipses to have the same aspect ratio, but they are co-aligned.

For the remaining model the likelihoods are similarly obtained. We do not incorporate any angle dependence for the exponents α, β or γ .

The position angle of the semi-major axis with respect to the Right Ascension axis (ϕ) is constrained using the equivalent of the radial symmetry likelihood term, except that now the position angle has its origin at the semi-major axis.

We infer the posterior distributions of the parameters in our biaxially symmetric models using the same approach as for the radially symmetric ones. However, we restrict the semi-major axes of the core and tidal radii to be larger, or at least equal, to their

corresponding semi-minor axis.

3.7.3 Models with luminosity segregation

In the previous Sections we have compared several alternative models for the spatial density distribution of the Pleiades cluster. Finally, in this Section we revisit another classical model selection problem in the context of the Pleiades number density distribution: luminosity segregation, where we hope to benefit from the Bayesian methodology.

We consider the previous biaxially symmetric models extended to introduce a dependence of the core radius with the J magnitude. We assume that stars of the same mass have approximately the same magnitude and that distance differences (due to the 3D spatial extend of the Pleiades) average out. The core radius dependence with the J magnitude is modelled as

$$r_c(\theta, J) = r_c(\theta) + \kappa \cdot (J - J_{mode}), \quad (3.89)$$

where J_{mode} is the mode of the J band distribution.

The slope of the relationship, κ , is independent of the angle θ . Therefore, for $J = J_{mode} = 13.6$ the model reduces to the elliptic profile described in Section 3.7.2. A positive value of κ corresponds to smaller values of the core radius for stars brighter than $J_{mode} = 13.6$. In other words, it describes a system where the more massive stars are more concentrated than the less massive ones.

3.7.4 Priors in the Projected Spatial Distribution models

Finally, the last ingredient to perform the inference of the parameters in the models describing the PSD of the Pleiades, is the prior probabilities. The prior probabilities must allow all possible combinations of the parameters, particularly if we are interested in selecting the best model.

Therefore, the we have assumed the following priors or the model comparison of the PSD models.

Exponential with scale of one for all exponent parameters. However, due to numerical overflows in the GDP and Restricted Generalised Density Profile (RGDP) models we are forced to truncate these exponentials at a value of 100. To be fair we also truncated these priors in the rest of the models.

Normal bivariate uncorrelated prior for the central coordinates with mean at $[56.65^\circ, 24.13^\circ]$ and standard deviations of one degree. This centre value is standard in the literature (e.g. [Bouy et al. 2015](#)) and the dispersion of several degrees ensures that no realistic centre value is discarded.

Half-Cauchy for radial parameters. The core radius have a scale parameter of 1 pc while the tidal one has it at 10 pc. These two priors convey our a priori information on

the scales of the core radius, which is in the order of a few pc, while the tidal radius is expected in a few decades.

Uniform in $[-\pi/2, \pi/2]$ for the angle ϕ , thus we put no a priori in the angle value³²

Normal univariate centred at zero with standard deviation of 0.5 pc mag^{-1} , as a prior for κ , the slope of the luminosity segregated core radii. It represents our prior believes of almost negligible luminosity segregation.

The previous priors (with the exception of the ϕ angle) fall in the category of *weakly informative* ones, as it is suggested by [Gelman \(2006\)](#).

Finally, to compare the previous PSD models, we use the model selection methodology described in Section 3.1.2. The results of this analysis are detailed in Section 4.4.

³²To the best of my knowledge, there is no position angle reported in the literature for the semi-major axis of the Pleiades. [Raboud & Mermilliod \(1998\)](#) estimates that this axis points towards the galactic centre but gives no specific value nor uncertainties.

Chapter 4

Results

In this Chapter, I characterise the methodology detailed in Chapter 3 and then I applied it to the RDDR2 data set (Sect. 2.7). To characterise the methodology as a classifier, I measure its precision and accuracy when applied on synthetic data where the true members of the cluster are known. With this characterisation, I am able to obtain an optimal probability threshold, but only for classification purposes. Afterwards, I apply the methodology to the RDDR2 and I find the candidate members of the cluster using the optimal probability threshold. Then, I compare these candidate members with those found by previous studies.

Later, I analyse the main results of this work, those that fulfil the objective: the statistical distributions that characterise of the cluster population. Then, I give the details of the spatial, velocity, luminosity and mass distributions. Finally, I end this Chapter describing the physical scenario of the evolution of the mass distribution of the Pleiades by comparing it with other mass distribution of younger and older clusters.

4.1 Performance of the classifier

As mentioned earlier, the main objective of the methodology of the BHM is the statistical characterisation of the NYC populations. However, as a by product, it also obtains the individual membership probability distributions of the objects comprising the data set. These membership probability distributions, together with a probability threshold, allow a direct classification of the objects into cluster and field members. The classification resulting from this procedure, as any other measured property, has an uncertainty. By evaluating this uncertainty under the results of synthetic data (in which the true members are known) we are able to measure the accuracy and precision of the classification process as a function of the probability threshold used. This section explains how an objective probability threshold can be found by maximising the accuracy of the classifier.

To measure the accuracy of our classifier, I test it over synthetic data sets that resemble

the real RDDR2 data set (Section 2.8). An ideal test to our classifier will be to apply it over well known dataset in which tags of cluster and field members were already present. However, if we may have access to these tags, a classifier may not be needed. The Pleiades cluster being one of the most studied cluster in history, it is the NYC with most of these tags (see Section 4.2). This is also one of the reasons for which we decided to benchmark our methodology on it. In spite of the large number of candidate members for the Pleiades clusters, the synthetic data and its true tags are still needed. The reasons are the following. First, the list of candidate members provided by the literature is not infallible. We can never be sure that this list is complete and unpolluted. Here it is important to note that the astrophysical domain of the phenomenon marks a very important distinction with common supervised classification methods. A perfect and real training set is not available. It must be created from simulations. Second, even if the most probable candidate members from the literature were used as a training set (as done for example by Sarro et al. 2014) the very faint end of the magnitude distribution (represented by brown-dwarfs) is still a *terra incognita* where candidate members are scarce or not even exist.

Thus, to overcome the problem of the true tags, we decided to create synthetic data sets. These synthetic true tags, and therefore the results obtained from them, rely on the assumption that our cluster and field models resemble the real data. I am aware that these models are far from perfect, but so far this assumption provides the best option. Although this assumption enable us to quantify the internal consistence (precision and accuracy) of our classifier, it does not give any indication about possible biases in the model. To explore this possibility, in the next Section, I compare our real data classification results with those of the literature.

The random nature of the synthetic data sets demands the repetition of the data sets and results. This repetitions avoid any bias caused by excursions of the random number generator (bad luck), and more importantly, they allow us to compute the uncertainty in the accuracy and precision of the classifier. As explained before, the methodology presented in this work is computing demanding. Thus, to be able to repeat at least five times the results of the synthetic data sets, we further reduce the data set size. The inference process in a data set of 10^4 objects demands almost week of computing time. Thus, we decided that such data set provided a good compromise between computing time and number of objects. Furthermore, to provide a better estimate of the contamination rate on the results over the real RDDR2 data set (the one with the 10^5 objects) we choose to work with the 10^4 objects with high membership probability according to Bouy et al. (2015). Since this sample is relatively more entangled with the cluster than that of the RDDR2, we assume that the contamination rate we measure on this sample will be comparable or even higher than that hypothetically obtained over the 10^5 RDDR2.

Briefly, to create the synthetic data set, the procedure is the following. First, using the methodology of the previous Chapter, I obtain a sample of the posterior distribution of

the parameters in the model given the 10^4 real data set. Then, I choose the particle with highest posterior probability as the MAP estimate of the posterior distribution. Using this particle positions in the parametric space, I generate five synthetic data sets of 10^4 objects each. Then, I tag these objects according to their parent population: cluster or field. Afterwards, using the vector of synthetic values of each object, I assign their uncertainties and missing value entries (more details below).

Finally, I run the methodology over the five synthetic data sets, and obtain a sample of the individual membership probability distributions of each synthetic object. Then, I compare the true tags with the measured ones as function of the probability threshold.

To further test the performance of the classifier, I apply it on a synthetic data set in two different cases. In the first case the data set is one of the five synthetic ones. Thus it contains objects with missing value entries in their vector of observables. In the second case the data set is the same as in the previous case, but this time all the objects have fully observed vectors (i.e. do not have missing value entries). The comparison of the results rendered by these two cases allows us to quantify the impact of missing values.

Objects in the RDDR2 have full observed proper motions vectors. Since missing values appear only in the photometric entries, I only mask as missing the photometric entries of the synthetic data sets. The procedure to mask entries as missing is the following.

For each synthetic datum, I use the mask of missing entries of one of its closer neighbours in the real data set. Here, distance is measured in the euclidean sense. If I were to use the missing value mask of the nearest neighbour in the real data set, then I will obtain a biased sample in which objects with fully observed vectors will be underestimated. This is the inevitable consequence of euclidean distances being measured in subspaces resulting from removing the dimensions of the missing entries. Since these distances are the smaller, or at most equal, to those measured in the complete space, the fully observed objects will be under represented.

The mask of missing entries is chosen from amongst the missing values of the closer neighbours in the available CMDs: $\{K_s, J - K_s\}$, $\{J, J - H\}$, $\{K_s, H - K_s\}$, $\{J, Y - J\}$, $\{K_s, i - K_s\}$. These CMDs comprise, in decreasing order, the bands and colours of the magnitudes with fewer missing values (see Table 2.2). The mask of missing entries is then chosen as follows. First, for each CMDs subspace, I find the set of real objects that has fully observed entries, I call it $C_{or,i}$ and its fraction from the total, f_r . Then, I take a random sample from the synthetic data with size such that its fraction, f_s , equals f_r . For objects in this sample I assign the missing value pattern of the nearest neighbour in $C_{or,i}$. I repeat this procedure for the rest of the CMDs. In this way, the synthetic data sets have fractions of objects with and without missing entries, similar to those of the objects in the real data set.

To assign uncertainties I proceed as follows. For uncertainties in the proper motions I use those of the nearest neighbour from the real data set. If I were to use the nearest

neighbour scheme for uncertainties in the photometry, then I will obtain biased results. These uncertainties will be biased towards those of the less precise measurements. Again, this is a consequence of the missing entries in the observable vectors. The euclidean metric results in the preferential choosing of objects with missing values. These missing values occur mostly at the faint end, where uncertainties are larger. Therefore, these uncertainties will be biased towards these larger values. To avoid this issue, I fit 8th degree Chebyshev polynomials to the uncertainties as a function of the magnitudes. Then, I use these polynomials to establish the photometric uncertainties of the synthetic data sets.

Once the synthetic data sets were created I run the methodology on each of them and recover the membership probability distribution of each object. Then, I classify each object as cluster or field member. To classify an object as a cluster member, the mode of its cluster membership probability distribution must be higher than the probability threshold. Otherwise it is classified as a field object.

The classifier performance was measured by counting, as a function of the probability threshold, the cluster members correctly classified or True Positives (TPs), the field members correctly classified or True Negatives (TNs), the field members classified as cluster members, or False Positives (FPs), and the cluster members classified as field members or False Negatives (FNs). With them I calculate the following quantities: the True Positive Rate (TPR), which is the ratio of true positives over the sum of true positives plus false negatives, the False Positive Rate (FPR), which is the ratio of false positives over the sum of false positives plus true negatives, the Contamination Rate (CR), which is the ratio of false positives over the sum of false positives plus true positives, the precision or Positive Predictive Value (PPV), which is the ratio of true positives over the sum of true positives plus false positives, and, the Accuracy (ACC), which is the ratio of the sum of true positives plus true negative over the sum of true and false positives and negatives.

These are,

$$\begin{aligned} TPR &= \frac{TP}{TP + FN} \\ FPR &= \frac{FP}{FP + TN} \\ CR &= \frac{FP}{FP + TP} \\ PPV &= \frac{TP}{TP + FP} \\ ACC &= \frac{TP + TN}{TN + FN + TP + FP}, \end{aligned}$$

which are defined at each probability threshold. I use the results of the five synthetic data sets to quantify the uncertainties of the previous quantities.

In Fig. 4.1, I show the mean and uncertainty of the TPR and CR measured on the five synthetic data sets. The uncertainty is represented by the maximum deviation from the

mean. Also, this Figure shows the TPR and CR measured on a synthetic data set with fully observed objects (i.e. objects with non missing entries). As this Figure shows, the missing values have a negative impact in our classification. They diminish the TPR and increase the CR. This negative impact is expected since the observables we are using are highly discriminant in the classification process (see Section 2.7.1). Since cluster and field are highly entangled in the 10^4 objects synthetic samples, when one of these observables is missing the classification is more uncertain or it could even be biased. Interestingly, the CR above probability threshold 0.8 is independent of the missing values and remains low ($\lesssim 5\%$). In spite of the negative impact of missing values, the methodology delivers low contamination rates ($\lesssim 5 - 10\%$) and high recovery rates ($\lesssim 90 - 96\%$) for probability thresholds in the $0.5 - 0.9$ range.

In Figure 4.1, I also show the CR and TPR of [Sarro et al. \(2014\)](#) (reported in their Table 4). Previous to discuss the differences between both works I inform the reader about the unfairness of this comparison. First, in the works of [Sarro et al. \(2014\)](#) and [Bouy et al. \(2015\)](#), the generative models are constructed using only fully observed objects (i.e. without missing entries), these objects represent only $\sim 1\%$ of our RDDR2. Afterwards, they apply those models to all the objects in the DDR2 data set (i.e. objects with and without missing entries). Thus, their results are more similar to those I find on the synthetic data set with only fully observed objects (blue lines in Fig. 4.1). Second, the synthetic data sets in which both works measure the TPR and CR are different. They are constructed with different generative models, different number of objects, and different missing value distributions.

From the comparison between [Sarro et al. \(2014\)](#) TPR and CR, with the ones I find on the synthetic data set comprising only fully observed objects, we see the following. The TPR of both works agree within the uncertainties. The CR of both works agree, within the reported uncertainties, for probability thresholds below 0.8. At higher probability thresholds, our methodology delivers lower CR. Even in the case of the unfair comparison between the TPR and CR of [Sarro et al. \(2014\)](#) with those I measure on the synthetic data sets including objects with missing entries, our CR outperforms that reported by [Sarro et al. \(2014\)](#) at the small price of a lower ($\sim 4\%$) TPR.

Now, I describe the procedure to set an optimal probability threshold. This probability threshold, although not needed to obtain the posterior distribution of the parameters modelling the cluster population, is needed, however, to objectively classify an object as a cluster member. I establish this threshold using only the synthetic data sets containing objects with missing entries in their vector of measurements. The approach I use to set this probability threshold is that of the maximum accuracy (ACC) for the classification.

Figure 4.2 shows the ACC and the PPV of the classifier when it is applied on synthetic data sets containing objects with missing value entries. The lines and the grey regions depict, respectively, the mean and the maximum deviations of the results of the

five synthetic data sets. The maximum deviation is used as a proxy for the uncertainty. The highest mean accuracy, $\text{ACC}=96.5 \pm 0.1\%$, happens at probability threshold $p_t = 0.84$. Thus, I choose it as the optimal classification threshold. At this value, the CR is $4.3 \pm 0.2\%$, the TPR is $90.0 \pm 0.05\%$, and the PPV is $95.6 \pm 0.2\%$.

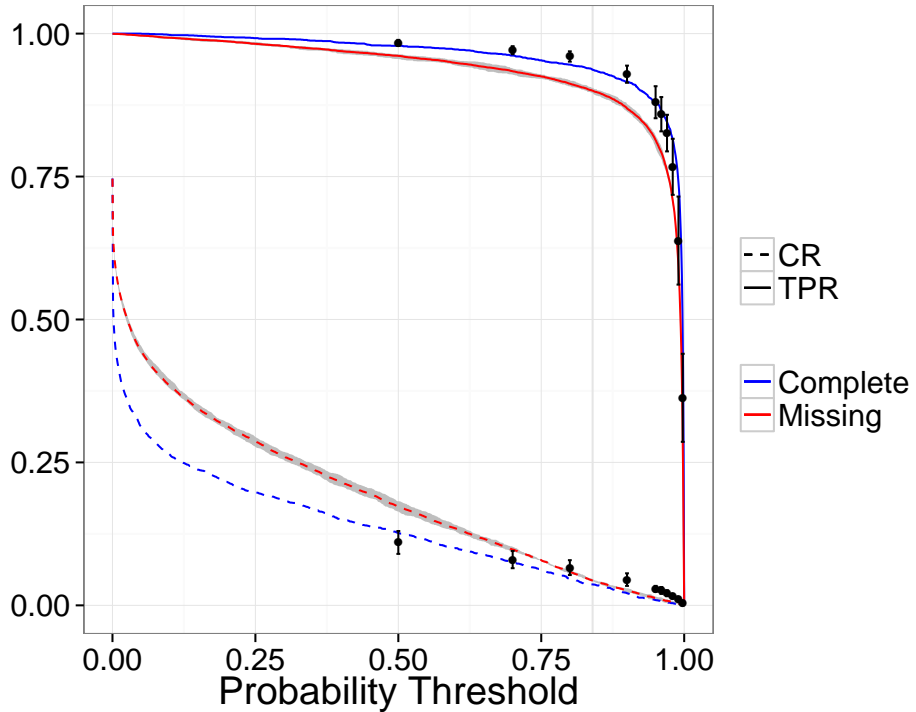


Figure 4.1: The mean TPR (solid line) and CR (dashed line) resulting from five synthetic data sets including objects with missing entries (red lines). Also the TPR and CR resulting from a synthetic data set comprising only objects with fully observed vectors (blue lines). The shaded regions (grey) show the uncertainties computed from the five synthetic data sets. The black dots show the TPR and CR reported by [Sarro et al. \(2014\)](#) for their model. See text for warnings on this comparison. Reproduced from Figure 3 of [Olivares et al. \(2017\)](#), *The Seven sisters DANCe III: Hierarchical Bayesian model*, A&A, Vol. submitted.

We further investigate the impact that objects with missing value have on our methodology. In specific, I analyse possible biases introduced by these objects. To do this, I compare the membership probabilities inferred by the BHM on: i) the synthetic data set with fully observed objects (i.e. not a single missing value), and ii) a synthetic data set, created from the previous one, but with some observables masked as missing (using the procedure previously described).

In Fig. 4.3, I compare the mode of the recovered membership probabilities. The

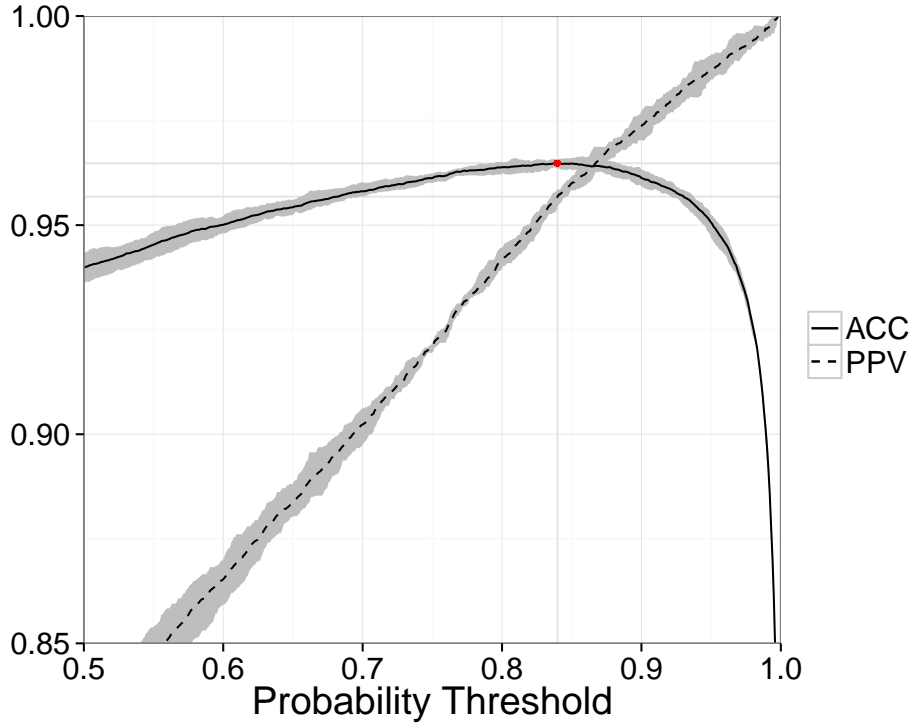


Figure 4.2: Mean accuracy (ACC, solid line) and precision (PPV, dashed line) of the classifier as a function of probability threshold. The shaded regions shows the uncertainties computed from the five synthetic data sets. The higher accuracy is obtained at $p_t = 0.84$ (red dot). Reproduced from Figure 3 of [Olivares et al. \(2017\)](#), *The Seven sisters DANCe III: Hierarchical Bayesian model*, A&A, Vol. submitted.

horizontal axis contains the membership probabilities of the data set with fully observed objects (I call this case the complete one). The vertical axis shows the membership probabilities of the same objects but in which some entries were masked as missing (I call this case the Incomplete one). As can be seen from this figure, the missing values impact our results by spreading the membership probabilities. Ideally, we would like to recover membership probabilities following the line of slope one. This is the case of the majority of fully observed objects (red squares) in the data set containing objects with missing entries. The most striking deviations come from those objects with the *CI* masked as missing (enclosed in black). The BHM methodology uses the *true CI* to prescribe the *true* photometry. Also, it uses the observed *CI* to constrain the marginalisation integral of the *true CI*. Thus, as expected, a missing *CI* produces a spread in the membership probability.

The objects with a missing *CI* show two different behaviours. In one hand, the

incomplete case (data set with missing values) overestimates the membership probabilities, while in the other case, it underestimate them. The former case is observed in the vertical stripe with $P \sim 0$ in the complete case, while the later case corresponds to those in the combed area below the line of unit slope. Objects in the former case increase the CR, and their effect can be seen by the difference between red and blue dashed lines in the lower-left region of Fig. 4.1. On the other hand, the objects in the latter case diminish the TPR, and their effect can also be seen by the difference between red and blue solid lines in the top-right region of Fig. 4.1.

The increase in CR reaches its maximum near probability zero in the horizontal axis (Complete case) and goes to zero at probability thresholds of ~ 0.9 . Therefore, the impact this increased CR has in our results is marginal. For example, at the optimal probability threshold $p_t = 0.84$, the increase of CR due to objects with missing entries represent only 1.8%. This fraction corresponds to those objects inside the black box of Fig. 4.3 (upper left corner). However, the objects in the second case, those that diminish the TPR, represent the typical unavoidable loss of members due to their missing entries. These amount to a 4% loss in the TPR, at the optimal probability threshold, $p_t = 0.84$.

The bias introduced in the recovered membership probabilities due to objects with missing value entries, can be quantified using the root-mean-square (rms) of the difference between the means of the two recovered membership probabilities (Complete and Incomplete cases). The total rms is 0.12. On the one hand, fully observed objects in both data sets (Complete and Incomplete cases) have a rms of only 0.02. On the other hand, objects with missing entries, excluding those with missing CI , have a rms of 0.08. The rms of objects lacking the CI is 0.14. The previous effects show an overall agreement between results on data sets with and without objects with missing entries. Nonetheless, care must be taken when dealing with individual membership probabilities. An object with a missing value in the Y, J, H and K_s may have a diminished membership probability (with a rms of 0.08), while an object with a missing CI may show an increased membership probability (with a rms of 0.14).

However, as have been mentioned before, the methodology described in this work aims at the statistical distributions of the cluster population. The individual membership probabilities are just a useful by product. The methodology develop here, though, works by ensuring that each object contributes to the posterior distribution of the parameters modelling the cluster population, proportionally to its cluster membership probability. In this sense our results are free of any possible bias introduced by cuts in the membership probability. Nevertheless, there is still contamination. In particular, that arising from objects with missing entries. This contamination in the statistical distributions that we aim to obtain must be quantified. To do this, I compute the expected value of the CR found in this section. It is $\langle CR \rangle = 5.8 \pm 0.2\%$. In this expected value, each CR contributes proportionally to the probability threshold at which it is measured. Since the

vast contribution to this CR comes from probability thresholds below 0.2 (see Fig. 4.1), the expected value of the CR remains low.

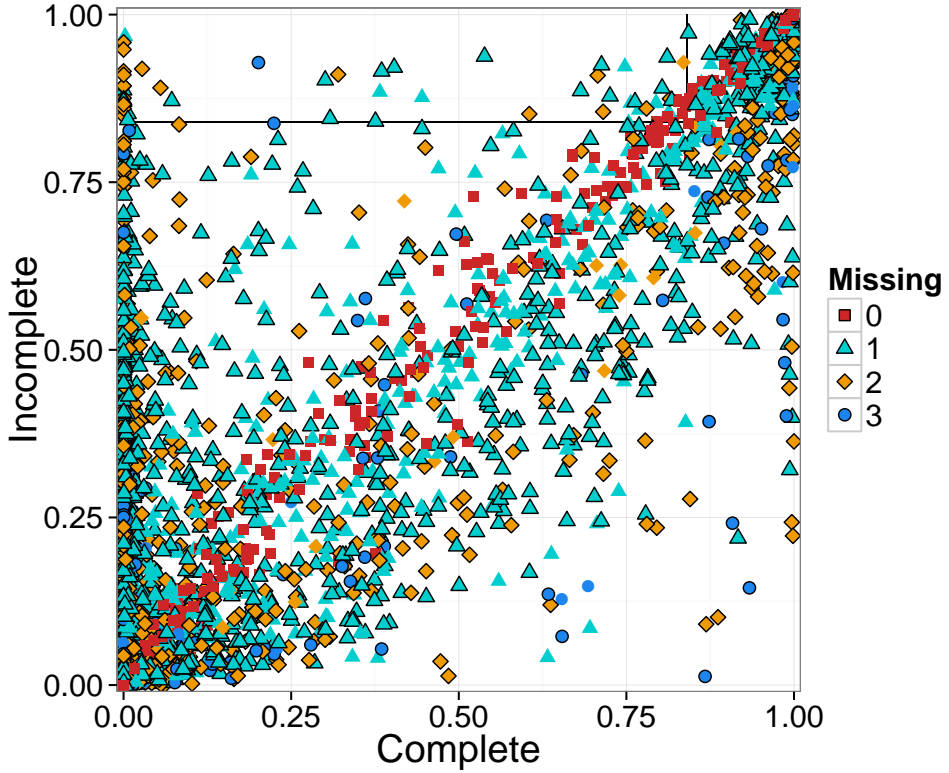


Figure 4.3: Comparison between the cluster membership probabilities recovered from the synthetic data set with objects having missing value entries (vertical axis, labeled Incomplete), and, the synthetic data set with fully observed objects (horizontal axis, labeled Complete). The colour and shape indicate the amount of missing entries. The symbols enclosed in black indicate a missing CI . The top left box contains objects considered as contaminants due to missing values at the probability threshold $p_t = 0.84$. Reproduced from Figure 4 of Olivares et al. (2017), *The Seven sisters DANCe III: Hierarchical Bayesian model*, A&A, Vol. submitted.

In statistical science, in machine learning particularly, is sometimes useful to analyse the performance of a binary classifier by means of the Receiver Operating Characteristic (ROC) space. It is a visual diagnostic of the ability of the classifier to perform its job. The ROC space plots the TPR as a function of the FPR. A perfect classifier would be that in which the TPR=1 and the FPR=0. On the other hand, a random classifier, which will assign the class with a random probability (e.g. flipping a coin), would be that with TPR=FPR=0.5. Such classifier lays in the line of slope one in the ROC space.

As an example, for one of the five synthetic data sets, I classified objects with a binary

random classifier with prior probabilities as those given by the fraction of field and cluster members (0.8 and 0.2, respectively, notice that the synthetic data sets have only 10^4 objects). This is given by a binomial distribution with probability of success equal to 0.2. In ten random realisations of this classification, the TPR=FPR=0.5. In addition, the PPV and CR of such random classifier are 0.074 ± 0.003 and 0.925 ± 0.003 , respectively.

Furthermore, if the classifier returns a continuous random variable which then is used to do the classification, like the probability returned by the BHM, instead of having a single point in the ROC space, the classifier produces a curve. The ROC curve of a perfect classifier will pass through the point TPR=1 and the FPR=0, for a given classification threshold. The quantitative diagnostic for this kind of binary classifier is the Area Under the Curve (AUC) ROC. As its name indicates, the AUC is the integral of the ROC curve. Thus the closer the AUC is to one, the better the classifier is. In Fig. 4.4, I show the ROC curve for our classifier when applied over synthetic data containing objects with missing entries. This ROC curve correspond to one of the five synthetic realisations described throughout this section. As can be seen from this Figure our classifier does an excellent job, with an AUC=0.992.

4.2 Comparison with the literature

In the following, I will compare the cluster membership probabilities recovered by the BHM methodology, after applying it to the real RDDR2, with three sources from the literature: [Stauffer et al. \(2007\)](#), [Bouy et al. \(2015\)](#) and [Rebull et al. \(2016\)](#).

In the following I will refer to the High Membership Probability Sample (HMPS) as those objects in the RDDR2 from which the BHM returns a membership probability distribution with a 84th percentile larger than the optimal probability threshold of 0.84 determined in the previous Section. The 84th percentile ensures that the uncertainty is taken into account. Figure 4.5 shows the proper motions and K_s vs CI CMDs of the HMPS of candidate members classified as single stars ($\langle p_{EMB} \rangle < 0.5$), and EMB ($\langle p_{EMB} \rangle \geq 0.5$). In a similar way, Fig. 4.6 shows the K_s vs $J - K_s$ CMDs of the HMPS of candidate members.

Since the RDDR2 is contained in the data set used by [Bouy et al. \(2015\)](#), the comparison in this case can be extended not just to the common candidate members, but to all objects in the RDDR2. Furthermore, after applying the learned BHM to the entire DDR2 we found no newer members, which confirms our original assumption of an almost negligible probability of leaving a cluster member out of the RDDR2. Since no members are found outside the RDDR2, in the following the comparison between [Bouy et al. \(2015\)](#) membership probabilities and those estimated here is done based on the RDDR2.

However, the comparison with [Stauffer et al. \(2007\)](#), and [Rebull et al. \(2016\)](#) can only be done in terms of the candidate members in common. Since [Rebull et al. \(2016\)](#)

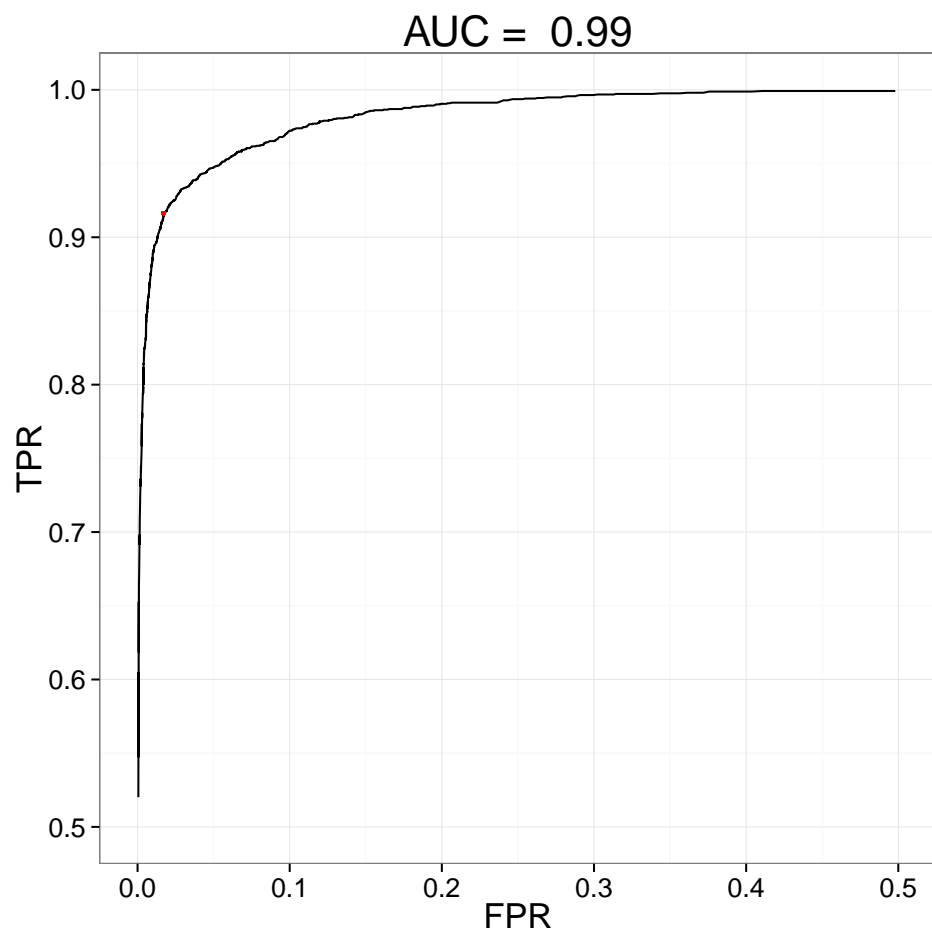


Figure 4.4: ROC curve of the BHM by-product classifier when applied on the synthetic data set containing objects with missing entries. As can be seen, the AUC=0.992 diagnose it as an excellent classifier.

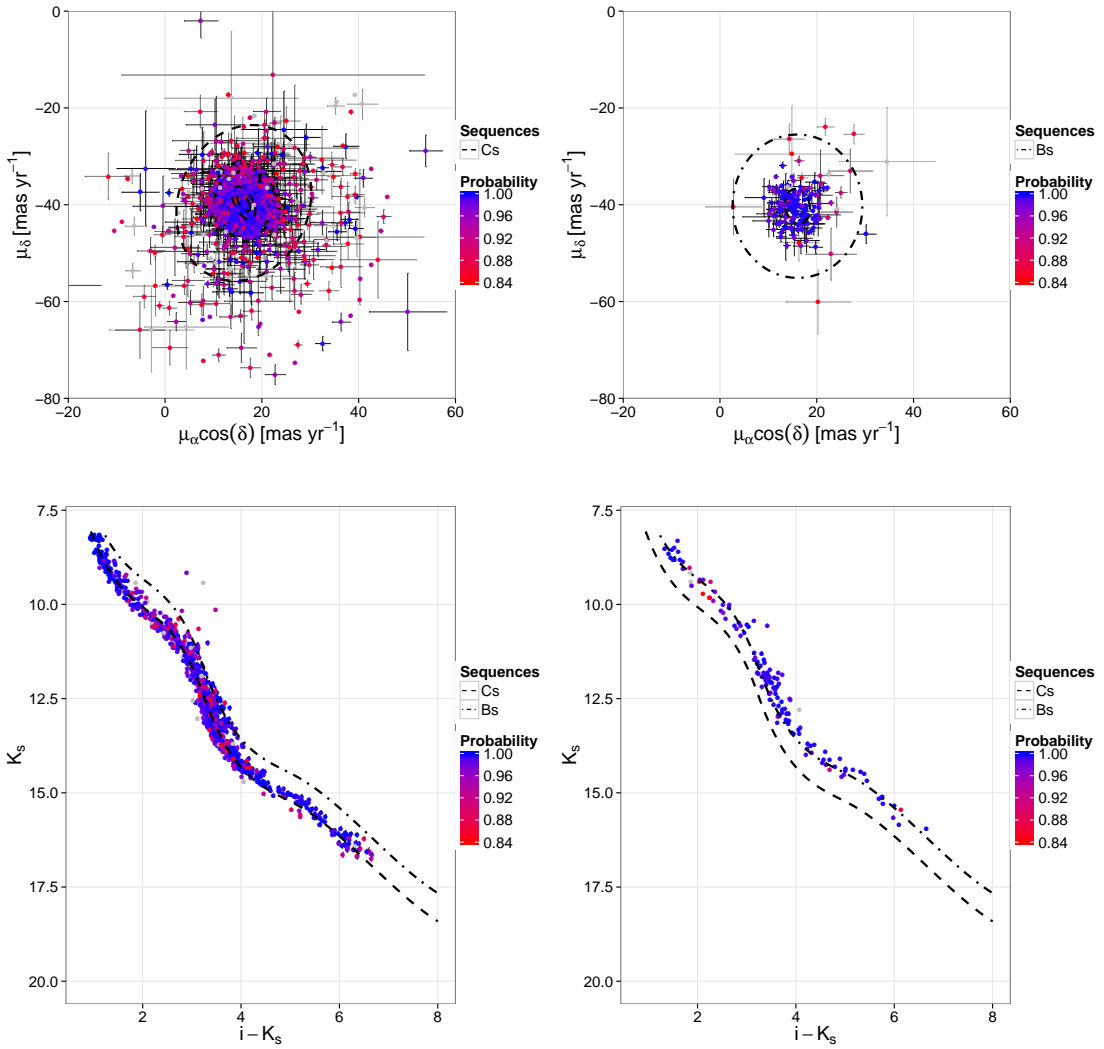


Figure 4.5: Proper motions (top panels), and K_s vs $i - K_s$ CMDs (bottom panels) of the HMPS of candidate members. The left panels show objects classified as single stars (with $\langle p_{EMB} \rangle < 0.5$), while the right panels those classified as EMB (with $\langle p_{EMB} \rangle \geq 0.5$). The colour code shows the mode of the individual cluster membership probabilities. Objects with $P_{84\%} > 0.84$ but mode lower than 0.84 are shown as grey dots. Also shown the mode of the parameters posterior distribution for single stars (Cs, dashed lines) and EMB (Bs, dot dashed lines).

obtain their list of candidates based on photometric variability, and this observable is not present in our set of observables, this comparison represent an important source of external validation.

4.2.1 Candidate members from Stauffer et al. (2007)

Stauffer et al. (2007) published two list of candidate members. The first one contains 1417 objects compiled from the literature (see Table 2 of the mentioned work). These objects were classified as candidate members by several authors. As Stauffer et al. (2007) mention, this list is inhomogeneous, incomplete and certainly includes non-members. I

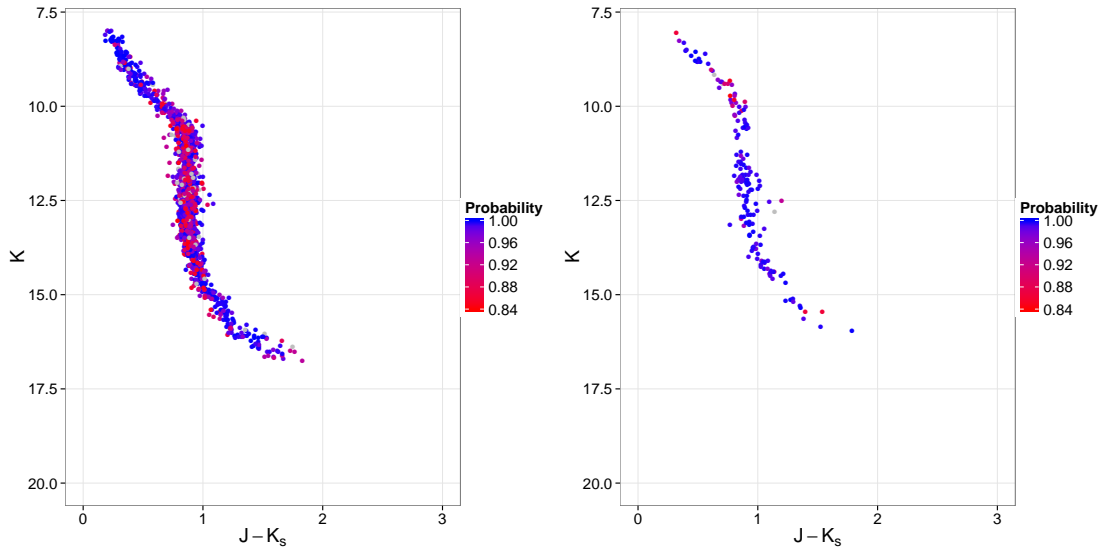


Figure 4.6: K_s vs $J - K_s$ CMDs of the HMPS of candidate members. The left panel shows objects classified as single stars (with $\langle p_{EMB} \rangle < 0.5$), while the right panels those classified as EMB. Captions as in Fig. 4.5.

refer to this list as Stauffer Table 1 (ST1). Their second list contains 55 candidate members (see Table 5 of the mentioned work). [Stauffer et al. \(2007\)](#) found these members using infrared photometry and proper motions. I refer to this list as Stauffer Table 2 (ST2).

Cross matching (at CDS¹, within 1 arcsec radius) the previous two lists with the DDR2 catalogue ([Bouy et al. 2015](#)), I find that only 1384 and 54 of the ST1 and ST2 lists have a counter part in the DDR2 catalogue, respectively.

Concerning our list of candidate members, after cross matching it with the two lists of [Stauffer et al. \(2007\)](#), ST1 and ST2, I recover 1146 and 34 of the candidate members, respectively. Compared to the candidate members of [Bouy et al. \(2015\)](#), our BHM recovers 28 more candidate members in ST1 and the same in ST2.

As mentioned before, the ST1 list is an exhaustive compilation of Pleiades members. It contains objects that were classified, at some point in history, as Pleiades candidate members, even when their membership probability are as low as 0.1 ([Stauffer et al. 2007](#)). For this reason I will not analyse the details of 238 rejected objects of ST1. It suffices to show that these rejected objects lie far from the cluster photometric or proper motions loci, as shown in Fig. 4.7.

On the other hand, from the 20 objects in ST2 that are rejected by the BHM, 18 of them lie below the cluster photometric sequence and far from the proper motion locus, see Fig. 4.8. The remaining two (DANCe IDs: J034552.57+235145.9 and J034543.47+233851.5), although have observed photometric vectors compatible with the clusters sequence, their proper motions still are far from the cluster centre (with $\mu_\alpha \cos(\delta) \sim 40 \text{ mas} \cdot \text{yr}^{-1}$), see Fig. 4.8.

¹ Using the service <http://cdsxmatch.u-strasbg.fr/xmatch>

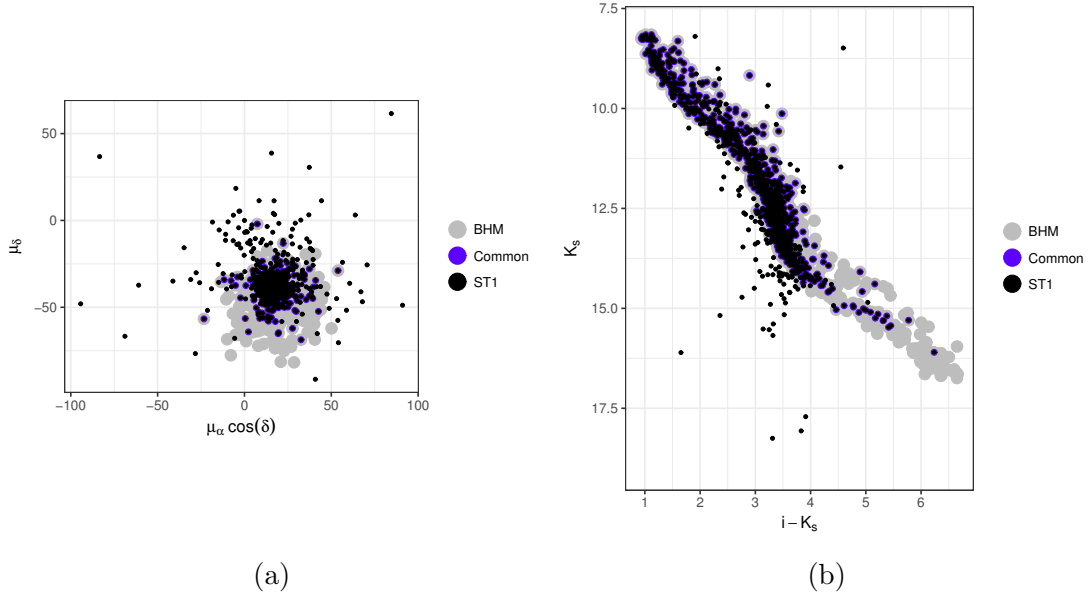


Figure 4.7: Proper motions (a) and K vs $i - K$ CMD (b) of the ST1 candidate members in the DDR2 catalogue (black). Also shown, the objects classified as candidate members in the BHM (grey), and in both ST1 and BHM (blue).

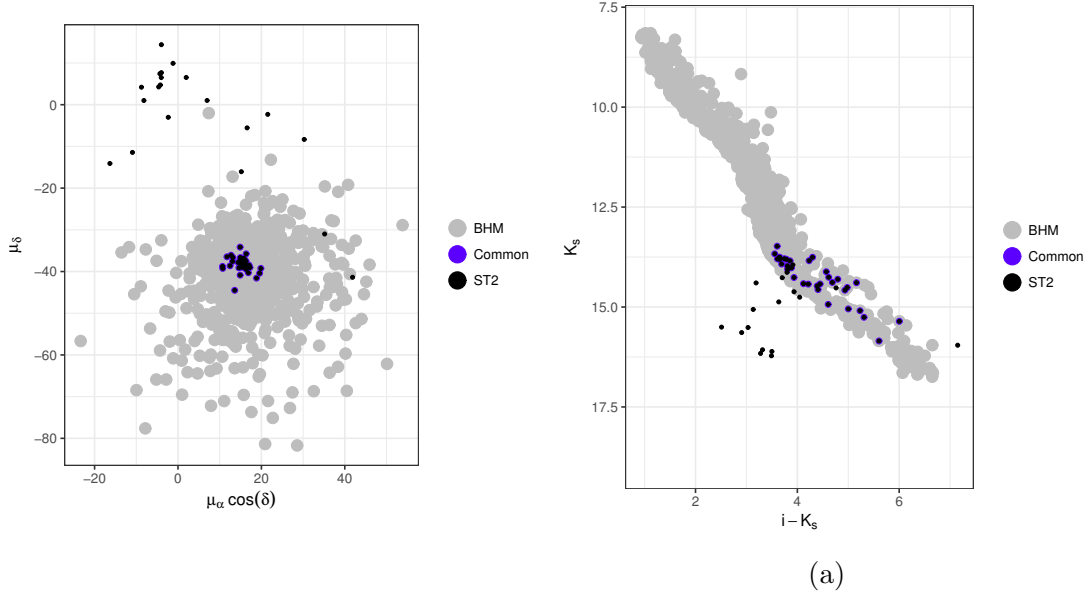


Figure 4.8: Proper motions (a) and K vs $i - K$ CMD (b) of the ST2 candidate members in the DDR2 catalogue (black). Also shown, the objects classified as candidate members in the BHM (grey), and in both ST2 and BHM (blue).

4.2.2 Candidate members from Bouy et al. (2015)

The fact that the work of [Bouy et al. \(2015\)](#) and the present one use the same DDR2 data set (although our model is constructed with the RDDR2), allow me to directly compare the membership probabilities of both works. As mentioned before, this comparison can be extended to all objects in the data set and not just to the candidate members of the Pleiades cluster. Since [Bouy et al. \(2015\)](#) reported only an statistic of the membership

probability distributions, to do a fair comparison, I summarise the membership probability distributions recovered by the BHM with the mode.

Using the optimal probability threshold of 0.84 to classify the cluster members, we can see that, as shown by Fig. 4.9, both methodologies agree on the outstanding 99.6% of the classified objects. Concerning just the candidate members, the agreement is still high, $\sim 90\%$. In the following I discuss the 10% discrepancies.

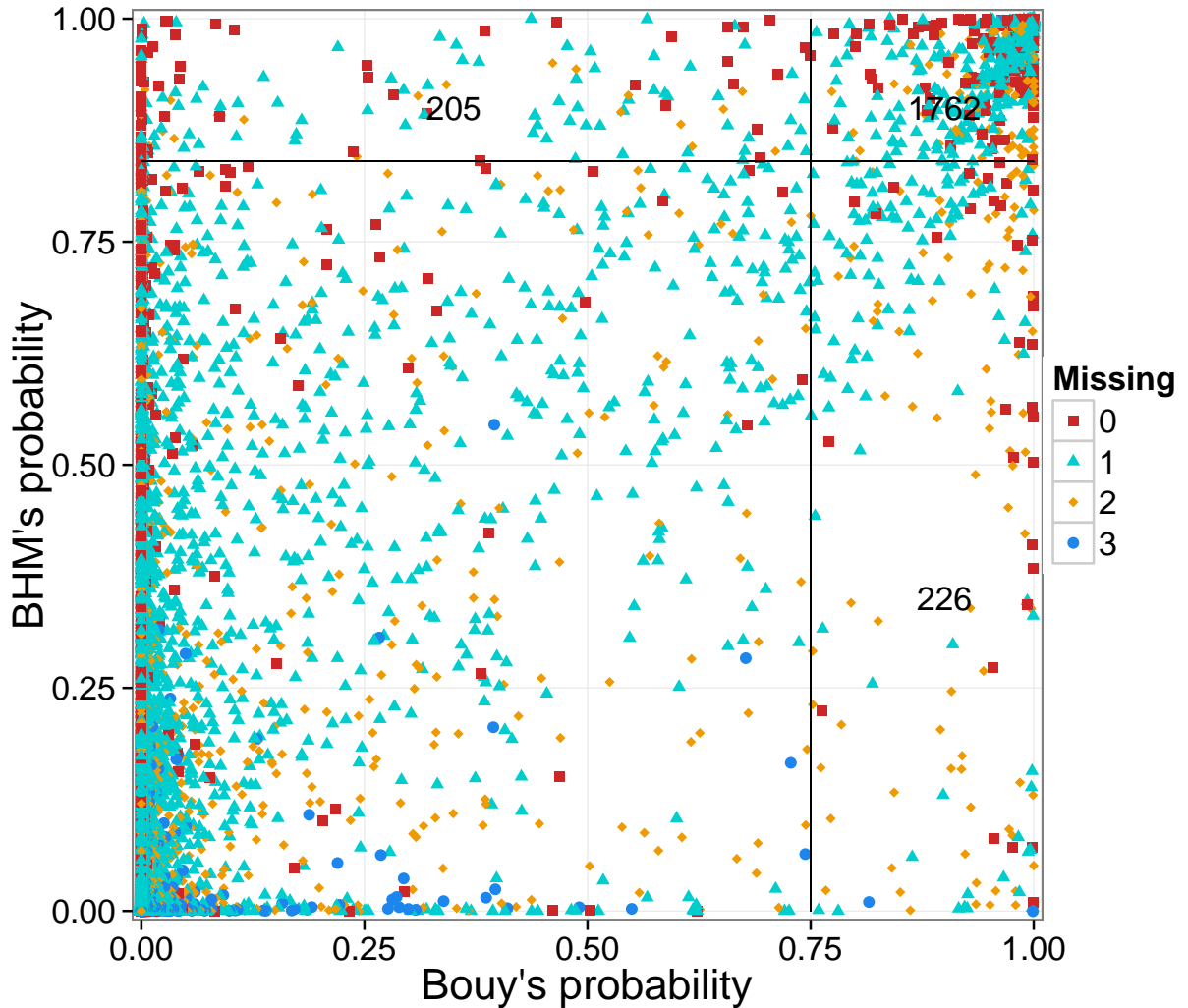


Figure 4.9: Mode of the membership probabilities recovered by the BHM compared to those of [Bouy et al. \(2015\)](#). The lines show the 0.75 and $p_t = 0.84$ probability thresholds used in both works. The numbers indicate our new candidate members (top left), the ones we rejected (bottom right), and the common ones (top right). Reproduced from Figure 11 of [Olivares et al. \(2017\)](#), *The Seven sisters DANCe III: Hierarchical Bayesian model*, A&A, Vol. submitted.

The candidate members of [Bouy et al. \(2015\)](#) that the BHM rejects, which I call the

rejected ones, are shown in lower right box of Fig. 4.9. They amount to 12% of the total number of candidate members recovered by Bouy et al. (2015), and to 12.5% of candidate members recovered in the present work. The 12% value is larger, by 4.7%, than the $7.3 \pm 1.4\%$ of CR reported by Sarro et al. (2014), while the 12.5% value is also larger, by 2.5%, than the 10% loss rate of the BHM (the TPR=90% measured in Section 4.1). These figures indicate that some true cluster members must be within the rejected objects, as expected from the TPR=90%.

Now, I analyse these objects with further detail. As it is shown in Figs. 4.10 and 4.11, the rejected objects have proper motions uncertainties with median $\tilde{\mu}_\alpha, \tilde{\mu}_\delta = \{3.19, 3.20\} \text{ mas} \cdot \text{yr}^{-1}$. This value is more than four times larger than that of the common candidate members (those objects classified as members by both works, see top right corner of Fig. 4.9), which have median $\tilde{\mu}_\alpha, \tilde{\mu}_\delta = \{0.68, 0.68\} \text{ mas} \cdot \text{yr}^{-1}$. Among the rejected ones, those with a relatively high membership probability occur mostly at the middle of the cluster photometric sequence (green squares of Fig. 4.11). On the other hand, those with lower membership probabilities occur at the bright and faint ends (blue and red triangles of Fig. 4.11, respectively). Furthermore, the proper motions uncertainties of the rejected objects at the bright, middle and faint ends of the cluster photometric sequence, have medians of $\tilde{\mu}_\alpha, \tilde{\mu}_\delta = \{4.3, 4.2\} \text{ mas} \cdot \text{yr}^{-1}$, $\tilde{\mu}_\alpha, \tilde{\mu}_\delta = \{2.4, 2.4\} \text{ mas} \cdot \text{yr}^{-1}$ and $\tilde{\mu}_\alpha, \tilde{\mu}_\delta = \{3.4, 3.4\} \text{ mas} \cdot \text{yr}^{-1}$, respectively. These figures are approximately 6, 4 and 5 times larger, respectively, than those of the candidates in common. These large uncertainties produce a proportional spread of the cluster likelihood. This effect could reduce the membership probability of these objects.

In addition to the large proper motion uncertainties of these objects, their membership probabilities are also affected by the different photometric cluster-to-field likelihood ratios in the BHM and in Sarro et al. (2014) methodology, the one used by Bouy et al. (2015).

Assuming that the field likelihoods of both models are the same, then the lower membership probabilities of the rejected objects result from the lower cluster likelihoods, which can be explained by the diverse ways in which both works model the spread of the cluster sequence. In Sarro et al. (2014) the latter is modelled as a multivariate normal with a covariance matrix estimated from objects in intervals of equal length along the cluster sequence (their so called λ). In addition, they mention that their methodology is sensitive to the observational uncertainties, thus their covariance matrices are overestimated. In summary, their method is sensitive to both the observational uncertainties and the number of objects along the cluster sequence. In the BHM the spread of the cluster sequence is also multivariate normal but with covariance matrix that is: i) the true cluster sequence (i.e. the observational uncertainties are deconvolved), and ii) constant across the cluster sequence (i.e. independent of the number of sources in the length interval) and with a value inferred as the average spread (see Section 3.3.4). Therefore, in Bouy et al. (2015) the spread of the cluster sequence compared to that of the BHM is: a) overestimated

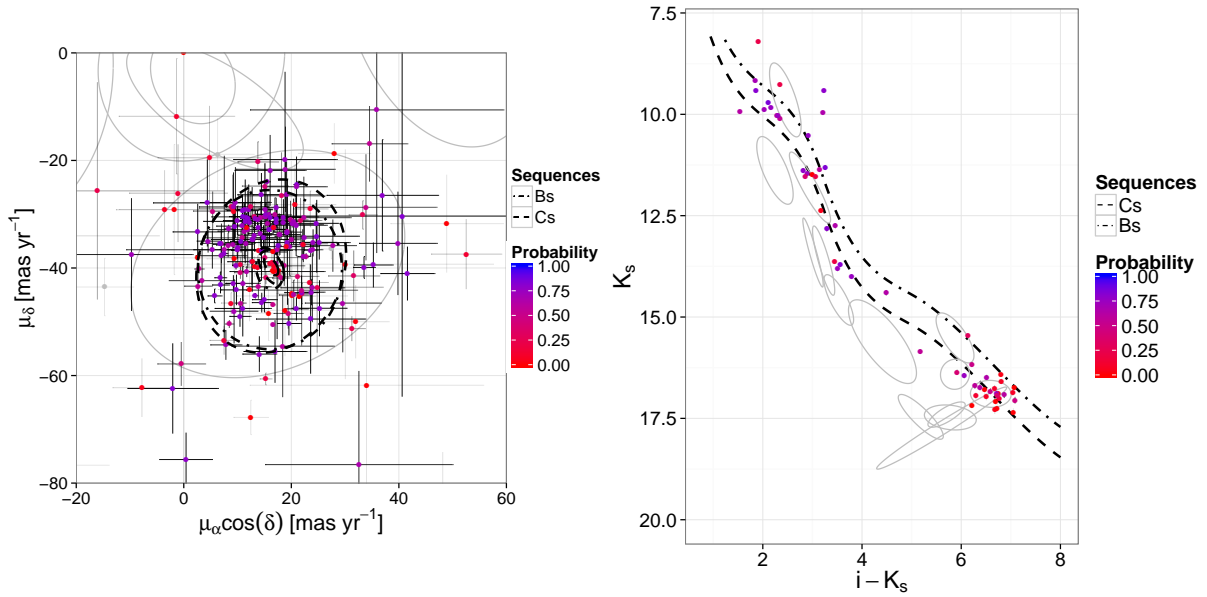


Figure 4.10: Proper motion (left) and K_s vs. $i - K_s$ CMD (right) showing the candidate members of Bouy et al. (2015) rejected by the BHM. Reproduced from Figure 13 of Olivares et al. (2017), *The Seven sisters DANCE III: Hierarchical Bayesian model*, A&A, Vol. submitted.

in the faint and bright ends, where members are fewer and uncertainties larger, and b) underestimated in the central region ($CI=3.2$) where members are copious and highly concentrated (see Figs. 4.5 and 4.16). Thus, in the BHM the the cluster likelihood of objects in cases a) and b) are both diminishes with respect to the cluster likelihood of Bouy et al. (2015). For the objects in the first case (a), the cluster sequence is narrower, and thus their membership probability diminishes in proportion to their distance to the sequence. For objects in the second case (b), the cluster sequence is wider and thus their cluster likelihood and membership probability diminishes. Both these effects are seen in Fig. 4.12, where objects in the first case have membership probabilities below 0.5 (red dots), while objects latter case have membership probabilities near the classification threshold 0.84 (purple dots).

Assuming the alternative scenario in which the cluster likelihood of the BHM and Bouy et al. (2015) is the same, the diminished membership probabilities of the rejected candidates Bouy et al. (2015) can be explained by the different ways in which the field likelihoods of both works are constructed. As explained in Section 1.4, the field likelihood in Sarro et al. (2014) methodology (the one used by Bouy et al. (2015)) is constructed only with fully observed objects (i.e. without missing values), which I called the *naivety* assumption in Section 3.3.1. In that Section it is shown that such assumption leads to underestimate the field density in the bright and faint regions, and overestimate it in the middle region (see Fig 3.3). Underestimating the field likelihood increases the cluster-to-field likelihood ratio and therefore the cluster membership probabilities.

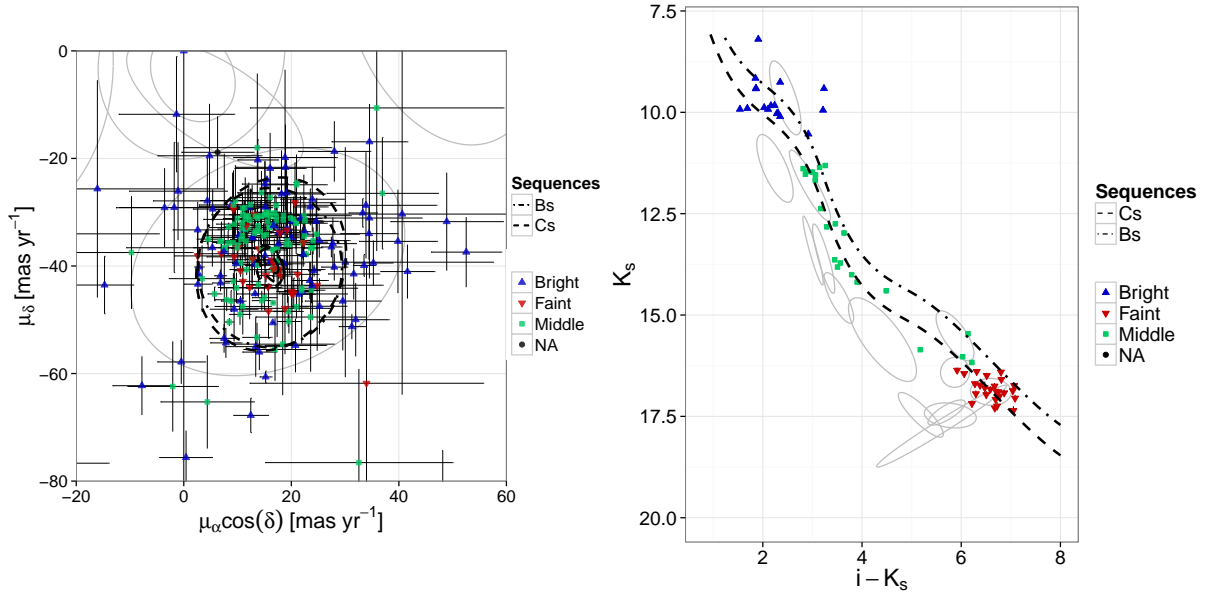


Figure 4.11: Proper motion (left) and K_s vs. $i - K_s$ CMD (right) showing the candidate members of Bouy et al. (2015) rejected by the BHM. The colours and shapes are a proxy for their K_s magnitude. Reproduced from Figure 14 of Olivares et al. (2017), *The Seven sisters DANCe III: Hierarchical Bayesian model*, A&A, Vol. submitted.

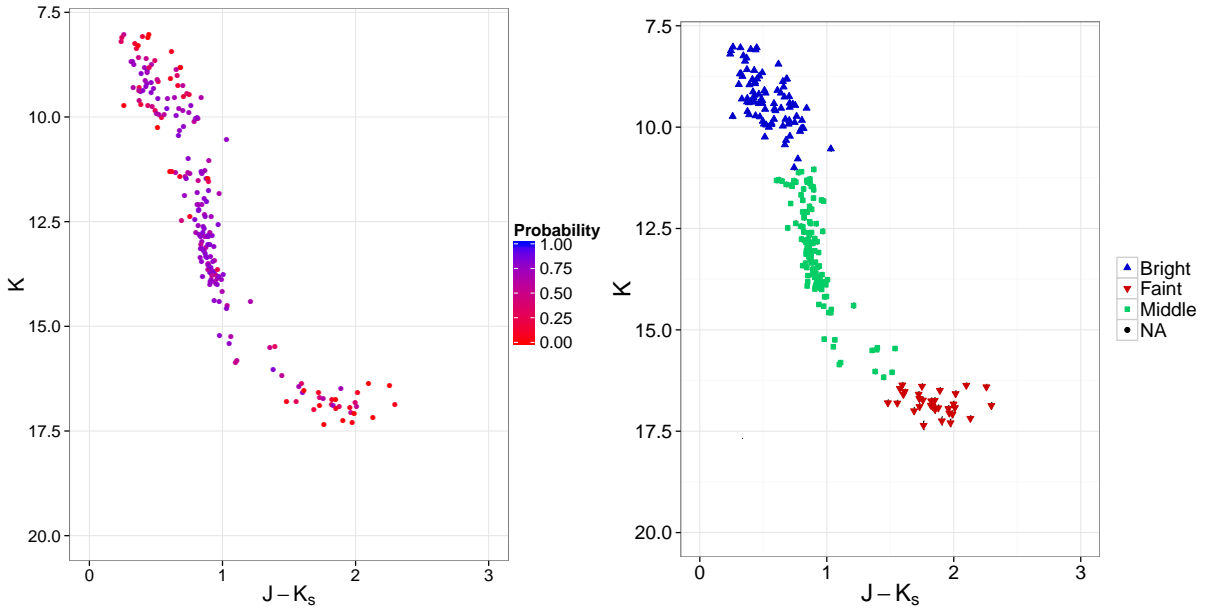


Figure 4.12: K_s vs. $J - K_s$ CMDs showing the candidate members of Bouy et al. (2015) rejected by the BHM. Captions in left and right panels are equivalent to those in Fig. 4.10 and 4.11, respectively.

The previous phenomena acting together are responsible for the relatively lower BHM membership probabilities of the rejected candidate members of Bouy et al. (2015). A detailed comparison of the cluster and field likelihoods in both the BHM and Bouy et al. (2015) models for each of the 226 objects lays beyond the objective of the present work.

Nevertheless, these objects can not be discarded as potential true cluster members. As detailed in Section 4.1, within these objects lays a fraction of the 10% true cluster members below the 0.84 probability threshold. It is left to future works to disentangle which of these objects are true cluster members.

On the other hand, the new candidates members found by the BHM, shown in the upper left box of Fig. 4.9, amount to 10% of the [Bouy et al. \(2015\)](#) candidate members. This figure is higher than the $\sim 3.5\%$ of missing rate (1-TPR) reported by [Sarro et al. \(2014\)](#). Also, these new candidates amount to 10% of the BHM recovered candidate members. This value is larger than the 4.3% CR reported in Section 4.1. These two larger figures may indicate that some truly new discoveries may be within these list of new candidate members. In Figs. 4.13 I show the proper motions and K_s vs $i - K_s$ CMD of these new candidates members.

The new candidate members have proper motions uncertainties whose median, $\tilde{\mu}_\alpha, \tilde{\mu}_\delta = \{1.41, 1.41\} \text{ mas} \cdot \text{yr}^{-1}$, is two times larger than those of the candidate members in common with [Bouy et al. \(2015\)](#). Also, as shown by Fig. 4.13, the majority of the new candidate members, 166, have probabilities lower than 0.95, are located in a halo around the locus of the cluster proper motions, and on top of the cluster photometric sequence in the K_s vs $i - K_s$ CMD. On the contrary, the new candidate members with probabilities higher than 0.95, which are 39, lie in the centre of the cluster proper motions and fall above the cluster sequence in the K_s vs $i - K_s$ CMD. Thus, I hypothesise that: i) Objects whose photometry is compatible with the cluster sequence but are in the proper motions halo, have higher membership probabilities in our methodology due to the increased flexibility of the cluster proper motions model: it now has four gaussians instead of the two of [Bouy et al. \(2015\)](#). And ii) objects near the centre of the cluster proper motions but located above the cluster photometric sequence sequence, are multiple systems (probably triple systems which can amount to 4% of the population [Duquennoy & Mayor 1991](#)) with an increased membership probability due to our more flexible photometric model of the cluster and equal-mass binaries sequences.

Summarising, the discrepancies between the BHM membership probabilities and those reported by [Bouy et al. \(2015\)](#) arise from subtle but important differences. The first difference is the treatment of object with missing entries. Although [Bouy et al. \(2015\)](#) report membership probabilities for this kind of objects, their field and cluster models were constructed discarding them. As it is shown in Section 3.3.1, working with completely observed objects leads to a density which is in average more than three times more biased than one derived in this work. Although the field density derived in this work is also biased (see Section 3.3.1), including in our model objects with missing entries has two important consequences. First, the photometric model is more accurate than any other model that discards objects with missing entries (see Section 3.3.1). This effect is important in the regions where these objects are more frequent. Second, the use of objects with missing

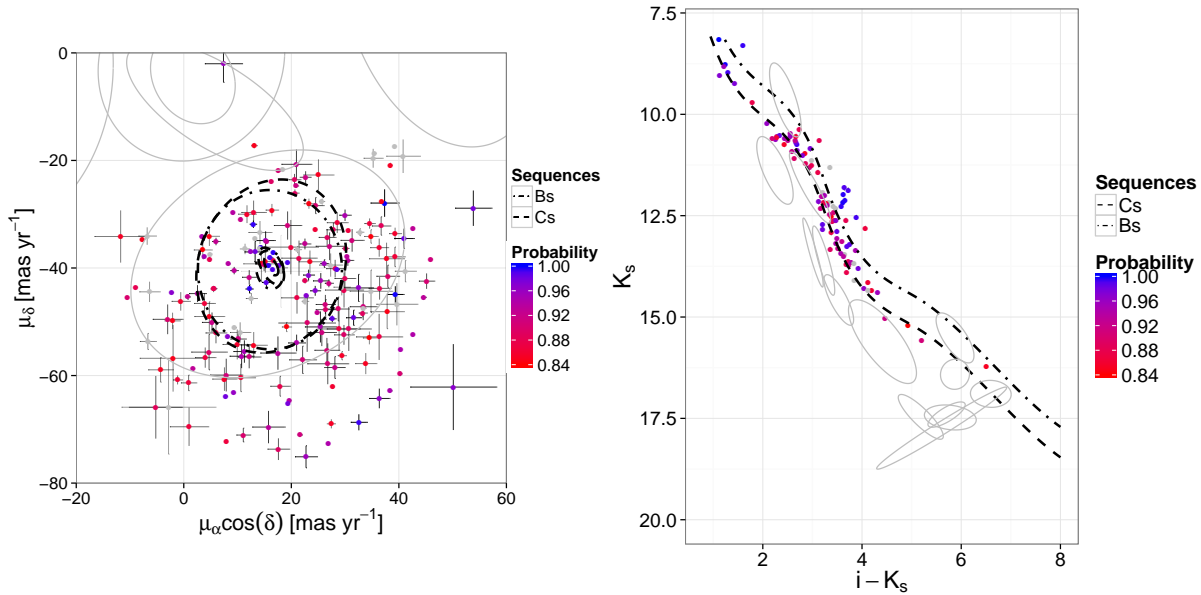


Figure 4.13: Proper motion (left) and K_s vs. $i - K_s$ CMD (right) showing the new candidate members found in this work. Reproduced from Figure 12 of Olivares et al. (2017), *The Seven sisters DANCe III: Hierarchical Bayesian model*, A&A, Vol. submitted.

entries in the construction of the cluster model allow us to include the information of good candidate members that were otherwise discarded a priori.

In addition to the mentioned bias in the field density, I remind the reader of the bias present in the membership probability of objects with missing CI (see Section 4.1). In Fig. 4.9, the vertical stripe at $p_{Bouy} < 0.1$ and $p_{BHM} > 0.5$ there are 536 objects, from which the 80% have missing entries, 76% have a missing CI and 4% a missing band, and only 20% have completely observed entries. While objects with missing CI could be biased with an rms of 0.14, the completely observed ones are basically unbiased with an rms of 0.02. In Section 4.1, I stressed that particular care must be taken with the membership probabilities of objects with a missing CI. However, the objects with completely observed entries laying within this stripe suggest that Bouy et al. (2015) methodology is too restrictive. Thus, the BHM has a higher cluster model flexibility, which allows it to increase the membership probability of the previously discarded candidates.

4.2.3 Candidate members from Rebull et al. (2016)

After cross matching (at CDS with a 0.5 arcsec radius) the list of candidate members from Rebull et al. (2016) (their Table 2, here after Rebull Table 1 (RT1)) with the DDR2, I find that 758 out of the 759 objects have a counter part in the DDR2 catalogue. The 91% of these objects (690 of them) are candidate members in the BHM. Under the assumption that the candidate members in RT1 are indeed true members, which may not be true, the ratio of recovered members is even better than the $TPR = 90 \pm 0.2\%$ reported in Section

4.1. These objects are shown in Fig. 4.14.

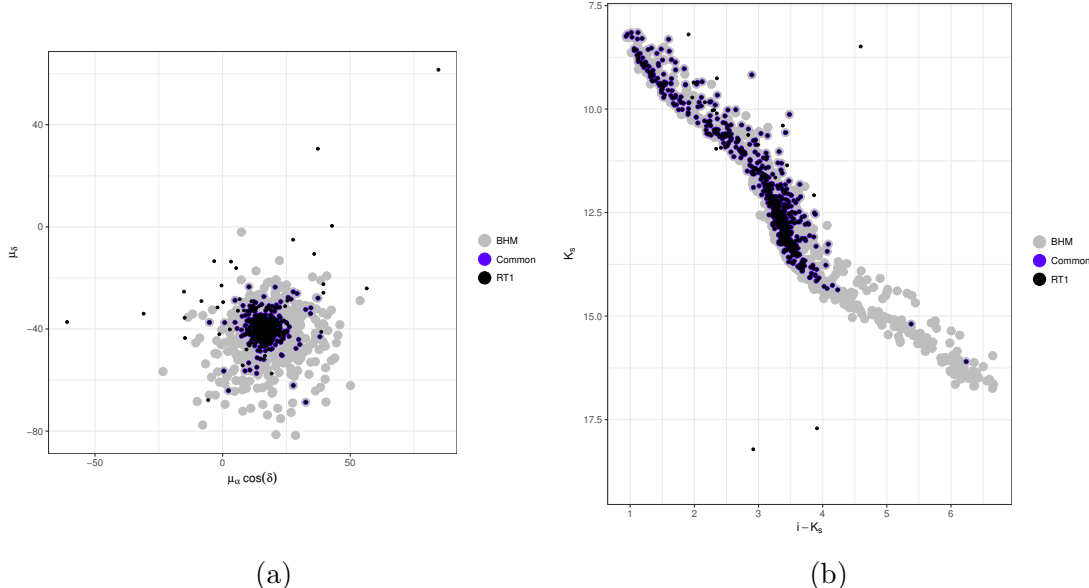


Figure 4.14: Proper motions (a) and K vs $i - K$ CMD (b) of the RT1 candidate members in the DDR2 catalogue (black). Also shown, the objects classified as candidate members in the BHM (grey), and in both RT1 and BHM (blue).

On the other hand, after cross matching (at CDS with a 0.5 arcsec radius) the list of 154 objects that [Rebull et al. \(2016\)](#) classify as non-members (their Table 6, here after Rebull Table 2 (RT2)) with the DDR2, I find that all these objects have a counter part on the DDR2. The 21% of objects in the RT2 list (33 of them) were classified as candidate members in the BHM. This is a value five times larger than the CR reported in Section 4.1 (CR=4.3%). However, we can not assume that the RT2 list comprises only non-members. First, this objects were at some point classified as members by other authors (Appendix B of [Rebull et al. 2016](#)). Second, not all of these objects have periods (only 20% according to [Rebull et al. 2016](#)). From the 33 objects classified as candidate members by the BHM, only nine of them have periods. It means that for the remaining 24 candidate members, these authors used other criteria to discard them as members. About their classification process, [Rebull et al. \(2016\)](#) say “This process was qualitative in the sense that we weighted all of the information in a subjective manner. However, the process was also extensive, with each star considered individually and with all available information considered in detail. [...] we believe that in the great majority of cases we have made the right decision.” In any case, the high rate of BHM candidate members found in this RT2 list may indicate that either our contamination rate is underestimated or that the criteria used by [Rebull et al. \(2016\)](#) are too restrictive. As can be seen in Fig. 4.15, these 33 objects have proper motions and photometric measurements consistent with those of the cluster. In order to clarify the status of these objects, further information is still needed.

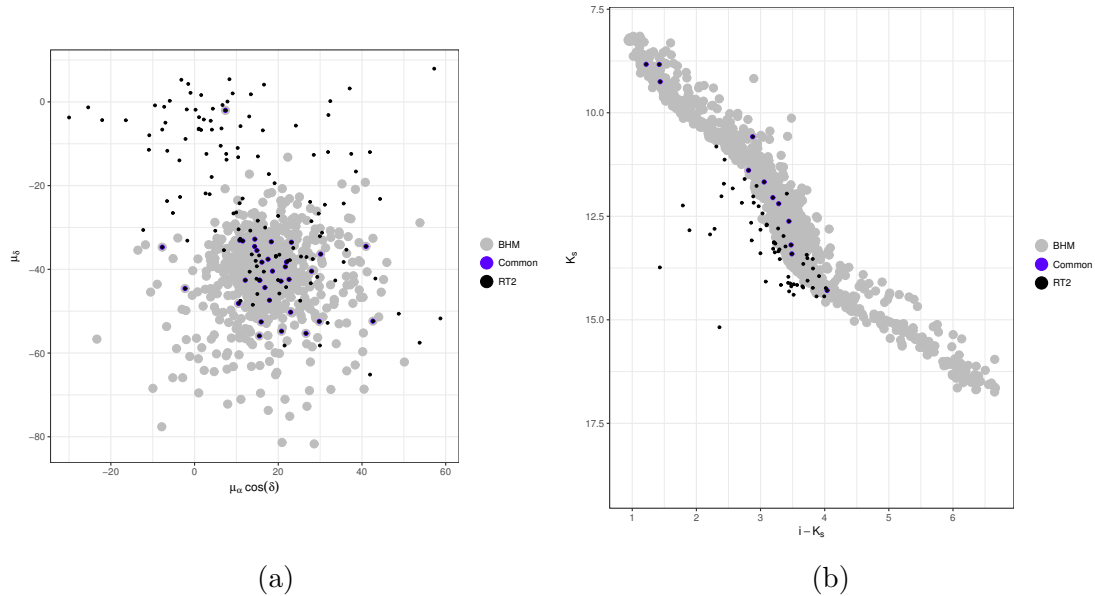


Figure 4.15: Proper motions (a) and K vs $i - K$ CMD (b) of the RT2 in the DDR2 catalogue (black). Also shown, the objects classified as candidate members in the BHM (grey), and those classified as non-members in the RT2 and as candidate members in the BHM (blue).

4.3 The statistical distributions of the Pleiades.

Now, I present the results of the statistical distributions that describe the cluster population, which are the main objective of the present work. These distributions result directly or indirectly from the posterior distribution of the parameters in our model. Indirectly means that I use them as parameters of other function (e.g. the mass distribution). Since we have 85 parameters in the BHM, I only discuss the posterior distributions of some of these parameters. In particular, those related with the velocity, luminosity and mass distributions. Nevertheless, in Table 4.1, I summarise the posterior distribution of the parameters in our model using the mode, also I use the 16th and 84th percentiles as a proxy for the uncertainty. The parameter names in this Table correspond to those given in Section 3.4 (at Table 3.4).

The posterior distributions of the parameters in the B-splines and the *true* CI distribution are shown in Figs. 4.16 and 4.17, respectively. The posterior distributions of the parameters in the proper motion models are described in Section 4.5.

Also, for the sake of completeness, in Fig. 4.18, I depict the values the correlation coefficients among the 85 parameters in the BHM. As can be seen from this Figure, the larger correlations appear among parameters describing the true CI distribution, and among these and almost the rest of the parameters. This is expected since the true CI is key parameter in the BHM. It is also interesting to notice that there is a strong correlation among the coefficients of the splines series modelling different magnitudes. For example,

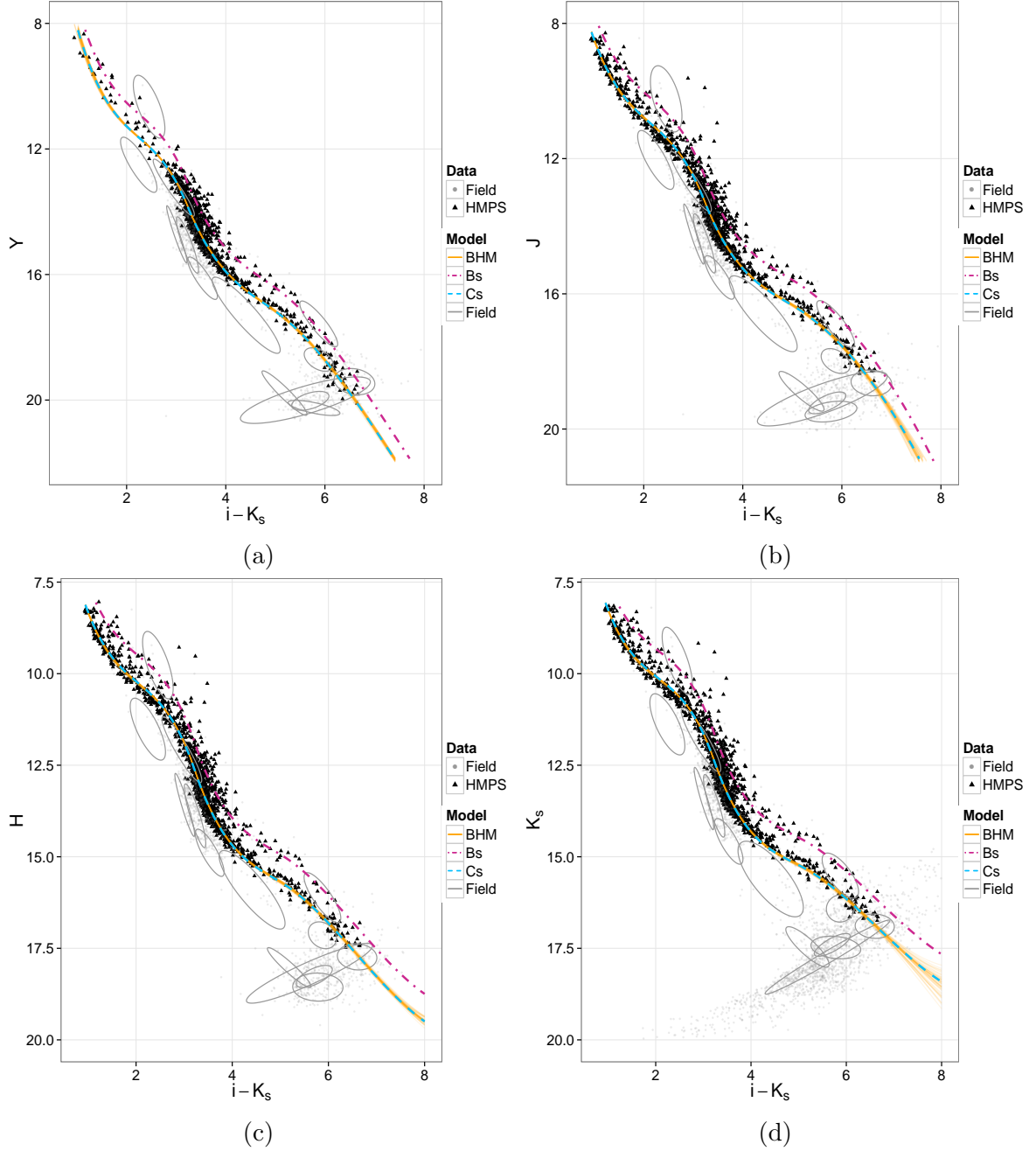


Figure 4.16: CMDs showing the cluster (HMPS) and field members (blue triangles and grey dots, respectively resulting from classification using the $p_t = 0.84$ derived in Sect. 4.1), together with 100 samples (orange spaghetti graphs) from the posterior distributions of the coefficients of the B-splines resulting in the *true* values of the cluster photometry. Also shown, the mode of these 100 samples (blue dashed line), the EMB sequence (magenta dot dashed line) and projections of the photometric field model (grey ellipses, see Fig. 3.4).

there is a strong correlation among the fourth coefficients of the splines. These correlations are expected since the shape of the cluster sequence is similar in the four CMDs.

Table 4.1: continued.

Parameter	Mode	$p_{16\%}$	$p_{84\%}$
-----------	------	------------	------------

Table 4.1: Mode, 16 and 84 percentiles of each parameter posterior distribution.

Parameter	Mode	$p_{16\%}$	$p_{84\%}$
Field fraction	0.967958	0.967474	0.969462
Cs fraction	0.909371	0.895137	0.919434
Cs PM fraction 1	0.001347	0.001347	0.001347
Cs PM fraction 2	0.525735	0.508956	0.543462
Cs PM fraction 3	0.190321	0.159262	0.224475
Bs PM fraction 1	0.104021	0.103894	0.104108
Color fraction 1	0.085997	0.075534	0.094833
Color fraction 2	0.353973	0.193003	0.469717
Color fraction 3	0.277648	0.224469	0.289170
Color fraction 4	0.251190	0.105385	0.376304
Mean color 1	1.307689	1.259029	1.338972
Mean color 2	3.204578	2.841093	3.241497
Mean color 3	3.341761	3.321369	3.359906
Mean color 4	3.575646	3.518013	3.641340
Mean color 5	5.446573	5.366774	5.560569
Variance color 1	0.086389	0.076258	0.125984
Variance color 2	0.369646	0.275289	0.435338
Variance color 3	0.026526	0.026468	0.026565
Variance color 4	0.269562	0.269046	0.270325
Variance color 5	0.375299	0.322775	0.537458
Mean PM Cs[1,1]	16.305803	16.220500	16.384057
Mean PM Cs[1,2]	-39.683588	-39.767616	-39.469303
Variance Cs[1,1]	0.000000	0.000000	0.000000
Variance Cs[1,2]	0.000000	0.000000	0.000000
Variance Cs[1,3]	0.000000	0.000000	0.000000
Variance Cs[2,1]	193.231940	193.035542	193.511106
Variance Cs[2,2]	17.895759	6.705775	30.727887
Variance Cs[2,3]	259.457517	259.296878	259.651477
Variance Cs[3,1]	7.049380	6.007706	9.154742
Variance Cs[3,2]	-3.350959	-3.924016	-1.704487
Variance Cs[3,3]	11.685825	11.684455	11.687112
Variance Cs[4,1]	1.685699	1.608666	1.740720
Variance Cs[4,2]	-0.830553	-0.833982	-0.823643
Variance Cs[4,3]	3.590195	3.511369	3.833215

Table 4.1: continued.

Parameter	Mode	$p_{16\%}$	$p_{84\%}$
Mean PM Bs[1,1]	15.719802	15.521532	16.230056
Mean PM Bs[1,2]	-40.314746	-40.365824	-40.182113
Variance Bs[1,1]	339.480156	278.765965	392.206780
Variance Bs[1,2]	-0.421560	-0.443185	-0.404809
Variance Bs[1,3]	150.552074	56.130431	330.515498
Variance Bs[2,1]	6.512542	6.498438	6.521515
Variance Bs[2,2]	-1.421797	-2.214778	0.327916
Variance Bs[2,3]	10.696936	10.234819	11.259143
Coefficient [1,1]	6.862152	6.698804	6.962798
Coefficient [1,2]	12.549203	12.543435	12.559731
Coefficient [1,3]	10.638663	10.624438	10.646821
Coefficient [1,4]	16.260306	16.253606	16.280723
Coefficient [1,5]	16.864151	16.796169	16.907984
Coefficient [1,6]	21.087408	21.010410	21.183274
Coefficient [1,7]	23.279645	23.273198	23.290056
Coefficient [2,1]	7.622220	7.605694	7.625557
Coefficient [2,2]	11.527325	11.517715	11.567059
Coefficient [2,3]	10.211935	10.211547	10.212698
Coefficient [2,4]	15.602847	15.599241	15.621497
Coefficient [2,5]	16.098859	16.055647	16.153988
Coefficient [2,6]	19.338719	19.289969	19.399707
Coefficient [2,7]	21.813285	21.715478	21.957425
Coefficient [3,1]	7.574385	7.564066	7.590012
Coefficient [3,2]	10.970652	10.955195	11.009520
Coefficient [3,3]	9.485289	9.480620	9.494432
Coefficient [3,4]	15.111703	15.100806	15.126351
Coefficient [3,5]	15.343240	15.302140	15.391826
Coefficient [3,6]	18.632106	18.591372	18.649827
Coefficient [3,7]	19.654121	19.622414	19.678001
Coefficient [4,1]	7.529844	7.521514	7.539968
Coefficient [4,2]	10.860704	10.845059	10.895944
Coefficient [4,3]	9.334359	9.331793	9.337694
Coefficient [4,4]	14.722486	14.717526	14.741820
Coefficient [4,5]	14.954292	14.909027	15.015568
Coefficient [4,6]	17.636682	17.582166	17.705691
Coefficient [4,7]	18.461156	18.254644	18.788302
Covariance Phot[1]	0.128241	0.128140	0.128294

Table 4.1: continued.

Parameter	Mode	$p_{16\%}$	$p_{84\%}$
Covariance Phot[2]	0.028797	0.027836	0.032340
Covariance Phot[3]	0.007540	0.007387	0.007617
Covariance Phot[4]	0.001356	0.000907	0.001813
Covariance Phot[5]	-0.012226	-0.012248	-0.012174
Covariance Phot[6]	0.000000	0.000000	0.000000
Covariance Phot[7]	-0.009281	-0.009301	-0.009267
Covariance Phot[8]	-0.027990	-0.028689	-0.027546
Covariance Phot[9]	-0.029916	-0.030951	-0.027921
Covariance Phot[10]	0.000028	0.000012	0.000109
Covariance Phot[11]	-0.002826	-0.004315	0.003619
Covariance Phot[12]	-0.000745	-0.004806	0.003091
Covariance Phot[13]	0.024524	0.024521	0.024527
Covariance Phot[14]	0.021316	0.021001	0.021807
Covariance Phot[15]	0.000590	0.000589	0.000592

4.4 Projected spatial distribution

In this Section, I present the results of the model selection analysis of the Projected Spatial Distribution (PSD) models of the Pleiades cluster. The Bayesian model selection approach and the PSD models are described in Sections 3.1.2 and 3.7, respectively. The Bayesian *evidence* is computed by means of the Python package *PyMultiNest* ([Buchner et al. 2014](#)), which is a Python wrapper of the C++ package *MultiNest* ([Feroz et al. 2009](#)) that implements the Nested Sampling algorithm of [Skilling \(2004, 2006\)](#) (see Section 3.5.2).

Appendix A contains the details of the inference process of the posterior distributions, figures of the fitted densities and marginal distributions, together with the uncertainties of the parameters in each analysed model. Table 4.3, given here, summarises the evidences and Bayes Factors resulting for all our models and extensions. In the following we will use the figures in this Table to discuss the model comparison.

In the Bayesian model selection methodology, the boundaries for decision making from Bayes Factors should be set *ab initio*. Thus, we discuss our results following the classical scale by [Jeffreys \(1961\)](#), which I show in Table 4.2.

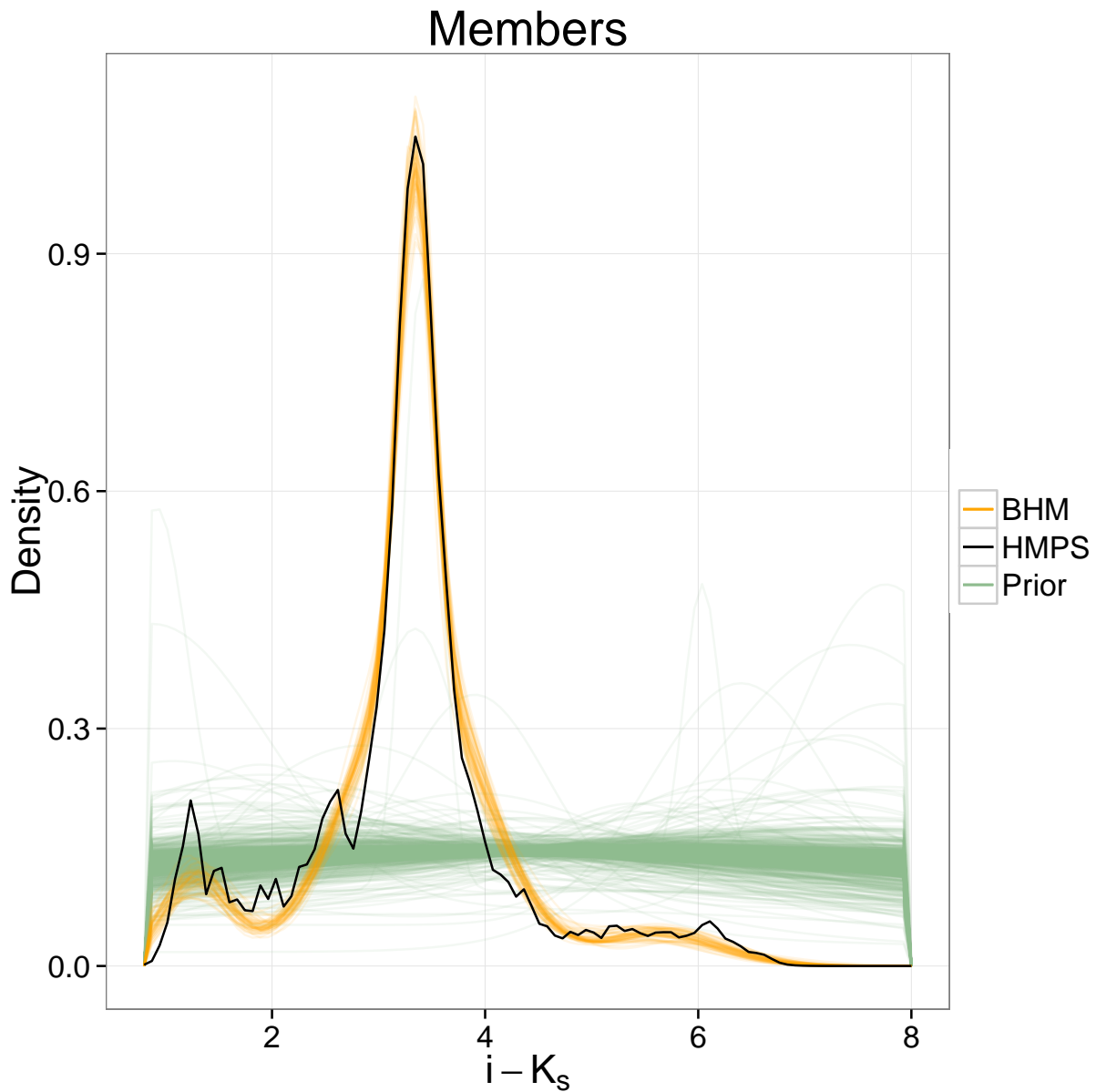


Figure 4.17: Posterior distribution of the *true* CI (orange lines, resulting from 100 samples of the posterior distributions of the parameters in the CI GMM). Also shown, the KDE (Gaussian kernel with bandwidth equal to observed uncertainty) for the observed CIs of the candidate members in the HMPS (black line), and the prior distribution of the *true* CI GMM (grey lines, resulting from 100 samples of the prior distributions of the parameters in the CI GMM).

Table 4.2: [Jeffreys \(1961\)](#) scale for Bayes factors.

Bayes factor	Strength of evidence
$\lesssim 3:1$	<i>Inconclusive</i>
$\sim 3:1$	<i>Weak</i>
$\sim 12:1$	<i>Moderate</i>
$\gtrsim 150 : 1$	<i>Strong</i>

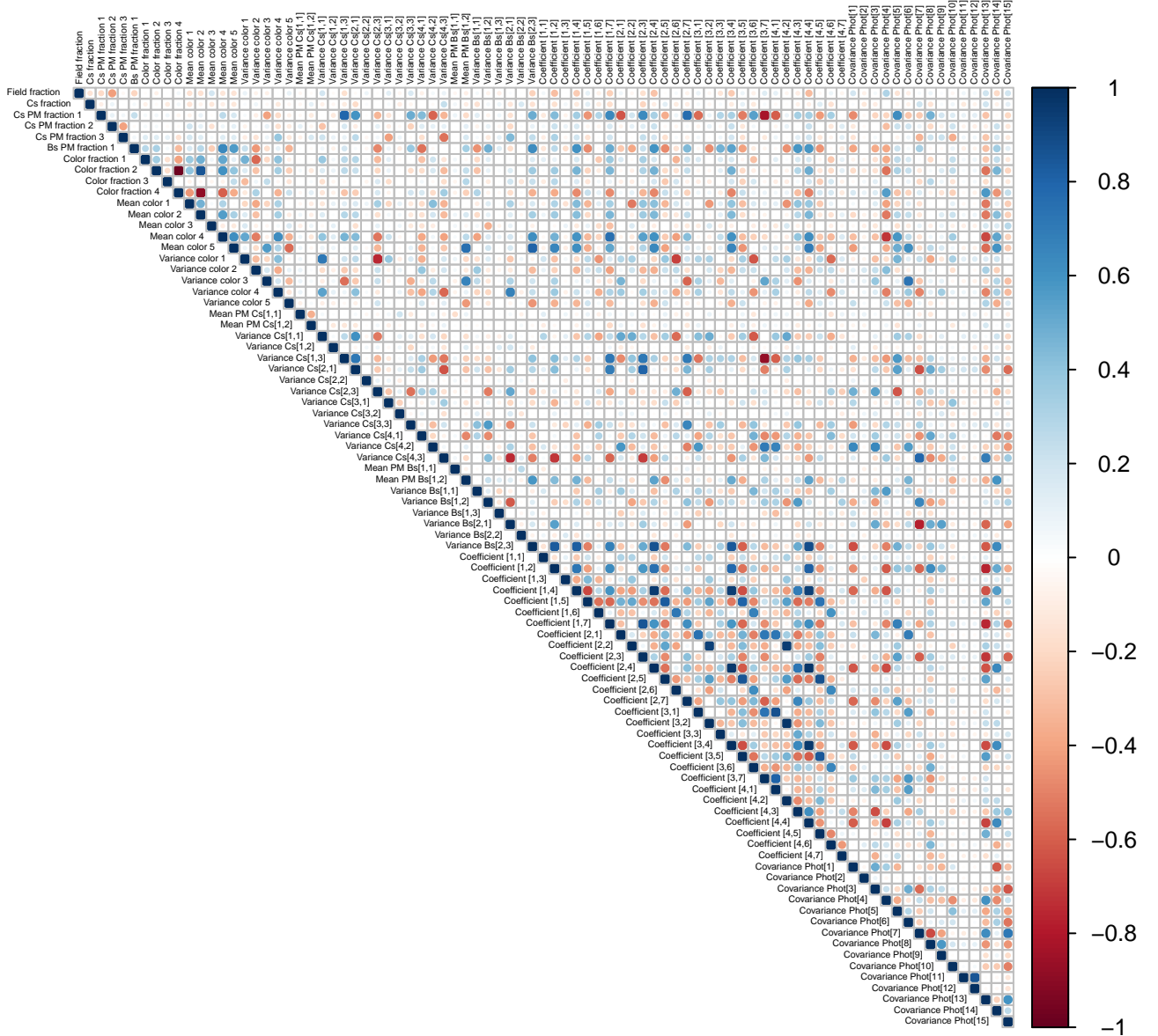


Figure 4.18: Correlation matrix of the posterior distributions of the parameters in the BHM. The colour code indicates the value of the correlation coefficient. Parameter names are the same as those in Table 4.1.

4.4.1 Selection of models with radial symmetry

The inferred posterior distributions of the parameters in our models with radial symmetry are shown in Fig. 4.19 by means of 100 samples randomly drawn, together with the MAP value. For comparison, the data has been binned and is shown with poisson uncertainties.

The upper-left panel of Table 4.3 summarises the evidences and Bayes factors obtained

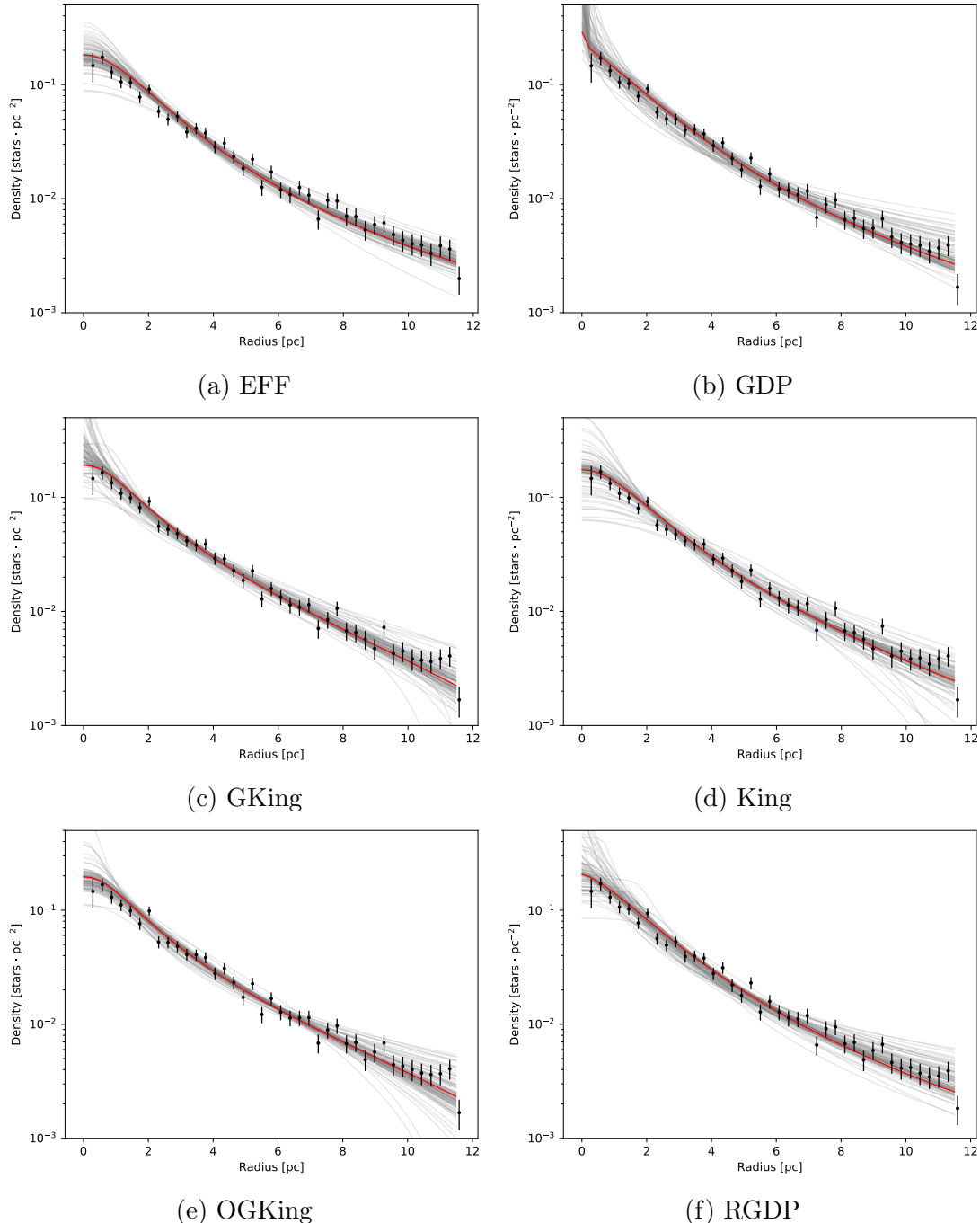


Figure 4.19: Inferred density of the radially symmetric profiles shown by means of the MAP value (red line) and samples from the posterior distribution (grey lines). For comparison the data has been binned with poissonian uncertainties (black dots).

Table 4.3: Natural logarithm of the evidence for each profile density (diagonal) and Bayes factors (off-diagonal elements, with the evidence for the model specified in the column header placed in the denominator). The evidence corresponds to data set truncated at 11.5pc.

	Radial						Biaxial						Segregated					
	EFF	GDP	GKing	King	OGKing	RGDP	EFF	GDP	GKing	King	OGKing	RGDP	EFF	GDP	GKing	King	OGKing	RGDP
Radial	EFF	-4569.15	8.83	0.83	0.40	0.19	2.53	<1e-2	<1e-2	<1e-2	<1e-2	<1e-2	<1e-2	<1e-2	<1e-2	<1e-2	<1e-2	<1e-2
	GDP	0.11-4571.33	0.09	0.05	0.02	0.29	<1e-2	<1e-2	<1e-2	<1e-2	<1e-2	<1e-2	<1e-2	<1e-2	<1e-2	<1e-2	<1e-2	<1e-2
	GKing	1.21	10.64-4568.97	0.48	0.23	3.05	<1e-2	<1e-2	<1e-2	<1e-2	<1e-2	<1e-2	<1e-2	<1e-2	<1e-2	<1e-2	<1e-2	<1e-2
	King	2.51	22.17	2.08-4568.23	0.49	6.35	<1e-2	<1e-2	<1e-2	<1e-2	<1e-2	<1e-2	<1e-2	<1e-2	<1e-2	<1e-2	<1e-2	<1e-2
	OGKing	5.13	45.31	4.26	2.04-4567.52	12.99	<1e-2	<1e-2	<1e-2	<1e-2	<1e-2	<1e-2	<1e-2	<1e-2	<1e-2	<1e-2	<1e-2	<1e-2
	RGDP	0.40	3.49	0.33	0.16	0.08-4570.08	<1e-2	<1e-2	<1e-2	<1e-2	<1e-2	<1e-2	<1e-2	<1e-2	<1e-2	<1e-2	<1e-2	<1e-2
Biaxial	EFF	>999	>999	>999	>999	>999	>999-4557.32	5.14	0.08	0.08	0.01	0.84	<1e-2	<1e-2	<1e-2	<1e-2	<1e-2	<1e-2
	GDP	>999	>999	>999	>999	>999	>999-4558.96	0.02	0.02	<1e-2	0.16	<1e-2	<1e-2	<1e-2	<1e-2	<1e-2	<1e-2	<1e-2
	GKing	>999	>999	>999	>999	>999	>999-4554.81	12.31	63.26-4554.81	0.97	0.13	10.37	<1e-2	0.01	<1e-2	<1e-2	<1e-2	<1e-2
	King	>999	>999	>999	>999	>999	>999-4554.78	12.64	64.93	1.03-4554.78	0.14	10.64	<1e-2	0.01	<1e-2	<1e-2	<1e-2	<1e-2
	OGKing	>999	>999	>999	>999	>999	>999-4552.80	91.95	472.37	7.47	7.28-4552.80	77.41	0.04	0.10	<1e-2	<1e-2	<1e-2	0.04
	RGDP	>999	>999	>999	>999	>999	>999-4557.15	1.19	6.10	0.10	0.09	0.01-4557.15	<1e-2	<1e-2	<1e-2	<1e-2	<1e-2	<1e-2
Segregated	EFF	>999	>999	>999	>999	>999	>999-4549.45	212.43	206.96	28.45	>999-4549.45	2.95	0.10	0.03	0.16	0.15		
	GDP	>999	>999	>999	>999	>999	>999-4550.53	886.29	999	71.98	70.13	9.64	746.15	0.34-4550.53	0.03	0.01	0.05	0.39
	GKing	>999	>999	>999	>999	>999	>999-4547.12	>999	>999	>999	293.70	>999	10.32	30.47-4547.12	0.32	1.64	11.86	
	King	>999	>999	>999	>999	>999	>999-4545.98	>999	>999	913.86	>999	32.12	94.81	3.11-4545.98	5.10	36.91		
	OGKing	>999	>999	>999	>999	>999	>999-4547.61	>999	>999	179.23	>999	6.30	18.59	0.61	0.20-4547.61	7.24		
	RGDP	>999	>999	>999	>999	>999	>999-4549.59	184.89	180.13	24.76	>999	0.87	2.57	0.08	0.03	0.14-4549.59		

from our radially symmetric models. In addition, Table 4.4, shows the MAP estimate of each parameter in the radially symmetric models (uncertainties are shown in the Appendix A.1 in the form of covariance matrices).

Table 4.4: Maximum-a-posteriori estimates of the inferred parameters in each radially symmetric model.

	α_c [°]	δ_c [°]	r_c [pc]	r_t [pc]	α	β	γ
EFF	56.66	24.18	2.23				2.53
GDP	56.66	24.17	3.02		0.64	2.95	0.09
GKing	56.66	24.16	1.42	18.17	0.46	1.48	
King	56.66	24.16	2.04	32.08			
OGKing	56.66	24.17	1.38	18.87			
RGDP	56.66	24.17	3.11		0.69	3.13	

We observe that the evidences cluster in two groups. In one hand there is the family of King's models, where the evidence to compare between them is inconclusive and moderate in favour of OGKing over GKing. On the other hand there are the EFF, GDP and RGDP, where there is moderate and weak evidence supporting EFF over GDP and RGDP, respectively. RGDP is moderately better than RGDP.

Comparing the two groups shows that models in King's family have evidences that are: inconclusive and weak over the EFF, weak and moderate over RGDP, and moderate over GDP. Only from the evidences we can conclude that the tidal radius is an important parameter.

In addition, we observe that in GDP and RGDP, the r_c and β parameters show large correlations (0.85 and 0.92 for GDP and RGDP, respectively) and are relatively

unconstrained with large uncertainties (see Appendix A). Despite this fact, the models still have evidences comparable to those of the rest of the models. It suggests that these two parameters, although necessary for the model, are unconstrained by the data, and therefore not penalised by the evidence. Aiming at eliminating this source of degeneracy, we tested models in which one of these two parameters was removed. However, the fits and evidence resulting from them were poorer than that of the RGDP. Thus, we consider these parameters as necessary for this model.

We find that the introduction of more flexibility in the analytical expressions of the classical radially symmetric profiles does not produce larger evidences, and results in some cases in unconstrained parameters and a loss of the interpretability associated to the original formulations. Therefore, the best models are those pertaining to the King's family, with not sufficient evidence to select which one of them is the best. Only additional, perfectly acceptable prejudices like physical interpretability or the ability to compare with previous results, can be invoked to choose one (e.g. King's profile) over the rest.

The evidences seem to indicate that the best model is the OGKing. However, the fact that this profile has a larger evidence than any of the remaining models should come as no surprise since it results from fixing the values of α and β of the GKing model to their MAP values.

Comparing the rest of the models, we see that the poorest model is GDP with moderate evidences against it. The best models are again in King's family followed by RGDP and EFF.

The conclusion from the comparison of these radially symmetric profiles is that i) there is no compelling reason to abandon the widely used King profile in the context of the complete and homogeneous data set, and ii) there are slightly better models, but we lack evidence to prove if they truly represent a need to make the King's profile more flexible to accommodate the data. In the following, we retain the models discussed above and take the comparison one step further in order to include simple deviations from radial symmetry in the form of elliptical density contours.

4.4.2 Selection of models with biaxial symmetry

The inferred posterior distributions of the parameters in our models with biaxial symmetry are shown in Fig. 4.20 by means of 100 samples randomly drawn, together with the MAP value. For comparison, the data has been binned and is shown with poisson uncertainties.

The central panel of Table 4.3 contains the logarithm of the evidences and Bayes Factors of the biaxially symmetric models. The evidences follow a pattern similar to that observed for the radially symmetric models, with the exception of the evidences against the GDP model. We can conclude that there is strong evidence for the family of King's models against the GDP one. The evidence is still moderate and weak to compare the rest

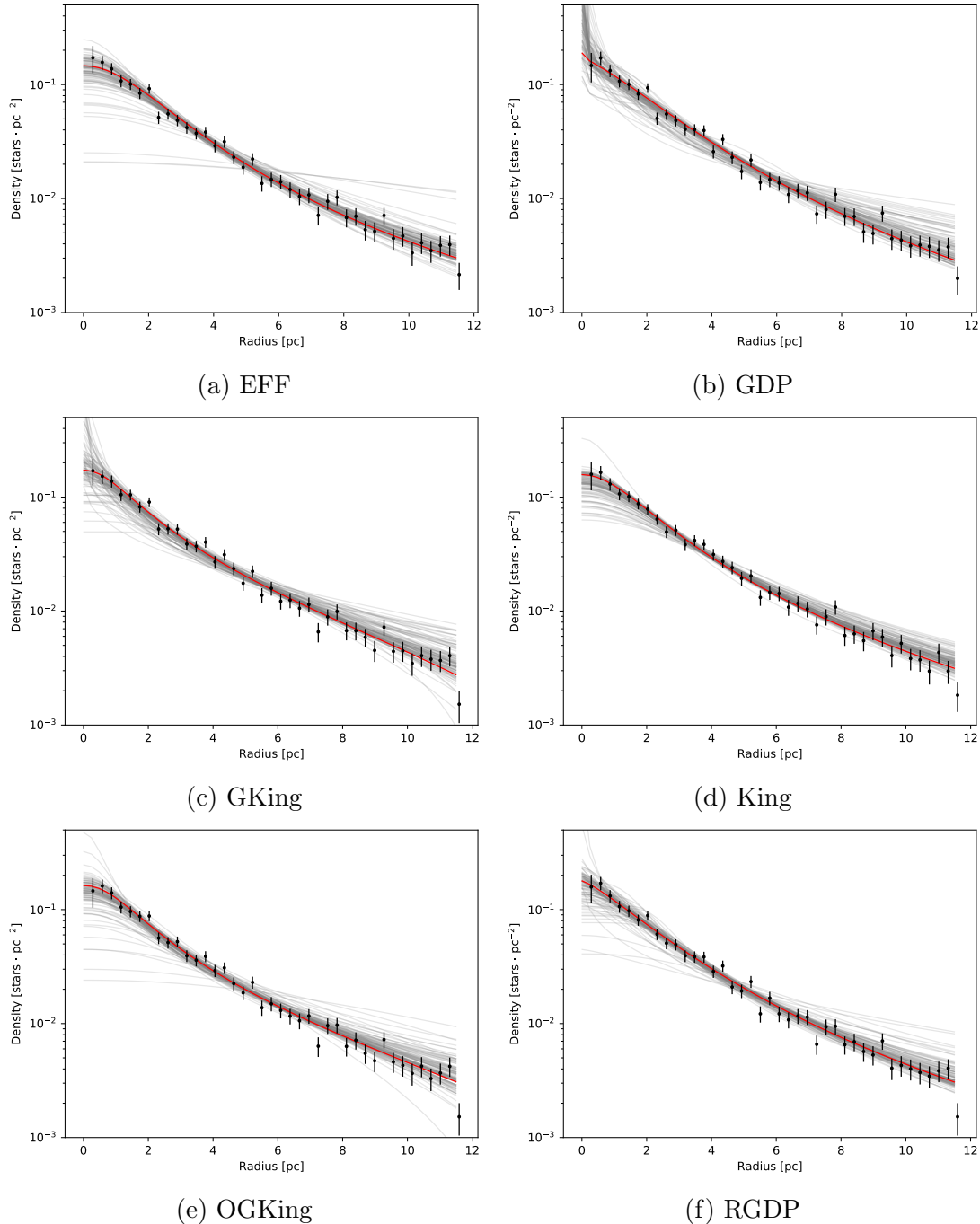


Figure 4.20: Inferred density of the biaxially symmetric profiles shown by means of the MAP value (red line) and samples from the posterior distribution (grey lines). For comparison the data has been binned with poissonian uncertainties (black dots).

of the models.

However, by comparing the evidences of the biaxially symmetric models to those of the radially symmetric ones (middle left panel of Table 4.3), we can conclude that in all cases there is strong evidence in favour of the biaxial models.

Additionally, we compute a posteriori (from the MCMC chains) the ellipticities² ϵ_{rc} and ϵ_{rt} , which are defined as,

$$\epsilon_{rc} = 1 - \frac{r_{cb}}{r_{ca}},$$

$$\epsilon_{rt} = 1 - \frac{r_{tb}}{r_{ta}},$$

with the latter available only for the King's family of models.

Table 4.5: Maximum-a-posteriori estimates of the inferred parameters in each biaxially symmetric model. Ellipticities are derived a posteriori using the inferred parameters.

	α_c [°]	δ_c [°]	ϕ [rad]	r_{ca} [pc]	r_{ta} [pc]	r_{cb} [pc]	r_{tb} [pc]	α	β	γ	ϵ_{rc}	ϵ_{rt}
EFF	56.66	24.15	0.99	2.61		2.11				2.58	0.22	
GDP	56.64	24.15	1.01	3.90		3.14		0.68	3.28	0.04	0.23	
GKing	56.66	24.14	0.94	1.35	18.00	1.21	12.79	0.48	1.34		0.10	0.30
King	56.64	24.20	1.01	2.05	51.23	2.04	20.92				0.07	0.64
OGKing	56.68	24.16	1.04	1.51	22.63	1.38	14.54				0.09	0.36
RGDP	56.68	24.17	0.96	4.05		3.04		0.78	3.32		0.24	

Table 4.5 shows the MAP estimate of the parameters in the models of this section, together with the mode of the distributions of ellipticities. Uncertainties for the latter are given in Appendix A.2.

We can observe that models that do not posses a tidal radius have similar ϵ_{rc} ellipticities with a mean value of 0.23 ± 0.01 . This value is similar to the 0.17 found by (Raboud & Mermilliod 1998), who use a multicomponent analysis to derive the directions (although its value is not given) and the aspect ratio of the ellipse axes. However, it is very interesting to see that the models within King's family result in lower values of the ellipticity in the central region and larger values in the outer one. This result is expected from the interaction with the galactic potential and is predicted by the numerical simulations of open clusters (see for example Terlevich 1987).

4.4.3 Selection of models with luminosity segregation

The inferred posterior distributions of the parameters in our models with biaxial symmetry and luminosity segregation are shown in Fig. 4.21 by means of 100 samples randomly drawn, together with the MAP value. For comparison, the data has been binned and is shown with poisson uncertainties. In addition, Fig. 4.22 shows the density profiles

²The ellipticity used here is also known as flattening.

of the luminosity segregated models, together with the J band data in three bins ($J < 12$, $12 \lesssim J \lesssim 15$, and $15 < J$). The three shown models have core radii as given by Eq. 3.89, in which the value of J band correspond to the mean of each bin.

The lower-right panel of Table 4.3 summarise the evidences and Bayes Factors of models with luminosity segregation. Also, Table 4.6 shows the MAP of the inferred distributions for this set of models, together with the derived ellipticities.

Table 4.6: Maximum-a-posteriori estimates of the inferred parameters in each luminosity segregated model. Ellipticities are derived a posteriori using the inferred parameters.

	α_c [°]	δ_c [°]	ϕ [rad]	r_{ca} [pc]	r_{ta} [pc]	r_{cb} [pc]	r_{tb} [pc]	α	β	γ	κ [pc mag $^{-1}$]	ϵ_{rc}	ϵ_{rt}
EFF	56.66	24.16	1.02	2.65		2.22				2.60		0.12	0.18
GDP	56.68	24.17	1.01	3.60		3.19		0.63	3.14	0.13		0.23	0.18
GKing	56.66	24.16	0.83	1.39	16.88	1.22	12.61	0.67	1.28			0.13	0.05 0.38
King	56.62	24.19	0.96	2.34	38.49	2.37	20.49					0.19	0.05 0.60
OGKing	56.61	24.17	0.99	1.62	22.08	1.59	14.04					0.10	0.07 0.36
RGDP	56.62	24.17	0.96	3.78		3.35		0.73	3.34			0.24	0.19

We observe that the ellipticities follow the same pattern as those of the previous Section. This is expected because we explicitly model the luminosity segregation as independent of the position angle.

The luminosity segregation inferred here is non negligible with κ in the range 0.1 to 0.25 pc mag $^{-1}$. Thus indicating that it is indeed an important parameter. However, in all the models, the marginal posterior distribution of κ does not discard the zero value.

The evidences of the models with luminosity segregation follow a similar pattern as those from radial symmetry. However, in this case the best model is the classical King's, which shows only moderate evidences against the EFF, RGDP and GDP models. The evidence of King's model over GKing and OGKing is weak.

The evidences of the luminosity segregated models strongly favour them against the radially and biaxially symmetric ones in all cases. We can conclude that although with a small value of κ the luminosity segregations is an important parameter regardless of the model used.

4.5 Proper motions distribution

The bivariate proper motions distributions of both single and EMB is directly recovered by the BHM. These bivariate distributions and their univariate projections, in the $\mu_\alpha \cdot \cos(\delta)$ and μ_δ components, are shown in Figs. 4.23, and, 4.24 and 4.25, respectively. These two latter figures also display the KDE of the proper motions of the candidate members in: i) [Bouy et al. \(2015\)](#), and ii) the HMPS. Interestingly, the densities rendered by this two samples of candidate members are almost identical, except perhaps by the small excess of [Bouy et al. \(2015\)](#) in the region at $\mu_\delta \sim -30$ mas yr $^{-1}$.

Notice that, the density resulting from the BHM differs from the KDE of the HMPS. I

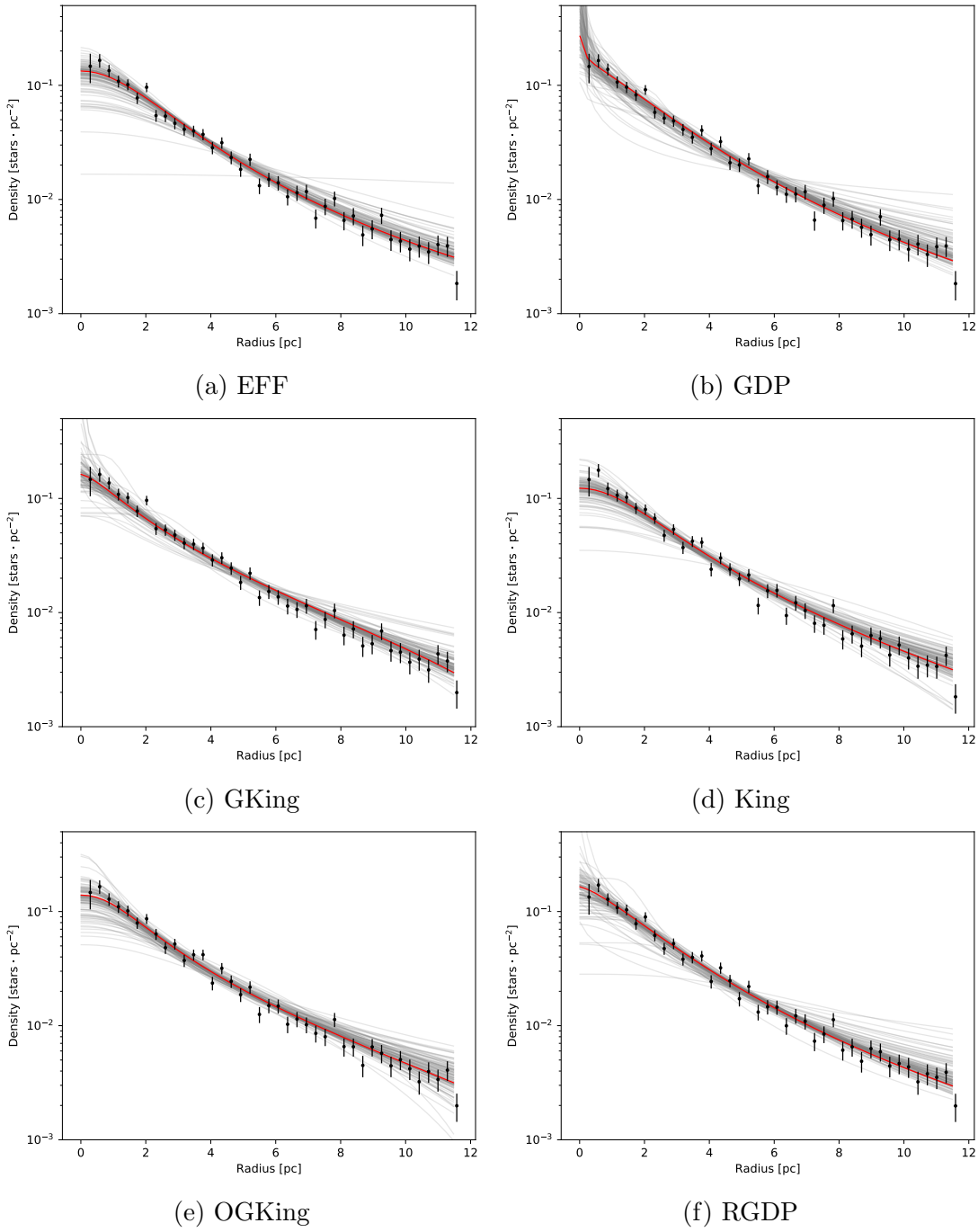


Figure 4.21: Inferred density of the biaxially symmetric and luminosity segregated profiles shown by means of the MAP value (red line) and samples from the posterior distribution (grey lines). For comparison the data has been binned with poissonian uncertainties (black dots).

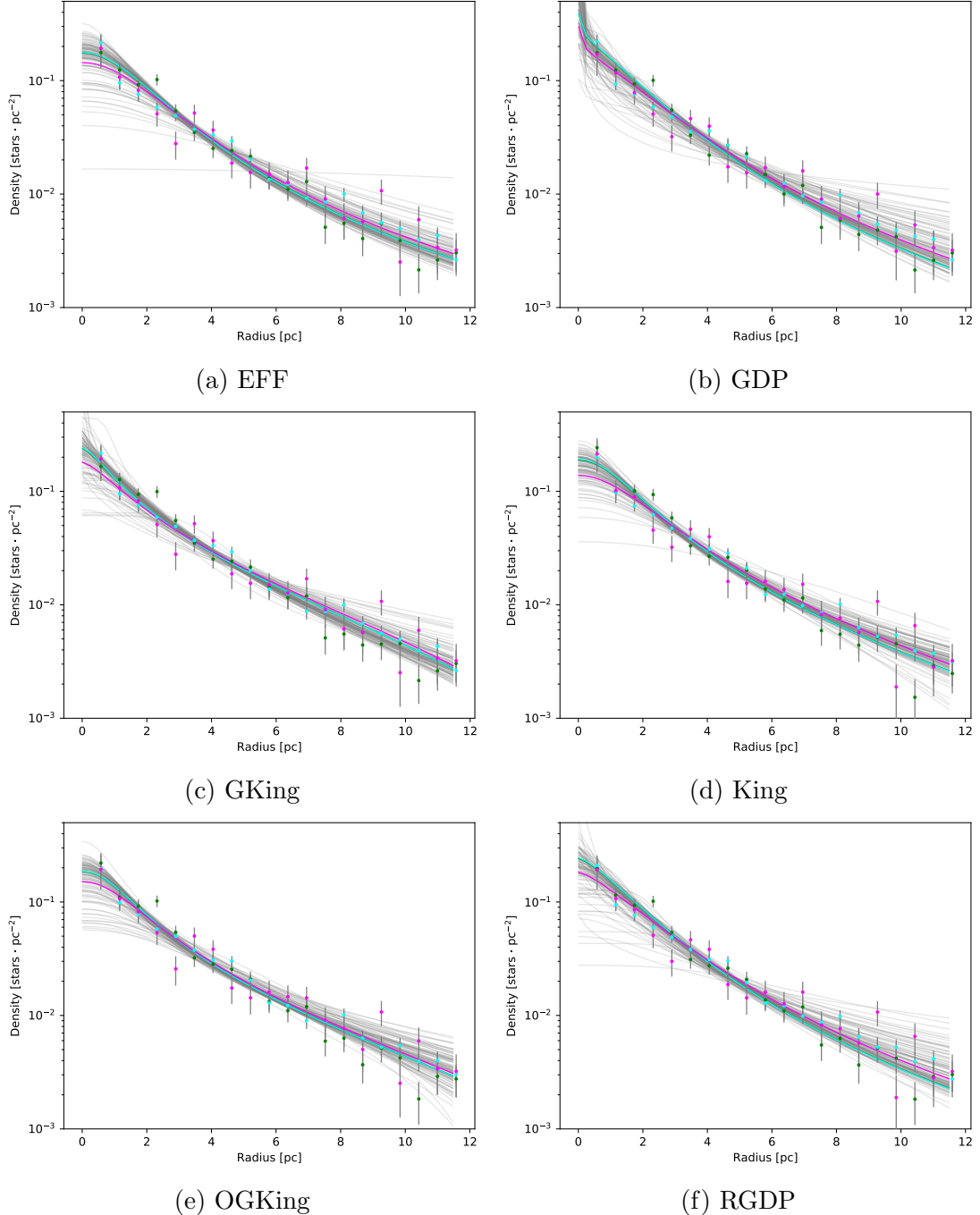


Figure 4.22: Density profiles of the data binned in J band ($J < 12$, green dots, $12 \lesssim J \lesssim 15$ cyan dots, and $15 < J$ magenta dots) together with the density models with parameters at the MAP values. The core radii r_c has been increased according to Eq. 3.89.

remember the reader that the BHM recovers the posterior distribution of its parameters using the likelihood of all the objects in the data set (the 10^5 in the RDDR2), with the contribution of individual objects proportional to their cluster membership probability. Therefore, the observed difference is the result of the two different samples of objects. The HMPS KDE uses only 1967 objects with cluster membership probability grater than 0.84, and not weighted by membership probability

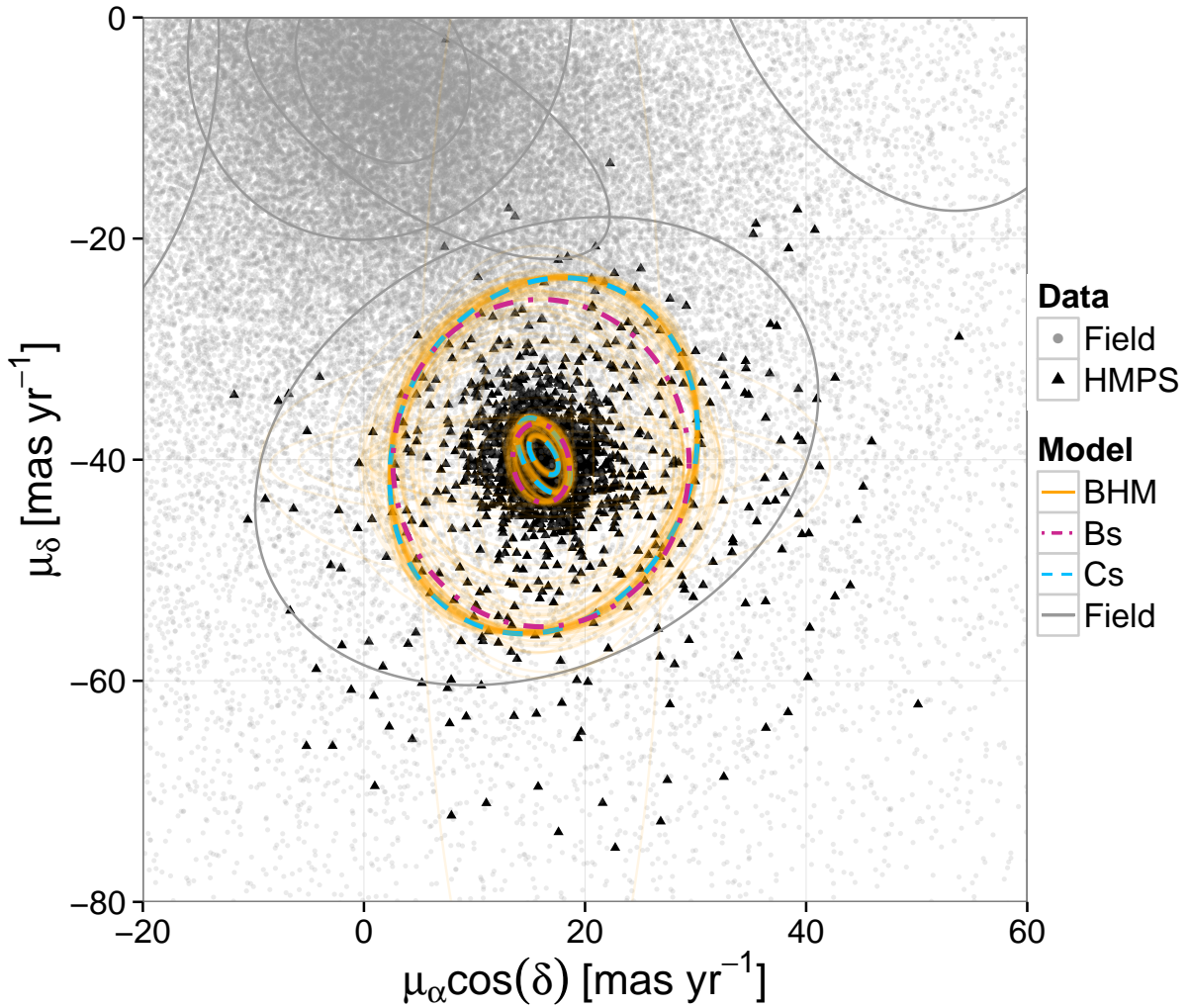


Figure 4.23: Proper motion distributions recovered by the BHM. The dashed and dot-dashed ellipses represent the mode of 100 samples (orange lines) from the posterior covariance matrices in the cluster and EMB GMMs, respectively. The grey ellipses depict the field model shown in panel (b) of Fig. 3.6. Reproduced from Figure 8 of Olivares et al. (2017), *The Seven sisters DANCE III: Hierarchical Bayesian model*, A&A, Vol. submitted.

Nevertheless, it is important to notice that, as the analysis of Section 4.1 indicates, objects with a missing CI may have a biased membership probability, preferably towards

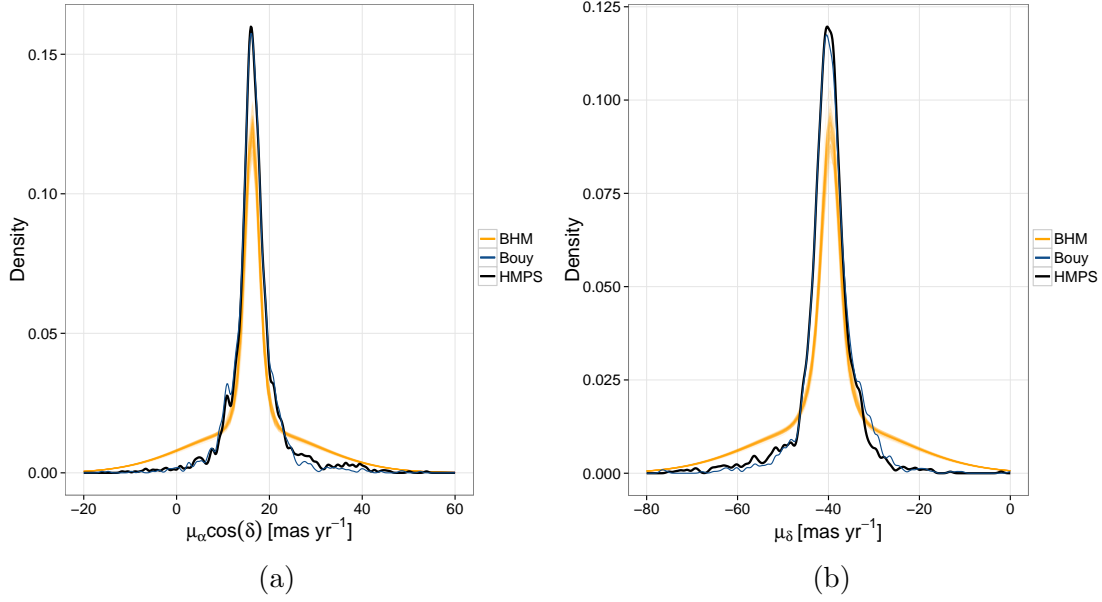


Figure 4.24: Proper motions densities resulting from: a 100 element sample from the posterior distributions of parameters in the GMM modelling the single stars (orange spaghetti lines), the kernel density estimation of the HMPS of candidate members classified as single stars (those whose cluster membership probability is higher than 0.84 and EMB membership probability is lower than 0.5), and, the kernel density estimation of the candidate members of [Bouy et al. \(2015\)](#) whose photometry lies below the EMB sequence (blue line).

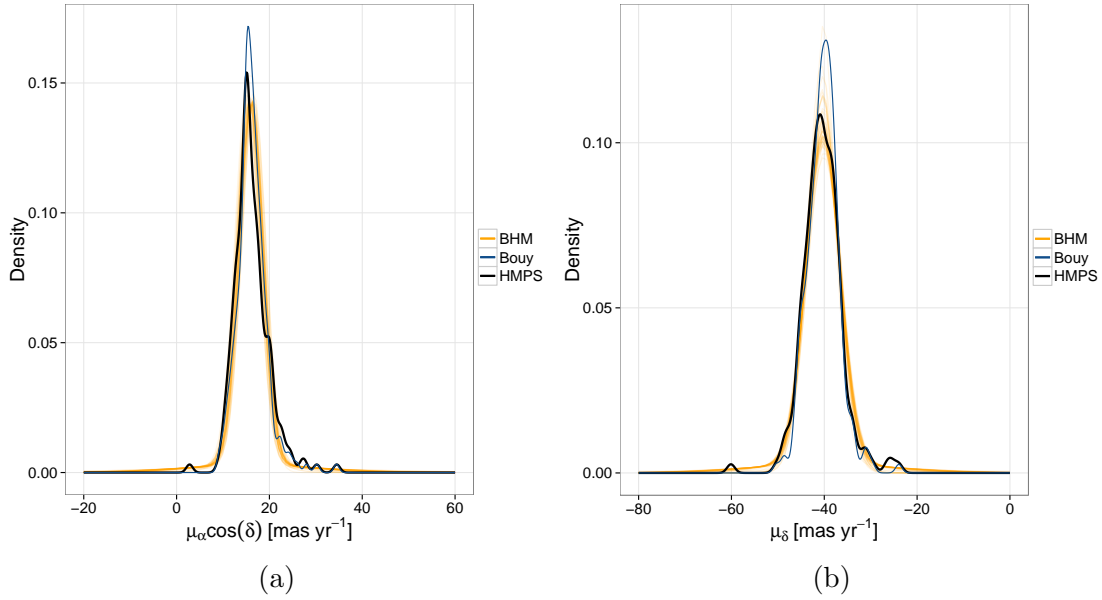


Figure 4.25: Proper motions densities resulting from: a 100 element sample from the posterior distributions of parameters in the GMM modelling the EMB stars (orange spaghetti lines), the kernel density estimation of the HMPS of candidate members classified as EMB stars (those whose cluster membership probability is higher than 0.84 and EMB membership probability is higher than 0.5), and, the kernel density estimation of the candidate members of [Bouy et al. \(2015\)](#) whose photometry lies near the EMB sequence (blue line).

higher values (see Fig. 4.3), and with a bias rms of 0.14. Thus, if I were to use a probability classification threshold of 0.5 instead of the 0.84 determined in Section 4.1, the result will be a sample of 2907 candidate members whose KDE proper motion probability distribution would match that of the BHM (see Fig. 4.26). From these 2907 hypothetical candidates, 50% (1453) have a missing CI. In contrast, using the correct probability threshold of 0.84 produces only 32% (629) of candidates members with missing CI. It is important to remark that not all objects with a missing CI are biased. As estimated in Section 4.1 based on the synthetic data, the expected value of these contaminants all along the entire range of probability threshold is $5.8 \pm 0.2\%$. Furthermore, the simulations with synthetic data, show no appreciable difference in the recovered proper motions distributions of objects with missing values when compared to those without them.

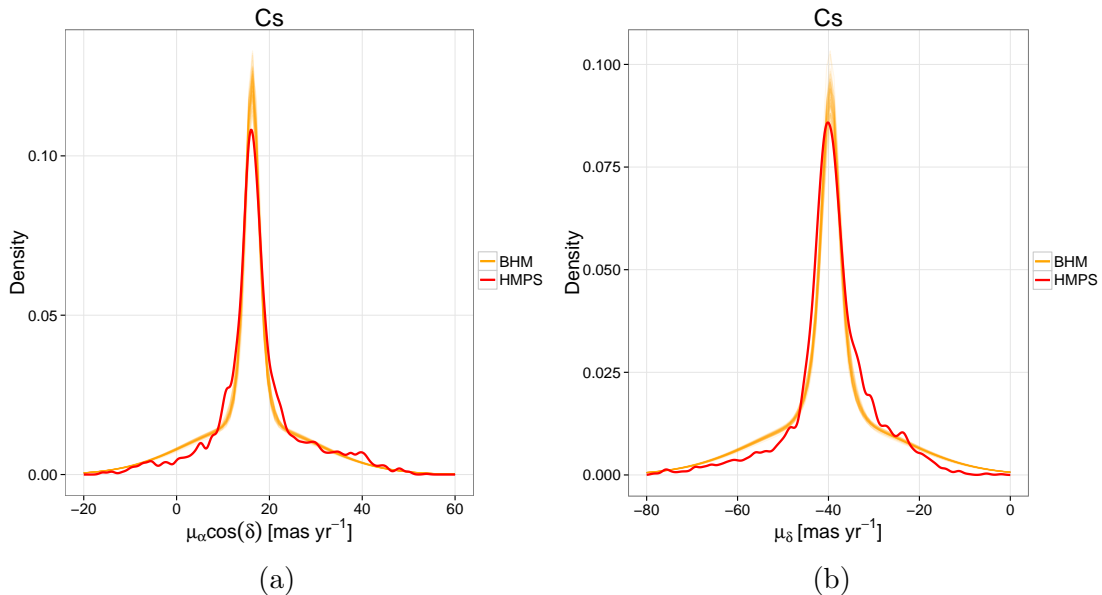


Figure 4.26: Proper motions densities resulting from: a 100 element sample from the posterior distributions of parameters in the GMM modelling the single stars (orange spaghetti lines), the kernel density estimation of the hypothetical HMPS of objects with cluster membership probability greater than 0.5 and classified as single stars (red line).

The large wings in the proper motions distribution of the BHM could be an effect of contamination, particularly because they are far from the cluster centre. However, proper motions and photometry have been independently modelled. Therefore, we have no reasons to believe that missing values affect predominately field objects with proper motions lying in this particular halo around the cluster centre.

In contrast, due to mass segregation, the cluster members could be predominantly affected by missing values. If mass segregation were indeed present, as shown in Section 4.4.3 with a luminosity proxy, then the fainter cluster members would be located in a halo around the cluster centre both in position and proper motions. This hypothesis is also supported by the lack of this effect in the proper motions distribution of EMB (see Fig. 4.25), this objects are massive than the average star, and therefore are brighter,

less affected by missing values (at least in CI), and due to the gravitational potential are located in the inner cluster region with lower proper motions. In any case, to taste the validity of this assumption we will have to wait the arrival of better data, with less missing values particularly.

4.6 Luminosity distribution

This Section describes the process to obtain the J, H , and K_s absolute magnitude distributions from the posterior distributions of the parameters in the BHM. Later, I compare them to those found by [Bouy et al. \(2015\)](#), in the K_s band specifically. As in the previous section, I also compare these distributions with those resulting from the kernel density estimates of the HMPS of candidate members resulting from the BHM.

4.6.1 Derivation of the magnitude distributions

In the BHM the photometric magnitudes are expressed as functions of the true CI (see Section 3.3.4) The J, H, K_s magnitude distributions are derived by transforming the true CI distribution into the J, H, K_s apparent magnitude distributions by means of the posterior distributions of the cluster photometric parameters. In particular, I use the B-splines and the intrinsic dispersion of the cluster photometric sequence. In this transformations, the fractions of EMB are taken into account by mixing the single and EMB populations according to their fractions. In the following paragraphs, I describe the process to obtain the K_s apparent magnitude. This process is similar for the rest of the bands.

Since we aim at the probability distribution of K_s , and it depends on the true CI , I use this as a nuisance parameter that I later marginalise. Thus,

$$p(K_s|\boldsymbol{\theta}_c) = \int p(K_s, CI|\boldsymbol{\theta}_c) \cdot dCI = \int p(K_s|CI, \boldsymbol{\theta}_c) \cdot p(CI|\boldsymbol{\theta}_c) \cdot dCI.$$

The term $p(K_s|CI, \boldsymbol{\theta}_c)$ represents the probability of K_s given the true CI and the cluster parameters $\boldsymbol{\theta}_c$. It is given by Eq. 3.39. The second term, $p(CI|\boldsymbol{\theta}_c)$ corresponds to the GMM modelling the distribution of the true CI , it is given by Eq. 3.40.

We include the EMB distribution with an amplitude equal to their fraction, $1 - \pi_{CB}$. Thus,

$$\begin{aligned}
p(K_s|\boldsymbol{\theta}_c) &= \int [\pi_{CB} \cdot p_{Cs}(K_s|CI, \boldsymbol{\theta}_c) + (1 - \pi_{CB}) \cdot p_{Bs}(K_s|CI, \boldsymbol{\theta}_c)] \\
&\quad \cdot p(CI|\boldsymbol{\theta}_c) \cdot dCI. \\
&= \pi_{CB} \int p_{Cs}(K_s|CI, \boldsymbol{\theta}_c) \cdot p(CI|\boldsymbol{\theta}_c) dCI \\
&\quad + (1 - \pi_{CB}) \int p_{Bs}(K_s|CI, \boldsymbol{\theta}_c) \cdot p(CI|\boldsymbol{\theta}_c) \cdot dCI.
\end{aligned} \tag{4.1}$$

In this equation, *Cs* and *Bs* are the subindices used to distinguish the probability of K_s under the cluster and EMB photometric models, respectively. These probabilities are defined for the vector of photometric measurements, \mathbf{d}_{ph} (see Eq. 3.39). Since we are interested only in the distribution of K_s (by now), we marginalise the rest of the photometric entries, including the observed CI (I use a tilde over the observed quantities). Also, the integration limits must change to those of the truncated true colour distribution ($CI_{min} = 0.8, CI_{max} = 8$). Hence,

$$\begin{aligned}
p(K_s|\boldsymbol{\theta}_c) &= \pi_{CB} \int_{CI_{min}}^{CI_{max}} \left[\left[\sum_{i=1}^5 \pi_{CI,i} \cdot \mathcal{N}_t(CI|\mu_{CI,i}, \sigma_{CI,i}) \right] \right. \\
&\quad \cdot \left. \int_{\tilde{CI}, \tilde{Y}, \tilde{J}, \tilde{H}} \mathcal{N}(\{\tilde{CI}, \tilde{Y}, \tilde{J}, \tilde{H}, K_s\} | \mathbf{S}(CI, \boldsymbol{\beta}), \Sigma_{clus}) d\tilde{CI} d\tilde{Y} d\tilde{J} d\tilde{H} \right] \cdot dCI \\
&\quad + (1 - \pi_{CB}) \int_{CI_{min}}^{CI_{max}} \left[\left[\sum_{i=1}^5 \pi_{CI,i} \cdot \mathcal{N}_t(CI|\mu_{CI,i}, \sigma_{CI,i}) \right] \right. \\
&\quad \cdot \left. \int_{\tilde{CI}, \tilde{Y}, \tilde{J}, \tilde{H}} \mathcal{N}(\{\tilde{CI}, \tilde{Y}, \tilde{J}, \tilde{H}, K_s\} | T_{Bs}(\mathbf{S}(CI, \boldsymbol{\beta})), \Sigma_{clus}) d\tilde{CI} d\tilde{Y} d\tilde{J} d\tilde{H} \right] \cdot dCI.
\end{aligned}$$

The derivations of the J and H magnitude distributions are similar. Since this process takes into account the unresolved EMB and the so called single stars, which in fact could be binaries with low mass ratios, then I call these distributions the apparent system magnitude distributions.

The previous distributions, together with the parallax and extinction of the cluster, are used to obtain the luminosity distributions, more properly the absolute system magnitude distributions. I assume that the distribution of parallaxes of the Pleiades members is normally distributed with mean, 7.44 mas, and standard deviation 0.42 mas (Galli et al. 2017). Then, to obtain the absolute magnitude distributions, I use the standard formulation

$$M = m - 5(\log_{10} d + 1) = m + 5(\log_{10} \pi + 1),$$

where M and m are the absolute and apparent magnitudes, and d and π the distance

and parallax, respectively. Thus, I convolve the distribution of the log parallax with the apparent J, H, K_s magnitude distributions. Notice that here, for simplicity, I assume that the distribution of the parallax leads to the distribution of distances. Formally, the individual distances to the Pleiades must be inferred from the individual parallaxes (see for example [Astraatmadja & Bailer-Jones 2016b](#)). Then the absolute magnitude distributions can be obtained by convolving this distance distribution with the apparent magnitude ones. Since the objective here is to compare the mass distribution with those in the literature, I proceed as in previous works and leave the formal treatment of distance inference to future works.

Finally, I deredden the previous distributions employing the canonical value of extinction for the Pleiades: $A_v = 0.12$ mag ([Guthrie 1987](#)). This last values were transformed into the J, H, K_s extinctions using the extinction law of [Cardelli et al. \(1989\)](#).

Since the BHM describe the magnitudes as functions of the CI, the completeness limits of the latter dictate those of the former, except for those of the i and K_s magnitude. The latter prescribe the completeness interval of the CI, which is defined as that of all the points, along the cluster sequence in the K_s vs. $i - K_s$ CMD, for which i and K_s are bounded by their upper and lower completeness limits, respectively. Using the completeness limits found in Section 2.7.3 results in a completeness interval of $2.7 < CI < 5.6$ mag. With it, and the cluster sequence (the splines and their parameters), I derive the completeness intervals for the J, H, K_s bands. Finally, I transform these intervals to absolute magnitudes and deredden them.

The luminosity distributions in the J, H, K_s bands derived from the BHM, together with their completeness limits are shown in Fig. 4.27. For the sake of comparison, I also show the luminosity distributions resulting from the KDE in the magnitudes of the candidate members from: i) the HMPS derived in previous sections, and, ii) [Bouy et al. \(2015\)](#). Since the luminosity distributions of Bouy and the HMPS, depend on the magnitudes of the individual candidate members, and many of them have missing entries, then I impute their missing values using those of the nearest euclidean neighbour.

The difference between the luminosity distributions derived using the posterior distribution of the cluster photometric parameters (i.e. the BHM) and that obtained from the HMPS of candidate members, comes as well from the fact that the HMPS is not a random sample of the cluster population, but it is selected based on the membership probability. Thus the latter is biased towards objects with high membership probability. Since the luminosity distributions derived from the cluster parameters takes into account all objects proportionally to their cluster membership probability, the it is free from this kind of bias. Another source of discrepancy comes from objects with missing entries. While in the luminosity resulting from the BHM the missing values are marginalised, in that of the HMPS they are imputed.

On the other hand, the differences between the discrete distributions, the BHM and

that of [Bouy et al. \(2015\)](#), arise mainly at the bright and faint ends ($K_s \sim 4$ mag and $K_s \sim 11$ mag). I hypothesise that the origin of these differences lie in the different list of candidate members. To quantify the discrepancies between these two distributions, I performed the Anderson-Darling similarity test. In the comparison between the each of the 100 samples from the luminosity distribution from the BHM and that of [Bouy et al. \(2015\)](#), all the probabilities that the two distributions come from the same parent distributions are below $p < 0.04$ (the statistics from this test are in all cases larger than 10).

As it has been discussed, the model of [Bouy et al. \(2015\)](#) is constructed only based in fully observed objects. The regions where the objects with missing entries happen more frequently is in the bright and faint regions. Therefore, the observed differences in the luminosity distributions may arise from the simplistic treatment that those authors made of objects with missing entries (see Section 3.3.1).

4.7 Mass distribution

In this Section I describe the procedure to transform the luminosities distributions into mass distributions. Transforming a probability distributions requires the transformation *per se* and its derivative (see Section 3.1). Once the mass distributions is obtained, then, I compare it to the IMFs of [Chabrier \(2005\)](#) and [Thies & Kroupa \(2007\)](#). Finally, I conclude this section with the analysis of some simple toy models that can be fitted to the derived mass distribution.

4.7.1 The mass-luminosity relation

The mass-luminosity relation is the non linear transformation that enables us to obtain the mass distribution from the luminosity distributions. Given the values of the upper limits of the luminosity distributions (the faint ends), the mass-luminosity relation relies entirely on the current models of stellar structure, where the atmospheres also play an important role. Among the different flavours of theoretical stellar evolution models in the literature (those from the Pisa, Padova, Trieste, Geneva, and Lyon research groups) we choose the BT-Settl models of [Allard et al. \(2012\)](#). These models go deeper into the lower masses reaching the planetary mass range thus allowing a complete coverage of our luminosity distributions. The rest of the models stay in the $0.1 - 10 M_\odot$ range, with the *PARSEC* models being the ones reaching the $0.1 M_\odot$ limit ([Bressan et al. 2012](#)). Figure 4.28 compares the BT-Settl models of [Allard et al. \(2012\)](#) to the RDDR2 data set (top panels), and to the cluster sequence obtained by the BHM and the HMPS of cluster candidate members (bottom panels). The BT-Settl model corresponds to the Pleiades isochrone (at a distance of 134 pc, with 120 Myr and solar metallicity, which are the canonical ones, see Section 3.2.1) given by the CIFIST2011bc grid, with J and K_s bands

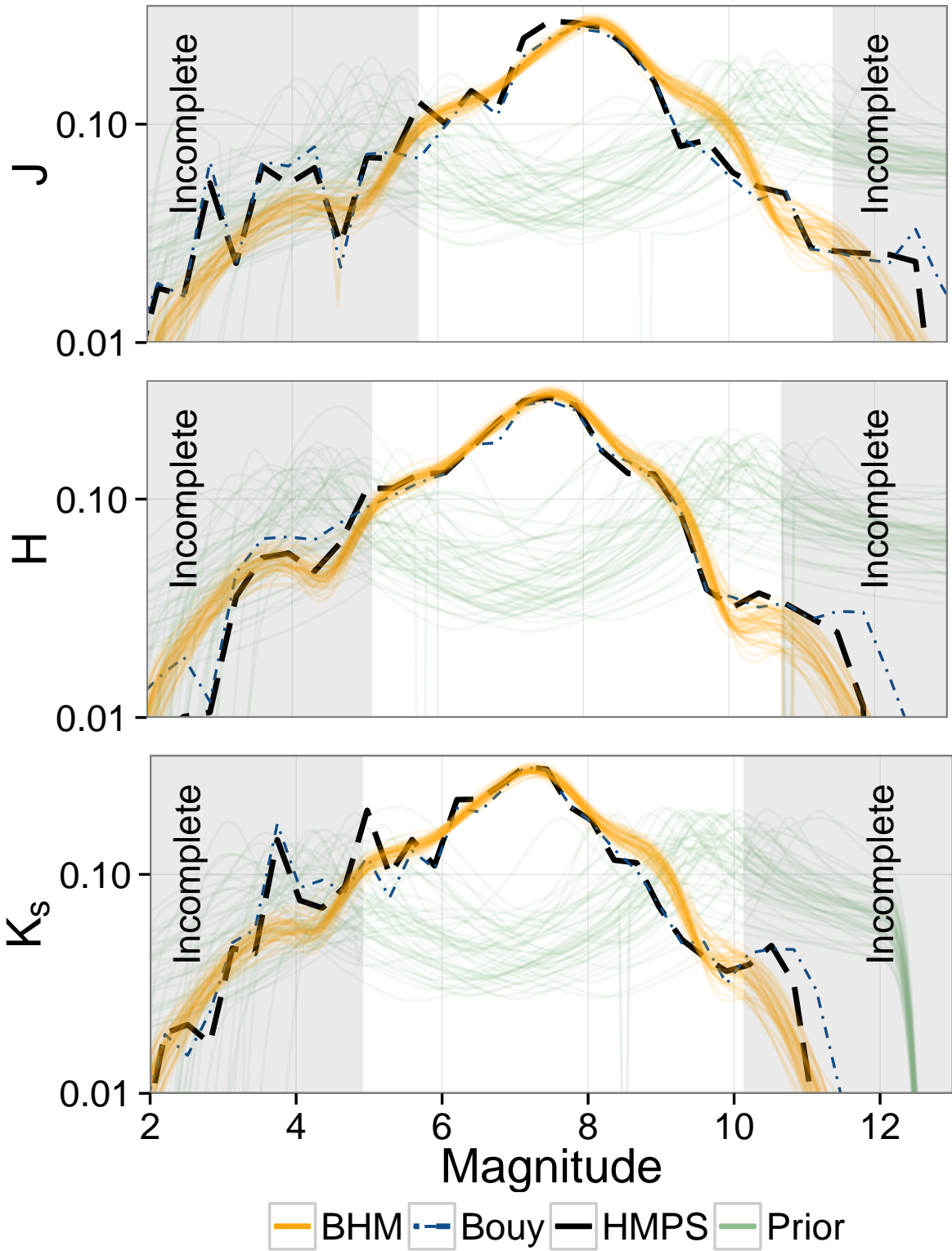


Figure 4.27: Luminosity distribution of J , H , K_s bands derived from the BHM (orange spaghetti lines). Also shown: the regions of incompleteness, the luminosity distributions computed from: the candidate members of Bouy et al. (2015) (dot-dashed blue line), and our HMPS of candidate members, ($p_{84\%} > p_t$, dashed black line), and the prior for the true CI, which was transformed in the same way as the posterior CI distribution.

in the 2MASS Vega photometric system and the i band in the Sloan AB system, which correspond to the ones used in the DDR2 data set (H. Bouy, private communication).

Notice that the i band photometry yielded by the BT-Settl model, contrary to the J and K_s ones, does not fit the observed data (solid lines in Fig. 4.28). It must be shifted by 0.7 mag in order to be in accordance with the observed values (dashed lines in Fig. 4.28). In a private communication with France Allard, she explained me that there was problem in the computation of some of the latest versions: a value from the earlier versions of Baraffe et al. (1998) remained unaltered in the new versions. She assured me that they were working to solve that problem. This is probably the reason for the discrepant values returned by the Sloan AB system. However, since the the J, H and K_s bands are unaffected, this issue pose no problem for the further results of the present work.

The CIFIST2011bc grid returns values of the luminosity for certain non uniformly distributed values of the mass. As shown in Eq. 3.6, the transformation of a probability distribution, in this case the luminosities probability distributions, into the mass distribution is proportional to the derivative of the transformation, which must be continuous. To avoid the discontinuities in the derivatives produced by the grid, we fit the grid values by spline series (see Fig. 4.29a). Then, derivative is obtained from these continuous series (see Fig. 4.29b). It is important to notice the following two assumptions. First, I assume that the luminosity distributions in J, H and K_s bands are independent between them, and then I obtain a mass distribution for each one of them. Second, I assume that the transformation from luminosities to masses does not have any associated uncertainty. I must assume that because the isochrone models do not provide neither uncertainties nor a way to incorporate correlations between the mass distributions of distinct photometric bands.

Figure 4.29a shows the spline fit to the mass-luminosity relations of the BT-Settl absolute J, H and K_s magnitudes (black points) as a function of the mass. Figure 4.29b shows the derivative of mass-luminosity relation. The grey shaded areas represent the incompleteness regions of the DANCE survey (see previous section).

4.7.2 Present day system mass distribution

The mass distribution is independently obtained for the J, H, K_s luminosity distributions by means of the mass-luminosity relations described in the previous section. Since the luminosity functions of Sect. 4.6 correspond to the luminosity of systems (single stars unresolved binaries and multiple systems), then, the derived mass function corresponds to the Present-Day System Mass Distribution (PDSMD). Figure 4.30 shows the logarithmic PDSMD (ξ_L) for the J, H, K_s bands normalised on the completeness limits of the DDR2. The logarithmic representation of the mass distribution is a transformation from the natural variable of mass into the logarithm of 10 scale. It is customary to represent the mass distribution in this scale.

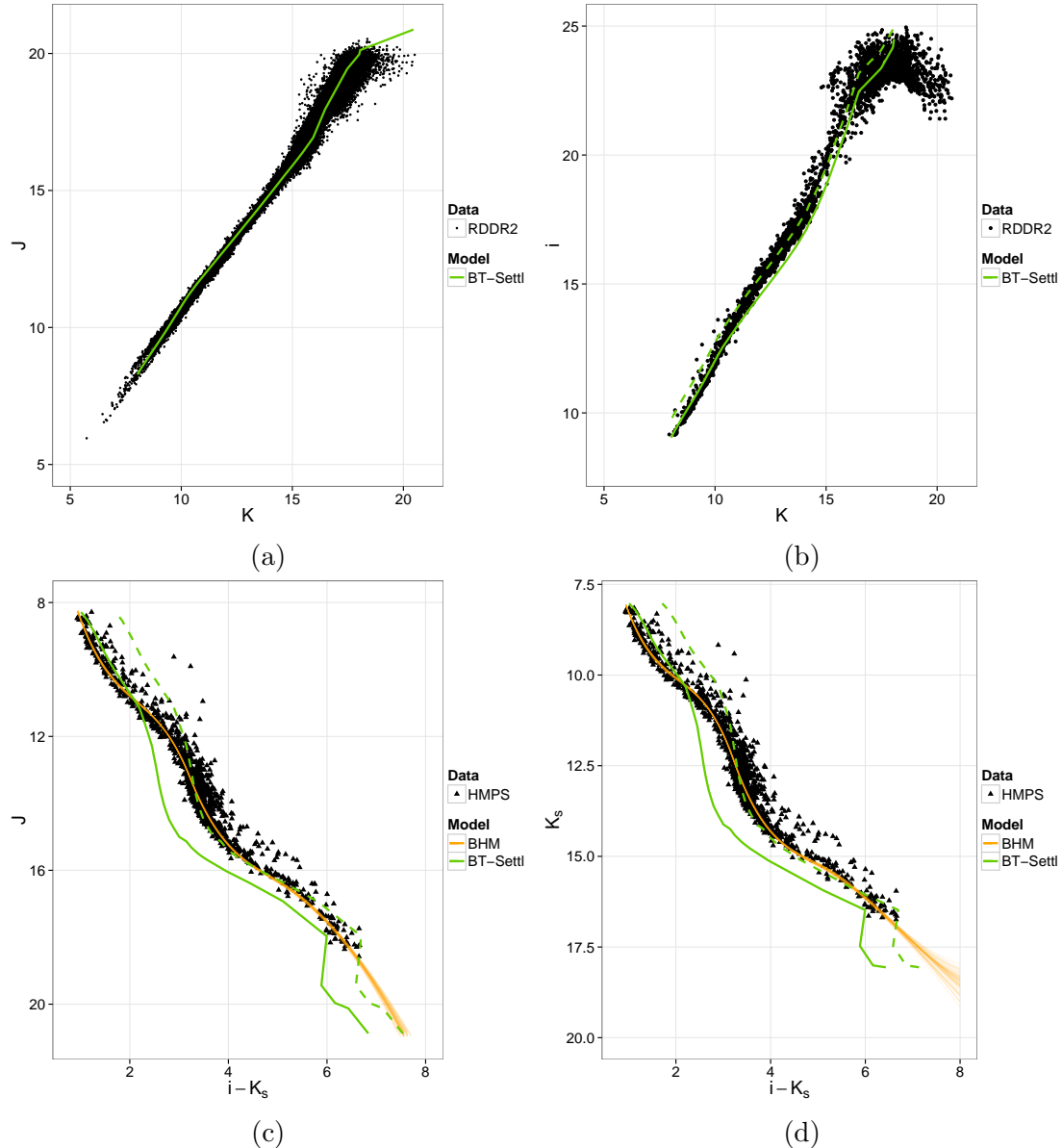


Figure 4.28: Comparison between observations and models. Top panels: J vs. K_s and i vs K_s magnitude-magnitude diagrams showing the RDDR2 objects (black dots), and the original (green solid lines) and shifted (green dashed lines) BT-Settl models. Bottom panels: J vs $i - K_s$ and K_s vs $i - K_s$ CMDs showing the HMPS of candidate members and the original (green solid lines) and shifted (green dashed lines) BT-Settl models. See text for details.

The derived PDSMD in J , H , and K_s bands are consistent with themselves for masses above $0.06 M_\odot$ ($-1.2 < \log M/M_\odot$). However, the J band PDSMD shows discrepancies with the H and K_s ones in the mass interval $0.025 - 0.06 M_\odot$ ($-1.6 < \log M/M_\odot < -1.2$), with a peak in discrepancy at $0.04 M_\odot$ ($-1.4 = \log M/M_\odot$), see Fig. 4.30. The latter correspond to an effective temperature of ~ 2200 K, which is at the middle of the transition between L and M dwarfs. This transition is not perfectly reproduced by any stellar structure and atmosphere model (Allard et al. 2012), and the BT-Settl one shows an excess in the flux of the J band (Allard et al. 2013).

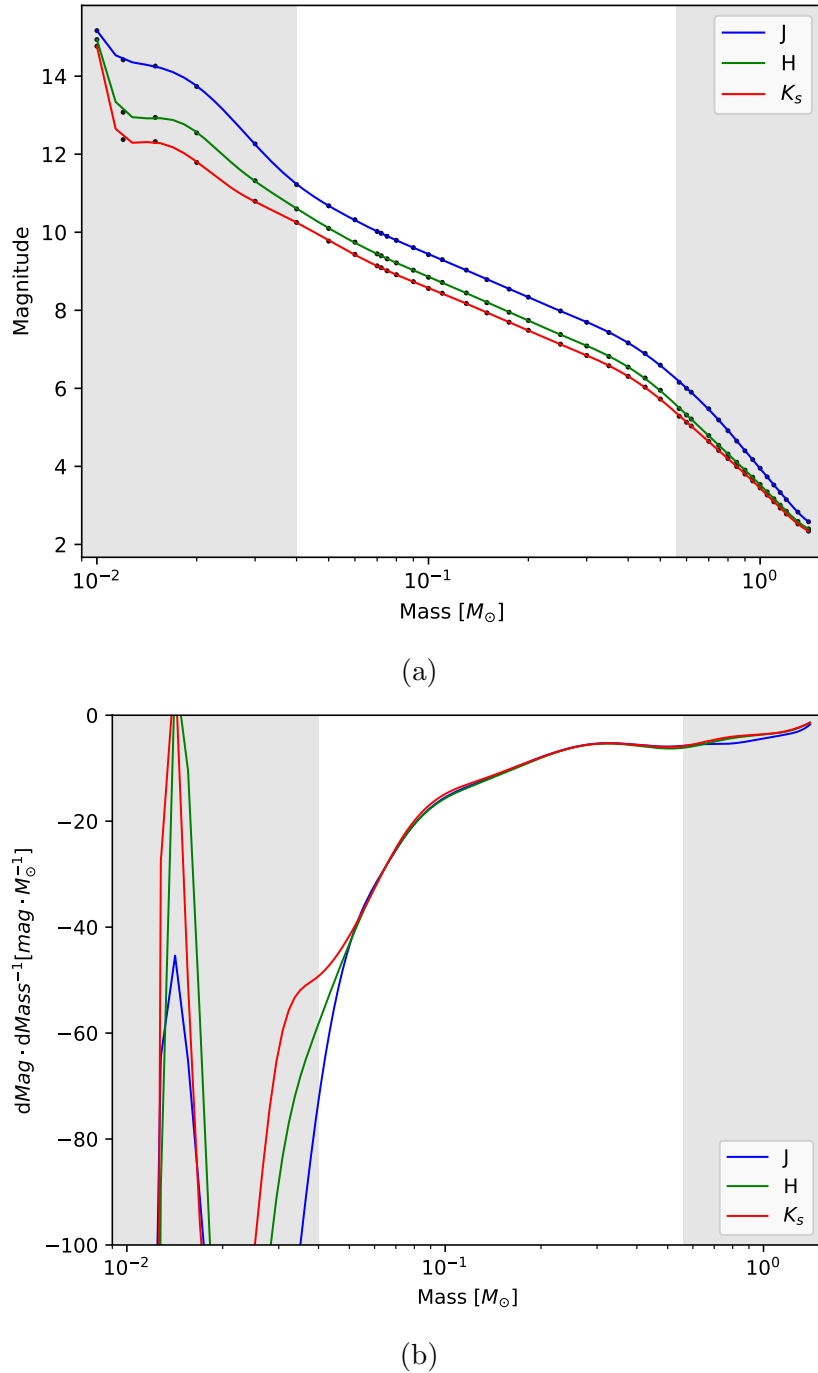


Figure 4.29: Upper panel: Mass-luminosity relations from the BT-Settl models (Allard et al. 2012) for the J , H and K_s bands of the 2MASS photometric system (black dots). Also shown, the splines fitted to the previous relations. Bottom panel: The derivative of the mass-luminosity relations in the upper panel. The incompleteness regions of the DANCe survey (grey areas) are shown in both panels.

Due to the mentioned issue with the J band, and the fact that the K_s band is less affected by the interstellar extinction, in the following I will continue the discussion based only on the PDSMD of this latter band.

For the sake of comparison, Figure 4.31 shows the PDSMD (ξ_L) for the K_s band of the previous Figure, together with the three-slope power-law function of Bouy et al. (2015),

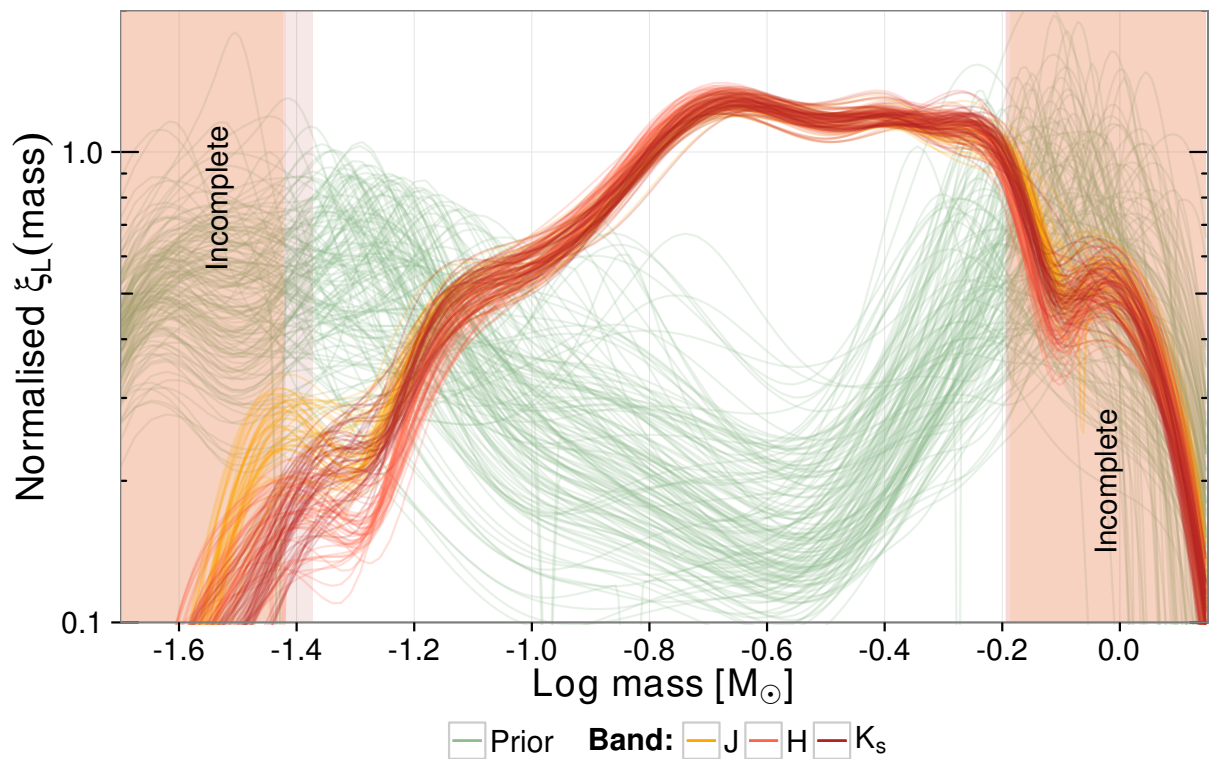


Figure 4.30: Normalised logarithmic PDSMD in J, H, K_s band. Also shown the completeness limits computed in previous section and transformed with the mass-luminosity relation, and the prior distribution, which was transformed in the same way as the posterior distribution.

and the IMF of [Thies & Kroupa \(2007\)](#) and [Chabrier \(2005\)](#). The standard uncertainties in [Chabrier \(2005\)](#) IMF are those reported in [Chabrier \(2003a\)](#).

This Figure shows that the PDSMDs derived from the BHM compare well, at least in the completeness interval, with the one proposed by [Bouy et al. \(2015\)](#). The discrepancies between these two, above $0.3M_{\odot}$ ($-0.5 < \log M/M_{\odot} < -0.2$) particularly, may have its origin on the following aspects.

The PDSMD of [Bouy et al. \(2015\)](#) is computed using only their candidate members within the central three degree region of the DDR2. First, their list of candidate members is not the same as those found by the BHM. Second, the PDSMD derived from the BHM uses all objects in the data set, not just the high membership probability candidates. Third, as mentioned in Section 4.6, the cut to the central three degree region may have biased the derived PDSMD of [Bouy et al. \(2015\)](#). Therefore, the lack of objects that it shows, in the mass range $0.3 - 0.7M_{\odot}$ ($-0.5 < \log M/M_{\odot} < -0.2$) particularly, may have its origin in the objects that [Bouy et al. \(2015\)](#) did not include in his analysis: those lying outside the inner three degree region.

For the sake of completeness, I fit a simple model to the PDSMD obtained by the BHM. To do it, I proceed as follows. First, I select three competing models: a log-normal function (like that of [Chabrier \(2003a, 2005\)](#)), and two power-law functions of the form $m^{-\alpha}$ with two and three segments. Second, from the derived PDSMD in the K_s band, I took a sample of 100 distributions (the ones shown as spaghetti lines in Fig. 4.31). Then, I divide the completeness interval into a grid with 200 steps, and at each step I compute the mean of the values given by the 100 distributions. After normalisation this function can be thought as a mean distribution of the mass. Third, from the latter, I draw a sample of 10^4 synthetic masses. Fourth, using *PyMultiNest* ([Buchner et al. 2014](#)) and the sample of synthetic masses, I obtain: i) the posterior distributions of the parameters in each of the three competing models, and ii) Bayesian evidences (Eq. 3.10) for each of these models. In Table 4.7 I report the MAP of the parameters in each model, together with the natural logarithm of the computed evidences. Judging by [Jeffreys \(1961\)](#) scale of evidence (see Table 4.2), there is decisive evidence in favour of the two and three segment power-law models and against the log-normal function. However, the Bayes factor of the former indicates an evidence which barely worth mentioning. Under inconclusive evidence, I am allowed to use a simplicity prior (prejudice for simpler models) for the two competing power-law models (see Eq. 3.18). Thus, I chose the two-segment power-law model, which I show in Fig. 4.31 by means of the black solid line.

The two segment power-law model agrees with the three segment model of [Bouy et al. \(2015\)](#). However, there are still differences, which are clear at the low and high mass ends particularly. Nevertheless, it is in clear discrepancy with the IMFs of [Chabrier \(2005\)](#), ($m_c = 0.25^{+0.021}_{-0.016}$ and $\sigma = 0.55^{+0.05}_{-0.01}$, the uncertainties are those reported by [Chabrier 2003a](#), for single objects) and of [Thies & Kroupa \(2007\)](#).

The discrepancy between the IMFs and the PDSMD derived from the BHM and the PDSMD of Bouy et al. (2015) may have its origin on the not yet established uncertainties in the mass-luminosity relation, on dynamical effects associated with age, or in a combination of the previous. In the next section I compare the PDSMD of the Pleiades with that of other younger and older clusters in order to analyse if there is evidence of dynamical effects associated with age.

Table 4.7: Parameters and evidence of models fitted to the PDSMD

Model	Parameters	Log Evidence
LogNormal	$m_c = 0.36 \pm 0.03$ $\sigma = 0.46 \pm 0.02$	18.1 ± 0.1
Two Segments	$\alpha_0 = -0.11 \pm 0.06$ $m \in [0.04, 0.22 \pm 0.01]$ $\alpha_1 = 1.13 \pm 0.1$ $m \in [0.22 \pm 0.01, 0.56]$	2222.7 ± 0.4
Three Segments	$\alpha_0 = -0.05 \pm 0.6$ $m \in [0.04, 0.08 \pm 0.03]$ $\alpha_1 = -0.1 \pm 0.1$ $m \in [0.08 \pm 0.03, 0.22 \pm 0.01]$ $\alpha_2 = 1.13 \pm 0.1$ $m \in [0.22 \pm 0.01, 0.56]$	2221.2 ± 0.3

However, ending this section, I use the PDSMD to give a lower limit to the mass of the cluster. Since the RDDR2 data set still lacks the very low mass range and most of the high mass range, the mass derived from this PDSMD is only a lower limit to the mass of the cluster. From the PDSMD, the cluster mean mass in the entire mass range is $0.257 \pm 0.006 M_\odot$. Thus, the product of this mean mass with the expected number ³ of cluster members (3301 ± 140), gives the expected mass of the cluster in this mass range. This value is $845^{+38}_{-33} M_\odot$.

Finally, I notice that, as mentioned in Sect. 4.7.1, the uncertainties in the mass-luminosity relations are yet to be established. Thus the quoted uncertainties of our mass results are underestimated.

4.8 The mass distribution on time

Assuming the universality of the IMF, the observed differences between the present day mass distribution and the initial mass functions may have their origin on the temporal evolution of the cluster population. To test this hypothesis, I compare the Pleiades PDSMD (~ 125 Myr) with those of the younger Trapezium (0.2 to 1.4 Myr Muench et al. 2002) and older Hyades (648 ± 45 Myr De Gennaro et al. 2009) clusters. Under the assumption of a universal IMF, the PDSMDs of these two cluster can be thought as snapshots of the Pleiades past and future mass distributions.

³As explained before, the expected number of cluster members is the integral, over the whole range of membership probabilities, of number of objects at each membership probability value.

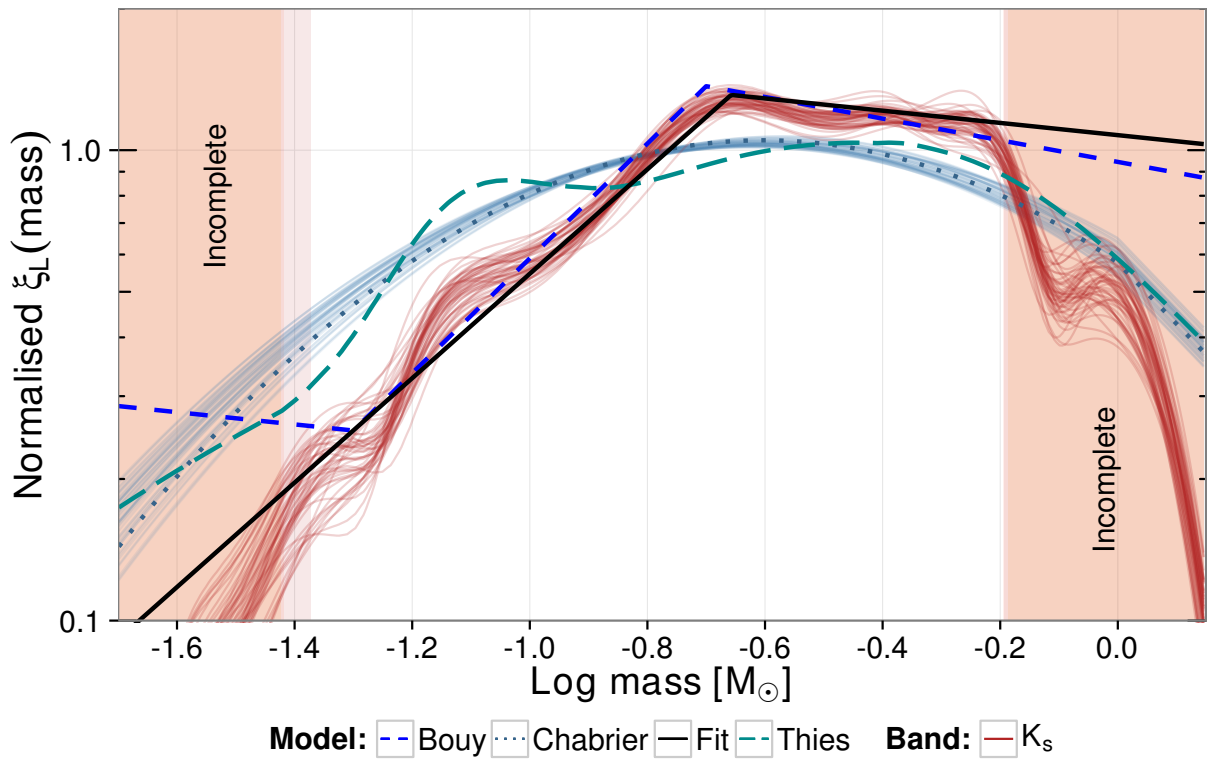


Figure 4.31: Normalised logarithmic PDSMD in K_s band. Also shown the IMFs of Chabrier (2005) (blue dotted line with uncertainties from Chabrier 2003a) and Thies & Kroupa (2007) (turquoise long-dashed line), and power-law models found here (black solid line, see text) and by Bouy et al. (2015) (blue dashed line).

Although this comparison formally lies beyond the objectives of the present work, nevertheless, it gives an idea of the importance that the PDSMD of other NYC have in the understanding of the formation and evolution of the mass distribution.

Figure 4.32 shows the PDSMD from the Pleiades, together with those of the Trapezium and Hyades⁴. These PDSMDs correspond to those of Fig. 11 of [Bouy et al. \(2015\)](#). As mentioned by [Bouy et al. \(2015\)](#), the abundance of low-mass stars and brown dwarfs in the range $0.03 - 0.1 M_{\odot}$ ($-1.4 < \log M/M_{\odot} < -1$) seems to diminish with time. The relative increase of objects in the range $-0.4 < \log M/M_{\odot} < -0.2$ is an effect of the normalisation⁵. This effect is consistent with the classical scenario in which low-mass stars and brown dwarfs are ejected as the cluster relaxes.

Since I lack the learned BHM for these two open clusters, the following comparison is made on a frequentist hypothesis testing approach, rather than on the proper Bayesian model selection scheme.

In this hypothesis test, the null hypothesis is that the Hyades and Trapezium PDSMDs came, each of them, from the same distribution than the Pleiades.

If we want to test the null hypothesis that two distributions come from the same parent distribution, Kolmogorov-Smirnov (KS) and the Anderson-Darling (AD) tests are classical options, with the AD the most robust one. To perform these tests, we must compute certain measures from the two distributions. Then, given the measure, the test distribution returns the probability that the two distributions came from the same parent distribution. Finally, we reject the null hypothesis only if the previous probability is lower than certain probability threshold (α), which is usually 0.1, 0.05, or 0.01.

To perform the KS tests we must obtain the maximum distance between the Cumulative Distribution Functions (CDFs) of the two distributions. Then, using this distance and the KS distribution, we obtain the probability that the two distributions came from the same parent distribution.

However, the KS test can also be applied in a graphical way. Given the α probability threshold, there is a d_{α} distance for which the KS distribution returns a probability α . For $d < d_{\alpha}$ $p_{KS}(d) > \alpha$ and for $d > d_{\alpha}$ $p_{KS}(d) < \alpha$. Therefore, given the CDF of one of the distributions that we want to compare and a probability threshold α , the region of distance d_{α} around the CDF depicts the hypothesis test. If the CDF of the other distribution lies entirely within this region, then its maximum distance from the first CDF is less than d_{α} . Therefore, its probability is greater than α and the null hypothesis can not be rejected.

Figure 4.33 shows the cumulative distribution functions (CDFs) of the Trapezium, Pleiades (in K_s band) and Hyades PDSMDs. Also and for comparison, I show the CDFs resulting of [Chabrier \(2005\)](#) and [Thies & Kroupa \(2007\)](#) IMFs. The grey area around the Pleiades CDF depicts the graphical KS hypothesis test in which I choose $\alpha = 0.01$.

⁴Kindly provided by Hervé Bouy in a private communication.

⁵The interesting alternative of open clusters gaining intermediate mass stars across their orbit is yet to be explored.

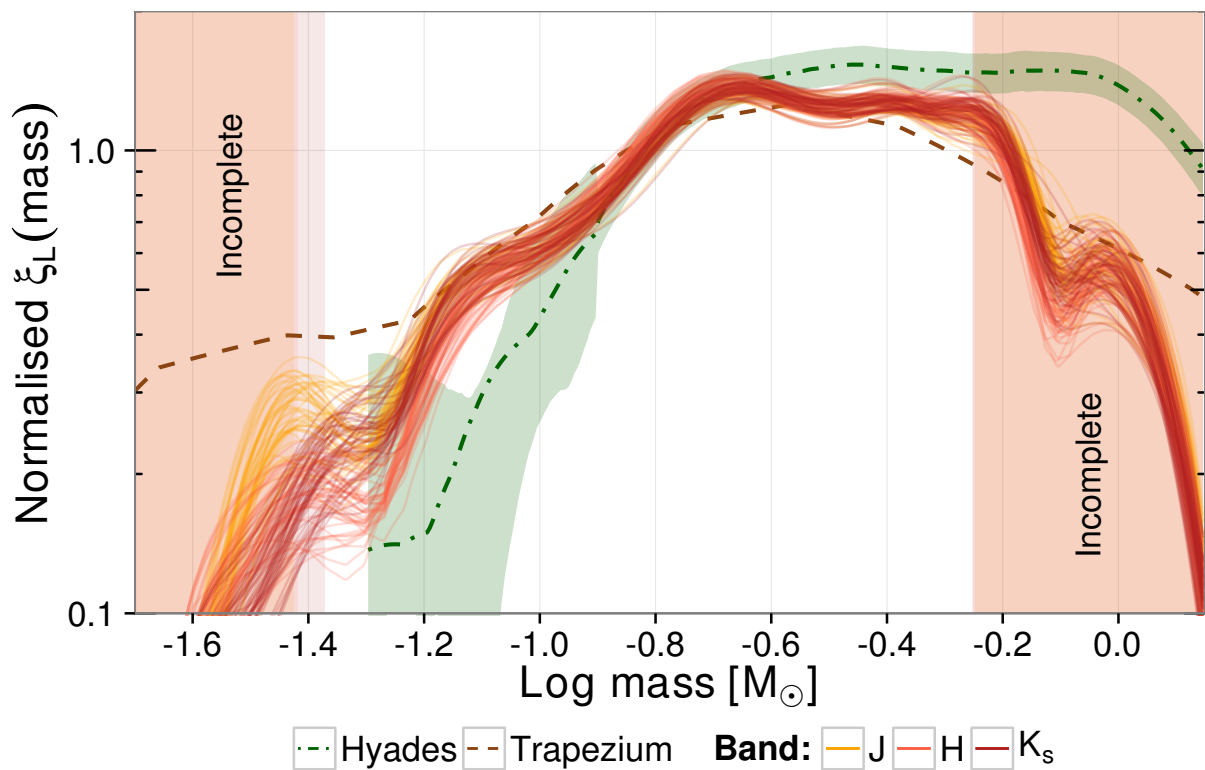


Figure 4.32: The PDSMDs of the Pleiades (derived here for J, H, K_s bands), Trapezium, and Hyades (both from Bouy et al. (2015)) clusters. They are normalised in the interval of completeness.

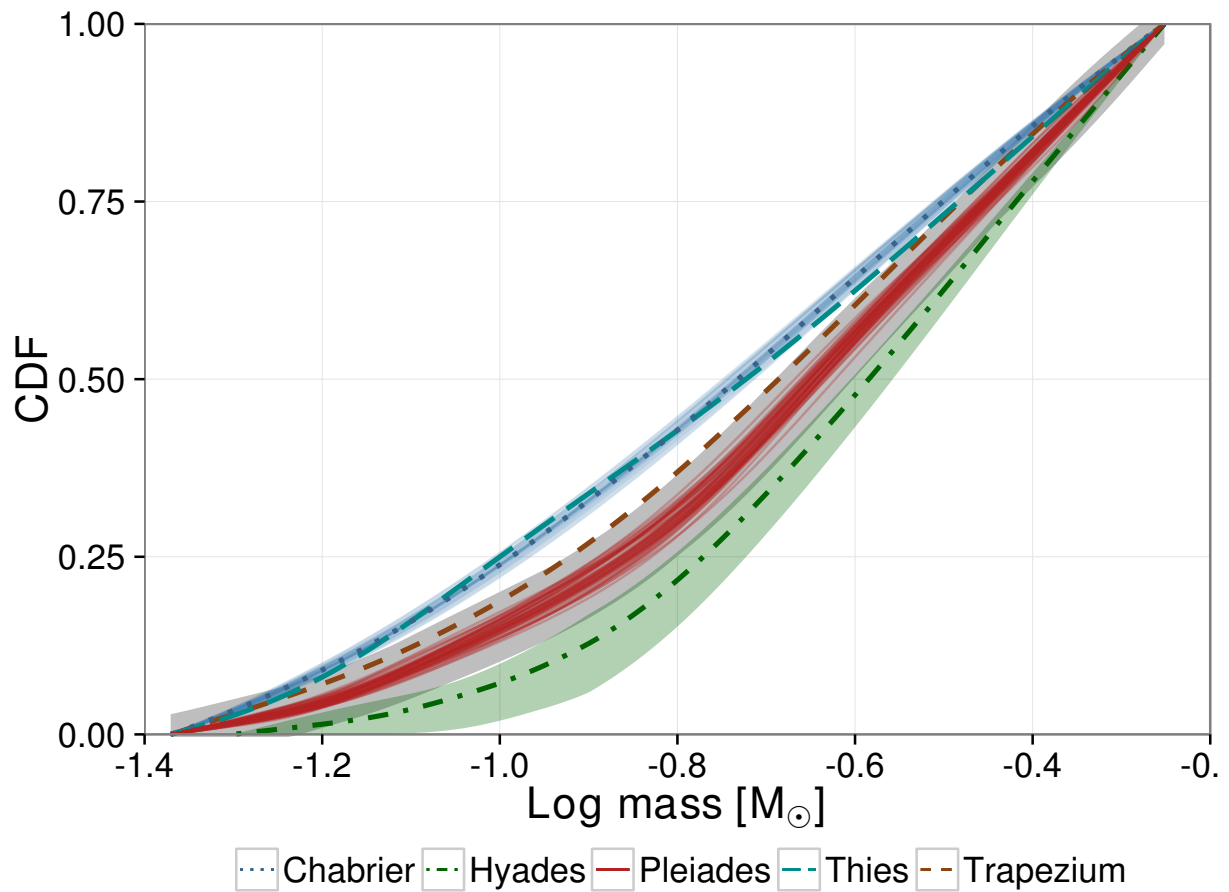


Figure 4.33: CDFs of the PDSMDs from left panel and that of Chabrier (2005) and Thies & Kroupa (2007) system initial mass function (normalised also in the interval of completeness). The shown Pleiades CDF correspond to the K_s band. The grey area depicts the area in which the CDFs (both Trapezium and Hyades) should lie for the null hypothesis not to be rejected (at $\alpha = 0.01$).

Furthermore, since the KS test uses only the maximum distance between CDFs, I also applied the more robust AD test. It also rejects the null hypotheses (at $p < 0.004$) that the Trapezium and Hyades PDSMDs and the [Chabrier \(2005\)](#) and [Thies & Kroupa \(2007\)](#) IMFs came from the same parent distribution as the Pleiades PDSMD.

The previous tests suggest that there is enough statistical evidence to support the diverse origins in the PDSMDs of these three clusters. Also, these evidences suggest that IMFs of [Chabrier \(2005\)](#) and [Thies & Kroupa \(2007\)](#) are statistically different from the Pleiades PDSMD. These observed differences, as mentioned in the previous Section, may have its origin on dynamical effects associated with age and relaxation. However, they can also arise due to the simpler assumption that no two clusters are born alike.

Whatever the answer to this question is, to obtain it, at least two issues must be solved. First, the uncertainties in the PDSMD must be properly established, particularly those of the mass-luminosity relation, distance, and extinction. Here, I have assumed that i) extinction is a single value instead of a distribution of values, ii) distance is the inverse of the parallax, which underestimates the uncertainties, and, iii) the mass-luminosity is a unique transformation, which in fact must be a set of transformations that must take into account the age spread and metallicities of clusters, and possible discrepancies amongst stellar structure models.

Second, the luminosity distributions of all compared clusters must include the properly propagated uncertainties from the data, as in the BHM, and not just from the poissonian counts as in those of the Trapezium and Hyades. Thus, in the future, the BHM of the remaining clusters must be computed.

Once this issues are solved, the BHMs of different clusters will allow us to gauge how similar these clusters are. Indeed, by comparing the posterior PDFs of the model parameters returned by the data sets of different clusters, given the same model and set of assumptions, we would be able to properly measure, by means of hypothesis tests (see for example [Rueda 1992](#)), the probability that these models were drawn from the same parent PDF.

4.9 Updating priors and assumptions

As mentioned by [Gelman \(2006\)](#), the posterior distribution must be inspected to update our previous knowledge. To inspect these posterior distribution, I use the statistics reported in Table 4.1. These values indicate, for example, that the number of GMM modelling the proper motions of the single stars is overestimated. The fraction and variance of the last gaussian are both to near zero values. Probably, a better model would be that in which the parameters of these extra gaussian will not be part of the model. Ideally, I should select one of these two models based on their evidence (see Section 3.1.2). To my knowledge, the only reliable approach to compute the evidence of a model inferred

using MCMC, is by means of the Nested Sampling algorithm (see Section 3.5.2). However, running the BHM in the *MultiNest* package lies far beyond our current computational resources.

The following are two examples of posterior checking that were performed in the iterative cycle of model and inference.

In a past run of the BHM on the RDDR2, I realised that the prior distribution for the parameter modelling field fraction was too narrow. Although the maximum of the posterior distribution was allowed by this prior (by definition), the prior density at this MAP was negligible. Therefore, I updated the prior to a distribution with a larger variance, thus weakening the prior information. As can be seen from Fig. 4.34, the posterior distribution of the π and π_{CB} fraction parameters in the BHM are now allowed by the prior distributions. It is important to notice that, given the large information provided by the data, the prior distributions play a small roll in the estimation of the posterior (i.e. the likelihood is highly informative).

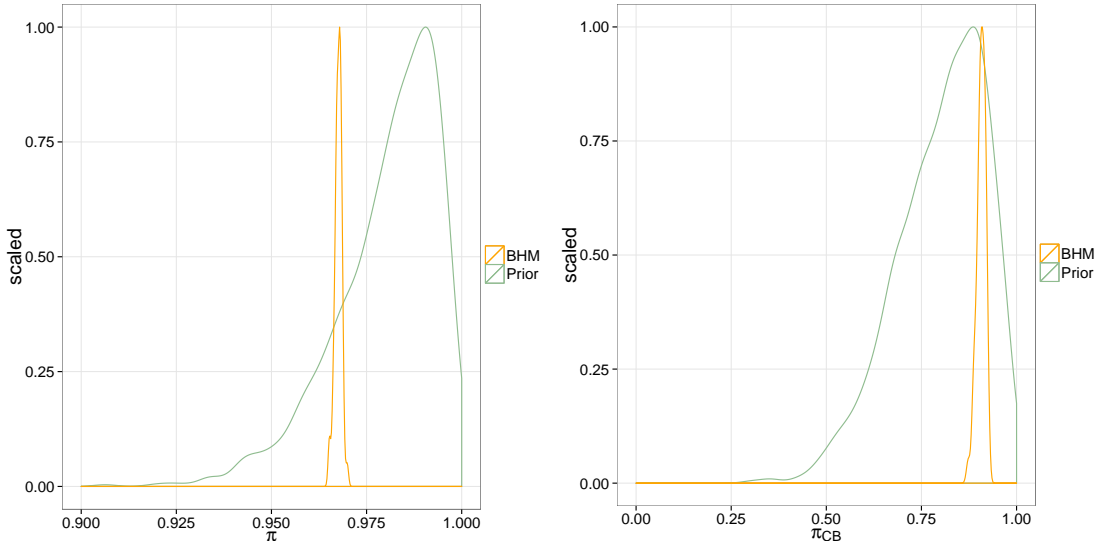


Figure 4.34: Posterior distributions of the π and π_{CB} parameters (orange lines) together with their corresponding priors. Notice that due to the large data set, the posterior distributions are highly concentrated.

In the first version of this manuscript, the evidences for the PSD models presented in Section 4.4 were computed using uniform priors for all parameters. As kindly pointed out by Coryn Bailer-Jones, one of the referees of this work, the truncation limits of those priors have an influence on the estimated evidences. By modifying those priors and allowing them to *reflect the available parameter space under the model \mathcal{M} , independently of experimental constraints we might already be aware of* (taken from [Trotta 2008](#)), we were able to measure the simplicity (evidence) of the model itself.

4.9.1 Assumptions

The posterior checking not only must be performed on the inferred parameters but also in the model itself. In such spirit, this section describes how two key assumptions in the field model have been modified by our posterior inference.

Finally, I hope that this last Section has transmitted the reader how dynamic, iterative and reflexive the creation of a model is. While the Bayesian formalism enable us to update our prior knowledge based on the data, transform it into posteriors, and select the best models based on evidence, the Bayesian Hierarchical approach allows us to directly update our prior beliefs within the inference process. In summary, the Bayesian formalism help us to update our knowledge based not just in the light of new data, but also in the light of new models.

Chapter 5

Conclusions and future work

In this work, I have created, tested, and validated a new Intelligent System (IS) that recovers the PDFs of star clusters kinematic and photometric observables. In particular, the proper motions and apparent magnitudes. When the distance to the cluster is known, the PDFs of these observables can be transformed into transverse velocity and luminosity distributions. In addition, using the cluster age and a mass-luminosity relation the latter can be transformed into a mass distribution. A compilation of kinematic and mass distributions of NYCs in diverse environments and spanning the ages of the early phases of cluster evolution will allow the astrophysical community to understand the effects that the environments and the internal dynamics have in the origin and evolution of stellar clusters. Since the majority of the stars form in clusters, understanding how these form and evolve will shed light into the knowledge of the past and future of our galaxy.

The IS presented in this work solves most of the issues found in current methodologies of cluster members determination and analysis. Furthermore, it steps ahead of the current paradigm of these methodologies, which is the classification of objects in cluster and field populations, and moves into a new one: *learning the kinematic and photometric distributions of the cluster populations*, both single and binary stars.

Thanks to its Bayesian framework, the Bayesian Hierarchical Models methodology and the use of weakly informative priors specifically, this new IS solves the issues present in current classifiers from the literature and minimises their biases. In particular, it fulfils its objective by properly propagating the observable multivariate and heteroscedastic uncertainties, using the valuable information provided by objects with missing values in their observables, and eliminating the sampling bias associated with the use of only high membership probability objects.

To learn the posterior distributions of the parameters in the cluster model, the BHM, as we call this new IS, uses a combination of learning techniques, the Particle Swarm Optimiser of [Kennedy & Eberhart \(1995\)](#); [Clerc & Kennedy \(2002\)](#) and the *emcee* Markov Chain Monte Carlo method of [Foreman-Mackey et al. \(2013\)](#). Both are implemented in High-Performance Computing environments to use large data sets (10^5 to 10^6 objects)

and multidimensional observable spaces. While the multidimensionality of the observable space (proper motions and photometry) add valuable information to constrain the cluster model and render it accurate, the large size of the data set increases its precision.

The performance of the BHM as a classifiers was analysed on synthetic data sets. The results of this analysis show that at an optimal probability threshold of $p = 0.84$ the it has a True Positive Rate (recovery rate) of $90.0 \pm 0.05\%$ and a contamination rate of $4.3 \pm 0.2\%$. The Area Under the Curve Receiver Operating Characteristic is 0.99 which indicates that it as an excellent classifier. The synthetic analysis reveals that the expected value of the contamination in the kinematic and photometric cluster distributions is $5.8 \pm 0.2\%$.

The BHM has been thoroughly tested and validated on the Pleiades DANCe Data Release 2 ([Bouy et al. 2015](#)). Since the Pleiades is one of the most studied clusters in the history of astronomy, it offers the perfect case study for the benchmarking of an IS aiming at the analysis of NYC. In addition, the high precision and carefully designed observations of the DANCe project for the Pleiades cluster provide the necessary detailed information and sufficient statistics to benchmark the BHM and constrain its posterior distribution, in the high dimensionality (85) of its parametric space specifically.

The results of applying the BHM to the Restricted Pleiades DANCe Data Release 2 (RDDR2) data set yield the following astrophysical results.

- The by-product cluster membership probabilities, which are now delivered as full PDFs, show that (see Section 4.2):
 - There is an outstanding agreement of 99% with the classification process done by [Bouy et al. \(2015\)](#) on the one hundred thousands objects data set.
 - From the 1967 pleiads candidate members found in this work, 205 are new ones. It represents 10% of the cluster population.
 - From the candidate members of [Rebull et al. \(2016\)](#), 91% are classified as members. This figure is better than our estimated value of the True Positive Rate, 90.0 ± 0.05 .
- The model selection analysis of the Projected Spatial Distribution (PSD) performed on the High Membership Probability Sample (HMPS) of candidate members recovered by the BHM shows that (see Section 4.4):
 - The King’s profile ([King 1962](#)) is not just a good model due to its physical interpretability, but also has the largest Bayesian evidence when compared to classical profiles from the literature.
 - There is enough Bayesian evidence to support luminosity segregation of the Pleiades cluster.

- The Pleiades data set supports, with large Bayesian evidence, PSD models with biaxial symmetry indicating the non negligible ellipticity of the cluster ($\epsilon = 0.13$).
- The kinematic and photometric distribution of the cluster populations show that (see Section 4.5 and 4.6):
 - The Equal-Mass Binaries (EMB) fraction is $9.9 \pm 0.1\%$.
 - The centroids of the cluster proper motions are $\{16.30, -39.68\}$ mas · yr⁻¹ and $\{15.71, -40.31\}$ mas · yr⁻¹ for single and EMB, respectively.
 - The derived luminosity distributions in the infrared bands (J , H , and K_s) in the completeness interval are in good agreement with the previous ones of [Bouy et al. \(2015\)](#).
- The derived Present-Day System Mass Distribution (PDSMD) (using an age of 120 Myr and the BT-Settl isochrone model of [Allard et al. 2012](#)) shows (see Sections 4.7 and 4.8):
 - A general agreement with the IMFs of [Chabrier \(2005\)](#) and [Thies & Kroupa \(2007\)](#), in the intermediate mass range specifically.
 - The IMFs of [Chabrier \(2005\)](#) and [Thies & Kroupa \(2007\)](#) predict too many low-mass stars and Brown Dwarfs (BD).
 - A trend of depletion in low-mass stars and BD with cluster age, when comparing it with the Trapezium and Hyades PDSMD from the literature.

By minimising bias, propagating uncertainties, including correlations and doing a comprehensive modelling of the data particularities (missing values and heteroscedastic uncertainties) the BHM, developed, tested and validated in the present work, delivers the kinematic and photometric distributions of the cluster single and equal-mass binary populations. This new intelligent system represents the state of the art in the statistical analysis of NYCs.

5.1 Current issues and future improvements

Despite the fact that the BHM presented here solves the issues present in current methodologies from the literature, the following is a non-exhaustive list of important aspects to tackle in the near future.

- The BHM must be able to deal with:

- Unresolved binaries of different mass ratios. Although the CSN has already been included in the BHM to deal with these objects, its application still demands fine tuning of the HPC elements (see Section 3.3.4).
- Proper motion and photometry from other surveys (e.g. *Pan-STARRS*, *Gaia*, *LSST*). Although so far untested, the BHM, thanks to its ability to cope with large amounts of missing values, it can deal with data sets from heterogeneous origins. For example, *Gaia* proper motion data (together with its correlated uncertainties) plus *Pan-STARRS* photometry, can be directly plugged into the BHM to improve the uncertainties of the kinematic and photometric cluster distributions.
- Other observables. As shown with the projected spatial distribution, other observables like radial velocities from the *Gaia-ESO* survey and parallaxes from *Gaia*, will give useful information to further refine the lists of candidate members.
- Extinction. The treatment of interstellar extinction is of paramount importance and is mandatory for the application of the BHM in younger and embedded clusters. Once done, it will allow the unravelling of kinematic and photometric distributions of embedded young clusters.
- Unresolved multiple systems. Although it is expected that these systems represent a small fraction of the cluster population (only 4% for the triple systems Duquennoy & Mayor 1991), they nevertheless have an important contribution to the mass distribution.
- Clusters with superimposed populations. The treatment of superimposed populations is also important to minimise contamination.
- The white dwarfs population. Although their numbers are negligible on NYC, their mass contribution nevertheless must be considered to properly constrain the PDSMD and the IMFs.
- The time needed to learn the BHM. Currently, the BHM takes four weeks to run in a 80 CPUs computing cluster. Although the DANCe team has lately translated the CPU code into GPU code, the latter still needs improvement, in memory allocation and parallel distribution particularly.
- The choosing of prior distributions in other non-well studied NYCs. In NYCs where the prior information is missing, other kind of prior distributions must be used (e.g. objective or non-informative priors). Nevertheless, the BHM still provides the less subjective path to parametric inference.
- Choosing the appropriate number of GMM components. As with the previous point, where the prior information is not available, we can nevertheless use non-

informative priors and large number of GMM components, so that those non-required components had small weight and covariance matrices. A model selection analysis must be implemented.

- Uncertainties to the mass-luminosity relation. Although non related to the BHM, the mass-luminosity relation is used univocally to transform a luminosity into mass. However, this knowledge is uncertain and its uncertainty must be incorporated into the derived mass distributions.

Once these issues will be solved, the improved BHM will render the inventory of cluster kinematic and luminosity distributions that will allow the DANCe team to fulfil the objective of understanding the effects that the environment (i.e. initial conditions) and the internal dynamics (e.g. evaporation, ejection, mass segregation) have on the clusters formation and evolution.

Finally, I list some future perspectives of the BHM.

- It will eventually become a free and open-source code for the use of the astronomical community.
- Although it has been created for the analysis of star clusters, it can also be applied to stellar associations.
- The empirical colour-magnitude relations that it learns can be used to constrain the theoretical evolutionary models once corrected by individual distances and extinctions.
- The lists of candidate members and equal-mass binaries that it delivers can be used to perform efficient searches and follow-ups.
- In the *Gaia* era, it will continue to provide not just accurate lists of candidate members, but also unbiased kinematic and photometric distributions with correctly propagated uncertainties for objects all along from the high mass domain down to the planetary mass regime.

USE OF OTHER COLOUR INDICES VARYING INTRINSIC DISPERSION

independence between proper motions and photometry

spatial incompleteness due to bright sources

Photometric incompleteness in the i band. Panstarss

- Because the field parameters are fixed, uncertainty in field parameters are not propagated to cluster parameters, in spite the field sample represents 98% of the data (a small change on it may have a large impact on the minority, cluster, population).

Appendix A

Posterior distributions of the PSD

This Appendix contains the details of the inference performed for each of the models and extensions presented in Section 4.4. It is structured in the same way as that Section. It starts with the radial models, then continues with the biaxial ones and finalises with the luminosity segregated ones. Each Section contains: i) the covariance matrices around the MAP of the joint posterior distribution of all parameters in each model, and, ii) figures depicting the univariate and bivariate marginal posterior distributions obtained from *PyMultiNest* in the form of a corner plot ([Foreman-Mackey 2016](#)). Notice that, since the MAP is computed in the joint posterior distribution, it does not necessarily coincides with the modes of the marginal distributions.

We summarise the uncertainties and correlations of the inferred parameter values by means of covariance matrices. These covariance matrices are computed using the 68.2% of samples from the MCMC that were the closest to the MAP value. They represent the 2σ uncertainties and correlations of the parameters at the vicinity of the MAP. The order of the parameters in these covariance matrices is the of the MAPs of Section 4.4.

In addition, Sections A.2 and A.3 contain also the ellipticity distributions computed a posteriori from the core and tidal (when available) semi-major and semi-minor axes resulting from the *PyMultiNest* samples. The numbers shown in brackets represent the 16th percentile, the mode, and the 84th percentile, of the distribution.

A.1 Models with radial symmetry

$$\Sigma_{\text{EFF}} = \begin{pmatrix} 0.007 & 0.000 & 0.000 & 0.000 \\ 0.000 & 0.006 & 0.001 & 0.000 \\ 0.000 & 0.001 & 0.058 & 0.030 \\ 0.000 & 0.000 & 0.030 & 0.027 \end{pmatrix} \quad \Sigma_{\text{GDP}} = \begin{pmatrix} 0.012 & 0.000 & 0.004 & 0.000 & 0.002 & 0.000 \\ 0.000 & 0.012 & 0.006 & 0.002 & 0.006 & -0.001 \\ 0.004 & 0.006 & 0.589 & 0.062 & 0.330 & 0.004 \\ 0.000 & 0.002 & 0.062 & 0.046 & 0.059 & -0.016 \\ 0.002 & 0.006 & 0.330 & 0.059 & 0.256 & -0.028 \\ 0.000 & -0.001 & 0.004 & -0.016 & -0.028 & 0.028 \end{pmatrix}$$

$$\Sigma_{\text{GKing}} = \begin{pmatrix} 0.022 & 0.001 & 0.002 & -0.021 & 0.001 & -0.000 \\ 0.001 & 0.019 & 0.007 & 0.046 & -0.004 & 0.005 \\ 0.002 & 0.007 & 1.376 & 1.469 & 0.126 & 0.317 \\ -0.021 & 0.046 & 1.469 & 19.684 & -0.214 & 1.139 \\ 0.001 & -0.004 & 0.126 & -0.214 & 0.364 & 0.027 \\ -0.000 & 0.005 & 0.317 & 1.139 & 0.027 & 0.141 \end{pmatrix} \quad \Sigma_{\text{King}} = \begin{pmatrix} 0.018 & 0.001 & 0.001 & -0.001 \\ 0.001 & 0.017 & 0.002 & 0.021 \\ 0.001 & 0.002 & 0.144 & -0.945 \\ -0.001 & 0.021 & -0.945 & 37.437 \end{pmatrix}$$

$$\Sigma_{\text{OGKing}} = \begin{pmatrix} 0.011 & 0.001 & -0.001 & -0.003 \\ 0.001 & 0.010 & -0.000 & -0.000 \\ -0.001 & -0.000 & 0.054 & -0.100 \\ -0.003 & -0.000 & -0.100 & 1.951 \end{pmatrix} \quad \Sigma_{\text{RGDP}} = \begin{pmatrix} 0.014 & 0.000 & 0.003 & -0.000 & 0.001 \\ 0.000 & 0.012 & 0.006 & 0.000 & 0.005 \\ 0.003 & 0.006 & 0.804 & 0.089 & 0.466 \\ -0.000 & 0.000 & 0.089 & 0.051 & 0.061 \\ 0.001 & 0.005 & 0.466 & 0.061 & 0.311 \end{pmatrix}$$

A.2 Models with biaxial symmetry

$$\Sigma_{\text{EFF}} = \begin{pmatrix} 0.007 & -0.000 & -0.001 & 0.000 & 0.000 & 0.000 \\ -0.000 & 0.006 & 0.001 & 0.000 & 0.001 & 0.001 \\ -0.001 & 0.001 & 0.063 & 0.000 & -0.002 & -0.000 \\ 0.000 & 0.000 & 0.000 & 0.131 & 0.056 & 0.049 \\ 0.000 & 0.001 & -0.002 & 0.056 & 0.093 & 0.047 \\ 0.000 & 0.001 & -0.000 & 0.049 & 0.047 & 0.040 \end{pmatrix} \quad \Sigma_{\text{GDP}} = \begin{pmatrix} 0.007 & -0.001 & -0.001 & 0.002 & 0.000 & -0.001 & 0.000 & 0.001 \\ -0.001 & 0.005 & 0.001 & 0.005 & 0.005 & 0.005 & 0.002 & 0.005 & -0.001 \\ -0.001 & 0.001 & 0.185 & 0.051 & 0.031 & 0.008 & 0.043 & -0.010 \\ 0.002 & 0.005 & 0.051 & 1.204 & 0.801 & 0.101 & 0.547 & -0.006 \\ 0.000 & 0.005 & 0.031 & 0.801 & 0.788 & 0.074 & 0.480 & -0.009 \\ -0.001 & 0.002 & 0.008 & 0.101 & 0.074 & 0.044 & 0.070 & -0.016 \\ 0.000 & 0.005 & 0.043 & 0.547 & 0.480 & 0.070 & 0.363 & -0.033 \\ 0.001 & -0.001 & -0.010 & -0.006 & -0.009 & -0.016 & -0.033 & 0.025 \end{pmatrix}$$

$$\Sigma_{\text{GKing}} = \begin{pmatrix} 0.013 & -0.001 & -0.004 & 0.001 & -0.004 & -0.002 & -0.015 & 0.002 & -0.001 \\ -0.001 & 0.010 & 0.001 & -0.002 & 0.014 & 0.004 & 0.005 & -0.002 & 0.002 \\ -0.004 & 0.001 & 0.256 & -0.029 & 0.205 & 0.058 & -0.003 & -0.022 & 0.027 \\ 0.001 & -0.002 & -0.029 & 1.587 & -0.041 & 0.379 & 0.437 & 0.194 & 0.131 \\ -0.004 & 0.014 & 0.205 & -0.041 & 25.850 & 0.956 & 5.304 & -0.227 & 0.677 \\ -0.002 & 0.004 & 0.058 & 0.379 & 0.956 & 0.433 & 0.575 & 0.031 & 0.144 \\ -0.015 & 0.005 & -0.003 & 0.437 & 5.304 & 0.575 & 6.150 & 0.015 & 0.436 \\ 0.002 & -0.002 & -0.022 & 0.194 & -0.227 & 0.031 & 0.015 & 0.291 & 0.028 \\ -0.001 & 0.002 & 0.027 & 0.131 & 0.677 & 0.144 & 0.436 & 0.028 & 0.076 \end{pmatrix} \quad \Sigma_{\text{King}} = \begin{pmatrix} 0.019 & -0.000 & -0.004 & 0.002 & -0.057 & 0.002 & 0.001 \\ -0.000 & 0.015 & 0.007 & -0.010 & 0.094 & 0.001 & -0.001 \\ -0.004 & 0.007 & 0.359 & -0.124 & 1.582 & 0.010 & -0.190 \\ 0.002 & -0.010 & -0.124 & 1.428 & -6.175 & 0.074 & -1.548 \\ -0.057 & 0.094 & 1.582 & -6.175 & 371.812 & -1.108 & 23.841 \\ 0.002 & 0.001 & 0.010 & 0.074 & -1.108 & 0.154 & -1.157 \\ 0.001 & -0.001 & -0.190 & -1.548 & 23.841 & -1.157 & 53.033 \end{pmatrix}$$

$$\Sigma_{\text{OGKing}} = \begin{pmatrix} 0.009 & -0.001 & -0.000 & -0.001 & -0.006 & -0.001 & -0.002 \\ -0.001 & 0.007 & 0.002 & -0.004 & 0.011 & 0.001 & -0.002 \\ -0.000 & 0.002 & 0.194 & -0.031 & 0.166 & 0.009 & -0.121 \\ -0.001 & -0.004 & -0.031 & 0.248 & -0.462 & 0.011 & -0.080 \\ -0.006 & 0.011 & 0.166 & -0.462 & 14.223 & -0.095 & -0.391 \\ -0.001 & 0.001 & 0.009 & 0.011 & -0.095 & 0.059 & -0.176 \\ -0.002 & -0.002 & -0.121 & -0.080 & -0.391 & -0.176 & 3.509 \end{pmatrix} \quad \Sigma_{\text{RGDP}} = \begin{pmatrix} 0.010 & -0.001 & -0.003 & 0.003 & -0.000 & -0.000 & -0.000 \\ -0.001 & 0.008 & 0.001 & 0.006 & 0.005 & 0.001 & 0.004 \\ -0.003 & 0.001 & 0.208 & 0.037 & 0.030 & 0.001 & 0.029 \\ 0.003 & 0.006 & 0.037 & 1.320 & 0.864 & 0.115 & 0.590 \\ -0.000 & 0.005 & 0.030 & 0.864 & 0.823 & 0.084 & 0.507 \\ -0.000 & 0.001 & 0.001 & 0.115 & 0.084 & 0.045 & 0.062 \\ -0.000 & 0.004 & 0.029 & 0.590 & 0.507 & 0.062 & 0.355 \end{pmatrix}$$

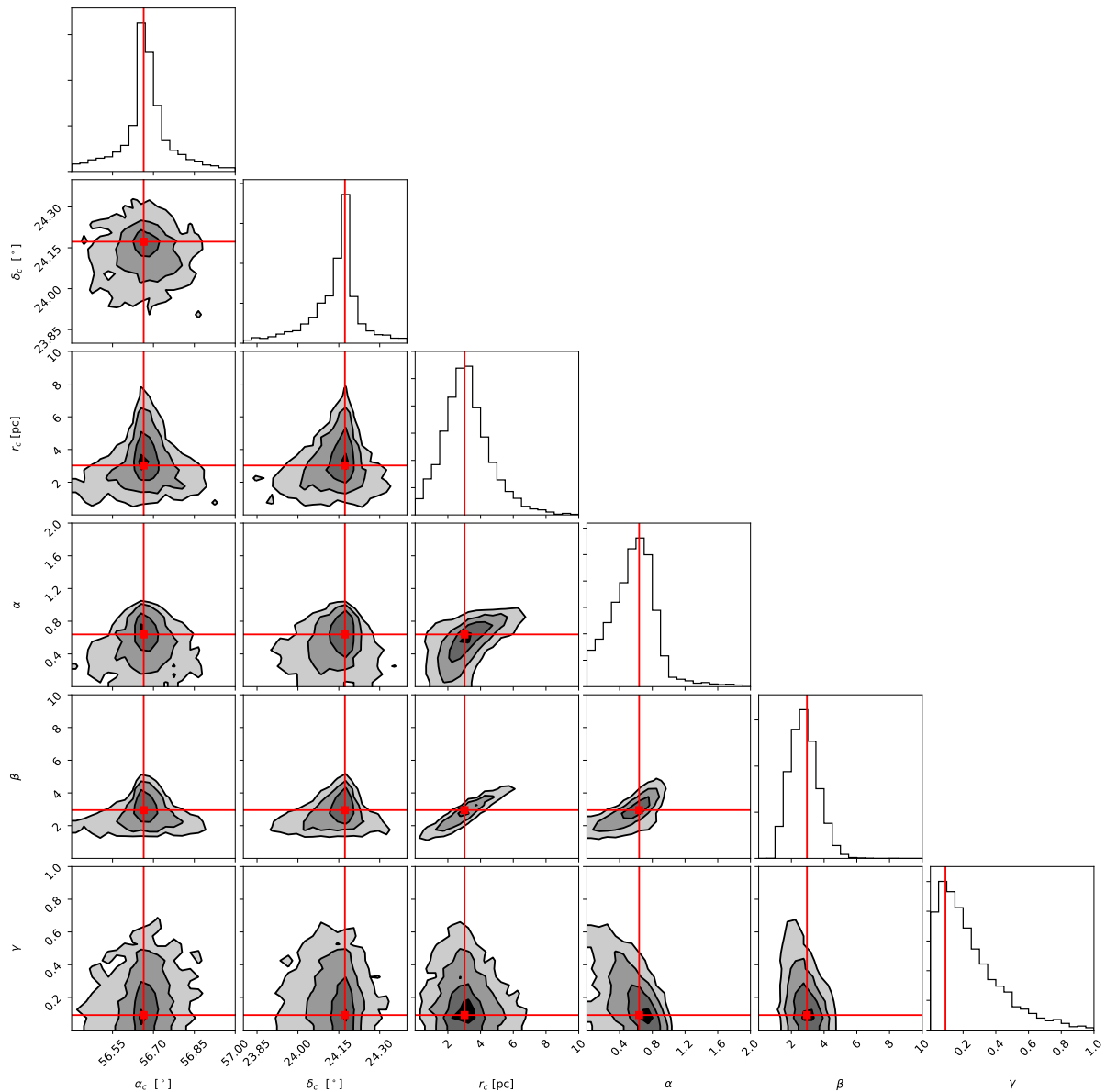


Figure A.1: Projections of the posterior distribution for the GDP model.

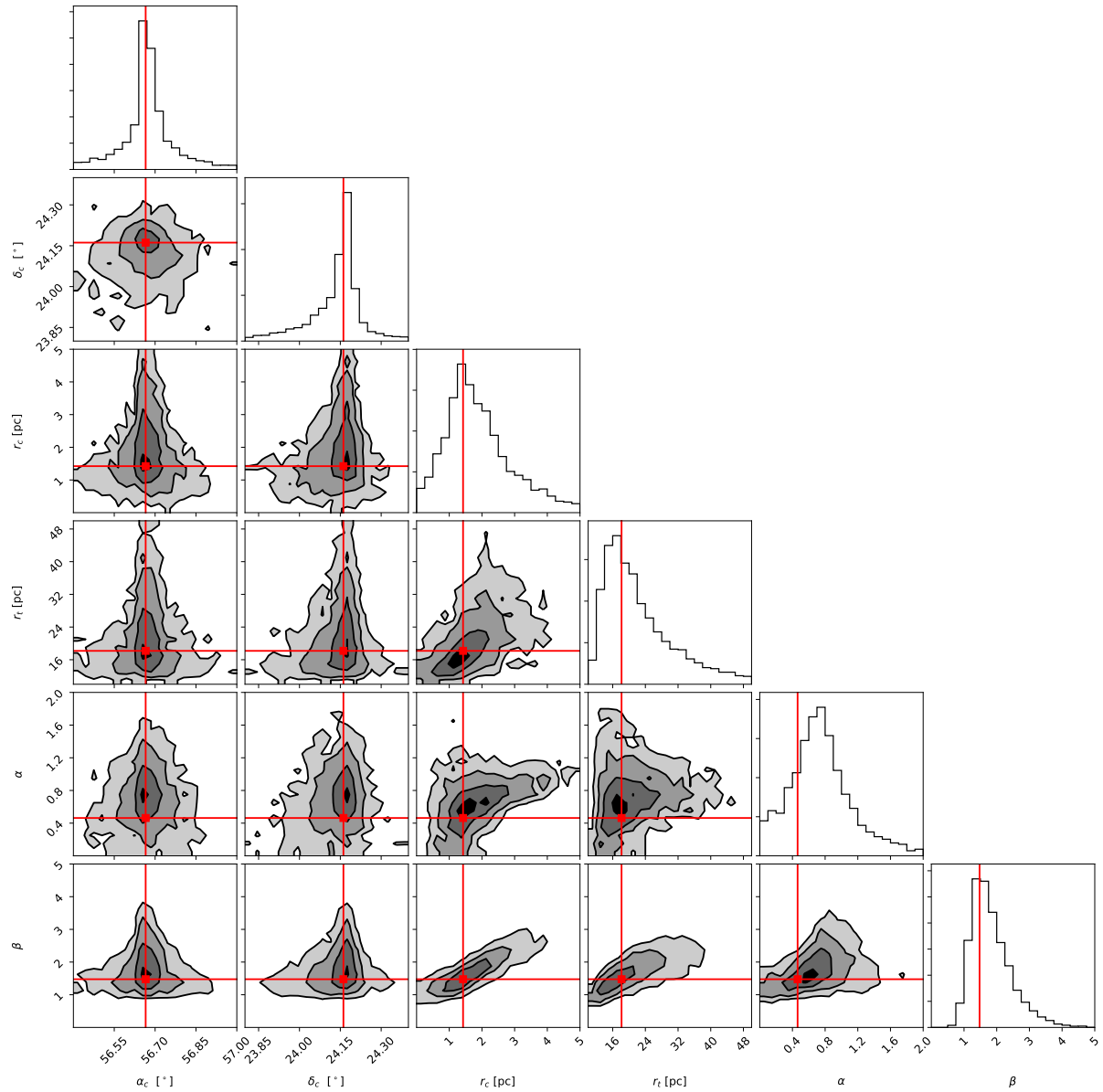


Figure A.2: Projections of the posterior distribution for the GKing model.

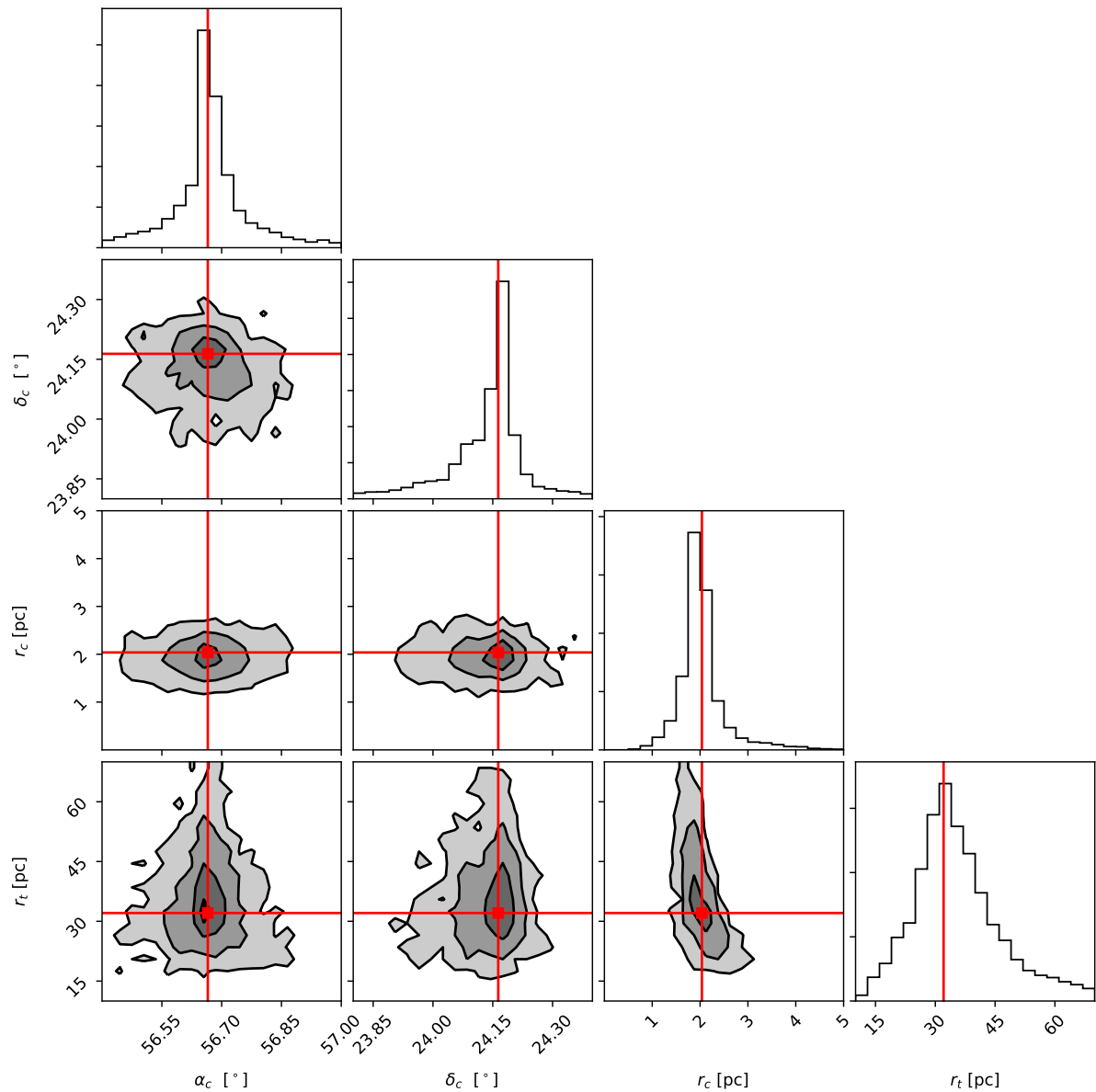


Figure A.3: Projections of the posterior distribution for the King's model.

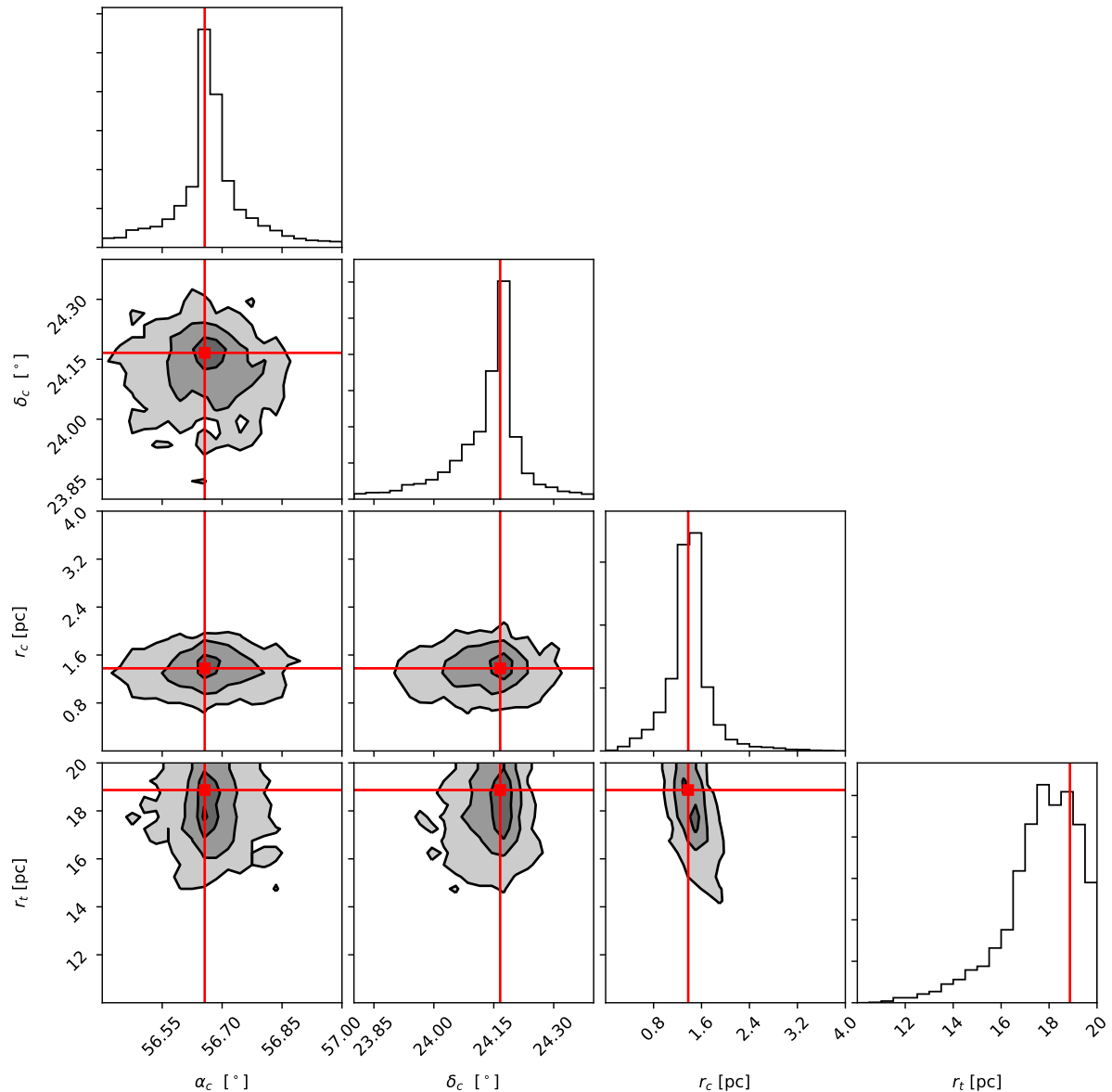


Figure A.4: Projections of the posterior distribution for the OGKing model.

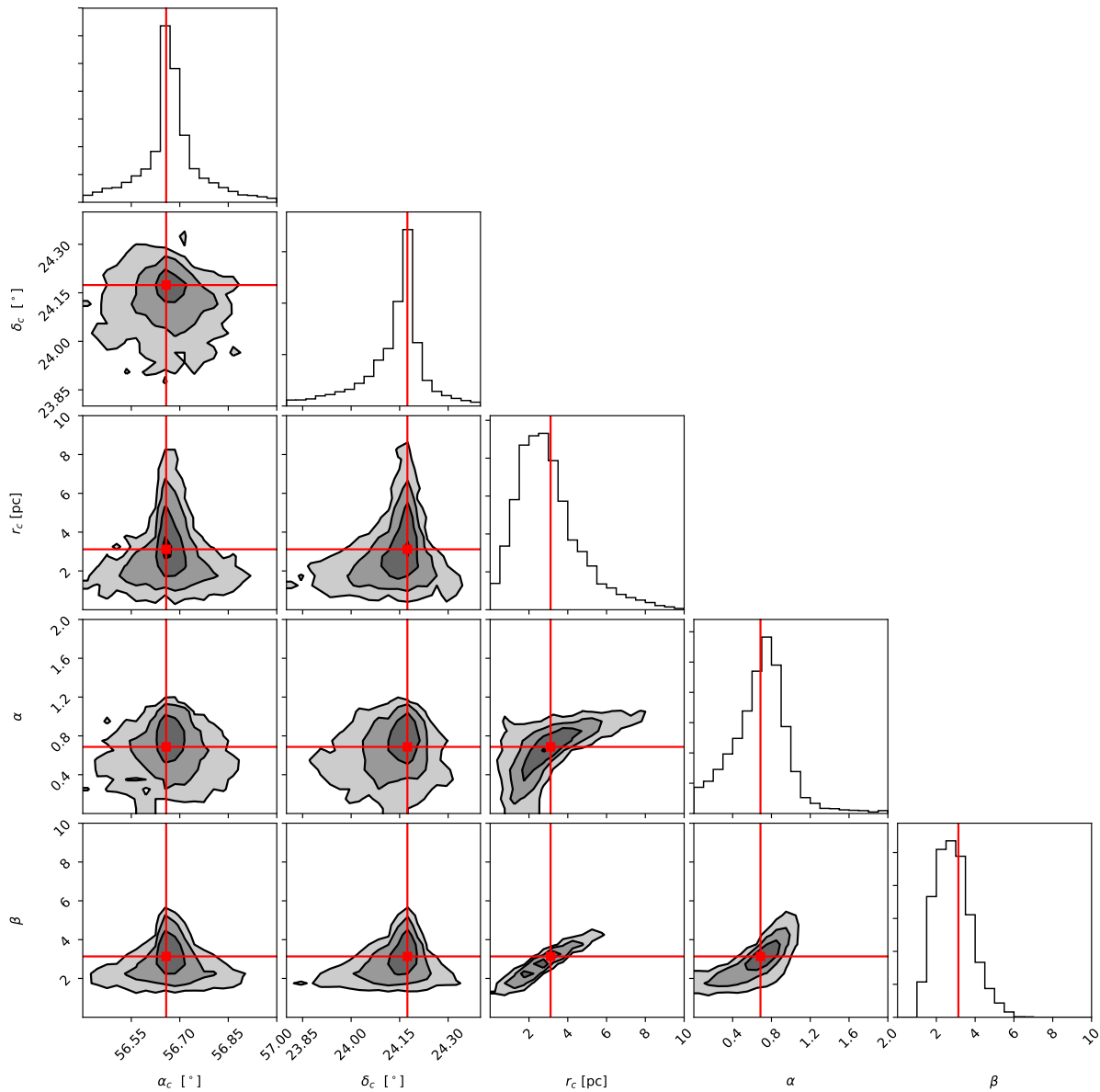


Figure A.5: Projections of the posterior distribution for the RGDP model.

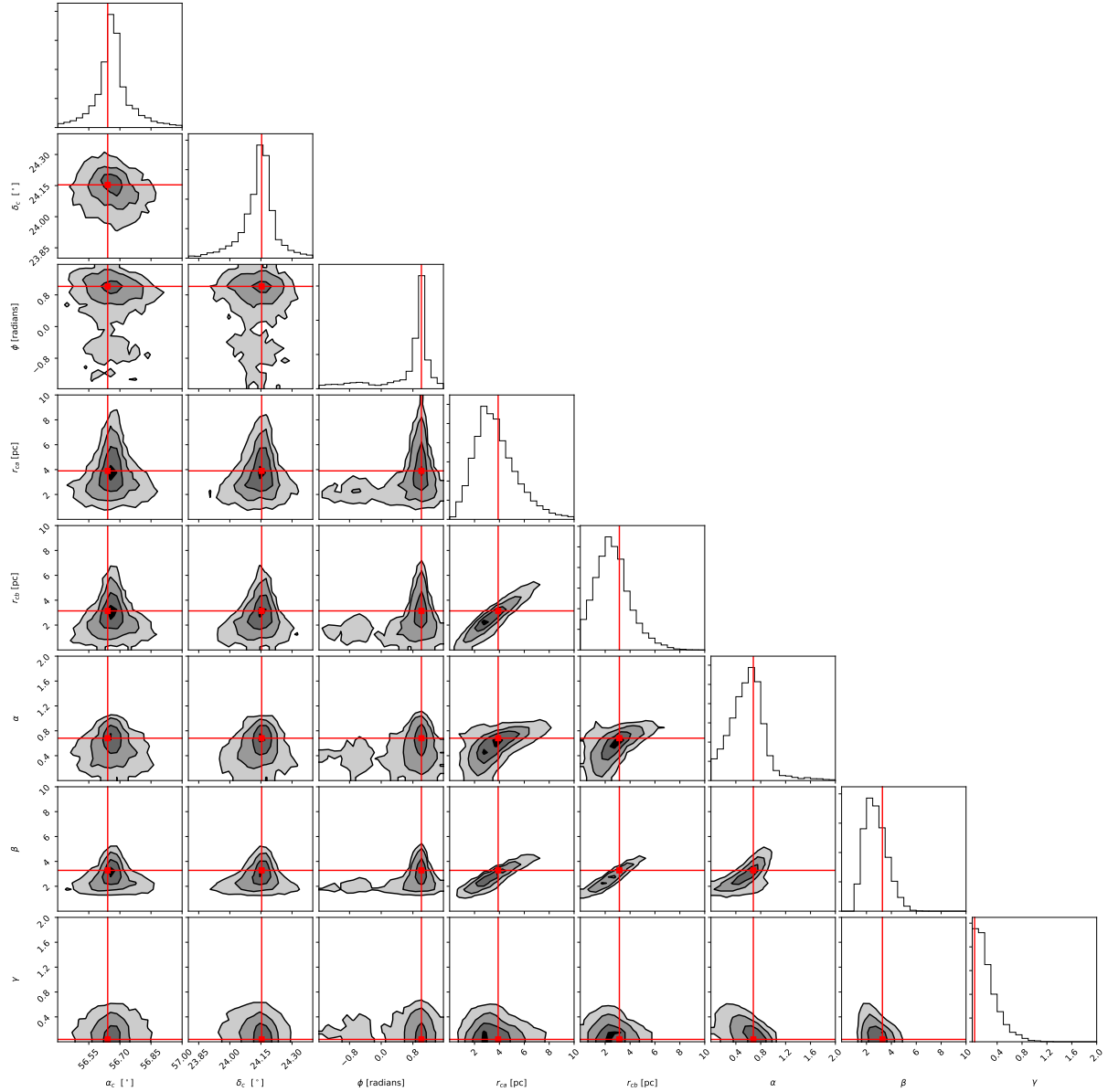


Figure A.6: Projections of the posterior distribution for the GDP biaxially symmetric model.

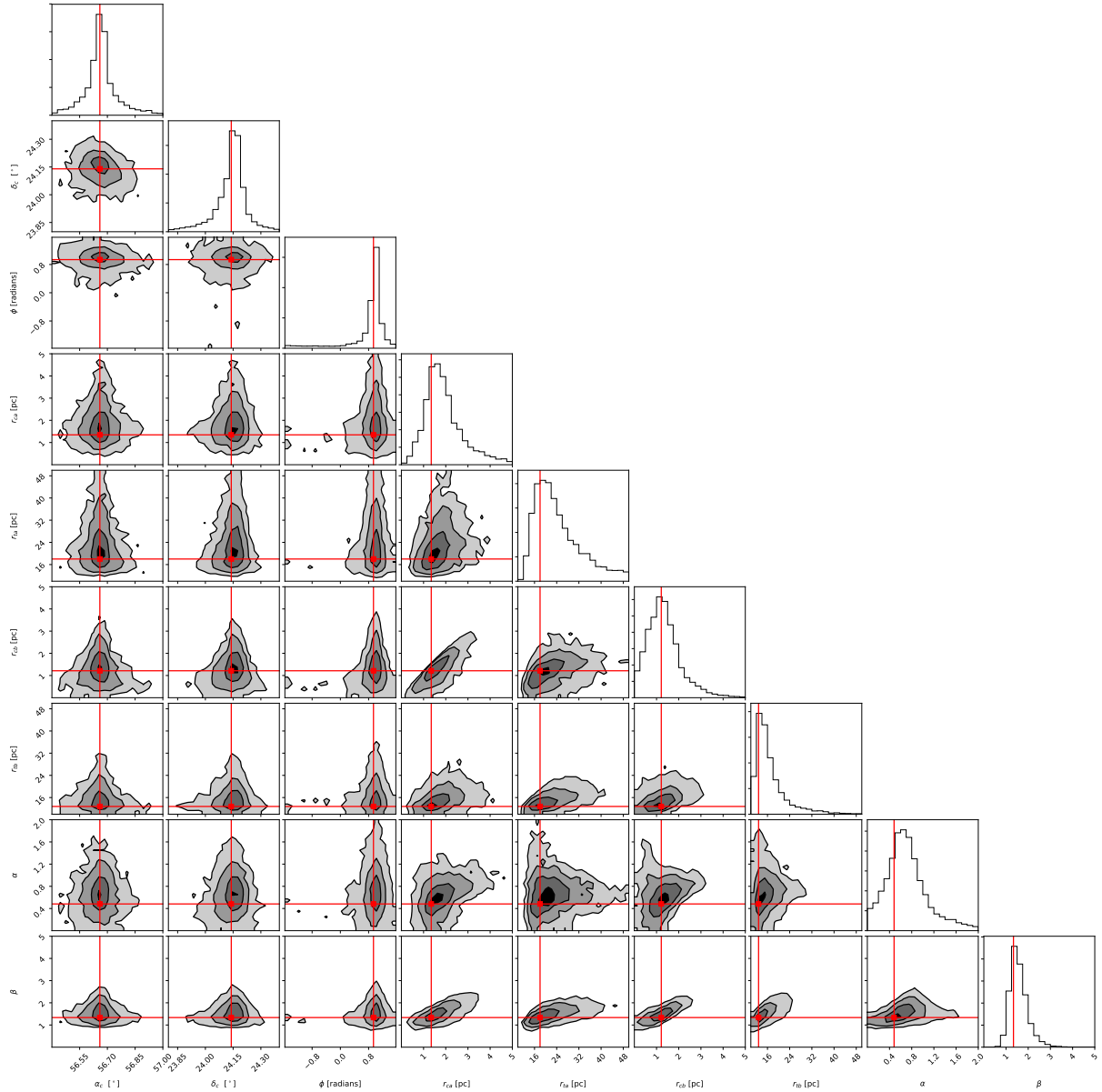


Figure A.7: Projection of the posterior distribution for the GKing biaxially symmetric model.

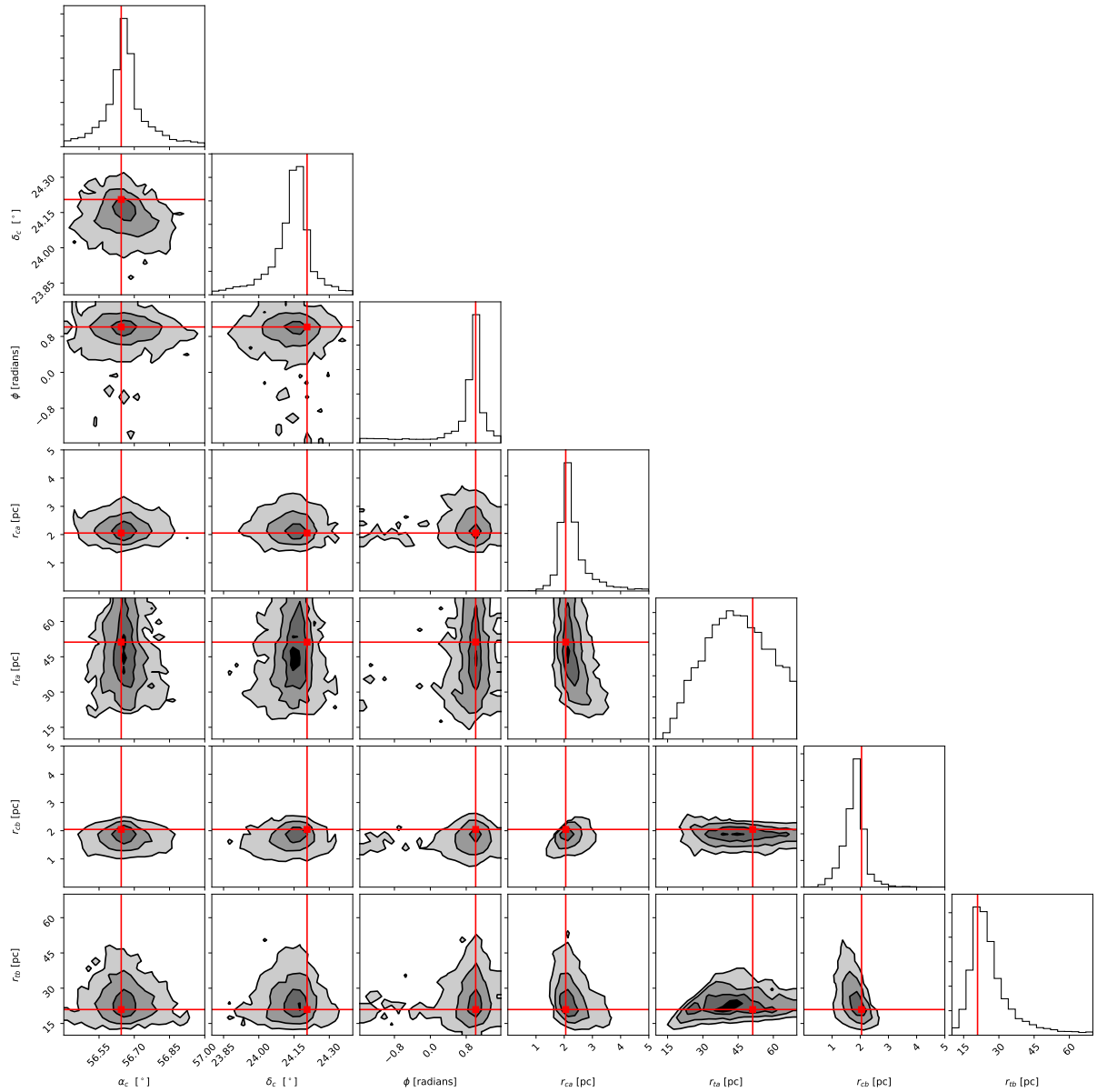


Figure A.8: Projection of the posterior distribution for the King's biaxially symmetric model.

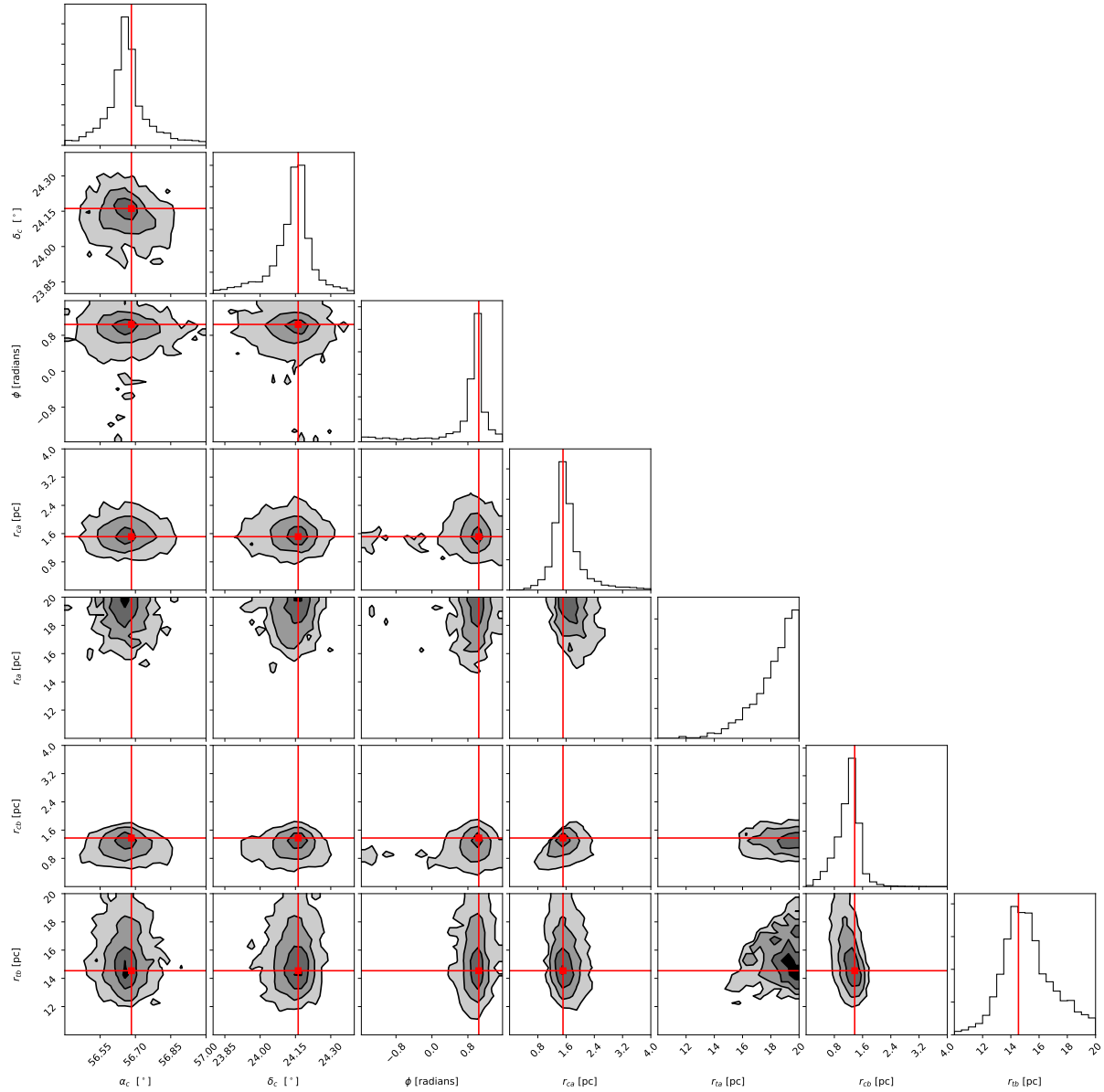


Figure A.9: Projection of the posterior distribution for the OGKing biaxially symmetric model.

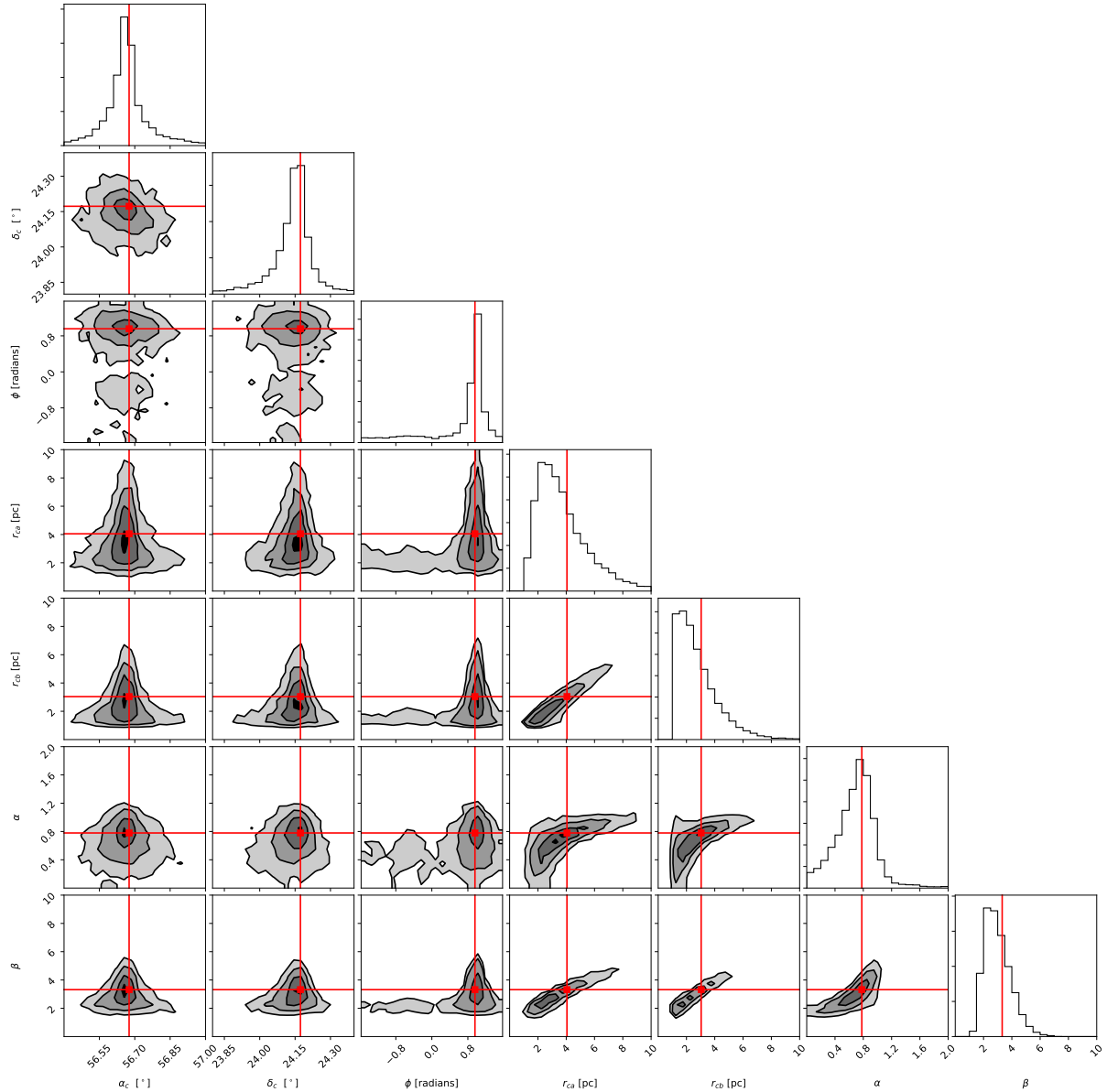


Figure A.10: Projection of the posterior distribution for the RGDP biaxially symmetric model.

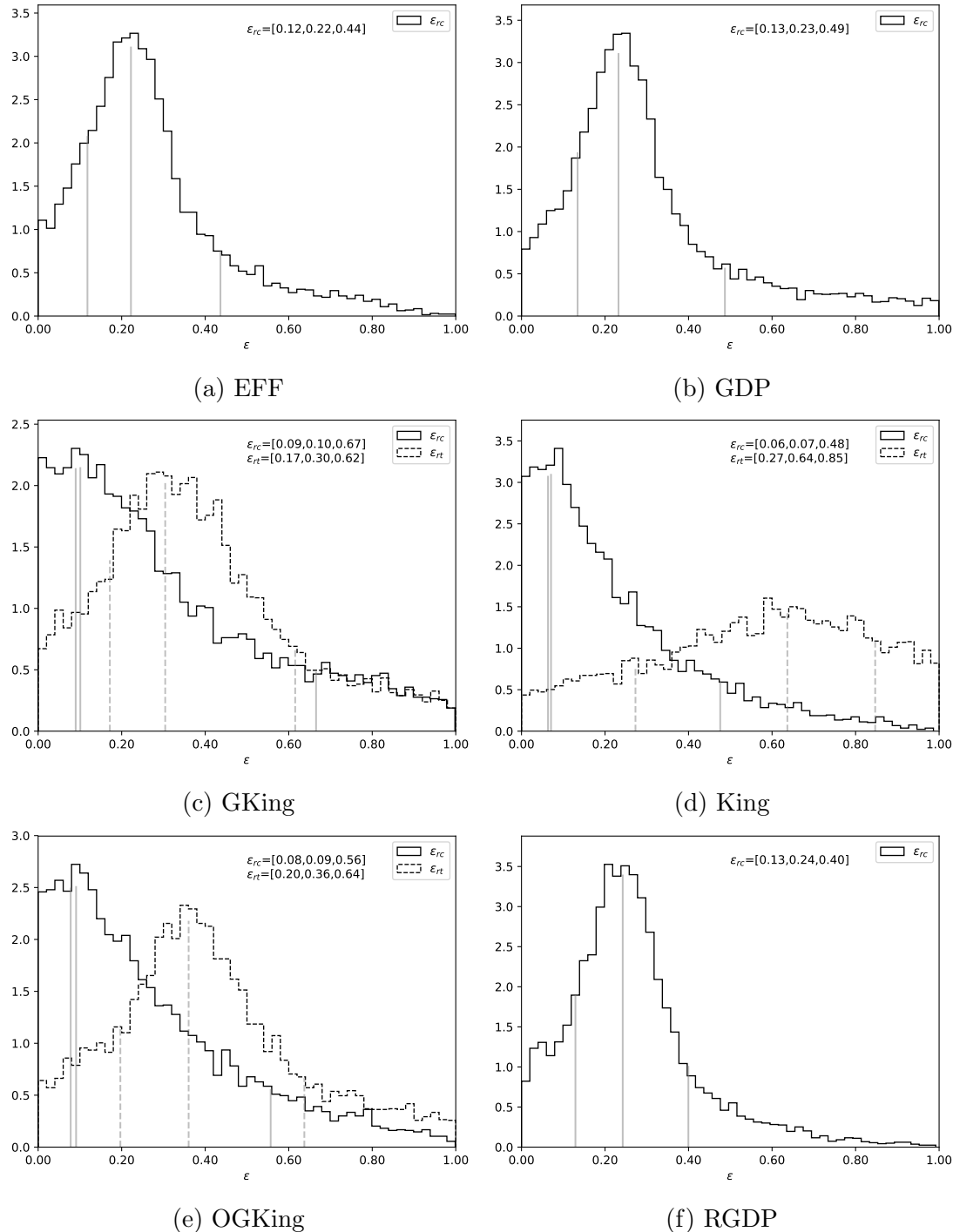


Figure A.11: Ellipticity distribution computed from the posterior distribution of the models with biaxial symmetry.

A.3 Models with luminosity segregation

$$\Sigma_{\text{EFF}} = \begin{pmatrix} 0.007 & -0.001 & -0.000 & 0.001 & -0.001 & -0.000 & -0.000 \\ -0.001 & 0.006 & 0.002 & 0.001 & 0.002 & 0.001 & 0.001 \\ -0.000 & 0.002 & 0.085 & 0.009 & 0.002 & 0.005 & 0.001 \\ 0.001 & 0.001 & 0.009 & 0.151 & 0.078 & 0.060 & 0.008 \\ -0.001 & 0.002 & 0.002 & 0.078 & 0.126 & 0.061 & 0.012 \\ -0.000 & 0.001 & 0.005 & 0.060 & 0.061 & 0.048 & 0.004 \\ -0.000 & 0.001 & 0.001 & 0.008 & 0.012 & 0.004 & 0.006 \end{pmatrix} \quad \Sigma_{\text{GDP}} = \begin{pmatrix} 0.010 & -0.001 & 0.000 & -0.000 & -0.003 & -0.001 & -0.003 & 0.001 & -0.001 \\ -0.001 & 0.008 & 0.002 & 0.003 & 0.004 & 0.000 & 0.004 & -0.001 & 0.001 \\ 0.000 & 0.002 & 0.321 & 0.102 & 0.064 & 0.010 & 0.071 & -0.012 & 0.014 \\ -0.000 & 0.003 & 0.102 & 1.122 & 0.789 & 0.092 & 0.506 & -0.003 & 0.061 \\ -0.003 & 0.004 & 0.064 & 0.789 & 0.828 & 0.072 & 0.472 & -0.011 & 0.069 \\ -0.001 & 0.000 & 0.010 & 0.092 & 0.072 & 0.051 & 0.068 & -0.019 & 0.004 \\ -0.003 & 0.004 & 0.071 & 0.506 & 0.472 & 0.068 & 0.354 & -0.040 & 0.040 \\ 0.001 & -0.001 & -0.012 & -0.003 & -0.011 & -0.019 & -0.040 & 0.031 & -0.003 \\ -0.001 & 0.001 & 0.014 & 0.061 & 0.069 & 0.004 & 0.040 & -0.003 & 0.016 \end{pmatrix}$$

$$\Sigma_{\text{GKing}} = \begin{pmatrix} 0.015 & -0.001 & -0.003 & 0.002 & -0.054 & -0.007 & -0.032 & 0.003 & -0.003 & -0.002 \\ -0.001 & 0.012 & 0.006 & 0.004 & 0.076 & 0.017 & 0.033 & -0.000 & 0.007 & 0.003 \\ -0.003 & 0.006 & 0.306 & 0.060 & 0.406 & 0.186 & 0.138 & -0.017 & 0.067 & 0.027 \\ 0.002 & 0.004 & 0.060 & 4.645 & 1.703 & 2.322 & 1.919 & 0.388 & 0.563 & 0.167 \\ -0.054 & 0.076 & 0.406 & 1.703 & 85.273 & 4.036 & 19.497 & -0.637 & 2.217 & 0.511 \\ -0.007 & 0.017 & 0.186 & 2.322 & 4.036 & 2.409 & 2.465 & 0.135 & 0.632 & 0.226 \\ -0.032 & 0.033 & 0.138 & 1.919 & 19.497 & 2.465 & 17.347 & -0.149 & 1.308 & 0.292 \\ 0.003 & -0.000 & -0.017 & 0.388 & -0.637 & 0.135 & -0.149 & 0.342 & 0.023 & -0.003 \\ -0.003 & 0.007 & 0.067 & 0.563 & 2.217 & 0.632 & 1.308 & 0.023 & 0.232 & 0.067 \\ -0.002 & 0.003 & 0.027 & 0.167 & 0.511 & 0.226 & 0.292 & -0.003 & 0.067 & 0.037 \end{pmatrix} \quad \Sigma_{\text{King}} = \begin{pmatrix} 0.018 & -0.001 & -0.003 & 0.015 & -0.105 & 0.002 & -0.019 & -0.000 \\ -0.001 & 0.014 & 0.004 & 0.009 & 0.123 & -0.001 & 0.010 & 0.000 \\ -0.003 & 0.004 & 0.328 & -0.118 & 1.317 & -0.005 & -0.064 & 0.004 \\ 0.015 & -0.009 & -0.118 & 1.547 & -5.348 & 0.110 & -1.293 & 0.002 \\ -0.105 & 0.123 & 1.317 & -5.348 & 220.118 & -1.423 & 16.847 & -0.041 \\ 0.002 & -0.001 & -0.005 & 0.110 & -1.423 & 0.192 & -1.046 & 0.014 \\ -0.019 & 0.010 & -0.064 & -1.293 & 16.847 & -1.046 & 32.386 & -0.069 \\ -0.000 & 0.000 & 0.004 & 0.002 & -0.041 & 0.014 & -0.069 & 0.004 \end{pmatrix}$$

$$\Sigma_{\text{OGKing}} = \begin{pmatrix} 0.009 & -0.000 & -0.002 & 0.002 & -0.010 & -0.000 & -0.005 & -0.001 \\ -0.000 & 0.006 & 0.002 & -0.002 & 0.013 & 0.002 & -0.005 & 0.001 \\ -0.002 & 0.002 & 0.176 & -0.019 & 0.137 & 0.008 & -0.104 & 0.008 \\ 0.002 & -0.002 & -0.019 & 0.175 & -0.381 & 0.025 & -0.080 & -0.002 \\ -0.010 & 0.013 & 0.137 & -0.381 & 10.973 & -0.093 & -0.386 & 0.009 \\ -0.000 & 0.002 & 0.008 & 0.025 & -0.093 & 0.070 & -0.186 & 0.008 \\ -0.005 & -0.005 & -0.104 & -0.080 & -0.386 & -0.186 & 2.807 & -0.023 \\ -0.001 & 0.001 & 0.008 & -0.002 & 0.009 & 0.008 & -0.023 & 0.005 \end{pmatrix} \quad \Sigma_{\text{RGDP}} = \begin{pmatrix} 0.010 & -0.000 & -0.000 & 0.002 & 0.001 & -0.000 & 0.001 & -0.001 \\ -0.000 & 0.008 & 0.003 & 0.006 & 0.009 & 0.001 & 0.006 & 0.002 \\ -0.000 & 0.003 & 0.237 & 0.078 & 0.056 & 0.003 & 0.046 & 0.012 \\ 0.002 & 0.006 & 0.078 & 1.481 & 1.074 & 0.125 & 0.667 & 0.081 \\ 0.001 & 0.009 & 0.056 & 1.074 & 1.078 & 0.090 & 0.609 & 0.088 \\ -0.000 & 0.001 & 0.003 & 0.125 & 0.090 & 0.050 & 0.062 & 0.005 \\ 0.001 & 0.006 & 0.046 & 0.667 & 0.609 & 0.062 & 0.390 & 0.047 \\ -0.001 & 0.002 & 0.012 & 0.081 & 0.088 & 0.005 & 0.047 & 0.016 \end{pmatrix}$$

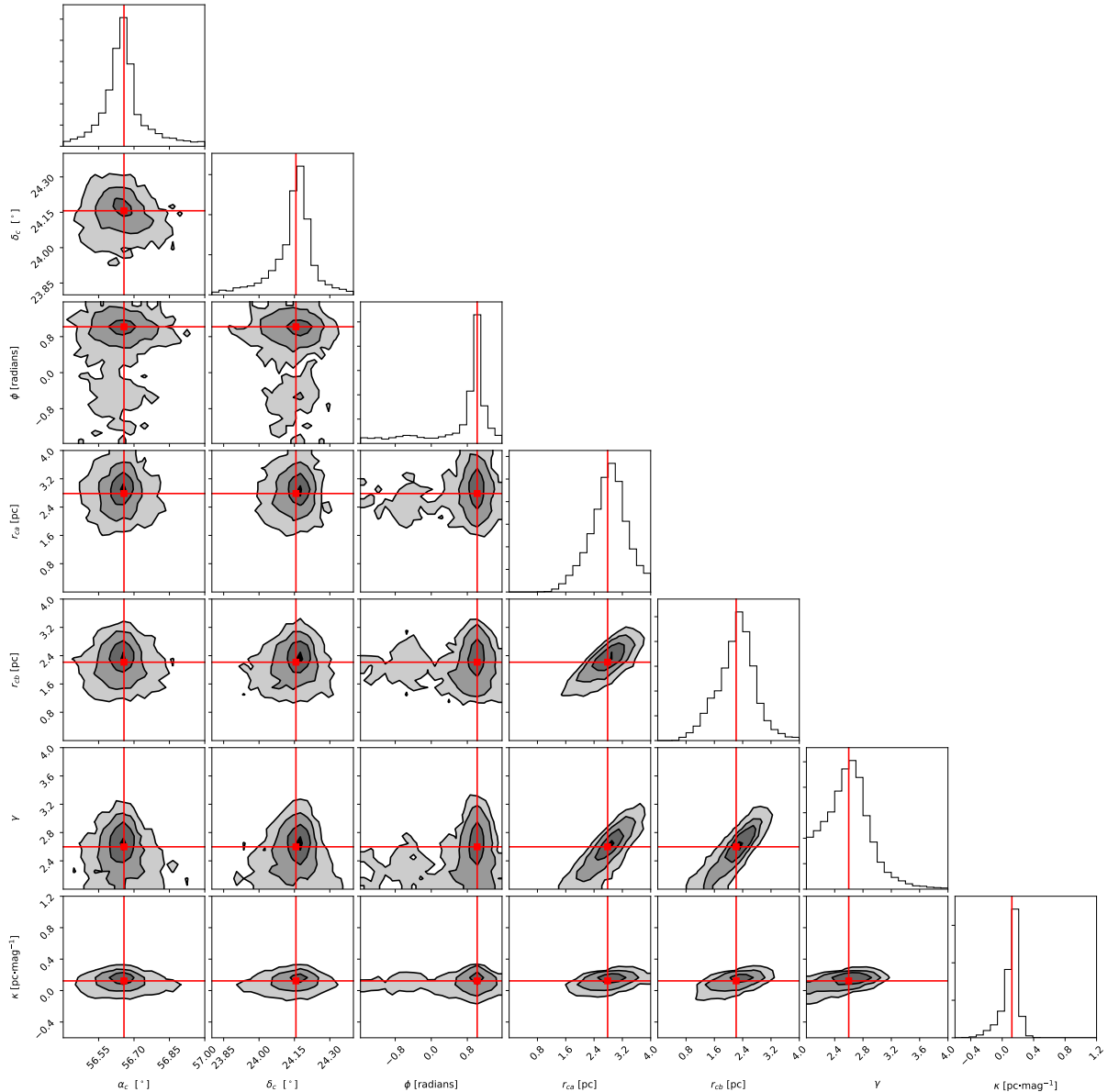


Figure A.12: Projections of the posterior distribution for the EFF luminosity segregated model.

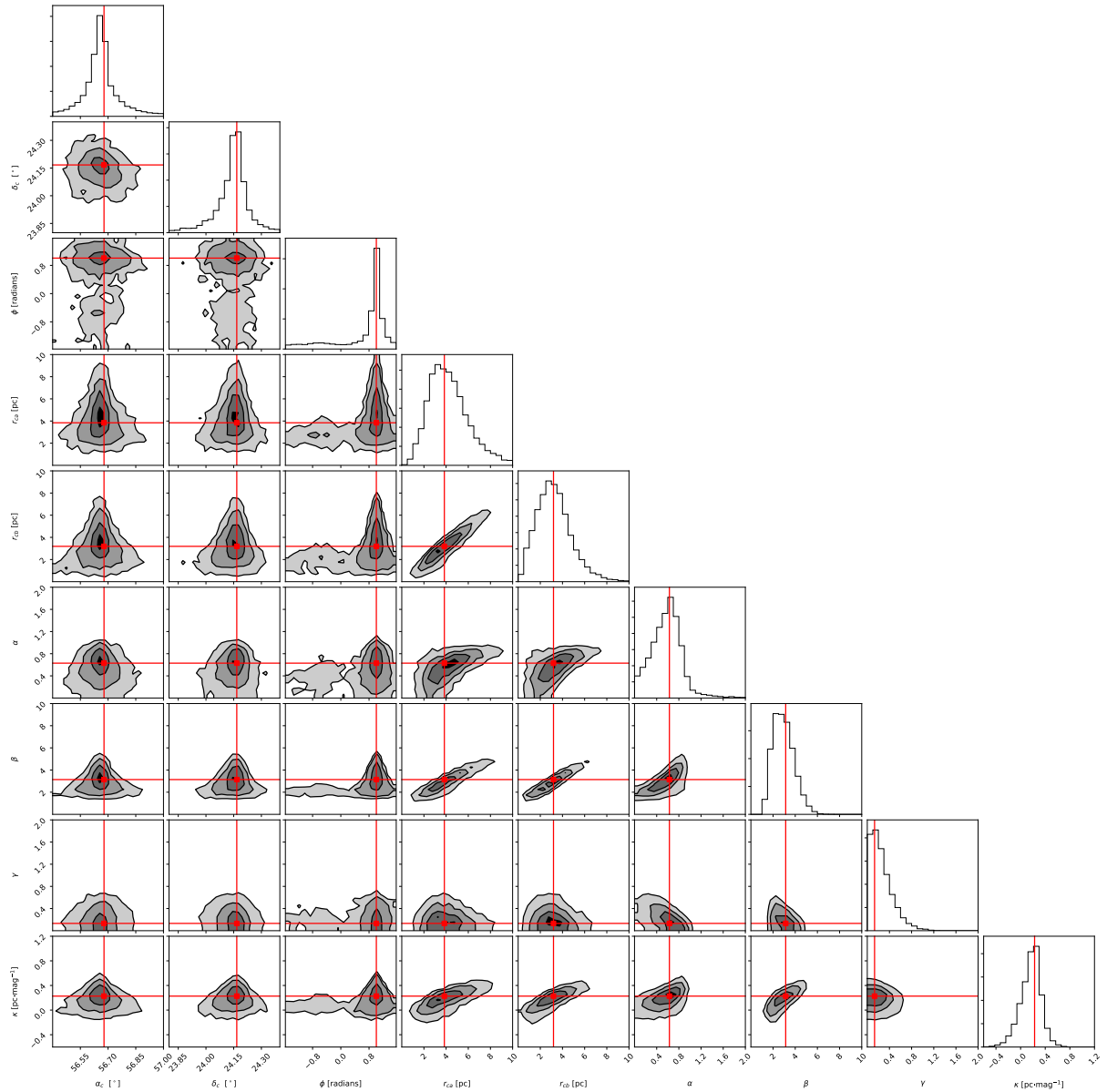


Figure A.13: Projections of the posterior distribution for the GDP luminosity segregated model.

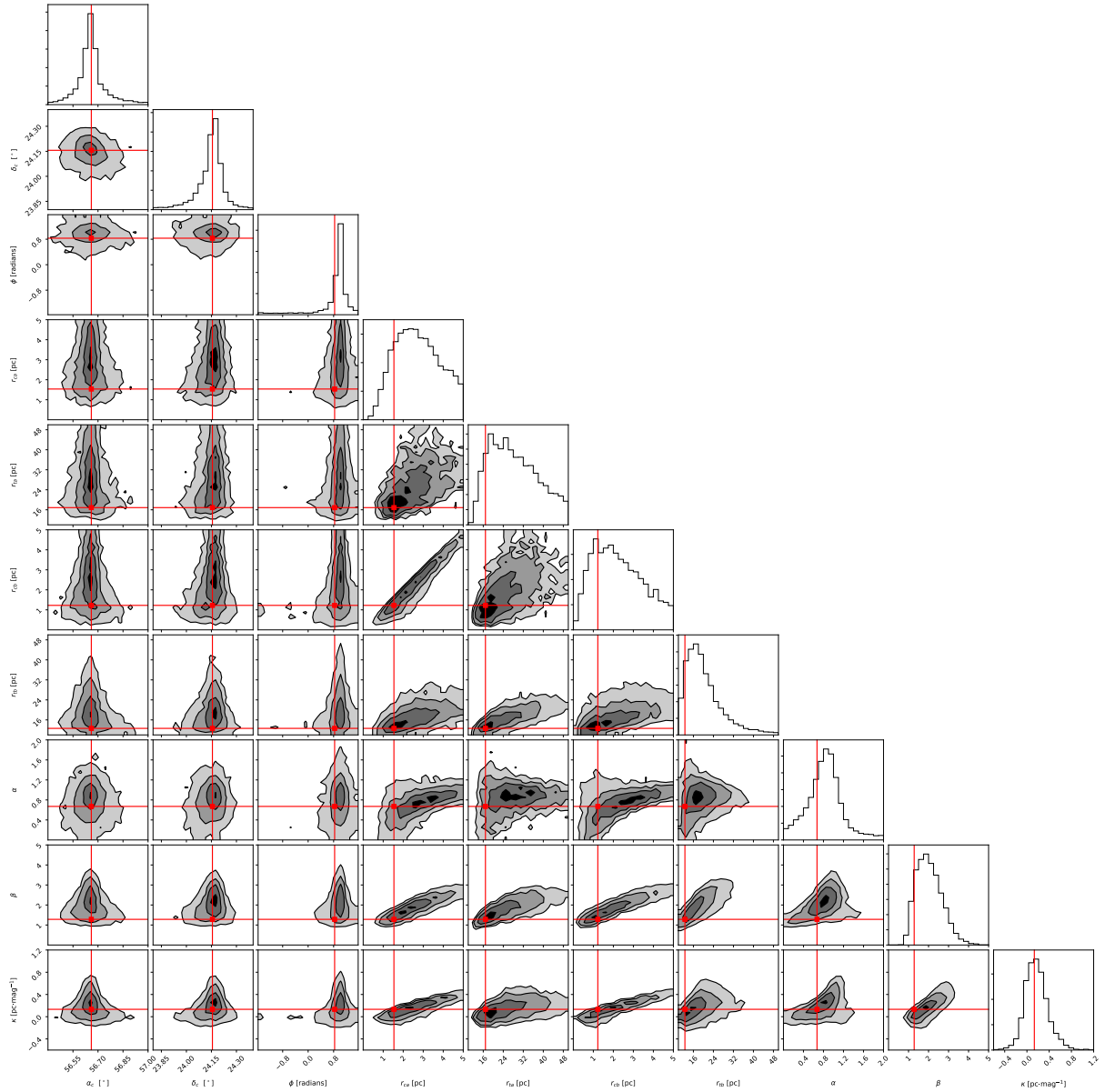


Figure A.14: Projections of the posterior distribution for the GKing luminosity segregated model.

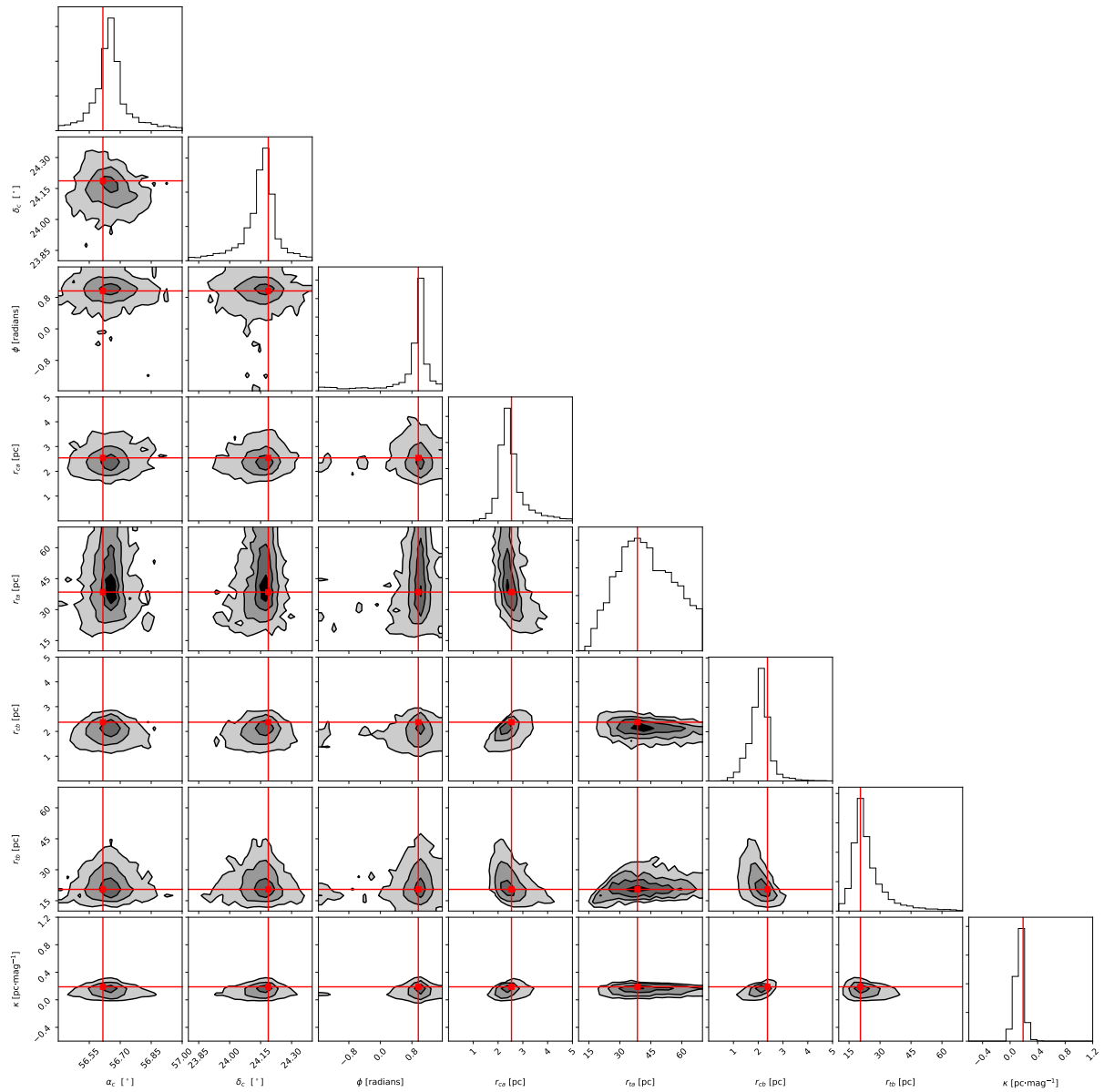


Figure A.15: Projections of the posterior distribution for the King's luminosity segregated model.

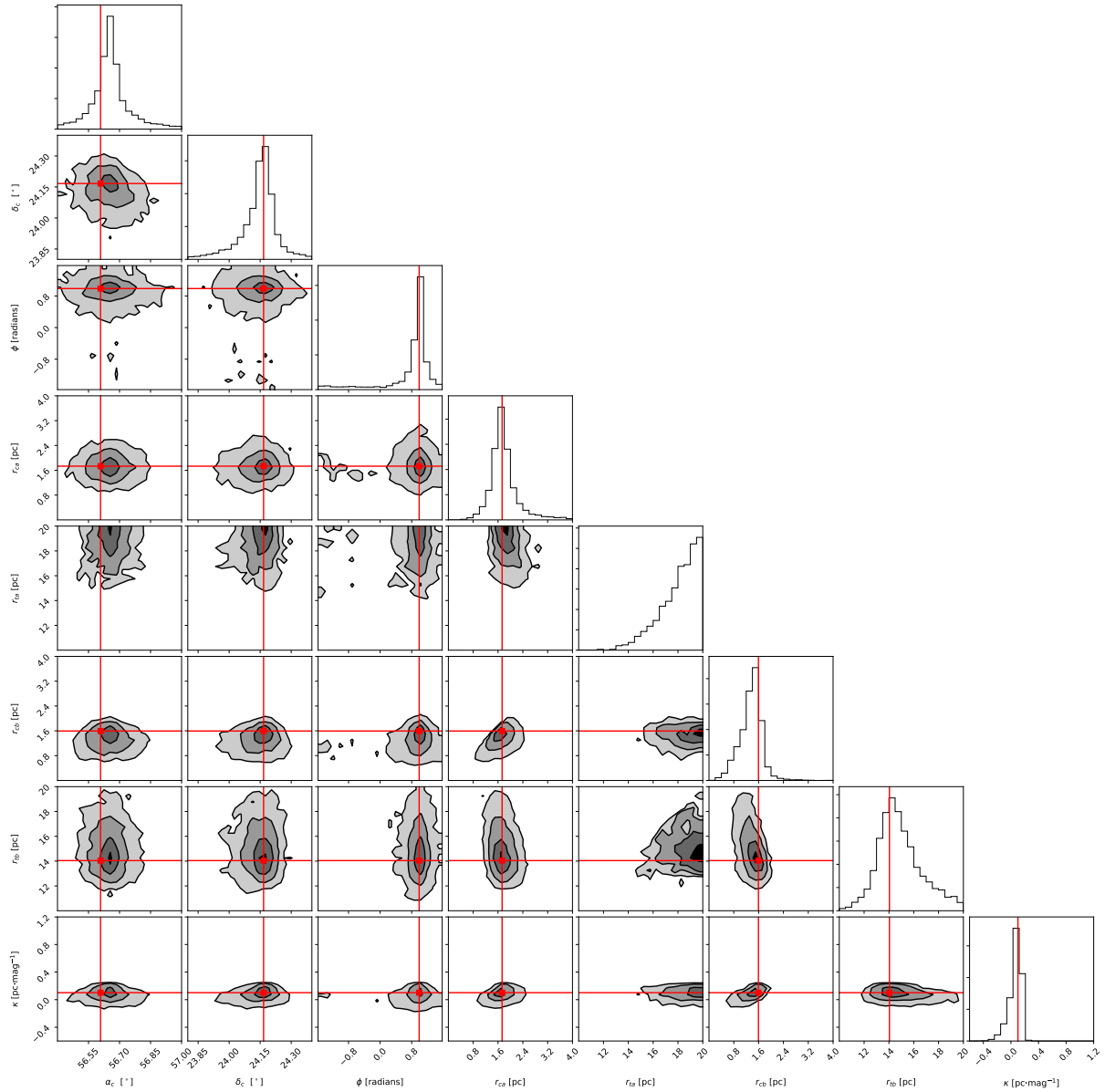


Figure A.16: Projections of the posterior distribution for the OGKing luminosity segregated model.

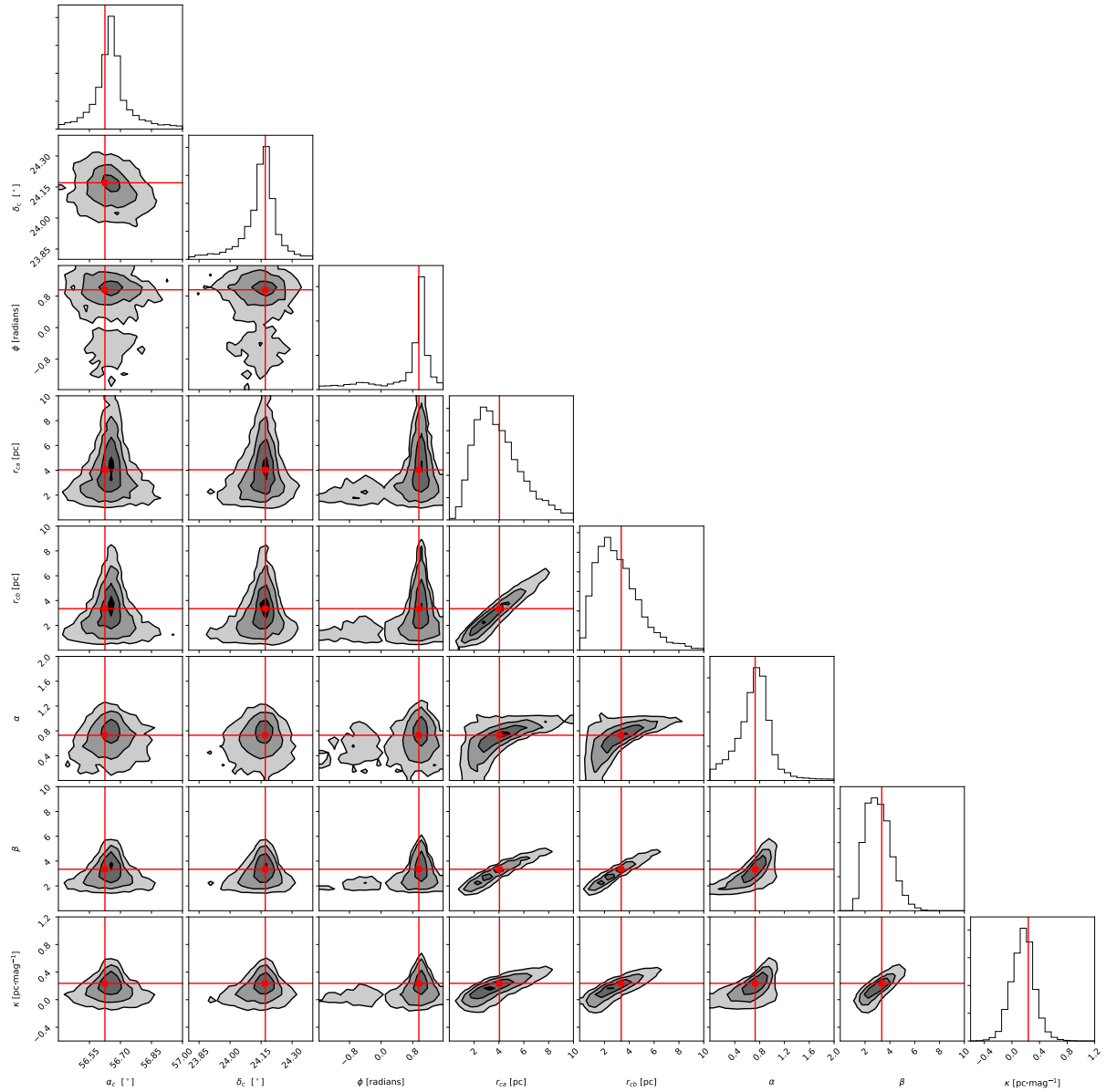


Figure A.17: Projections of the posterior distribution for the RGDP luminosity segregated model.

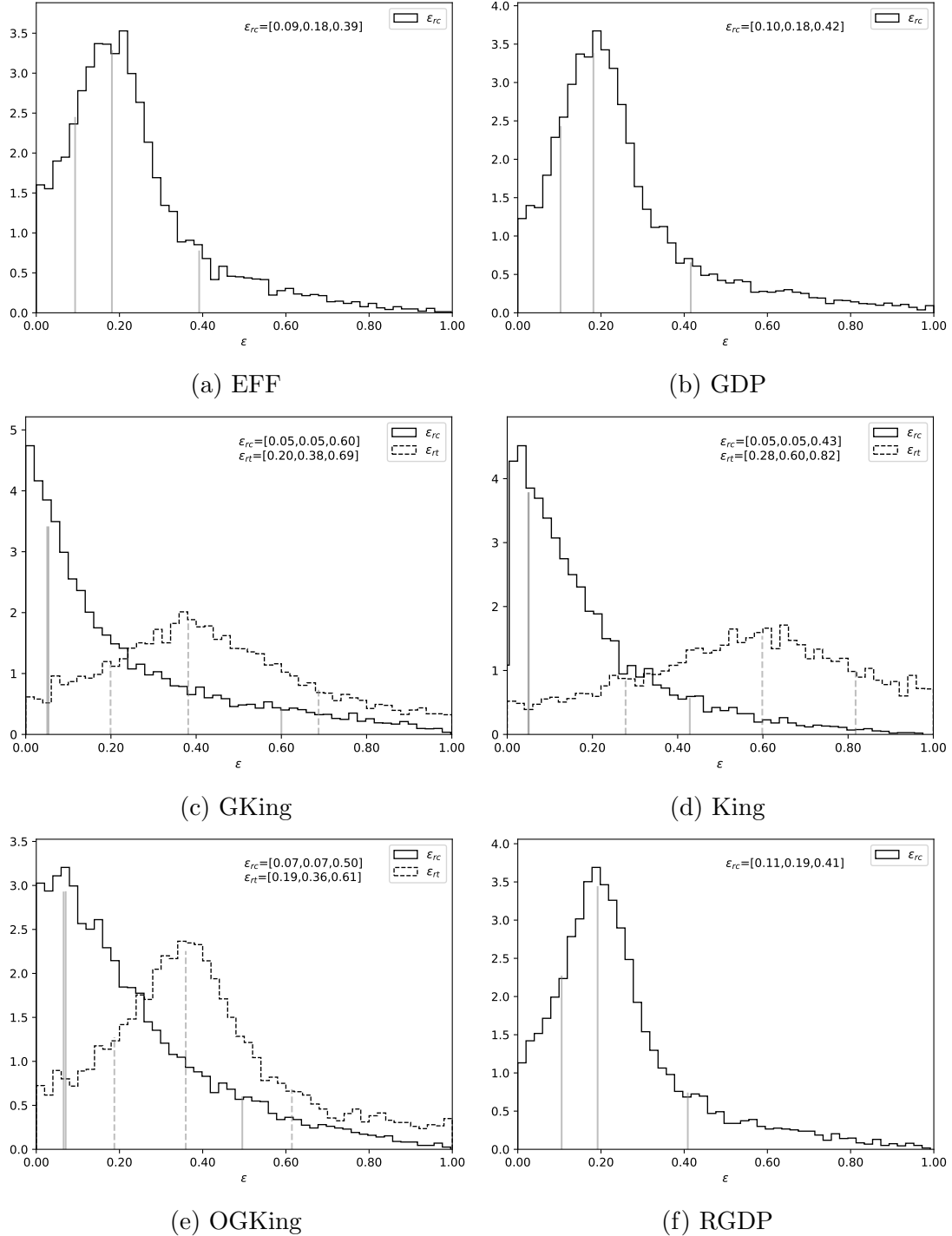


Figure A.18: Ellipticity distribution computed from the posterior distribution of the models with biaxial symmetry and luminosity segregation.

Bibliography

- Adams, J. D., Stauffer, J. R., Monet, D. G., Skrutskie, M. F., & Beichman, C. A. 2001, AJ, 121, 2053
- Adams, W. S. 1904, ApJ, 19
- Akeret, J., Seehars, S., Amara, A., Refregier, A., & Csillaghy, A. 2013, Astronomy and Computing, 2, 27
- Allard, F. 2014, in IAU Symposium, Vol. 299, Exploring the Formation and Evolution of Planetary Systems, ed. M. Booth, B. C. Matthews, & J. R. Graham, 271–272
- Allard, F., Homeier, D., & Freytag, B. 2013, Mem. Soc. Astron. Italiana, 84, 1053
- Allard, F., Homeier, D., Freytag, B., & Sharp, C. M. 2012, in EAS Publications Series, Vol. 57, EAS Publications Series, ed. C. Reylé, C. Charbonnel, & M. Schultheis, 3–43
- Alonso-Santiago, J., Negueruela, I., Marco, A., et al. 2017, MNRAS, 469, 1330
- Alsing, J., Heavens, A., & Jaffe, A. H. 2017, MNRAS, 466, 3272
- Anderes, E., Wandelt, B. D., & Lavaux, G. 2015, ApJ, 808, 152
- Andreoni, S. & Hurn, M. 2013, Statistical Analysis and Data Mining: The ASA Data Science Journal, Vol. 9, Issue 1, p. 15-33, 6, 15
- Andrieu, C., de Freitas, N., Doucet, A., & Jordan, M. I. 2003, Machine Learning, 50, 5
- Astraatmadja, T. L. & Bailer-Jones, C. A. L. 2016a, ApJ, 832, 137
- Astraatmadja, T. L. & Bailer-Jones, C. A. L. 2016b, ApJ, 833, 119
- Bailer-Jones, C. A. L. 2015, PASP, 127, 994
- Balaguer-Núñez, L., Galadí-Enríquez, D., & Jordi, C. 2007, A&A, 470, 585
- Ballesteros-Paredes, J., Hartmann, L. W., Pérez-Goytia, N., & Kuznetsova, A. 2015, MNRAS, 452, 566
- Baraffe, I., Chabrier, G., Allard, F., & Hauschildt, P. H. 1998, A&A, 337, 403

- Barnes, III, T. G., Moffett, T. J., Jefferys, W. H., & Forestell, A. D. 2004, in Astronomical Society of the Pacific Conference Series, Vol. 310, IAU Colloq. 193: Variable Stars in the Local Group, ed. D. W. Kurtz & K. R. Pollard, 95
- Barrado, D., Bouy, H., Bouvier, J., et al. 2016, *A&A*, 596, A113
- Bate, M. R. 2009a, *MNRAS*, 392, 590
- Bate, M. R. 2009b, *MNRAS*, 397, 232
- Bate, M. R. 2009c, *MNRAS*, 392, 1363
- Bate, M. R., Bonnell, I. A., & Bromm, V. 2003, *MNRAS*, 339, 577
- Berger, J. O., Bernardo, J. M., & Sun, D. 2009, *Ann. Statist.*, 37, 905
- Bessell, M. S., Castelli, F., & Plez, B. 1998, *A&A*, 333, 231
- Binney, J. & Tremaine, S. 2008, Galactic Dynamics: Second Edition (Princeton University Press)
- Bishop, C. 2006, Pattern Recognition and Machine Learning, Information Science and Statistics (Springer)
- Blaauw, A. 1964, in IAU Symposium, Vol. 20, The Galaxy and the Magellanic Clouds, ed. F. J. Kerr, 50
- Blackwell, T. & Bentley, P. 2002, in Proceedings of the 4th Annual Conference on Genetic and Evolutionary Computations, ed. W. Langdon, E. Cantu-Paz, K. Mathias, R. Roy, & D. Davis (San Francisco, CA, USA: Morgan kaufmann Publishers Inc.), 19–26
- Boss, L. 1910, Preliminary General Catalogue of 6188 stars for the epoch 1900
- Bouy, H., Bertin, E., Moraux, E., et al. 2013, *A&A*, 554, A101
- Bouy, H., Bertin, E., Sarro, L. M., et al. 2015, *A&A*, 577, A148
- Bovy, J., Hogg, D. W., & Roweis, S. T. 2009, *ApJ*, 700, 1794
- Bressan, A., Marigo, P., Girardi, L., et al. 2012, *MNRAS*, 427, 127
- Brooks, S., Gelman, A., Jones, G., & Meng, X. 2011, Handbook of Markov Chain Monte Carlo, Chapman & Hall/CRC Handbooks of Modern Statistical Methods (CRC Press)
- Buchner, J., Georgakakis, A., Nandra, K., et al. 2014, *A&A*, 564, A125
- Byun, Y.-I., Grillmair, C. J., Faber, S. M., et al. 1996, *AJ*, 111, 1889
- Cardelli, J. A., Clayton, G. C., & Mathis, J. S. 1989, *ApJ*, 345, 245

- Carpenter, B., Gelman, A., Hoffman, M., et al. 2017, Journal of Statistical Software, Articles, 76, 1
- Carpenter, J. M. 2000, AJ, 120, 3139
- Cartwright, A. & Whitworth, A. P. 2012, MNRAS, 423, 1018
- Chabrier, G. 2003a, PASP, 115, 763
- Chabrier, G. 2003b, ApJ, 586, L133
- Chabrier, G. 2005, in Astrophysics and Space Science Library, Vol. 327, The Initial Mass Function 50 Years Later, ed. E. Corbelli, F. Palla, & H. Zinnecker, 41
- Chung, Y., Gelman, A., Rabe-Hesketh, S., Liu, J., & Dorie, V. 2015, Journal of Educational and Behavioral Statistics, 40, 136
- Clerc, M. & Kennedy, J. 2002, Trans. Evol. Comp, 6, 58
- Converse, J. M. & Stahler, S. W. 2008, ApJ, 678, 431
- Converse, J. M. & Stahler, S. W. 2010, MNRAS, 405, 666
- Dahn, C. C., Liebert, J., & Harrington, R. S. 1986, AJ, 91, 621
- De Boor, C. 1978, A practical guide to splines / Carl de Boor (Springer-Verlag New York), xxiv, 392 p. :
- De Gennaro, S., von Hippel, T., Jefferys, W. H., et al. 2009, ApJ, 696, 12
- de Graeve, E. 1979, Publications of the Vatican Observatory V.1:16, P. 1, 1979, 1, 1
- de Marchi, G. & Paresce, F. 2001, in Astronomische Gesellschaft Meeting Abstracts, Vol. 18, Astronomische Gesellschaft Meeting Abstracts, ed. E. R. Schielicke
- de Zeeuw, T. 1985, MNRAS, 216, 273
- Deacon, N. R. & Hambly, N. C. 2004, A&A, 416, 125
- Delfosse, X., Forveille, T., Ségransan, D., et al. 2000, A&A, 364, 217
- Demory, B.-O. 2014, ApJ, 789, L20
- Dempster, A. P., Laird, N. M., & Rubin, D. B. 1977, JOURNAL OF THE ROYAL STATISTICAL SOCIETY, SERIES B, 39, 1
- Diard, J. & Bessiere, P. 2008, Probabilistic reasoning and decision making in sensory-motor systems, 153

- Dirac, P. A. M. 1942, Proceedings of the Royal Society of London Series A, 180, 1
- Duane, S., Kennedy, A. D., Pendleton, B. J., & Roweth, D. 1987, Physics Letters B, 195, 216
- Duquennoy, A. & Mayor, M. 1991, A&A, 248, 485
- Eggen, O. J. 1986, PASP, 98, 755
- Elson, R. A. W., Fall, S. M., & Freeman, K. C. 1987, ApJ, 323, 54
- Faherty, J. K., Burgasser, A. J., Walter, F. M., et al. 2012, ApJ, 752, 56
- Fan, Y. & Sisson, S. 2011, Handbook of Markov Chain Monte Carlo, 67
- Feeney, S. M., Johnson, M. C., McEwen, J. D., Mortlock, D. J., & Peiris, H. V. 2013, Phys. Rev. D, 88, 043012
- Fei-Fei, L. & Perona, P. 2005, in Computer Vision and Pattern Recognition, 2005. CVPR 2005. IEEE Computer Society Conference on, Vol. 2, Ieee, 524–531
- Feroz, F., Hobson, M. P., & Bridges, M. 2009, Monthly Notices of the Royal Astronomical Society, 398, 1601
- Flegal, J. M., Hughes, J., & Vats, D. 2016, mcmcse: Monte Carlo Standard Errors for MCMC, Riverside, CA and Minneapolis, MN, r package version 1.2-1
- Foreman-Mackey, D. 2016, The Journal of Open Source Software, 24
- Foreman-Mackey, D., Hogg, D. W., Lang, D., & Goodman, J. 2013, Publications of the Astronomical Society of the Pacific, 125, 306
- Franklin, J. 2002, The Science of Conjecture: Evidence and Probability Before Pascal, A Johns Hopkins paperback (Johns Hopkins University Press)
- Gagné, J., Lafrenière, D., Doyon, R., Malo, L., & Artigau, É. 2014, ApJ, 783, 121
- Gaia Collaboration, Prusti, T., de Bruijne, J. H. J., et al. 2016a, A&A, 595, A1
- Gaia Collaboration, Prusti, T., de Bruijne, J. H. J., et al. 2016b, A&A, 595, A1
- Gaia Collaboration, van Leeuwen, F., Vallenari, A., et al. 2017, A&A, 601, A19
- Galli, P. A. B., Moraux, E., Bouy, H., et al. 2017, A&A, 598, A48
- Gatewood, G., de Jonge, J. K., & Han, I. 2000, ApJ, 533, 938
- Gelman, A. 2006, Bayesian Analysis, 1, 515

- Gelman, A. 2012, CHANCE, 25, 52
- Gelman, A., Carlin, J., Stern, H., et al. 2013, Bayesian Data Analysis, third edition edn. (CRC)
- Gelman, A. & Hill, J. 2007, Data Analysis Using Regression and Multilevel/Hierarchical Models, Analytical Methods for Social Research (Cambridge University Press)
- Gelman, A., Jakulin, A., Pittau, M. G., & Su, Y.-S. 2008, Ann. Appl. Stat., 2, 1360
- Geman, S. & Geman, D. 1984, IEEE Trans. Pattern Anal. Mach. Intell., 6, 721
- Giannuzzi, M. A. 1995, A&A, 293, 360
- Gong, L. & Flegal, J. M. 2016, Journal of Computational and Graphical Statistics, 25, 684
- González-Farias, G., Dominguez-Molina, A., & Gupta, A. K. 2004, Journal of Statistical Planning and Inference, 126, 521
- Good, I. J. 1980, Trabajos de Estadistica Y de Investigacion Operativa, 31, 489
- Goodman, J. & Weare, J. 2010, Communications in Applied Mathematics and Computational Science, 5, 65
- Gupta, A. K., González-Farias, G., & Dominguez-Molina, J. 2004, Journal of Multivariate Analysis, 89, 181
- Guthrie, B. N. G. 1987, QJRAS, 28, 289
- Hambly, N. C. & Jameson, R. F. 1991, MNRAS, 249, 137
- Hastings, W. K. 1970, Biometrika, 57, 97
- Henry, T. J. & McCarthy, Jr., D. W. 1990, ApJ, 350, 334
- Hernquist, L. 1990, ApJ, 356, 359
- Hertzsprung, E. 1947, Annalen van de Sterrewacht te Leiden, 19, A1
- Hillenbrand, L. A., Bauermeister, A., & White, R. J. 2008, in 14th Cambridge Workshop on Cool Stars, Stellar Systems, and the Sun, ed. G. van Belle, Vol. 384, 200
- Hodgkin, S. T. & Jameson, R. F. 2000, in Astronomical Society of the Pacific Conference Series, Vol. 198, Stellar Clusters and Associations: Convection, Rotation, and Dynamos, ed. R. Pallavicini, G. Micela, & S. Sciortino, 59
- Hogg, D. W., Bovy, J., & Lang, D. 2010a, ArXiv e-prints
- Hogg, D. W., Myers, A. D., & Bovy, J. 2010b, ApJ, 725, 2166

- Holl, B., Hobbs, D., & Lindegren, L. 2010, in IAU Symposium, Vol. 261, Relativity in Fundamental Astronomy: Dynamics, Reference Frames, and Data Analysis, ed. S. A. Klioner, P. K. Seidelmann, & M. H. Soffel, 320–324
- Hong, D., Balzano, L., & Fessler, J. A. 2016, Towards a theoretical analysis of PCA for heteroscedastic data, arxiv 1610.03595
- Huang, A. & Wand, M. P. 2013, Bayesian Analysis, 8, 439
- Jaffe, W. 1983, MNRAS, 202, 995
- Jameson, R. F., Dobbie, P. D., Hodgkin, S. T., & Pinfield, D. J. 2002, MNRAS, 335, 853
- Jappsen, A.-K., Klessen, R. S., Larson, R. B., Li, Y., & Mac Low, M.-M. 2005, A&A, 435, 611
- Jaynes, E. 2003, Probability Theory: The Logic of Science (Cambridge University Press)
- JCGM. 2008, JCGM 100: Evaluation of Measurement Data - Guide to the Expression of Uncertainty in Measurement, Tech. rep., Joint Committee for Guides in Metrology
- Jefferys, T. R., Jefferys, W. H., Barnes, III, T. G., & Dambis, A. 2007, in Astronomical Society of the Pacific Conference Series, Vol. 371, Statistical Challenges in Modern Astronomy IV, ed. G. J. Babu & E. D. Feigelson, 433
- Jeffreys, H. 1961, Theory of Probability, 3rd edn. (Oxford, England: Oxford)
- Jiang, F. & van den Bosch, F. C. 2016, MNRAS, 458, 2848
- Johnson, H. L. & Mitchell, R. I. 1958, ApJ, 128, 31
- Jones, B. F. 1970, AJ, 75, 563
- Jordi, C., Gebran, M., Carrasco, J. M., et al. 2010, A&A, 523, A48
- Kass, R. E. & Raftery, A. E. 1995, Journal of the American Statistical Association, 90, 773
- Kennedy, J. & Eberhart, R. 1995, in Neural Networks, 1995. Proceedings., IEEE International Conference on, Vol. 4, 1942–1948 vol.4
- Kennicutt, Jr., R. C. 1998, in Astronomical Society of the Pacific Conference Series, Vol. 142, The Stellar Initial Mass Function (38th Herstmonceux Conference), ed. G. Gilmore & D. Howell, 1
- King, I. 1962, AJ, 67, 471
- Koller, D. & Friedman, N. 2009, Probabilistic Graphical Models: Principles and Techniques, Adaptive computation and machine learning (MIT Press)

- Kordopatis, G., Gilmore, G., Steinmetz, M., et al. 2013, AJ, 146, 134
- Kozhurina-Platais, V., Girard, T. M., Platais, I., et al. 1995, AJ, 109, 672
- Krone-Martins, A. & Moitinho, A. 2014, A&A, 561, A57
- Kroupa, P. 2001, MNRAS, 322, 231
- Kroupa, P. 2002, Science, 295, 82
- Kroupa, P., Gilmore, G., & Tout, C. A. 1991, MNRAS, 251, 293
- Kroupa, P., Weidner, C., Pflamm-Altenburg, J., et al. 2013, The Stellar and Sub-Stellar Initial Mass Function of Simple and Composite Populations, ed. T. D. Oswalt & G. Gilmore, 115
- Küpper, A. H. W., Kroupa, P., Baumgardt, H., & Heggie, D. C. 2010a, MNRAS, 407, 2241
- Küpper, A. H. W., Kroupa, P., Baumgardt, H., & Heggie, D. C. 2010b, MNRAS, 401, 105
- Kuznetsova, A., Hartmann, L., & Ballesteros-Paredes, J. 2015, ApJ, 815, 27
- Lada, C. J. & Lada, E. A. 2003, ARA&A, 41, 57
- Lauer, T. R., Ajhar, E. A., Byun, Y.-I., et al. 1995, AJ, 110, 2622
- Lawrence, A., Warren, S. J., Almaini, O., et al. 2007, MNRAS, 379, 1599
- Lee, S.-W. & Sung, H. 1995, Journal of Korean Astronomical Society, 28, 45
- Limber, D. N. 1960, ApJ, 131, 168
- Limber, D. N. 1961, ApJ, 134, 537
- Limber, I. D. N. 1962, ApJ, 135, 16
- Lin, T., Lee, J., & Ho, H. 2006, WOS:000236696400015
- Lindstrom, M. 1999, Journal of Computational and Graphical Statistics, 8, 333
- Liu, T., Janes, K. A., & Bania, T. M. 1991, ApJ, 377, 141
- Lodieu, N., Deacon, N. R., & Hambly, N. C. 2012, MNRAS, 422, 1495
- Lodieu, N., Dobbie, P. D., Deacon, N. R., et al. 2007, MNRAS, 380, 712
- Loktin, A. V. 2006, Astronomy Reports, 50, 714
- Lutz, T. E. & Kelker, D. H. 1973, PASP, 85, 573

- Luyten, W. J. 1939, Publications of the Astronomical Observatory University of Minnesota, 7, 121
- Luyten, W. J. 1941, Annals of the New York Academy of Sciences, 42, 201
- Maíz-Apellániz, J. 2003, in HST Calibration Workshop : Hubble after the Installation of the ACS and the NICMOS Cooling System, ed. S. Arribas, A. Koekemoer, & B. Whitmore, 346
- Malo, L., Doyon, R., Lafrenière, D., et al. 2013, ApJ, 762, 88
- March, M. C., Karpenka, N. V., Feroz, F., & Hobson, M. P. 2014, MNRAS, 437, 3298
- Martin, E. L., Rebolo, R., & Zapatero-Osorio, M. R. 1996, ApJ, 469, 706
- Maschberger, T. 2013, MNRAS, 429, 1725
- McMichael, D. W. 1996, in Proc. Fourth International Symposium on Signal Processing and its Applications (ISSPA, 377–378
- Melis, C., Reid, M. J., Mioduszewski, A. J., Stauffer, J. R., & Bower, G. C. 2014, Science, 345, 1029
- Mermilliod, J.-C. 1979, Bulletin d'Information du Centre de Donnees Stellaires, 16, 2
- Mermilliod, J.-C., Bratschi, P., & Mayor, M. 1997, A&A, 320, 74
- Mermilliod, J.-C., Mayor, M., & Udry, S. 2009, A&A, 498, 949
- Metropolis, N., Rosenbluth, A. W., Rosenbluth, M. N., Teller, A. H., & Teller, E. 1953, The Journal of Chemical Physics, 21, 1087
- Miller, G. E. & Scalo, J. M. 1979, ApJS, 41, 513
- Moore, B., Quinn, T., Governato, F., Stadel, J., & Lake, G. 1999, MNRAS, 310, 1147
- Moraux, E., Bouvier, J., & Stauffer, J. R. 2001, A&A, 367, 211
- Moraux, E., Bouvier, J., Stauffer, J. R., & Cuillandre, J.-C. 2003, A&A, 400, 891
- Moraux, E., Kroupa, P., & Bouvier, J. 2004, A&A, 426, 75
- Morris, C. N. 1983, Journal of the American Statistical Association, 78, 47
- Muench, A. A., Lada, E. A., Lada, C. J., & Alves, J. 2002, ApJ, 573, 366
- Mulders, G. D., Pascucci, I., & Apai, D. 2015, ApJ, 814, 130
- Myeong, G. C., Jerjen, H., Mackey, D., & Da Costa, G. S. 2017, ApJ, 840, L25

- Narayanan, D. & Davé, R. 2012, MNRAS, 423, 3601
- Navarro, J. F., Frenk, C. S., & White, S. D. M. 1997, ApJ, 490, 493
- Neal, R. M. 1996, Bayesian Learning for Neural Networks (Secaucus, NJ, USA: Springer-Verlag New York, Inc.)
- O'dell, M. A., Hendry, M. A., & Collier Cameron, A. 1994, MNRAS, 268, 181
- Offner, S. S. R., Clark, P. C., Hennebelle, P., et al. 2014, Protostars and Planets VI, 53
- Olivares, J., Sánchez, L. J., Ruelas-Mayorga, A., et al. 2013, AJ, 146, 106
- Olivares, J., Sarro, L., Moraux, E., Berihuete, A., & Bouy, H. 2017, A&A, submitted
- Panwar, N., Samal, M. R., Pandey, A. K., et al. 2017, MNRAS, 468, 2684
- Parker, R. J., Goodwin, S. P., Wright, N. J., Meyer, M. R., & Quanz, S. P. 2016, MNRAS, 459, L119
- Patel, P. K., Sharma, V., & Gupta, K. 2013, International Journal of Computer Applications, 73
- Perryman, M. A. C., Lindegren, L., Kovalevsky, J., et al. 1997, A&A, 323, L49
- Pinfield, D. J., Jameson, R. F., & Hodgkin, S. T. 1998, MNRAS, 299, 955
- Plummer, H. C. 1911, MNRAS, 71, 460
- Porras, A., Christopher, M., Allen, L., et al. 2003, AJ, 126, 1916
- Press, W. H. 1997, in Unsolved Problems in Astrophysics, ed. J. N. Bahcall & J. P. Ostriker, 49–60
- Pritchard, C. 1884, MNRAS, 44, 355
- Raboud, D. & Mermilliod, J.-C. 1998, A&A, 329, 101
- Rebull, L. M., Stauffer, J. R., Bouvier, J., et al. 2016, AJ, 152, 113
- Reid, I. N., Cruz, K. L., Allen, P., et al. 2004, AJ, 128, 463
- Reid, I. N., Gizis, J. E., & Hawley, S. L. 2002, AJ, 124, 2721
- Riedel, A. R., Blunt, S. C., Lambrides, E. L., et al. 2017, AJ, 153, 95
- Robotham, A. S. G., Taranu, D. S., Tobar, R., Moffett, A., & Driver, S. P. 2017, MNRAS, 466, 1513
- Roberts, G. O. & Rosenthal, J. S. 2004, Probability Surveys, 1, 20

- Rosvick, J. M., Mermilliod, J.-C., & Mayor, M. 1992, A&A, 255, 130
- Rueda, R. 1992, Test, 1, 61
- Sackett, P. D. & Sparke, L. S. 1990, ApJ, 361, 408
- Sale, S. E. 2012, MNRAS, 427, 2119
- Salpeter, E. E. 1955, ApJ, 121, 161
- Sampedro, L. & Alfaro, E. J. 2016, MNRAS, 457, 3949
- Sanders, W. L. 1971, A&A, 14, 226
- Sarro, L. M., Berihuete, A., Carrión, C., et al. 2013, A&A, 550, A44
- Sarro, L. M., Bouy, H., Berihuete, A., et al. 2014, Astronomy & Astrophysics, 14
- Scalo, J. M. 1986, Fund. Cosmic Phys., 11, 1
- Schwarz, G. 1978, Ann. Statist., 6, 461
- Shariff, H., Dhawan, S., Jiao, X., et al. 2016, MNRAS, 463, 4311
- Shkedy, Z., Decin, L., Molenberghs, G., & Aerts, C. 2007, MNRAS, 377, 120
- Simon, M. 1997, The Astrophysical Journal Letters, 482, L81
- Skilling, J. 2004, in American Institute of Physics Conference Series, Vol. 735, American Institute of Physics Conference Series, ed. R. Fischer, R. Preuss, & U. V. Toussaint, 395–405
- Skilling, J. 2006, Bayesian Anal., 1, 833
- Smart, W. M. & Green, E. b. R. M. 1977, Textbook on Spherical Astronomy
- Smith, B. & Struve, O. 1944, ApJ, 100, 360
- Soderblom, D. R., Nelan, E., Benedict, G. F., et al. 2005, AJ, 129, 1616
- Sohn, S. T., Majewski, S. R., Muñoz, R. R., et al. 2007, ApJ, 663, 960
- Spiriti, S., Eubank, R., Smith, P. W., & Young, D. 2013, Journal of Statistical Computation and Simulation, 83, 1020
- Stauffer, J. R., Hartmann, L. W., Fazio, G. G., et al. 2007, ApJS, 172, 663
- Stauffer, J. R., Liebert, J., Giampapa, M., et al. 1994, AJ, 108, 160
- Stauffer, J. R., Schultz, G., & Kirkpatrick, J. D. 1998, ApJ, 499, L199

- Takeda, Y., Hashimoto, O., & Honda, S. 2017, PASJ, 69, 1
- Tapiador, D., Berihuete, A., Sarro, L. M., Julbe, F., & Huedo, E. 2017, Astronomy and Computing, 19, 1
- Terlevich, E. 1987, MNRAS, 224, 193
- Terndrup, D. M., Stauffer, J. R., Pinsonneault, M. H., et al. 2000, AJ, 119, 1303
- Thies, I. & Kroupa, P. 2007, ApJ, 671, 767
- Thies, I. & Kroupa, P. 2008, MNRAS, 390, 1200
- Titus, J. 1938, AJ, 47, 25
- Trotta, R. 2008, Contemporary Physics, 49, 71
- Trumpler, R. J. 1921, Lick Observatory Bulletin, 10, 110
- van de Ven, G., van den Bosch, R. C. E., Verolme, E. K., & de Zeeuw, P. T. 2006, A&A, 445, 513
- van Leeuwen, F. 1980, in IAU Symposium, Vol. 85, Star Clusters, ed. J. E. Hesser, 157–162
- van Leeuwen, F. 1997, in ESA Special Publication, Vol. 402, Hipparcos - Venice '97, ed. R. M. Bonnet, E. Høg, P. L. Bernacca, L. Emiliani, A. Blaauw, C. Turon, J. Kovalevsky, L. Lindegren, H. Hassan, M. Bouffard, B. Strim, D. Heger, M. A. C. Perryman, & L. Woltjer, 203–206
- van Leeuwen, F. 2009, A&A, 497, 209
- van Leeuwen, F. & Hansen Ruiz, C. S. 1997, in ESA Special Publication, Vol. 402, Hipparcos - Venice '97, ed. R. M. Bonnet, E. Høg, P. L. Bernacca, L. Emiliani, A. Blaauw, C. Turon, J. Kovalevsky, L. Lindegren, H. Hassan, M. Bouffard, B. Strim, D. Heger, M. A. C. Perryman, & L. Woltjer, 689–692
- van Rhijn, P. J. 1925, Publications of the Kapteyn Astronomical Laboratory Groningen, 38
- van Rhijn, P. J. 1936, Publications of the Kapteyn Astronomical Laboratory Groningen, 47, 1
- Vasilevskis, S., Klemola, A., & Preston, G. 1958, AJ, 63, 387
- Wells, A. E. 1924, PhD thesis, THE UNIVERSITY OF MICHIGAN.
- Wheeler, C. 2009, in Bulletin of the American Astronomical Society, Vol. 41, American Astronomical Society Meeting Abstracts #213, 202

Wolfgang, A. & Lopez, E. 2015, ApJ, 806, 183

Woolley, R. V. D. R. 1956, MNRAS, 116, 296

Zhao, H. 1997, MNRAS, 287, 525

Acronyms

ACC Accuracy. 102–105

AD Anderson-Darling. 145

AUC Area Under the Curve. 108, 150

B-spline Basis-spline. 65–67

BANYAN Bayesian Analysis of Nearby AssociatioNs. 13, 14

BD Brown Dwarfs. 4–8, 151

BHM Bayesian Hierarchical Model. ii–v, 17, 18, 44, 54–57, 68, 69, 71, 72, 78, 82, 83, 91, 92, 97, 99, 105, 108–117, 120, 129–133, 135, 137, 142, 145, 148–153

BIC Bayesian Information Criterion. 62, 63, 65, 66, 68, 70

CDF Cumulative Distribution Function. 145, 147

CI Colour Index $i - K_s$. 39, 40, 42, 43, 65, 68, 69, 79, 81, 92, 105–107, 117, 131, 132, 134, 135

CMD Colour Magnitude Diagram. 12, 13, 40, 65, 83, 101, 110, 113–117, 135

CPU Central Processing Unit. 66, 152

CR Contamination Rate. 102–104, 106, 107, 111, 112, 115

CSN Closed Skewed Normal. 66, 152

DANCe Dynamical Analysis of Nearby Clusters. ii, iv, 2, 7–9, 11, 18, 36, 39, 40, 45, 93, 109, 125, 139, 140, 150, 152, 153

DDR2 Pleiades DANCe Data Release 2. 18, 22, 36–38, 40, 42–44, 57–59, 61, 69, 72, 95, 103, 109, 110, 114–116, 128, 135, 136, 139, 142, 150

EFF Elson, Fall and Freeman. 73–75, 122, 124

EM Expectation Maximisation. 63, 68, 70, 94–96

EMB Equal-Mass Binaries. 64–66, 68, 70, 71, 78–81, 92, 129, 131–134, 151

ESS Effective Sample Size. 91

FN False Negative. 102

FP False Positive. 102

FPR False Positive Rate. 102, 107

GKing General King’s Profile. 75, 122, 124, 125

GMM Gaussian Mixture Model. 57, 61–63, 68, 70, 78, 79, 81, 91, 92, 94, 95, 119, 129, 130, 132–134, 152, 153

. 73, 75, 122, 124

GPU Graphics Processing Unit. 93, 97, 152

HMC Hamiltonian Monte Carlo. 86, 87

HMPS High Membership Probability Sample. 44, 72, 75, 150

HPC High-Performance Computing. 91, 92, 96, 149, 152

IMF Initial Mass Function. 2–7, 9, 33–35, 137, 142, 144, 145, 148, 151, 152

IS Intelligent System. 9, 11, 16–18, 149, 150

KDE Kernel Density Estimator. 3, 80

King-Bs King’s Biaxially symmetric and luminosity Segregated. 126, 128, 131

King-RS King’s Radially symmetric and luminosity Segregated. 126, 128, 131

KS Kolmogorov-Smirnov. 145

LACeWING LocAting Constituent mEmbers In Nearby Groups. 14

MAP Maximum A Posteriori. 49, 84, 85, 101, 121, 122, 124–126, 128, 142

MCMC Markov Chain Monte Carlo. 45, 70, 84–89, 91, 93, 120, 125, 149

MD Mass Distribution. 2

MF Mass Function. 2, 3

MH Metropolis-Hastings. 86, 87

MLE Maximum-Likelihood Estimator. 14, 63, 65, 70, 92, 94, 95

MPI Message Passing Interface. 92, 96, 97

Myr millions of years. 1, 7, 20, 29, 33, 139, 143, 151

NYC Nearby Young Clusters. ii–v, 8, 9, 39, 60, 99, 100, 143, 149–152

NYMG nearby young moving group. 13, 14

OGKing Optimised General King’s Profile. 75, 77, 122, 124, 125

PCA Principal Components Analysis. 14, 16

PDF Probability Density Function. ii, iv, 2, 46, 47, 49–51, 60, 74, 78, 79, 128, 149, 150

PDFCP Probability Density Function of the Cluster Population. ii–iv

PDMF Present-Day Mass Function. 3, 4

PDSMD Present-Day System Mass Distribution. iii, v, 33, 39, 139–148, 151, 152

PDSMF Present-Day System Mass Function. 4

PGM Probabilistic Graphical Model. 56, 57, 71

PPV Positive Predictive Value. 102–105

PSD Projected Spatial Distribution. 22, 24, 25, 36, 39, 44, 72, 121, 150, 151

PSO Particle Swarm Optimiser. 84, 85, 90, 91, 93, 94, 149

RDDR2 Restricted Pleiades DANCe Data Release 2. 43, 44, 61–63, 99–101, 103, 108, 109, 120, 143, 150

. 75, 77, 121, 124, 125, 128

ROC Receiver Operating Characteristic. iii, iv, 107, 108, 150

RT1 Rebull Table 1. 114, 115

RT2 Rebull Table 2. 115, 116

ST1 Stauffer Table 1. 109, 110

ST2 Stauffer Table 2. 109, 110

TGAS *Tycho-Gaia* Astrometric Solution. 22, 24

TN True Negative. 102

TP True Positive. 102

TPR True Positive Rate. 102–104, 106, 107, 112, 114, 150

TVD Transverse Velocity Distribution. 26, 27

UPMASK Unsupervised Photometric Membership Assignment in Stellar cluster. 14